



# Development of Advanced In-Cylinder Components and Tribological Systems for Low Heat Rejection Diesel Engines

## Phases 2, 3, and 4 Final Report

T.M. Yonushonis, P.D. Wiczynski, M.R. Myers, D.D. Anderson, A.C. McDonald, H.G. Weber, D.E. Richardson, R.J. Stafford, and M.G. Naylor  
Cummins Engine Company, Columbus, Indiana

Distribution A  
Approved for public release;  
Further dissemination unlimited.  
(Unclassified Unlimited)

Prepared under Contract DEN3-375  
National Aeronautics and  
Space Administration  
Glenn Research Center

Under Interagency Agreement DE-AI05-960R22547  
for  
U.S. Department of Energy  
Conservation and Renewable Energy  
Office of Vehicle and Engine R&D  
Washington, D.C.

This report was prepared as an account of work sponsored by an agency of the United States Government. Neither the United States Government nor any agency thereof, nor any of their employees, nor any of their contractors, subcontractors or their employees, makes any warranty, expressed or implied or assumes any legal liability or responsibility for the accuracy, completeness, or any third party's use or the results of such use of any information, apparatus, product, or process disclosed, or represents that its use would not infringe privately owned rights. Reference herein to any specific commercial product, process or service by trade name, trademark, manufacturer or otherwise, does not necessarily constitute or imply its endorsement, recommendation, or favoring by the United States Government or any agency thereof or its contractors or subcontractors. The views and opinions of authors expressed herein do not necessarily state or reflect those of the United States Government or any agency thereof.

Available from

NASA Center for Aerospace Information  
7121 Standard Drive  
Hanover, MD 21076  
Price Code: A13

National Technical Information Service  
5285 Port Royal Road  
Springfield, VA 22100  
Price Code: A13

# TABLE OF CONTENTS

<b>List of Figures .....</b>	<b>vii</b>
<b>List of Tables .....</b>	<b>xxi</b>
<b>List of Equations .....</b>	<b>xxv</b>
<b>1.0 Summary .....</b>	<b>1</b>
<b>2.0 Introduction .....</b>	<b>3</b>
2.1 Phase 1 Results.....	5
2.2 Phase 2, Phase 3, and Phase 4 Objectives .....	5
2.3 Background on Advances in Diesel Engines.....	6
<b>3.0 Component Development, Fabrication and Testing .....</b>	<b>8</b>
3.1 Spherical Joint Piston.....	8
3.1.1 Aluminum Squeeze Cast Piston .....	9
3.1.2 Niresist Chip Ring Carrier Insert.....	11
3.1.3 Pulsation Testing.....	11
3.1.4 Assembly and Engine Testing .....	13
3.1.4.1 Motoring Tests .....	14
3.1.4.2 Firing Tests.....	18
3.1.5 Piston Rotation Measurement .....	20
3.1.6 Modeled Temperature Comparison.....	23
3.1.7 Design for Manufacture.....	25
3.1.8 Conclusions - Spherical Joint Piston.....	27
3.2 Spherical Joint Connecting Rod.....	28
3.2.1 Baseline Design.....	28
3.2.2 Finite Element Analysis .....	28
3.2.3 Machining Development .....	37
3.2.4 Fabrication and Testing.....	38
3.2.5 Conclusions - Spherical Joint Connecting Rod.....	41
3.3 Spherical Joint Piston Telemetry.....	42
3.3.1 Design Specifications.....	42
3.3.2 Power Generator.....	45
3.3.3 Rig Test and Validation.....	48

3.3.4	Conclusions - Spherical Joint Piston Telemetry .....	51
3.4	Alternative Piston Designs .....	52
3.4.1	Nickel Aluminide Crown for Articulated Pistons .....	52
3.4.2	Titanium Aluminide Crown for Articulated Pistons .....	53
3.4.3	Conclusions - Alternative Piston Designs .....	54
3.5	Steel Compression Rings .....	55
3.5.1	Material Selection .....	55
3.5.2	Ring Geometry .....	58
3.5.3	Face Coating Selection .....	59
3.5.4	Conclusions - Steel Compression Rings .....	61
3.5.5	Engine Testing of Steel Compression Rings .....	61
3.5.5.1	Oil Consumption - Reduced Cross Section Steel Rings	61
3.5.5.2	Description of Full Cross Section Steel Rings Tested ...	62
3.5.5.3	Summary of Results - Full Cross Section Steel Rings ...	62
3.5.5.3.1	Oil Consumption .....	62
3.5.5.3.2	Coating Durability .....	63
3.5.5.3.3	Metallurgical Evaluation .....	63
3.5.5.3.4	Conclusions - Engine Testing .....	63
3.6	Thermal Barrier Coatings .....	64
3.6.1	Coating Development for Diesel Engines .....	65
3.6.1.1	Modeling .....	65
3.6.1.2	Spray Fabrication and Rig Tests .....	68
3.6.2	Engine Evaluation .....	69
3.6.3	Nondestructive Evaluation .....	70
3.6.4	Coating Crack Initiation .....	71
3.6.5	Emissions and Engine Fuel Economy .....	72
3.6.6	Conclusions - Thermal Barrier Coatings .....	74
3.7	Insulated Cylinder Head .....	75
3.7.1	Strategic Oil Cooling .....	77
3.7.2	Combustion Face Insert .....	78
3.7.3	Finite Element Analysis .....	78
3.7.4	Port Liner Development .....	84



3.7.5	Casting Development .....	84
3.7.6	Port Flow Testing .....	85
3.7.7	Engine Testing - Port Liners .....	86
3.7.8	Engine Testing - Oil Drilling Turbulators .....	92
3.7.9	Conclusions - Insulated Cylinder Head .....	100
3.8	Radial Combustion Seal Cylinder Liner .....	102
3.8.1	Bore Distortion Testing .....	103
3.8.2	Sealability Testing .....	106
3.8.3	Cooling Jacket Heat Transfer Enhancement .....	107
3.8.4	Conclusions - Radial Combustion Seal Cylinder Liner .....	115
3.9	Alternative Combustion Seals .....	116
3.9.1	C-Ring Seal and Omega Seal .....	116
3.9.2	Assembly and Engine Test .....	117
3.9.3	Conclusions - Alternative Combustion Seals .....	118
3.10	Powdered Metal Cylinder Liner .....	119
3.10.1	Material Selection .....	119
3.10.2	Wear Testing .....	121
3.10.3	Wear Surfaces .....	124
3.10.4	Conclusions - Powdered Metal Cylinder Liner .....	125
3.11	System Demonstration Testing .....	126
3.11.1	Engine Test Matrices .....	126
3.11.2	Post Test Analysis .....	127
3.11.3	Conclusions - System Demonstration Testing .....	128
3.12	Effects of Insulation on Performance and In-Cylinder Heat Transfer .....	129
3.12.1	Experimental Measurements on the Effects of Piston Insulation .....	129
3.12.1.1	Experimental Set-Up .....	129
3.12.1.2	Experimental Method .....	131
3.12.1.3	Error Analysis .....	133
3.12.1.4	Results .....	135
3.12.1.5	Discussion of Results .....	145
3.12.1.6	Conclusions .....	149

3.12.2 Experimental Measurements on the Effects of Piston Surface Roughness and Porosity .....	150
3.12.2.1 Experimental Set-Up .....	150
3.12.2.2 Experimental Method .....	152
3.12.2.3 Results .....	155
3.12.2.4 Discussion of Results .....	162
3.12.2.5 Conclusions .....	164
3.13 Variable Geometry Turbocharger .....	165
3.13.1 Systems Considered .....	166
3.13.2 Turbocharger Design and Bench Test .....	167
3.13.3 Control Strategy and Design .....	170
3.13.4 System Testing .....	172
3.13.5 Conclusions - Variable Geometry Turbocharger .....	175
3.14 Silicon Carbide Particulate Trap .....	176
3.14.1 Filter Development .....	176
3.14.2 Microwave Heating .....	180
3.14.3 System Evaluation .....	182
3.14.4 Economics .....	184
3.14.5 Conclusions - Silicon Carbide Particulate Trap .....	185
3.15 Lightweight Low Magnetic Signature Engine Development .....	186
3.15.1 Aluminum Cylinder Head Analysis .....	186
3.15.2 Aluminum Cylinder Block Analysis .....	195
3.15.3 Mechanical Properties of Aluminum Alloys for Cylinder Blocks and Heads .....	208
3.15.4 Structural Analysis and Testing .....	214
3.15.4.1 Cylinder Block .....	214
3.15.4.1.1 Photostress Analysis .....	215
3.15.4.1.2 Strain Gage Analysis .....	216
3.15.4.1.3 Block Fatigue Test .....	218
3.15.4.2 Cylinder Head .....	221
3.15.4.2.1 Head Lift .....	221
3.15.4.2.1 Cylinder Pressure Resistance .....	221
3.15.5 Structural Reinforcement Strategy .....	222

3.15.6	Metallurgical Bonding Study .....	223
3.15.7	Engine Testing and Validation .....	225
3.15.7.1	Engine #1.....	225
3.15.7.1.1	Engine #1, Test 1.....	225
3.15.7.1.2	Engine #1, Test 2.....	226
3.15.7.2	Engine #2.....	226
3.15.7.2.1	Engine #2, Test 1.....	226
3.15.7.2.2	Engine #2, Test 2.....	227
3.15.7.2.3	Engine #2, Test 3.....	227
3.15.7.3	Engine #3.....	228
3.15.8	Cylinder Head Testing.....	228
3.15.9	Lightweight Connecting Rods.....	228
3.15.10	Lightweight Low Magnetic Signature Main Bearing Caps .....	231
3.15.11	Conclusions - Lightweight Low Magnetic Signature Engine Development.....	233
<b>4.0</b>	<b>Acknowledgements.....</b>	<b>235</b>
<b>5.0</b>	<b>References .....</b>	<b>237</b>
<b>6.0</b>	<b>Appendices .....</b>	<b>240</b>
6.1	Appendix I - LE-55 Performance Development .....	240
6.1.1	Performance Basis Development .....	240
6.1.2	Engine Test Verification .....	241
6.2	Appendix II - LE-55 Emissions Prediction .....	243
6.2.1	Methodology .....	243
6.2.2	Measured and Simulated Data Comparison .....	244
6.2.3	LE-55 Emissions Prediction.....	245
6.2.4	Conclusions - LE-55 Emissions Prediction.....	246
6.3	Appendix III - CD-50 Performance Analysis.....	247
6.3.1	Baseline Engine Optimization.....	247
6.3.1.1	TRANSENG Calibration.....	247
6.3.1.2	Baseline Optimization .....	248
6.3.2	Application of Subsystem Improvements .....	249
6.3.2.1	Port Insulation .....	250

6.3.2.2	Shortened Heat Release Duration.....	252
6.3.2.3	Reduced FMEP .....	252
6.3.2.4	Improved Turbomachinery Efficiencies .....	252
6.3.3	Optimization at “Design Point” .....	252
6.3.4	Fixed Versus “Ideal” Variable Geometry Turbomachinery .....	254
6.3.5	Two Stage Turbocharging .....	255
6.3.6	Conclusions - CD-50 Performance Analysis.....	256
6.4	Appendix IV - Piston Surface Porosity Volume Calculation .....	257

## LIST OF FIGURES

<b>Figure No.</b>	<b>Description</b>	<b>Page</b>
3.1.1	Spherical joint piston assembly.	8
3.1.2	Squeeze cast aluminum spherical joint piston casting with alumina fiber reinforcement.	9
3.1.3	Conventional and spherical joint piston bearing area comparison.	10
3.1.4	Schematic of hydropulse test rig.	12
3.1.5	Initial design iteration of the spherical joint piston and connecting rod.	13
3.1.6	Single cylinder L10 engine (SCE L10).	14
3.1.7	Spherical joint piston motoring test sequence.	15
3.1.8	Galled holder ring (top) and connecting rod sphere (bottom) from the first motoring test.	16
3.1.9	Comparison of original and redesigned holder rings.	17
3.1.10	Piston rotation measurement hardware.	20
3.1.11	Map of skirt groove radii.	21
3.1.12	Piston angular position – idle-to-full-load conditions.	22
3.1.13	Piston angular position – full-load-to-idle conditions.	22
3.1.14	Modeled temperatures (°C) versus measured temperatures comparison.	24
3.1.15	Proposed one-piece spherical joint piston design.	25
3.1.16	Proposed connecting rod installation for the one-piece spherical joint piston.	26
3.2.1	Stress contours for the combustion stroke – baseline connecting rod design.	29
3.2.2	Stress contours for the intake stroke – baseline rod design.	30

<b>Figure No.</b>	<b>Description</b>	<b>Page</b>
3.2.3	Stress contours for the combustion stroke – initial modified connecting rod design.	31
3.2.4	Stress contours for the intake stroke – initial modified connecting rod design.	31
3.2.5	Final finite element model of the spherical joint connecting rod.	32
3.2.6	Stress contours for the preloaded case – final modified rod design	33
3.2.7	Stress contours for the preloaded case – final modified design viewed from the bearing side.	33
3.2.8	Von Mises stress contours for the combustion stroke – final modified design.	34
3.2.9	Von Mises stress contours for the combustion stroke – final modified design viewed from the bearing side.	35
3.2.10	Equivalent fully reversed stress contours for the combustion stroke – final modified design.	35
3.2.11	Equivalent fully reversed stress contours for the combustion stroke – final modified design viewed from the bearing side.	35
3.2.12	Von Mises stress contours for the intake stroke – final modified design.	36
3.2.13	Von Mises stress contours for the intake stroke – final modified design.	36
3.2.14	Connecting rod oil drillings.	39
3.2.15	Slotted connecting rod big end bearings.	40
3.2.16	Final design (finished) of the spherical joint connecting rod.	41
3.3.1	Telemetry system module packaging for the spherical joint piston.	44
3.3.2	Piston mounted temperature telemetry module functional block diagram.	44

<b>Figure No.</b>	<b>Description</b>	<b>Page</b>
3.3.3	Schematic of linear power generator.	46
3.3.4	Calculated power generator voltage waveform.	47
3.3.5	Cast iron cylinder liner with axial grooves in the OD as used in the lathe (rotating) test rig.	48
3.3.6	Plot of power generator output versus rig rotational speed and total number of coil turns.	49
3.3.7	Single cylinder engine motoring test rig.	50
3.3.8	Linear commutator system on motoring engine test rig.	50
3.4.1	Comparison of specific strength versus temperature for nickel aluminide, 4140 steel and aluminum.	52
3.4.2	Comparison of specific strength versus temperature for titanium aluminide, nickel aluminide, 4140 steel and aluminum.	53
3.5.1	Ring and ring carrier wear coefficients in fresh and sooted oils for various ring and ring carrier materials.	57
3.5.2	Cross section comparison for a standard and reduced cross section top compression ring.	59
3.5.3	Ring and cylinder liner wear coefficients for various ring materials and ring coatings.	61
3.6.1	Coating strength to stress ratio through the thickness of a multilayer zirconia based coating.	66
3.6.2	Coating temperature changes during cooling from steady state engine conditions.	67
3.6.3	Estimated stresses in a multilayer zirconia based coating during cooling.	67
3.6.4	Lifetime improvements in thermal barrier coatings in cyclic diesel engine tests.	70

<b>Figure No.</b>	<b>Description</b>	<b>Page</b>
3.6.5	Comparison of metal and zirconia coated pistons at 1800 rpm and rated load. Indicated specific fuel consumption (ISFC) versus centroid of area where 95% of heat release has occurred.	73
3.6.6	Comparison of metal and mullite coated pistons at 1800 rpm and rated load. Sweeps refer to specific timing sweeps when data was collected.	73
3.6.7	Fuel specific NO <sub>x</sub> and particulate trade-off curve for metal, zirconia, and mullite coated pistons at 1800 rpm and part load conditions.	74
3.7.1	Finite element mesh of the LE-55 cylinder head.	76
3.7.2	Experimental convection coefficient versus flow rate for various turbulator designs.	77
3.7.3	Experimental pressure drop versus flow rate for various turbulator designs.	78
3.7.4	Finite element mesh of the NASA cylinder, cylinder liner, and engine block.	79
3.7.5	Structural boundary conditions used in the NASA cylinder head FEA.	80
3.7.6	Convective boundary conditions used in the NASA cylinder head FEA.	81
3.7.7	Percent reduction in metal temperature as compared to the baseline cylinder head for various insulating design options.	82
3.7.8	Steady state FE temperature analysis of the fully insulated NASA cylinder head at 1500 rpm and full load (355 kW).	83
3.7.9	Steady state FE temperature analysis of the fully insulated NASA cylinder head at 1500 rpm and full load (355 kW). Sectioned view.	83
3.7.10	Effective flow area versus valve lift comparison for the L10 and LE-55 cylinder heads.	86
3.7.11	Metal temperatures measured above the exhaust port with and without ceramic insulation.	88



<b>Figure No.</b>	<b>Description</b>	<b>Page</b>
3.7.12	Metal temperatures measure at the exhaust-exhaust valve bridge with and without ceramic insulation.	88
3.7.13	Metal temperatures measured below the exhaust port with and without ceramic insulation.	89
3.7.14	Specific fuel consumption comparison, 1500 rpm, 30:1 air-fuel ratio.	90
3.7.15	Specific fuel consumption measured at 1500 rpm, 25:1 air-fuel ratio, with and without port insulation.	91
3.7.16	Volumetric efficiency measured at 1500 rpm, 25:1 air-fuel ratio, with and without insulation.	91
3.7.17	Volumetric efficiency measured at 1800 rpm, 30:1 air-fuel ratio, with and without insulation.	92
3.7.18	Exhaust gas temperature measure at 1800 rpm, 25:1 air-fuel ratio, with and without insulation.	92
3.7.19	Metal temperatures above the exhaust port, with and without turbulators, 25:1 air-fuel ratio.	94
3.7.20	Metal temperatures above the exhaust port, with and without turbulators, 30:1 air-fuel ratio.	95
3.7.21	Metal temperatures below the exhaust port, above the oil drilling, 27 mm above the combustion surface, with and without turbulators, 25:1 air-fuel ratio.	95
3.7.22	Metal temperatures below the exhaust port, above the oil drilling, 27 mm above the combustion surface, with and without turbulators, 30:1 air-fuel ratio.	96
3.7.23	Metal temperatures at the exhaust-exhaust valve bridge, 9 mm above the combustion face, with and without turbulators, 25:1 air-fuel ratio.	96
3.7.24	Metal temperatures at the exhaust-exhaust valve bridge, 9 mm above the combustion face, with and without turbulators, 30:1 air-fuel ratio.	97
3.7.25	Metal temperatures above the oil drilling, intake side, with and without turbulators, 25:1 air-fuel ratio.	97

<b>Figure No.</b>	<b>Description</b>	<b>Page</b>
3.7.26	Metal temperatures above the oil drilling, intake side, with and without turbulators, 30:1 air-fuel ratio.	98
3.7.27	Metal temperatures 9 mm above the combustion surface, intake-exhaust valve bridge side, with and without turbulators, 25:1 air-fuel ratio.	98
3.7.28	Metal temperatures 9 mm above the combustion surface, intake-exhaust valve bridge side, with and without turbulators, 30:1 air-fuel ratio.	99
3.7.29	Percent temperature reduction at head thermocouple location, 25:1 air-fuel ratio.	99
3.7.30	Percent temperature reduction at head thermocouple location, 30:1 air-fuel ratio.	100
3.8.1	Radial combustion seal cylinder liner concept.	102
3.8.2	Standard cylinder liner versus radial combustion seal cylinder liner force comparison and the effects on bore distortion.	103
3.8.3	RMS distortion comparison between a 1991 Cummins L10 cylinder liner and a radial combustion seal cylinder liner at the upper region of the bore.	104
3.8.4	RMS distortion comparison between a 1991 Cummins L10 cylinder liner and a radial combustion seal cylinder liner at the lower region of the bore.	105
3.8.5	Harmonic orders of distortion.	105
3.8.6	Heat transfer rate comparison for various cylinder liner heat transfer enhancements.	107
3.8.7	Thermocouple locations on the cylinder liner with large axial cooling jacket fins. All dimensions in millimeters.	108
3.8.8	Cylinder liner temperatures at first ring top reversal, 25:1 air-fuel ratio.	109
3.8.9	Cylinder liner temperatures at first ring top reversal, 30:1 air-fuel ratio.	110

<b>Figure No.</b>	<b>Description</b>	<b>Page</b>
3.8.10	Cylinder liner temperatures at second ring top reversal, 25:1 air-fuel ratio.	110
3.8.11	Cylinder liner temperatures at second ring top reversal, 30:1 air-fuel ratio.	111
3.8.12	Cylinder liner temperatures at first ring bottom reversal, 25:1 air-fuel ratio.	111
3.8.13	Cylinder liner temperatures at first ring bottom reversal, 30:1 air-fuel ratio.	112
3.8.14	Finned cylinder liner temperatures at first ring top reversal versus coolant oil flow rate, 25:1 air-fuel ratio.	112
3.8.15	Finned cylinder liner temperatures at second ring top reversal versus coolant oil flow rate, 25:1 air-fuel ratio.	113
3.8.16	Finned cylinder liner temperatures at first ring bottom reversal versus coolant oil flow rate, 25:1 air-fuel ratio.	113
3.8.17	Standard cylinder liner temperatures at first ring top reversal versus coolant oil flow rate, 25:1 air-fuel ratio.	114
3.8.18	Standard cylinder liner temperatures at second ring top reversal versus coolant oil flow rate, 25:1 air-fuel ratio.	114
3.8.19	Standard cylinder liner temperatures at first ring bottom reversal versus coolant oil flow rate, 25:1 air-fuel ratio.	115
3.9.1	Installed C-ring combustion seal geometry.	116
3.9.2	Installed Omega combustion seal geometry.	116
3.10.1	Normalized average wear for various cylinder liner materials.	121
3.10.2	Normalized average ring wear tested against various cylinder liner materials.	122
3.10.3	Normalized average friction for various cylinder liner materials.	122
3.10.4	Ring wear coefficient for various cylinder liner materials in fresh oil at 200°C. Rings coated with HVOF CR <sub>3</sub> C <sub>2</sub> – 20% NiCr.	123

<b>Figure No.</b>	<b>Description</b>	<b>Page</b>
3.10.5	Ring wear coefficient for various cylinder liner materials in fresh oil at 350°C. Rings coated with HVOF $\text{CR}_3\text{C}_2$ – 20% NiCr.	123
3.10.6	Ring wear coefficient for various cylinder liner materials in sooted oil at 200°C. Rings coated with HVOF $\text{CR}_3\text{C}_2$ – 20% NiCr.	124
3.12.1	Typical ISFC versus centroid curve for a diesel engine.	132
3.12.2	Two timing sweeps for 1200 rpm, part load using the uncoated piston.	136
3.12.3	Two timing sweeps for 1200 rpm, full load using the uncoated piston.	136
3.12.4	Four timing sweeps for 1800 rpm, part load using two identical uncoated pistons.	136
3.12.5	Two timing sweeps for 1800 rpm, full load using the uncoated piston.	137
3.12.6	Two timing sweeps for 1800 rpm, part load using the uncoated piston.	138
3.12.7	All four uncoated piston and two zirconia coated piston timing sweeps at 1800 rpm, part load.	138
3.12.8	Two uncoated piston and two zirconia coated piston timing sweeps at 1800 rpm, full load.	139
3.12.9	BSFC comparison of uncoated piston and zirconia coated piston timing sweeps at 1800 rpm, part load.	140
3.12.10	BSFC comparison of uncoated piston and zirconia coated piston timing sweeps at 1800 rpm, full load.	140
3.12.11	Uncoated piston and four timing sweeps with the mullite coated piston, 1800 rpm, part load.	141
3.12.12	Uncoated piston and mullite coated piston timing sweeps, 1800 rpm, full load.	142
3.12.13	BSFC comparison of uncoated piston and mullite coated piston timing sweeps at 1800 rpm, part load.	142

<b>Figure No.</b>	<b>Description</b>	<b>Page</b>
3.12.14	BSFC comparison of uncoated piston and mullite coated piston timing sweeps at 1800 rpm, full load.	143
3.12.15	Uncoated piston and mullite coated piston apparent heat release rates, 1800 rpm, full load.	143
3.12.16	Premixed burn fraction for the three piston coating conditions, 1800 rpm, part load as a function of nominal injection timing (TVC).	144
3.12.17	Fuel specific NO <sub>x</sub> /particulate trade-off curve for the three piston coating conditions, 1800 rpm, part load.	144
3.2.18	Push tube loads for uncoated piston and mullite coated piston timing sweeps, 1800 rpm, part load. Push tube loads for -10, -20, -30, -40 and -60 TVC.	145
3.12.19	Prediction of the percentage of fuel which could potentially reach the piston or bowl as a function of injection timing.	146
3.12.20	Results of engine simulation analysis on ISFC as a function of heat transfer and heat release shape compared to the measured data.	147
3.12.21	Photomicrograph of the low porosity coating.	153
3.12.22	Photomicrograph of the high porosity coating.	154
3.12.23	ISFC versus centroid for the uncoated piston, rough bond coating and high porosity coating at 1200 rpm, part load.	155
3.12.24	ISFC versus centroid for the uncoated piston, rough bond coating and high porosity coating at 1200 rpm, full load.	155
3.12.25	ISFC versus centroid for the uncoated piston, rough bond coating and high porosity coating at 1800 rpm, part load.	156
3.12.26	ISFC versus centroid for the uncoated piston, rough bond coating and high porosity coating at 1800 rpm, full load.	156
3.12.27	ISFC versus centroid for the uncoated piston, rough bond coating and high porosity coating at 1200 rpm, part load.	157
3.12.28	ISFC versus centroid for the uncoated piston, rough bond coating and high porosity coating at 1200 rpm, full load.	157

<b>Figure No.</b>	<b>Description</b>	<b>Page</b>
3.12.29	ISFC versus centroid for the uncoated piston, rough bond coating and high porosity coating at 1800 rpm, part load.	158
3.12.30	ISFC versus centroid for the uncoated piston, rough bond coating and high porosity coating at 1800 rpm, full load.	158
3.12.31	ISFC versus start of injection for the uncoated piston, rough bond coating and high porosity coating at 1800 rpm, part load.	159
3.12.32	Apparent heat release rates for the uncoated piston, rough bond coating and high porosity coating at 1200 rpm, part load, -15 cad SOI.	160
3.12.33	Apparent heat release rates for the uncoated piston, rough bond coating and high porosity coating at 1800 rpm, full load, -15 cad SOI.	160
3.12.34	ISFC versus centroid for the high, medium and low porosity coatings 1200 rpm, full load.	161
3.12.35	ISFC versus centroid for the high, medium and low porosity coatings 1800 rpm, full load.	161
3.12.36	Apparent heat release rates for the high, medium and low porosity coatings at 1200 rpm, part load.	162
3.12.37	Apparent heat release rates for the high, medium and low porosity coatings at 1800 rpm, part load.	162
3.13.1	Scheme used to vary VG turbine nozzle height.	167
3.13.2	Cutaway of turbocharger with variable geometry turbine.	168
3.13.3	Close-up of partly opened VG turbine nozzles.	168
3.13.4	Close-up of fully opened VG turbine nozzles.	169
3.13.5	VG turbine performance map at one nozzle opening condition.	169
3.13.6	VG turbine performance at 2.0 pressure ratio, peak efficiency and several nozzle openings.	170
3.13.7	Block diagram of VG turbocharger engine system showing measured and compared parameters.	171

<b>Figure No.</b>	<b>Description</b>	<b>Page</b>
3.13.8	VG turbocharger control system.	172
3.13.9	VG turbocharger installed for testing on engine.	173
3.13.10	VG turbocharger system test and development plan.	173
3.13.11	VG turbocharger test results from constant engine speed snap throttle testing.	174
3.13.12	Results from VG turbocharger system tests on the FTP transient cycle.	175
3.14.1	Efficiency and pressure drop versus time for a Microglass filter.	177
3.14.2	Microwave particulate filter dimensions and geometry.	179
3.14.3	Gas flow through filter media.	179
3.14.4	SiC coated alumina fiber filter.	180
3.14.5	Microwave heating showing large thermal gradient.	181
3.14.6	Improved thermal gradient.	181
3.14.7	Test cell evaluation of microwave particulate filter.	182
3.14.8	Magnetron power turned on at 1000 seconds.	183
3.14.9	Temperature increase observed at engine idle speed with magnetron powered.	184
3.15.1	Temperature distribution of the cast iron firedeck.	187
3.15.2	Temperature distribution for the aluminum firedeck.	188
3.15.3	Local 3-D mesh geometry of 6B-series aluminum cylinder head with bow tie.	189
3.15.4	Thermal stress contours on the firedeck for the aluminum baseline.	190
3.15.5	Effect of the bow tie material and thickness on the stress/strength ratio on the valve bridge.	191

<b>Figure No.</b>	<b>Description</b>	<b>Page</b>
3.15.6	Effect of bow tie insert material and aluminum head alloy on the stress/strength ratio in the valve bridge.	194
3.15.7	Effect of bow tie insert material and aluminum head alloy on the ratio of alternating stress to fatigue strength in the valve bridge.	194
3.15.8	Temperature plot for the cast iron cylinder block – bore side.	195
3.15.9	Temperature plot for the aluminum cylinder block – bore side.	196
3.15.10	Alternating stresses in the cast iron cylinder block.	196
3.15.11	Alternating stresses in the aluminum cylinder block.	197
3.15.12	Steady state temperature distribution with perfectly bonded cylinder liners.	198
3.15.13	Strain (in the y-direction) contours of aluminum cylinder block.	199
3.15.14	Cylinder block model showing the zones reinforced by steel inserts.	200
3.15.15	Assembly stress contours at the end of the capscrews in saddle #7.	202
3.15.16	Dynamic stress contours in the center plane of the capscrew holes.	203
3.15.17	Dynamic stress contours at the ends of the capscrews in saddle #7.	204
3.15.18	Maximum stresses comparison between the exhaust side and cam bore side at the capscrew ends of saddles #5 and #7.	204
3.15.19	Modified Goodman diagram comparing saddle #5 and saddle #7.	205
3.15.20	Assembly stress contours at the ends of the capscrews (with insert).	206
3.15.21	Dynamic stress contours in the center plane of the capscrew holes (with saddle inserts).	206



<b>Figure No.</b>	<b>Description</b>	<b>Page</b>
3.15.22	Dynamic stress contours at the ends of the capscrews (with saddle inserts).	207
3.15.23	Modified Goodman diagram with saddle #7 with and without saddle inserts.	208
3.15.24	Elastic modulus as a function of temperature after 500 hours thermal aging.	209
3.15.25	Ultimate tensile strength as a function of temperature after 500 hours thermal aging.	210
3.15.26	Compressive yield strength as a function of temperature after 500 hours thermal aging.	211
3.15.27	Elongation as a function of temperature after 500 hours thermal aging.	212
3.15.28	Strain-life fatigue data for the aluminum alloys at room temperature.	212
3.15.29	Strain-life fatigue data for the aluminum alloys tested at 260°C after 100 hours of thermal aging.	213
3.15.30	Photostress results on the main bearing saddles with the application of bolt torque.	215
3.15.31	Photostress results on the maid bearing saddles with the application of 15.2 MPa cylinder pressure.	216
3.15.32	Location of strain gages in the main bulkhead region.	217
3.15.33	Design margin as a function of cylinder pressure for the location at the end of the capscrew in the main bearing saddles.	217
3.15.34	Cylinder block fatigue data.	218
3.15.35	Crack locations in the aluminum cylinder block.	219
3.15.36	Cylinder block with thickened main bearing saddles.	219
3.15.37	Comparison of the fatigue strength of threads with helicoil inserts and rolled threads.	220
3.15.38	Hydraulic pressure test results on aluminum alloy heads.	222

<b>Figure No.</b>	<b>Description</b>	<b>Page</b>
3.15.39	Main bearing saddle inserts.	223
3.15.40	Comparison of fatigue curves for the 50-55 Vf.% SiC <sub>p</sub> /Al and Al <sub>2</sub> O <sub>3</sub> /Al MMC's at room temperature.	232
I.1	LogP-LogV plot of cylinder pressure at LE-55 operating point.	242
III.1	Cross-section of port with corresponding heat transfer elements.	250
III.2	Port wall with insulation.	251
III.3	Diagram of two-stage compression model.	255
IV.1	Porosimetry sample.	257

## LIST OF TABLES

<b>Table No.</b>	<b>Description</b>	<b>Page</b>
2.1	Engine configuration for achieving LE-55 fuel consumption target	3
2.2	Components designed, fabricated and tested in Phases 2, 3 and 4	4
3.1.1	Test sequence for the third motoring test	18
3.1.2	SCE L10 operating conditions for first firing test	18
3.1.3	SCE L10 operating conditions for the 25 hour, high peak cylinder pressure test	19
3.1.4	SCE L10 operating conditions compared to LE-55 operating point for the piston temperature telemetry test	23
3.2.1	Stress maxima for three connecting rod designs	32
3.2.2	FE analysis stresses and limits in the final modified connecting rod design	37
3.2.3	Connecting rod E4340H alloy steel chemistry	38
3.2.4	Summary of sphere surface finish	38
3.3.1	Telemetry system design goals	43
3.3.2	Telemetry measurement and environmental specifications	43
3.4.1	Percentage composition by weight of nickel aluminide alloy IC-221M	52
3.4.2	Percentage composition by weight of titanium aluminide alloy	54
3.5.1	Endurance limit data (mm) from the fatigue tests on different materials and coatings	56
3.5.2	Wear rate coefficient in $\text{mm}^3/\text{N-mm} \times 10^{10}$ for various ring and ring groove materials in fresh and sooted oils	58

<b>Table No.</b>	<b>Description</b>	<b>Page</b>
3.5.3	Results from the physical property tests conducted on various ring coatings and bond coats	59
3.5.4	Oil consumption results comparing steel and ductile iron rings in a single cylinder engine	62
3.7.1	Properties of materials used in ceramic port development	84
3.7.2	LE-55 engine recipe and actual test conditions	87
3.7.3	Cylinder head temperature reduction comparison	89
3.7.4	Engine conditions run during evaluation of oil drilling turbulators	93
3.7.5	Benefits of ceramic port insulation	101
3.8.1	Engine operating parameters held constant for cylinder liner heat transfer fin evaluation	108
3.9.1	C-ring and Omega combustion seal data	117
3.9.2	Test results of C-ring combustion seal – 20.7 MPa peak cylinder pressure	118
3.9.3	Test results of Omega combustion seal – 20.7 MPa peak cylinder pressure	118
3.10.1	Comparison of mechanical properties of gray cast iron, TS56, TS62 and TS29 cylinder liner materials. Values listed are typical for the materials studied.	120
3.10.2	Percent composition by weight for gray cast iron and various PM cylinder liner materials	120
3.11.1	100 hour steady state and thermal cycle engine parameters for system demonstration testing	126
3.12.1	Test matrix for back-to-back engine tests	130
3.12.2	Piston coatings and the number of timing sweeps at each speed and load	131

<b>Table No.</b>	<b>Description</b>	<b>Page</b>
3.12.3	Error types associated with ISFC and heat release centroid measurements	133
3.12.4	Error sources associated with ISFC and heat release centroid measurements	135
3.12.5	Test matrix for back-to-back engine testing	151
3.12.6	Number of injection timing sweeps taken at each speed and load with each of the pistons	152
3.12.7	Piston coating characterization	154
3.13.1	Specifications for the VG turbocharger test engine	165
3.13.2	VG turbocharger limiting parameters	170
3.15.1	Material properties	186
3.15.2	Temperature and stresses between valve ports	187
3.15.3	Maximum compressive stress (P3) and temperature values (T) during an engine thermal cycle	191
3.15.4	Final results of the bow tie study	192
3.15.5	Assembly stress results due to valve seat insert press fit.	193
3.15.6	Results of the cylinder block stretch with different materials	200
3.15.7	Results of the cylinder block stretch with steel reinforcements	201
3.15.8	Engine test points – Engine #1, Test 1	225
3.15.9	Engine test points – Engine #2, Test 1	227
3.15.10	Cyclic endurance test conditions	227
3.15.11	Example of benefits of a lighter weight connecting rod	229
3.15.12	Alternate materials for connecting rods	230
I.1	SCE L10 operating condition achieved using the 1994 Cummins fuel system hardware	241

<b>Table No.</b>	<b>Description</b>	<b>Page</b>
II.1	Heavy duty diesel transient test simulation by 8-Mode cycle	243
II.2	Comparison of measured and simulated 8-Mode data – 1994 L10 design validation engine	244
II.3	Summary comparison of simulated 8-Mode weighted average, measured EPA FTP and measured 8-Mode data	245
III.1	M11 torque curve speeds and loads	248
III.2	Optimization results for baseline TRANSENG input files at each speed-load combination along the torque curve (PCP<19.3 MPa)	249
III.3	Comparison of engine performance parameters (baseline versus improved) at the “Design Point”	253
III.4	Magnitude of each improvement relative to fuel economy	253
III.5	Comparison of “Ideal” VG and FG turbomachinery	254
IV.1	Data used to calculate total pore volume	259

## LIST OF EQUATIONS

<b>Equation No.</b>	<b>Description</b>	<b>Page</b>
3.2.1	Equivalent fully reversed stress for a connecting rod	30
3.7.1	Volumetric efficiency - intake manifold	90
3.7.2	Turbulator wire spring diameter	93
3.7.3	Turbulator wire spring pitch	93
3.9.1	Cylinder head bolt clamping load	117
I.1	Gross mean indicated effective pressure (GIMEP)	240
III.1	Intake and exhaust port wall resistance	250
III.2	Reynold's equation	251
III.3	Nusselt equation	251
III.4	Convection coefficient	251
III.5	Friction mean effective pressure (FMEP)	252
III.6	Engine thermal efficiency	254
III.7	Turbocharger compressor power	255
III.8	Turbocharger compressor ideal intermediate pressure	256
IV.1	Sample total pore volume	257
IV.2	Coating volume	258
IV.3	Steel substrate volume	258
IV.4	Coating thickness/steel substrate thickness ratio	258
IV.5	Mass of porosimetry sample	258
IV.6	Final expression of coating volume	258

1  
2  
3  
4  
5  
6  
7  
8  
9  
10  
11  
12  
13  
14  
15  
16  
17  
18  
19  
20  
21  
22  
23  
24  
25  
26  
27  
28  
29  
30  
31  
32  
33  
34  
35  
36  
37  
38  
39  
40  
41  
42  
43  
44  
45  
46  
47  
48  
49  
50  
51  
52  
53  
54  
55  
56  
57  
58  
59  
60  
61  
62  
63  
64  
65  
66  
67  
68  
69  
70  
71  
72  
73  
74  
75  
76  
77  
78  
79  
80  
81  
82  
83  
84  
85  
86  
87  
88  
89  
90  
91  
92  
93  
94  
95  
96  
97  
98  
99  
100  
101  
102  
103  
104  
105  
106  
107  
108  
109  
110  
111  
112  
113  
114  
115  
116  
117  
118  
119  
120  
121  
122  
123  
124  
125  
126  
127  
128  
129  
130  
131  
132  
133  
134  
135  
136  
137  
138  
139  
140  
141  
142  
143  
144  
145  
146  
147  
148  
149  
150  
151  
152  
153  
154  
155  
156  
157  
158  
159  
160  
161  
162  
163  
164  
165  
166  
167  
168  
169  
170  
171  
172  
173  
174  
175  
176  
177  
178  
179  
180  
181  
182  
183  
184  
185  
186  
187  
188  
189  
190  
191  
192  
193  
194  
195  
196  
197  
198  
199  
200  
201  
202  
203  
204  
205  
206  
207  
208  
209  
210  
211  
212  
213  
214  
215  
216  
217  
218  
219  
220  
221  
222  
223  
224  
225  
226  
227  
228  
229  
230  
231  
232  
233  
234  
235  
236  
237  
238  
239  
240  
241  
242  
243  
244  
245  
246  
247  
248  
249  
250  
251  
252  
253  
254  
255  
256  
257  
258  
259  
260  
261  
262  
263  
264  
265  
266  
267  
268  
269  
270  
271  
272  
273  
274  
275  
276  
277  
278  
279  
280  
281  
282  
283  
284  
285  
286  
287  
288  
289  
290  
291  
292  
293  
294  
295  
296  
297  
298  
299  
300  
301  
302  
303  
304  
305  
306  
307  
308  
309  
310  
311  
312  
313  
314  
315  
316  
317  
318  
319  
320  
321  
322  
323  
324  
325  
326  
327  
328  
329  
330  
331  
332  
333  
334  
335  
336  
337  
338  
339  
340  
341  
342  
343  
344  
345  
346  
347  
348  
349  
350  
351  
352  
353  
354  
355  
356  
357  
358  
359  
360  
361  
362  
363  
364  
365  
366  
367  
368  
369  
370  
371  
372  
373  
374  
375  
376  
377  
378  
379  
380  
381  
382  
383  
384  
385  
386  
387  
388  
389  
390  
391  
392  
393  
394  
395  
396  
397  
398  
399  
400  
401  
402  
403  
404  
405  
406  
407  
408  
409  
410  
411  
412  
413  
414  
415  
416  
417  
418  
419  
420  
421  
422  
423  
424  
425  
426  
427  
428  
429  
430  
431  
432  
433  
434  
435  
436  
437  
438  
439  
440  
441  
442  
443  
444  
445  
446  
447  
448  
449  
450  
451  
452  
453  
454  
455  
456  
457  
458  
459  
460  
461  
462  
463  
464  
465  
466  
467  
468  
469  
470  
471  
472  
473  
474  
475  
476  
477  
478  
479  
480  
481  
482  
483  
484  
485  
486  
487  
488  
489  
490  
491  
492  
493  
494  
495  
496  
497  
498  
499  
500  
501  
502  
503  
504  
505  
506  
507  
508  
509  
510  
511  
512  
513  
514  
515  
516  
517  
518  
519  
520  
521  
522  
523  
524  
525  
526  
527  
528  
529  
530  
531  
532  
533  
534  
535  
536  
537  
538  
539  
540  
541  
542  
543  
544  
545  
546  
547  
548  
549  
550  
551  
552  
553  
554  
555  
556  
557  
558  
559  
560  
561  
562  
563  
564  
565  
566  
567  
568  
569  
570  
571  
572  
573  
574  
575  
576  
577  
578  
579  
580  
581  
582  
583  
584  
585  
586  
587  
588  
589  
590  
591  
592  
593  
594  
595  
596  
597  
598  
599  
600  
601  
602  
603  
604  
605  
606  
607  
608  
609  
610  
611  
612  
613  
614  
615  
616  
617  
618  
619  
620  
621  
622  
623  
624  
625  
626  
627  
628  
629  
630  
631  
632  
633  
634  
635  
636  
637  
638  
639  
640  
641  
642  
643  
644  
645  
646  
647  
648  
649  
650  
651  
652  
653  
654  
655  
656  
657  
658  
659  
660  
661  
662  
663  
664  
665  
666  
667  
668  
669  
670  
671  
672  
673  
674  
675  
676  
677  
678  
679  
680  
681  
682  
683  
684  
685  
686  
687  
688  
689  
690  
691  
692  
693  
694  
695  
696  
697  
698  
699  
700  
701  
702  
703  
704  
705  
706  
707  
708  
709  
710  
711  
712  
713  
714  
715  
716  
717  
718  
719  
720  
721  
722  
723  
724  
725  
726  
727  
728  
729  
730  
731  
732  
733  
734  
735  
736  
737  
738  
739  
740  
741  
742  
743  
744  
745  
746  
747  
748  
749  
750  
751  
752  
753  
754  
755  
756  
757  
758  
759  
760  
761  
762  
763  
764  
765  
766  
767  
768  
769  
770  
771  
772  
773  
774  
775  
776  
777  
778  
779  
780  
781  
782  
783  
784  
785  
786  
787  
788  
789  
790  
791  
792  
793  
794  
795  
796  
797  
798  
799  
800  
801  
802  
803  
804  
805  
806  
807  
808  
809  
810  
811  
812  
813  
814  
815  
816  
817  
818  
819  
820  
821  
822  
823  
824  
825  
826  
827  
828  
829  
830  
831  
832  
833  
834  
835  
836  
837  
838  
839  
840  
841  
842  
843  
844  
845  
846  
847  
848  
849  
850  
851  
852  
853  
854  
855  
856  
857  
858  
859  
860  
861  
862  
863  
864  
865  
866  
867  
868  
869  
870  
871  
872  
873  
874  
875  
876  
877  
878  
879  
880  
881  
882  
883  
884  
885  
886  
887  
888  
889  
890  
891  
892  
893  
894  
895  
896  
897  
898  
899  
900  
901  
902  
903  
904  
905  
906  
907  
908  
909  
910  
911  
912  
913  
914  
915  
916  
917  
918  
919  
920  
921  
922  
923  
924  
925  
926  
927  
928  
929  
930  
931  
932  
933  
934  
935  
936  
937  
938  
939  
940  
941  
942  
943  
944  
945  
946  
947  
948  
949  
950  
951  
952  
953  
954  
955  
956  
957  
958  
959  
960  
961  
962  
963  
964  
965  
966  
967  
968  
969  
970  
971  
972  
973  
974  
975  
976  
977  
978  
979  
980  
981  
982  
983  
984  
985  
986  
987  
988  
989  
990  
991  
992  
993  
994  
995  
996  
997  
998  
999  
1000



## 1. Summary

The objective of Phase 2 was to develop the component concepts defined in Phase 1 into detailed component designs capable of surviving in an engine operating at 55% thermal efficiency. During Phase 3, component designs were fabricated and initial testing was performed. Component testing and final demonstration testing were completed in Phase 4.

A squeeze cast, fiber reinforced aluminum, spherical joint piston was designed and fabricated. For superior ring carrier durability, a ni-resist chip insert was integrated into the piston casting. The piston/connecting rod assembly used a unique spherical joint for geometric symmetry and increased thermal and mechanical load resistance. The bearing area between the piston and rod was increased through the use of the spherical joint.

As a contingency plan to the spherical joint piston, a nickel aluminide articulated piston and a titanium aluminide articulated piston were also developed. The main advantage of nickel aluminide as a piston material is its high temperature strength and oxidation resistance. The advantage of titanium aluminide as a piston material is that it is half the weight of steel with high yield strength.

An advanced cylinder head was designed incorporating ceramic insulated ports and strategic oil cooling. The conventional water jackets were removed from the cylinder head and replaced with oil drillings in the critical valve bridge areas. Flow turbulators incorporated into the oil drillings were predicted to increase the heat transfer to the oil by at least a factor of four. Intake and exhaust port inserts fabricated from aluminum titanate were developed to reduce heat transfer from the exhaust gas to the cylinder head and reduce heating of the intake air by the cylinder head. The ports have been successfully cast into the gray iron cylinder head. A finite element analysis predicted a maximum metal temperature in the cylinder head of 420°C which translates to infinite thermal fatigue life.

A cylinder liner with a radial combustion seal and heat transfer fins was developed. The unique combustion seal utilizes radial instead of axial forces to seal combustion pressures. It was predicted that the radial combustion seal can effectively seal at 50% lower head bolt loads than a conventional combustion seal.

Oil was chosen as the engine coolant. In order to provide sufficient cylinder liner cooling it was necessary to design heat transfer fins into the cylinder liner cooling jacket. The use of large axial heat transfer fins was predicted to increase heat transfer to the oil by 1.7 times.

Piston rings were designed and fabricated that were predicted to reduce both ring/cylinder liner wear and friction. Stainless steel 440B was chosen as the optimum ring material due to its high fatigue strength and tribological properties. To improve ring conformability the ring cross section was reduced. Cermets and ceramic ring face coatings were developed to aid in reducing friction and wear.

A turbocharger whose turbine inlet geometry could be changed during engine operation was designed, developed and tested. Tests showed that the variable geometry (VG) turbocharger reduced particulate emissions by 20% through increased responsiveness of the turbine. Engine transient torque with the VG turbocharger was also improved.

To effectively reduce diesel particulate emissions, a microwave regenerated, silicon carbide particulate trap was designed. Development of the trap filter media has shown that Saffil with chemical vapor infiltrated (CVI) silicon carbide is the prime material for the system. The candidate materials demonstrated effective particulate trapping, high temperature stability and sufficient coupling with microwave energy. The economics of the microwave regenerated particulate trap appeared favorable.

In order to increase the thermal fatigue resistance of an aluminum piston, mullite and zirconia thermal barrier coatings were investigated. The use of thermal barrier coatings was predicted to reduce the maximum heat input to the piston by 34%. However, analytical studies on the in-cylinder effects of thermal barrier coatings on engine performance indicated that thermal barrier coatings on pistons may actually degrade combustion and therefore decrease performance. Based on the results of this study, a thermal barrier coating was not incorporated into the final piston design.

## 2. Introduction

The DOE/NASA sponsored Cummins In-Cylinder Components program has designed and demonstrated advanced in-cylinder components and tribological systems required for a concept LE-55 heavy duty diesel engine. The objective of the program was to identify and develop advanced in-cylinder components for engines with a target production date of the early 2000's. The project was based on an advanced diesel engine with the following characteristics:

- Low Brake Specific Fuel Consumption (BSFC) of 152 g/kW-hr
- Low exhaust emissions that meet standards of the early 2000's
- Improved durability and reliability
- Improved cost effectiveness

During Phase 1 of the project, an engine configuration capable of meeting the aforementioned performance goals was formulated. This target engine configuration, summarized in Table 2.1, required technology advances in both the in-cylinder and external components. The piston is representative of in-cylinder components, while the turbocharger is a typical external component. Using the thermal and mechanical requirements imposed by this target configuration, preliminary concepts for components capable of supporting these requirements were developed.

**TABLE 2.1:** Engine configuration for achieving LE-55 fuel consumption target

Engine Parameter	Design Target
BSFC (g/kW-hr)	152
Engine Speed (rpm)	1500
Power (kW)	354
BMEP (MPa)	2.83
Air-Fuel Ratio	30:1
Peak Cylinder Pressure (MPa)	19.3
Compression Ratio	17.3:1
Dynamic Timing ( $^{\circ}$ bTDC)	7.5
Engine Turbocharger Combined Efficiency (%)	75
Interstage Temperature ( $^{\circ}$ C)	16
Intake Manifold Temperature ( $^{\circ}$ C)	10
Power Turbine Pressure Ratio	1.60:1
Power Turbine Efficiency (%)	90
Reduced Heat Transfer (%)	40
Reduced Heat Release Duration (%)	18
Reduced Engine Friction (kPa)	48

In Phase 2, the component concepts were developed into designs for hardware to be assembled into a single cylinder research engine. The components chosen for development and fabrication, summarized in Table 2.2, were those that constrained engine performance or durability. Phases

3 and 4 involved the transition of the concepts from the design stage to component fabrication and engine testing. Table 2.2 also shows the fabrication and testing summary of the component concepts.

**TABLE 2.2:** Components designed, fabricated and tested in Phases 2, 3 and 4

Components	Hardware	Tested	Final Test
<b>SPHERICAL JOINT PISTON</b>	X		
Squeeze Cast, Fiber Reinforced Piston	X	X	X
Connecting Rod	X	X	X
Rotation Measurement	X	X	
Telemetry	X	X	
<b>ARTICULATED PISTON CROWN</b>			
Thermal Barrier Coating	X	X	
Nickel Aluminide Piston	X	X	
Titanium Aluminide Piston	X		
<b>PISTON RINGS</b>			
High Conformability Steel Top Ring	X	X	X
Wear Resistant Coating	X	X	X
Steel Oil Ring	X	X	X
<b>CYLINDER HEAD</b>			
Ceramic Intake Ports	X	X	
Ceramic Exhaust Ports	X	X	X
Strategic Oil Cooling	X	X	X
Oil Drilling Turbulators	X	X	
Valve Bridge Insert	X	X	
<b>CYLINDER LINER</b>			
Radial Combustion Seal	X	X	X
Cooling Jacket Heat Transfer Fins	X	X	X
C-Ring Combustion Seal	X	X	
Omega Combustion Seal	X	X	
<b>VARIABLE GEOMETRY TURBOCHARGER</b>			
Dual Flow Turbine Casing	X	X	
Lightweight Turbine Rotor	X		
<b>SILICON CARBIDE PARTICULATE TRAP</b>	X	X	

In addition to the in-cylinder components, two component development tasks were added to the project. An advanced, low cost, variable geometry turbocharger and control system was developed which improves particulate emissions through improved availability of combustion air

at low engine speed and during transient operations. The variable geometry turbocharger also improves fuel consumption by reducing back pressure during steady state conditions. A silicon carbide particulate trap with higher trap strength and higher temperature capacity than conventional cordierite materials was also investigated.

## **2.1. Phase 1 Results**

In order to achieve the Heavy Duty Transport Technology (HD TT) program goal of 152 g/kW-hr (0.250 lb/bhp-hr) brake specific fuel consumption, an engine system was proposed consisting of two stage turbocharging (to enable high BMEP at low engine speed), turbocompounding, low intake manifold temperature, low heat rejection, and high fuel injection and peak cylinder pressures. All components and systems were based on the Cummins L10 engine: a state-of-the-art, 10 liter production engine with proven performance. Thermal analysis of the cylinder head and cylinder liner determined that by using strategically placed oil cooling with suitable enhancement, it was possible to achieve acceptable component temperatures and thermal fatigue life. This strategy significantly reduced the overall system size and complexity by eliminating engine cooling water. A cylinder head concept with oil cooled gray cast iron, and cast-in ceramic intake and exhaust ports was pursued. The key in-cylinder component which received much attention in Phase 1 was the piston. The refined concept consisted of a spherical joint piston/connecting rod for high load carrying capabilities and uniform thermal loads, ceramic fiber reinforced aluminum for light weight and high strength, and a combustion chamber thermal barrier coating of sprayed mullite or zirconia.

## **2.2. Phase 2, Phase 3, and Phase 4 Objectives**

The general objective of the program was to create components and systems that would be an improvement over contemporary engines in the areas of:

- Fuel consumption - 152 g/bkW-hr (0.250 lb/bhp-hr) BSFC
- Exhaust emissions - 1/2 1998 standards
- Cost effectiveness
- Durability and reliability

Reduced heat rejection and waste heat recovery will be integral parts of the energy efficient diesel engine of the future.

Phase 2 of the program involved the detailed design and analysis of the concepts selected in Phase 1, bench and rig tests to qualify and refine the concepts, and development of unique manufacturing processes to support prototype part production. Cummins' engineering expertise was complemented by that of the major subcontractors on the program which included Kolbenschmidt AG or Karl Schmidt (pistons), Combustion Technologies Inc. (piston rings), and United Technologies Research Center (piston coatings).

Initial testing of prototype parts was performed in Phase 3. The majority of the testing was performed on a single cylinder version of a Cummins L10 production engine. The main objective of the initial component testing was to work through the major issues and to ensure proper operation of the advanced componentry. Final component design and demonstration testing were conducted in Phase 4.

In order to answer basic questions about the effects of in-cylinder insulation on diesel engine performance and combustion, an investigation was conducted to experimentally and analytically compare uncoated and ceramic coated combustion chambers.

### **2.3. *Background on Advances in Diesel Engines***

Future diesel engine designs are dictated by customer expectations, environmental requirements, market demands and competitive pressures. While considerable effort is directed toward exhaust emissions reductions, most improvements in emissions control are transparent to the end user. Users of heavy duty diesels are becoming more sophisticated in their approach to trucking, and, therefore, more demanding of their engines. Each improvement from the engine manufacturers in the areas of transient response, fuel consumption, oil consumption, or durability results in increased customer expectations for future diesel engines. Fuel costs continue to dominate the cost structure of the trucking industry, so the informed customer will demand continued improvement in fuel consumption. Matching of drive train components and controls to the duty cycle will allow engines to spend much of their time in efficient low rotational speed operation. This will require high torque and fast response at low engine speeds to allow good driveability during transitions between speed and load regimes.

Deregulation of the trucking industry has resulted in an increase in the average gross combined weight of highway trucks. Vehicle and tire improvements are resulting in large reductions in rolling and wind resistance. An interesting outcome of these changes is that the horsepower to maintain a steady speed on level highways is being reduced. However, the horsepower required to climb grades and meet customer transient response expectations is increasing. An engine design which meets this demand should have a relatively low displacement and component size for low friction, and good fuel economy during cruising conditions. However, the same engine design must have the capability of delivering high power when required for acceleration or climbing grades. Vehicle designs for improved aerodynamics give preference to compact engines and cooling systems. These are some of the factors making a small, high output engine attractive in the future.

The basis for all component design and analysis on this program was the Cummins L10 engine. The L10 has a 125 mm bore and a 136 mm stroke for 10 liters displacement. It is sold in turbocharged and aftercooled configuration for highway truck applications at ratings from 180 to 245 kW. The combustion system utilizes high pressure unit injectors and a low swirl combustion chamber. While compact in overall size, the L10 is designed with large connecting rods and bearings mated to a large crankshaft for durability at high cylinder pressures and output levels.

Realizing that meeting the program goals required a total system approach, some definition of the total system was required before in-cylinder component design and development could take place. To assist in the system definition and development of boundary conditions for detailed component analyses, parametric cycle simulations were conducted using the Cummins code TRANSENG. These simulations predicted a 152 g/kW-hr (0.250 lb/bhp-hr) BSFC while suitably constraining injection timing to reflect a low NO<sub>x</sub> engine. At the time the simulations were conducted, emissions standards were not in place for the year 2000, which is the time frame for production of the concepts developed in this program. For the purposes of concept selection,

the assumed 1994 limits of 5.0 g/bhp-hr NO<sub>x</sub> and 0.1 g/bhp-hr particulate were used. Concepts that lend themselves to even lower emission levels were given preference.

While meeting performance and emissions targets requires a system solution, the primary emission control functions are performed by the fuel injection and air induction systems in a diesel engine. The in-cylinder components define the geometry and heat transfer of the combustion chamber and are significant to achieving the objectives of an advanced diesel engine. All components must be consistent with the system requirements for cylinder pressure, temperature, frictional losses and more. The future trends in the engine system are generally known and the analyses performed on this program further define the demands on the in-cylinder components. Developing pistons, piston rings, cylinder liners, and cylinder heads consistent with the total system requirements of the year 2000 was the objective of this program. Durability targets appropriate for the year 2000 included improvements over contemporary production engines which average from 644,000 to 1,126,000 kilometers before the first overhaul. A target of 1,610,000 kilometer durability was chosen reflecting the customer expectation of continual improvement.

## 1. Component Development, Fabrication and Testing

### 3.1 Spherical Joint Piston

A spherical joint piston was chosen as the primary piston design for the contract. The piston is comprised of a monoblock piston, a set of holder rings and a threaded ring. Figure 3.1.1 illustrates the piston assembly. The connecting rod sphere is positioned against the piston saddle or upper bearing area located beneath the piston crown. No conventional bearing material is present at the piston/sphere interface as the steel connecting rod sphere rides against the parent aluminum of the piston. The holder rings retain the connecting rod sphere within the piston and provide a lower bearing surface for the sphere. The threaded ring captures the holder rings and fastens the holder rings and connecting rod within the piston.

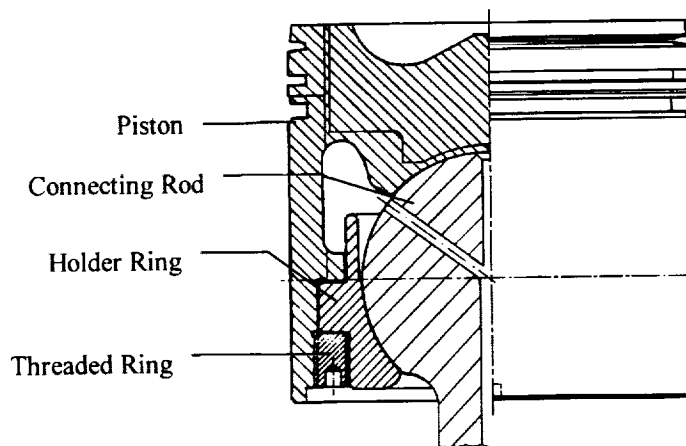


**Figure 3.1.1:** Spherical joint piston assembly.

Mechanical load capability of the spherical joint design is excellent because of the large load bearing area within the joint and axisymmetric connecting rod support which eliminates the piston deflection around the piston pin. An axisymmetric spherical joint piston also provides uniform thermal growth at operating temperatures. Uniform thermal growth allows for a smaller clearance between the piston and cylinder liner resulting in improved guidance and reduced oil consumption [Ref 1].

The ball (sphere) and socket joint is the unique feature of the spherical joint piston design. Unlike a conventional wrist pin piston with a hole through the piston skirt, the connection between the spherical joint piston and connecting rod does not interfere with the piston skirt or oil control ring. The horizontal axis of rotation of the joint can be located closer to the piston's center of mass. This results in a more stable piston with the added possibilities of reducing the skirt length and lowering the location of the oil control ring. The axisymmetry of the spherical joint allows the piston to freely rotate on the connecting rod sphere. Piston rotation promotes uniform piston



temperatures resulting in uniform thermal growth. A 16 to 29% larger bearing area than a standard wrist pin piston along with symmetrical load support translates to higher cylinder pressure capabilities with the spherical joint. The spherical joint piston was designed and fabricated by Kolbenschmidt AG.

### 3.1.1 Aluminum Squeeze Cast Piston

The monoblock piston is made of squeeze cast aluminum with a sintered niresist chip ring carrier insert and alumina ( $\text{Al}_2\text{O}_3$ ) fiber reinforcement in the combustion bowl area and skirt area as shown in Figure 3.1.2. The squeeze casting process is initiated by placing the alumina fiber preforms and sintered niresist chip ring carrier insert into the piston mold. Molten aluminum is then squeezed into the mold under pressure and fills the interstices of the preforms and insert. The result is an alumina fiber reinforced aluminum piston. At the time of the first piston casting, this design was the most extensive use of fiber reinforcement known to be incorporated into a metal matrix composite (MMC) piston.

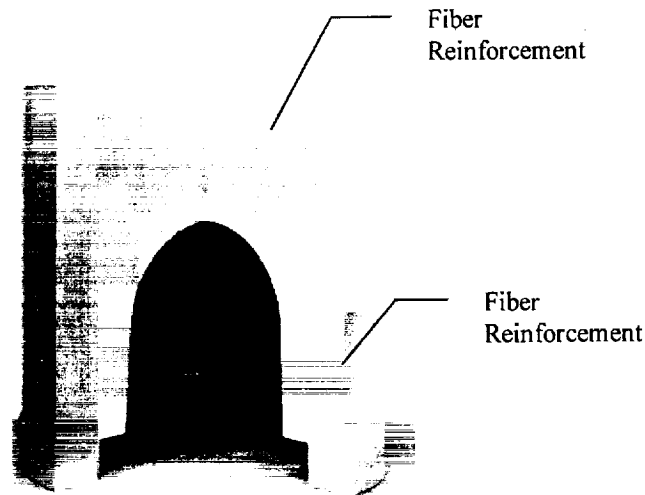


**Figure 3.1.2:** Squeeze cast aluminum spherical joint piston casting with alumina fiber reinforcement.

The combustion bowl is reinforced with 20% by volume alumina fibers while the piston skirt is reinforced with 8% by volume alumina fibers. The fibers used have a planar-random orientation – the fibers are arranged in layers in one direction but are randomly oriented in the remaining two directions. The fiber arrangement results in a non-isotropic stress-strain behavior. In the direction perpendicular to the alumina layers the material properties of the MMC nearly match the properties of the unreinforced, parent aluminum. However, in the direction parallel to the alumina layers, the material properties of the MMC are greatly enhanced. The enhancements include greater stiffness, higher strength and reduced thermal expansion. Therefore, by tailoring the orientation of the fibers, one can greatly increase the thermal fatigue resistance of the MMC. For example, in the combustion bowl the fibers are oriented so as to reduce the thermal fatigue hoop

stresses. In the skirt, the fibers are oriented in a manner to reduce radial thermal growth thus allowing for tighter skirt/cylinder liner clearances which leads to reduced oil consumption.

The most distinctive feature of this piston design is the spherical connection between the piston and the connecting rod. A major reason for selecting a spherical geometry is that it provides for more piston/connecting rod bearing area (16 to 29% more) as compared to a conventional piston and pin (Figure 3.1.3). In addition, the spherical joint piston is symmetric and free to rotate upon the spherical joint connecting rod. The advantage of symmetry and free rotation is uniform mechanical deformation. This allows a decrease in the piston-to-liner clearance which helps reduce oil consumption.

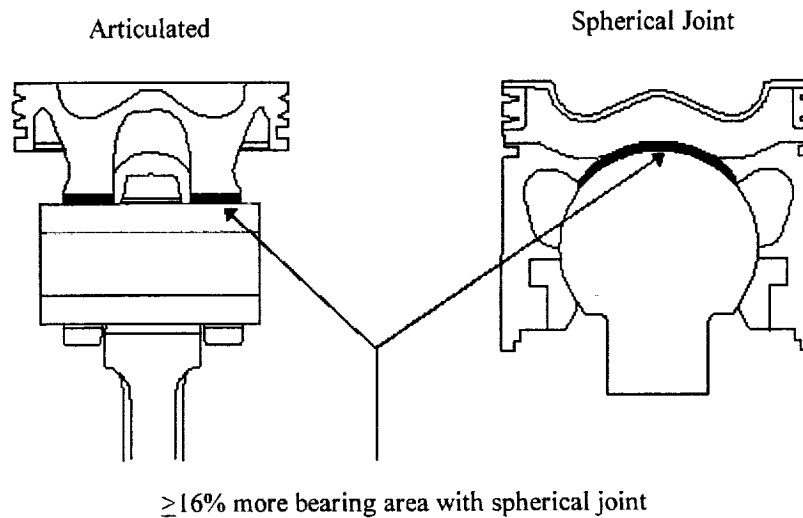


**Figure 3.1.3:** Conventional and spherical joint piston bearing area comparison.

Skirt pads have been considered to reduce skirt-to-liner friction. These pads would be designed as raised triangular regions on the skirt. The interaction between the pads and the cylinder liner oil film is expected to produce a rotational force on the piston. Rotation helps to equalize the temperatures across the piston and minimizes non-uniform temperatures caused by impinging injector fuel plumes. Again, this allows for a reduction in piston-to-liner clearance and reduces stresses in a crown thermal barrier coating.

The holder rings retain the connecting rod sphere within the piston as well as form the inside wall of the piston cooling gallery. A series of drain grooves were machined into the bearing surfaces of the holder rings. The grooves allow the cooling oil to drain from the cooling gallery. The original holder rings were machined from nodular cast iron.

The threaded ring was made of the parent piston aluminum. Four, equally spaced holes were drilled into the backside of the threaded ring. The dowels on a specially made spanner wrench are

aligned within the holes so that the threaded ring can be torqued into place during piston assembly.

### **3.1.2 Niresist Chip Ring Carrier Insert**

A ring carrier insert was integrated into the spherical joint piston design to prevent the piston rings from beating in or deforming the parent aluminum. In order to increase the bond strength between the piston and ring carrier, a sintered niresist chip ring carrier insert was developed. The insert consists of niresist lathe turnings from the ring groove machining of conventional ring carrier inserts. The chips (turnings) were collected, degreased and then sintered into a preform. The end result was a ring carrier insert with interstices or voids among the niresist chips.

A conventional cast niresist ring carrier insert relies on a metallurgical bond for joining with the parent aluminum. The niresist chip ring carrier insert, however, relies on both a metallurgical bond and a mechanical bond. During squeeze casting, the chip preform is completely infiltrated with aluminum. The aluminum forms a metallurgical (Alfin) bond with each of the chips. In addition, the aluminum serves to enmesh the chips in place, thus creating a mechanical bond. The result is an aluminum/chip bond which has twice the strength as the bond developed between the same aluminum material and a conventional cast niresist insert.

Due to the unique structure of the niresist chip insert, machining processes to produce ring groove finishes within standard specifications required considerable development. A machining study conducted by Kolbenschmidt AG yielded procedures which produce ring groove surface finishes within the niresist chip carrier which are superior to those achievable within a conventional cast niresist insert. Therefore, the niresist chip insert provides advantages over a conventional cast niresist insert in terms of better wear characteristics as well as twice the bond strength to the base aluminum.

### **3.1.3 Pulsation Testing**

The original design of the holder rings called for a interference fit between the holder rings and the piston to compensate for the greater radial expansion of the piston at operating temperatures. Because of the interference fit it was necessary to heat the piston to 205°C for assembly. Once the piston was at temperature the connecting rod and holder rings were placed within the piston socket. This was a difficult maneuver to execute due to the high handling temperature of the piston. In addition, the fact that the piston had been heated up did not ensure an easy insertion of the holder rings into the piston. Disassembly of the piston assembly was a more difficult task, often resulting in the irreparable damage to the hardware.

An investigation was initiated to determine whether the interference fit between the holder rings and piston was necessary to maintain the integrity of the assembled spherical joint. Kolbenschmidt AG conducted a inertia load fatigue strength study of the spherical joint to determine whether a clearance fit between the holder rings and piston was feasible under the projected piston operating conditions. Using a hydropulse technique, several pistons were evaluated. A schematic of the hydropulse test rig is shown in Figure 3.1.4. In the hydropulse test, a test oil is supplied to a chamber on the underside of the piston in order to create a constant reaction pressure. Identical test oil is supplied to a chamber above the piston crown in a manner

to provided a pulsed pressure loading. The magnitude of the pressure loading at the piston crown is increased in a stepwise manner until a piston failure occurs. The maximum pressure loading, number of pressure cycles and the frequency of the pressure cycles are then used to calculate a fatigue strength for the piston assembly.

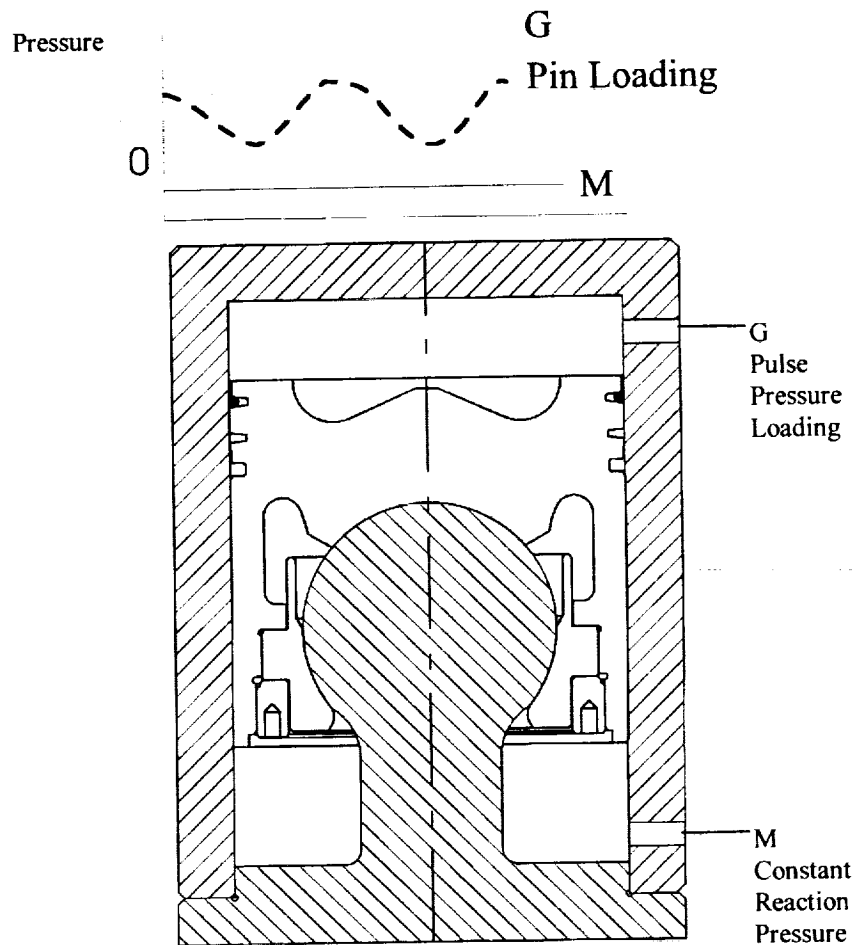


**Figure 3.1.4:** Schematic of hydropulse test rig.

The results from the hydropulse test indicated the interference fit between the holder rings and the piston was not necessary for satisfactory fatigue strength of the spherical joint. Test results showed the joint, without the interference fit, could be operated at engine speeds up to 4100 rpm with a design factor of 1.2. At the LE-55 engine design speed, 1500 rpm, the test results indicated the joint had a design factor of 4.1. Based on these test results the holder rings were redesigned with a clearance fit, allowing assembly of a piston at room temperature.

### 3.1.4 Assembly and Engine Testing

The initial design iteration of the spherical piston and connecting rod assembly is shown in Figure 3.1.5. The first attempt by Cummins to assemble the spherical joint piston and connecting rod resulted in binding between the piston and rod. When tried by hand, the assembly could not be made to oscillate or rotate.

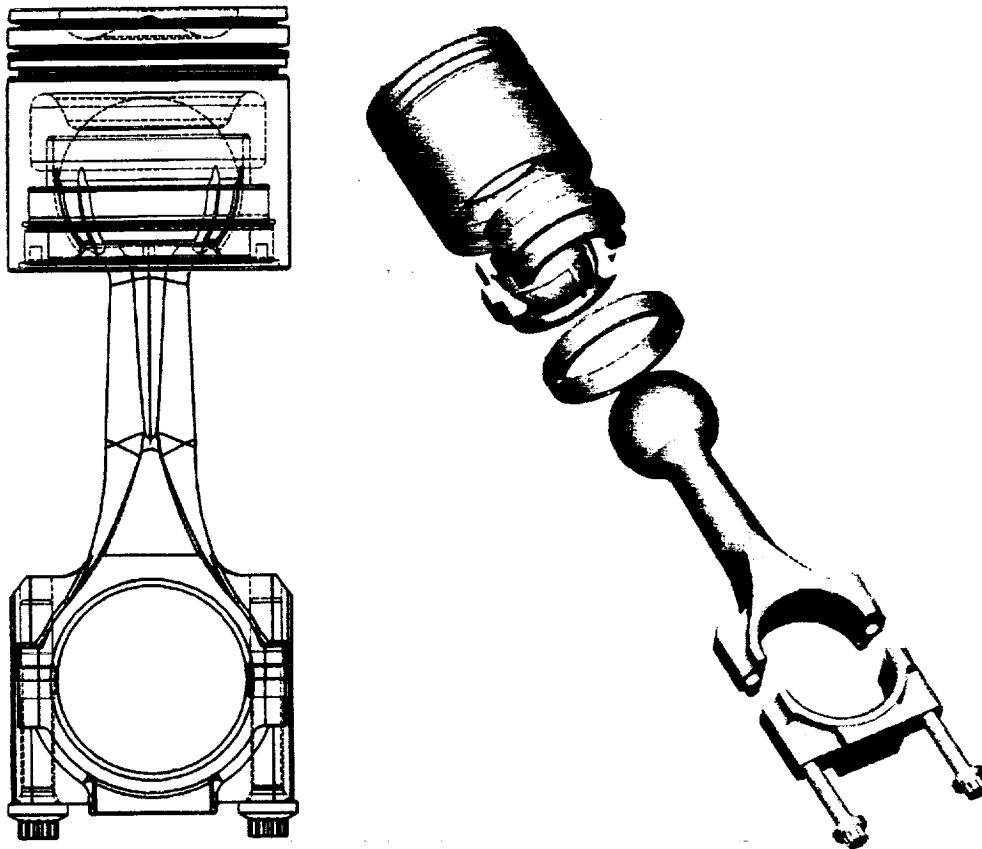


**Figure 3.1.5:** Initial design iteration of the spherical joint piston and connecting rod.

The binding resulted from an incorrectly machined clearance between the aluminum piston and nodular cast iron holder rings. Small errors in machining can make the spherical joint piston and connecting rod incompatible. The tight clearances at room temperature – a required clearance of  $20\text{ }\mu\text{m}$  between the piston socket and the connecting rod – are required to compensate for the different coefficients of thermal expansion of the piston, holder rings and connecting rod. To illustrate, at piston operating temperatures, the  $20\text{ }\mu\text{m}$  piston/holder rings rod clearance was anticipated to expand to  $120\text{ }\mu\text{m}$  at the operating temperature.

The spherical joint piston, along with a spherical joint connecting rod, were returned to Kolbenschmidt AG in order to resolve the binding issue. A functional piston/connecting rod assembly was received back from Kolbenschmidt AG. This piston assembly was placed on motoring test.

#### 3.1.4.1 Motoring Tests

Cummins used a single cylinder version of the L10 engine (SCE L10) to perform DOE/NASA contract work including the development of the spherical joint piston. The SCE L10 design incorporates two cylinders from a production multi-cylinder engine block. The six cylinder block is cut through cylinder #4 (cylinder #1 is located at the front of the block). Cylinder #6 is the power cylinder while cylinder #5 is the balance cylinder. The crankshaft is a specially fabricated 180° offset design. The front of the engine uses a production gear plate, gear train and gear cover. The valve cover, overhead and camshaft are all production hardware modified to accommodate the shortened cylinder block. The SCE L10 is literally a dual cylinder version of the six cylinder L10: no balance box is incorporated in the design.

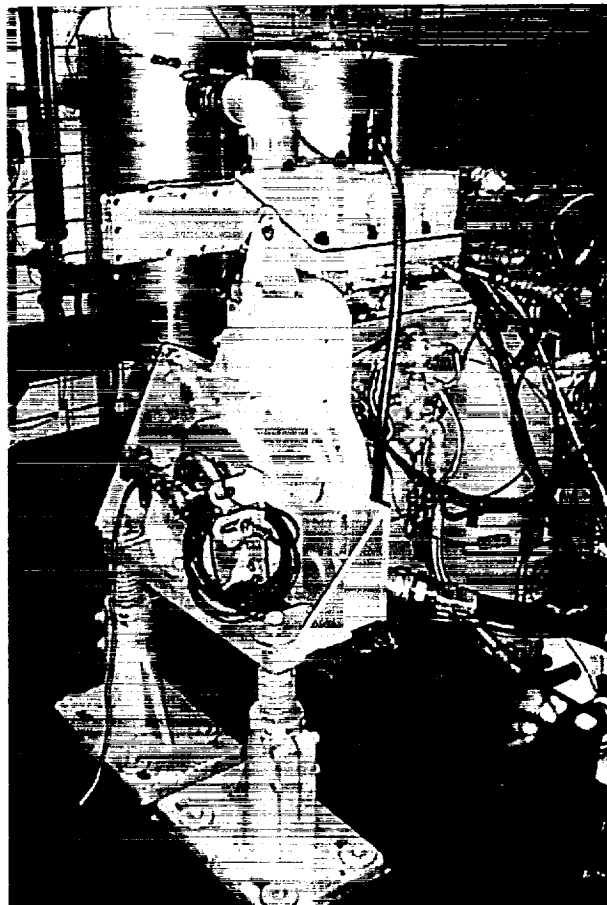


**Figure 3.1.6:** Single cylinder L10 engine (SCE L10).

The spherical joint piston/connecting rod assembly was initially motored in a SCE L10 to determine the mechanical integrity of the spherical joint. A top block cover plate was used on the SCE L10 in place of the cylinder head for the motoring tests. The cover plate had a hole in it at the location of the power cylinder but otherwise sealed the top of the cylinder block. The hole in the cover plate allowed physical and visual access to the spherical joint piston. The cover plate hole also served to unload the piston leaving only inertia loads to operate on the joint.

The test sequence involved motoring the piston at different engine speeds as shown in Figure 3.1.7. The piston was motored at 500, 1200, 1500, 1700 and again at 500 rpm at 10 minute intervals. The second 500 rpm speed interval was performed as an audio knock check on the piston assembly. Early in the motoring testing it was learned that a loud knocking sound emanating from the cylinder kit indicated failure (increased clearances/galling) of the joint. By performing the knock check at a low engine speed noise interference from the front gear train was minimized. After completing the knock check the piston was motored at 1000 rpm for 90 minutes. The SCE L10 lubrication system was set at 115°C and 275 kPa for the motoring test.

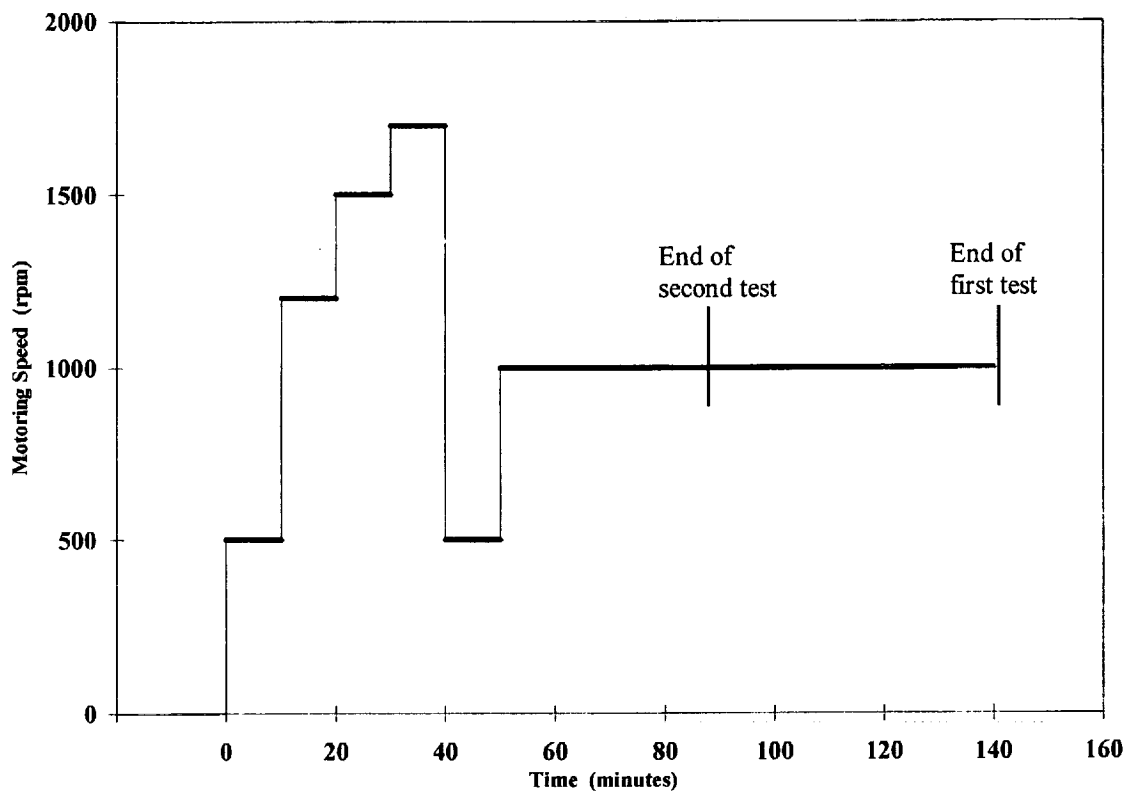


**Figure 3.1.7:** Spherical joint piston motoring test sequence.

Near the end of the first piston motoring test a loud knocking sound could be heard emanating from within the engine. After stopping the engine, attempts to manually rotate the piston within

the cylinder liner failed. Disassembly of the piston revealed that the parent aluminum piston saddle was in good condition. However, the holder rings and the underside of the connecting rod sphere showed distress and metal transfer from the holder rings to the sphere as shown in Figure 3.1.8.



**Figure 3.1.8:** Galled holder ring (top) and connecting rod sphere (bottom) from the first motoring test.

Metrological analysis of several untested spherical joint pistons found that the as-received holder ring seat bore in the pistons was not within specifications for concentricity with the piston saddle. Misalignment due to the lack of concentricity results in reduced clearances between the holder rings and the connecting rod sphere. Reduced clearances may lead to galling, as was observed in the first motoring test.

The spherical joint piston was reworked to bring the concentricity between the holder ring seat bore and the piston saddle within specifications. The piston was assembled and placed on motoring test. The engine speed and time intervals for the second motoring test were identical to the first test. However, after only 30 minutes at 1000 rpm the knocking sound emanating from the engine was so great that the test was aborted. Disassembly of the piston showed that the holder rings and connecting rod sphere had suffered similar damage (galling) as that seen in the first motoring test.



The holder rings were redesigned in order to prevent galling. The following changes were made to the holder ring design.

1. Aluminum bronze was substituted for nodular cast iron.
2. The socket area was increased by extending the bearing surface above the equator of the original socket.
3. Large straight-through oil drain grooves were replaced with thin dead-ended oil drain grooves set at an angle of 30° from horizontal.
4. Grooves were designed into the back side of the holder rings to allow oil to drain from the piston cooling gallery.
5. A chamfer was included on the seating O.D. of the holder ring.

Aluminum bronze was incorporated into the design to provide an improved material for the connecting rod sphere to bear against. The aluminum bronze chosen is typically found in aircraft landing gear. The socket area of the holder ring was modified to provide improved guidance of the connecting rod sphere for the instance when the sphere transitions between bearing on the holder rings and bearing on the piston saddle. The oil drain grooves were modified to prevent lubricating oil from draining from the holder ring/connecting rod sphere interface. Drainage of cooling oil from the piston cooling gallery has been facilitated by cutting grooves the backside of the holder rings and extending the spanner wrench holes in the threaded ring. Placement of a chamfer on the holder ring seating O.D. increases ease of assembly/disassembly of the piston. A comparison between the original and redesigned holder rings is presented in Figure 3.1.9.

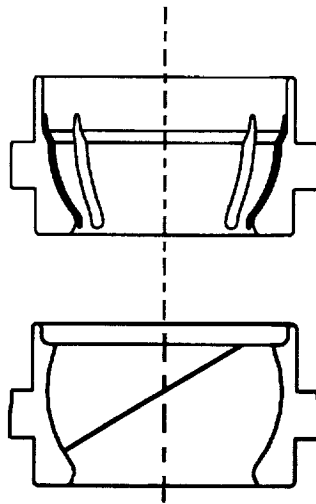


**Figure 3.1.9:** Comparison of original and redesigned holder rings.

A set of redesigned holder rings was machined, assembled into the piston and placed on motoring test. The sequence for the third motoring test was modified with additional knock checks as

shown in Table 3.1.1. The number of knock checks was increased based on the expectation that the holder ring galling could be detected in the earlier stages.

**Table 3.1.1:** Test sequence for the third motoring test

Engine Speed (rpm)	Time at Speed (minutes)
500	10
1200	10
500	(knock check)
1500	10
500	(knock check)
1700	10
500	(knock check)
1000	18
500	(knock check)

The spherical joint piston completed the third motoring test without knocking. Disassembly of the piston showed the holder rings to be in excellent condition. The piston saddle showed no distress. The connecting rod sphere showed light contact bands. The holder rings showed light shine patches. The piston and connecting rod were reassembled for installation into the SCE L10 for an engine firing test.

#### 3.1.4.2 Firing Tests

For the first firing test the SCE L10 was started and allowed to idle for a short period before being set at the engine conditions shown in Table 3.1.2.

**Table 3.1.2:** SCE L10 operating conditions for first firing test

Engine Speed:	1500 rpm
Engine Torque:	68 N-m <sup>†</sup>
Air-Fuel Ratio:	30:1
Intake Manifold Temperature:	43°C
Coolant Temperature:	91°C
Oil Sump Temperature:	116°C

<sup>†</sup> Peak cylinder pressures were on the order of 9.7 MPa at this operating point.

The light load run during the initial engine firing test was chosen for two reasons. First, since this was the first time that this spherical joint piston design was to be fired without a prior experience base, caution was exercised. Second, the piston being tested had porosity in the bearing saddle due to less-than-optimal squeeze casting conditions. Running light loads reduced the probability of cracking the piston.

Piston #1 was on firing test for four hours. Post-test inspection showed the piston/connecting rod hardware to be in similar condition as after the third motoring test. The piston saddle was virtually unmarked. The connecting rod sphere showed the same contact bands but with greater definition. The holder rings showed increased shine patches. Piston #1 survived the first engine firing test.

A high peak cylinder pressure test was planned for the next engine firing test. Due to the porosity in the saddle of Piston #1, Piston #2 was assembled for this test. Piston #2 completed 25 hours of 20.7 MPa peak cylinder pressure testing. The SCE L10 operating conditions for the test are shown in Table 3.1.3.

**Table 3.1.3:** SCE L10 operating conditions for the 25 hour, high peak cylinder pressure test

Engine Speed:	1500 rpm
Engine Torque:	247 N-m <sup>†</sup>
Air-Fuel Ratio:	30:1
Intake Manifold Temperature:	43°C
Coolant Temperature:	91°C
Oil Sump Temperature:	116°C

<sup>†</sup> Blow-by at 20.7 MPa peak cylinder pressures was 250 to 750 Pa. GIMEP at these conditions was 2.28 MPa.

Before shutting down the SCE L10 at the end of the high peak cylinder pressure test the peak cylinder pressure was increased in increments of 690 kPa by increasing the engine boost pressure. The maximum peak cylinder pressure measured was 24.6 MPa. After 15 minutes at these high peak cylinder pressures, the SCE L10 was safely shut down for end of test. Disassembly of the piston revealed the hardware to be in excellent condition.

Piston #3 was assembled for a transient cycle test. The transient cycle involved cycling the fueling between full load and no load on a three minute interval so that a complete cycle was comprised of six minutes. Peak cylinder pressures were on the order of 17.2 MPa. Peak exhaust temperatures were on the order of 695°C. Piston #3 completed 100 hours (1000 cycles). Post-test inspection of the piston and connecting rod showed the hardware to be in excellent condition.

Piston #4 was assembled for general combustion and performance testing. The piston scuffed during an SCE L10 low cooling rate test. Before scuffing, Piston #4 had accumulated over 300 engine hours at engine speeds as high as 3000 rpm and extended periods of high peak cylinder pressures in excess of 22 MPa.

Piston #5 was assembled for temperature telemetry testing (see section 3.3 **Spherical Joint Piston Telemetry**). Piston #6 was assembled for the final system demonstration tests of the high speed diesel engine spherical joint piston concept (see section 3.11 **System Demonstration Testing**).

### 3.1.5 Piston Rotation Measurement

A unique characteristic of the spherical joint piston is that the piston can rotate upon the connecting rod sphere. Evidence of piston rotation was found during the engine test activities. After engine test, several spherical joint pistons showed a continuous burn band at the combustion bowl rim. With a conventional wrist pin piston, one can typically observe discrete injector spray plume burns at the combustion bowl rim. The continuous burn band on the spherical joint piston is evidence that the piston rotates. However, one cannot determine from the burn band whether the piston rotation was continuous or intermittent, progressive or oscillatory. A rotation measurement method was developed in order to determine the nature of the spherical joint piston rotation.

**MEASUREMENT METHOD** - The piston rotation measurement method developed consisted of a groove cut into the piston skirt and two diametrically mounted proximity sensors in the cylinder liner wall. An illustration of the measurement hardware is shown in Figure 3.1.10.

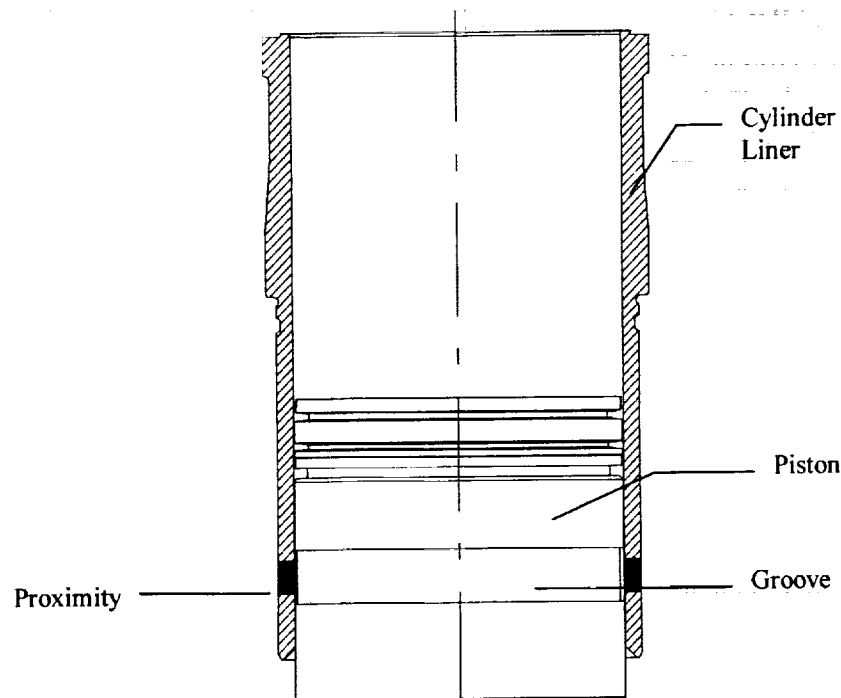


**Figure 3.1.10:** Piston rotation measurement hardware.

The proximity sensors were used to measure the depth of the piston skirt groove on opposite sides of the piston. The groove was cut so that its depth varied as a function of angular position. The mathematical function used to describe the depth of the groove was based on the spiral of Archimedes. For the spiral of Archimedes, the radius at any angular position has a unique length. Summing any two diametrically opposed radii on the spiral yields a "diameter" of unique length.

With a premeasured map of the groove radii and knowing the operating engine speed, one can use scaled proximity sensor output to determine the position, angular velocity and rotational direction of the piston. The map of the piston skirt groove radii is shown in Figure 3.1.11.

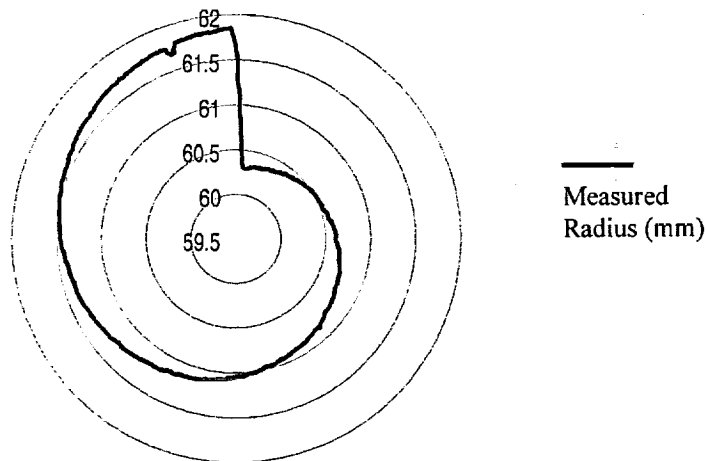


**Figure 3.1.11:** Map of skirt groove radii.

The position of the piston skirt groove was chosen so as not to impact the function of the skirt. Pistons from the previous engine firing tests showed a consistent unmarked band where the piston skirt had not made contact with the cylinder liner wall. This band was the result of the profile originally machined into the skirt to compensate for the skirt stiffness induced by the holder ring seating bore. Since this area of the skirt was not contacting the cylinder liner it was judged to be the ideal location for the groove.

The proximity sensors were located on the cylinder liner so they would sense the center of the groove while the piston approached and exited the bottom dead center (BDC) position. The piston slows down entering BDC, stops at BDC, and slowly speeds up exiting BDC. This motion allows the maximum time window for the proximity sensors to measure the depth of the skirt groove.

**TEST RESULTS** - Piston rotation measurements made in an operating SCE L10 indicate that this spherical joint piston design does not continuously rotate or oscillate. Piston rotation appeared to be confined to limited engine speed and load operating conditions. The piston showed the greatest propensity to rotate at low idle conditions (low engine speed, no load). During a change in engine speed and load from idle conditions to near rated conditions the piston would tend to rotate to a specific angular position and then remain there. A change in speed and load back to idle conditions would also cause the piston to rotate. Rotation under these conditions was slow

and unpredictable. The piston did not rotate under steady state engine operating conditions. Plots of piston angular position versus time under idle-to-full-load conditions and full-load-to-idle conditions are shown in Figure 3.1.12 and Figure 3.1.13, respectively.

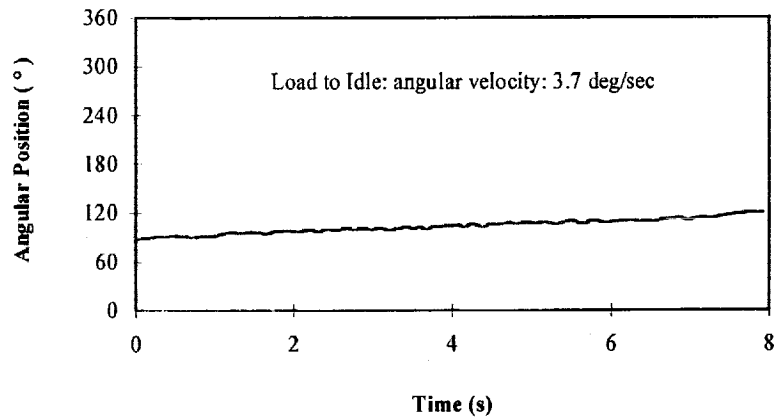


**Figure 3.1.12:** Piston angular position - idle-to-full-load conditions.

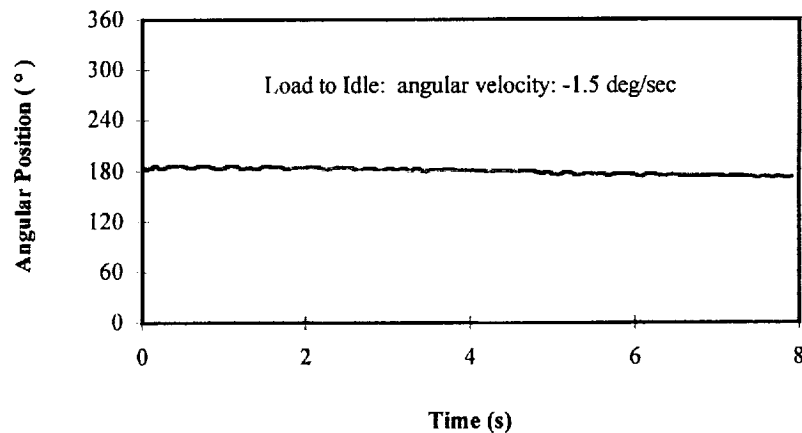


**Figure 3.1.13:** Piston angular position - full-load-to-idle conditions.

The benefits to a rotating piston are reduced scuffing, improved ring sealing, improved lubrication, mechanical and thermal load symmetry, reduced bearing loads, reduced running clearances and reduced oil consumption [Ref 1]. These benefits are reduced if the piston does not rotate in a consistent manner. What is required for controlled piston rotation is a mechanism or piston skirt geometry which provides a positive drive. The challenge remains to design this

positive drive which can operate within the space envelope of the piston and can withstand the substantial inertia loads present at the piston speeds of a high speed diesel engine.

### 3.1.6 Modeled Temperature Comparison

Early in the contract, Kolbenschmidt AG performed a 2-D FE temperature analysis of the spherical joint piston. The FE analysis was conducted using boundary conditions derived from the LE-55 operating point. A temperature map from the spherical joint piston FE analysis is shown in Figure 3.1.14.

In order to verify the modeled piston temperatures, a piston telemetry system was developed. The piston telemetry system was developed because a conventional mechanical linkage system would have restrained the spherical joint piston's rotation and thus would have seriously compromised the validity of the temperature measurements (see section 3.3 **Spherical Joint Piston Telemetry**).

A spherical joint piston was instrumented with a temperature telemetry system and the piston system assembly installed into a SCE L10. The SCE L10 engine verification testing was planned to be run at the LE-55 operating point. However, operating conditions achieved during the engine test were not identical to the LE-55 operating point as shown in Table 3.1.4.

**Table 3.1.4:** SCE L10 operating conditions compared to LE-55 operating point for the piston temperature telemetry test

Parameter	LE-55 Target	SCE L10
Engine Speed (rpm)	1500	1500
GIMEP (MPa)	2.47	2.37
Air-fuel ratio	30:1	32.2:1
Peak cylinder pressure (MPa)	20.7	22.1
Intake manifold temperature (°C)	16	38
Fuel in temperature (°C)	40	40
Oil rifle temperature (°C)	116	116

The spherical joint piston in this test was instrumented with seven J-Type thermocouples located in the combustion bowl center, combustion bowl bottom, combustion bowl rim, socket top center, back of top ring groove, back of second ring groove and skirt bottom, respectively. The thermocouples were positioned in vertical radial planes, 60° apart. Each thermocouple was mounted within 2.54 mm of the respective piston surface. The piston temperature measured at each thermocouple location is shown in bold in Figure 3.1.14. Note that no data were available for the back of the top ring groove location due to a failed thermocouple.

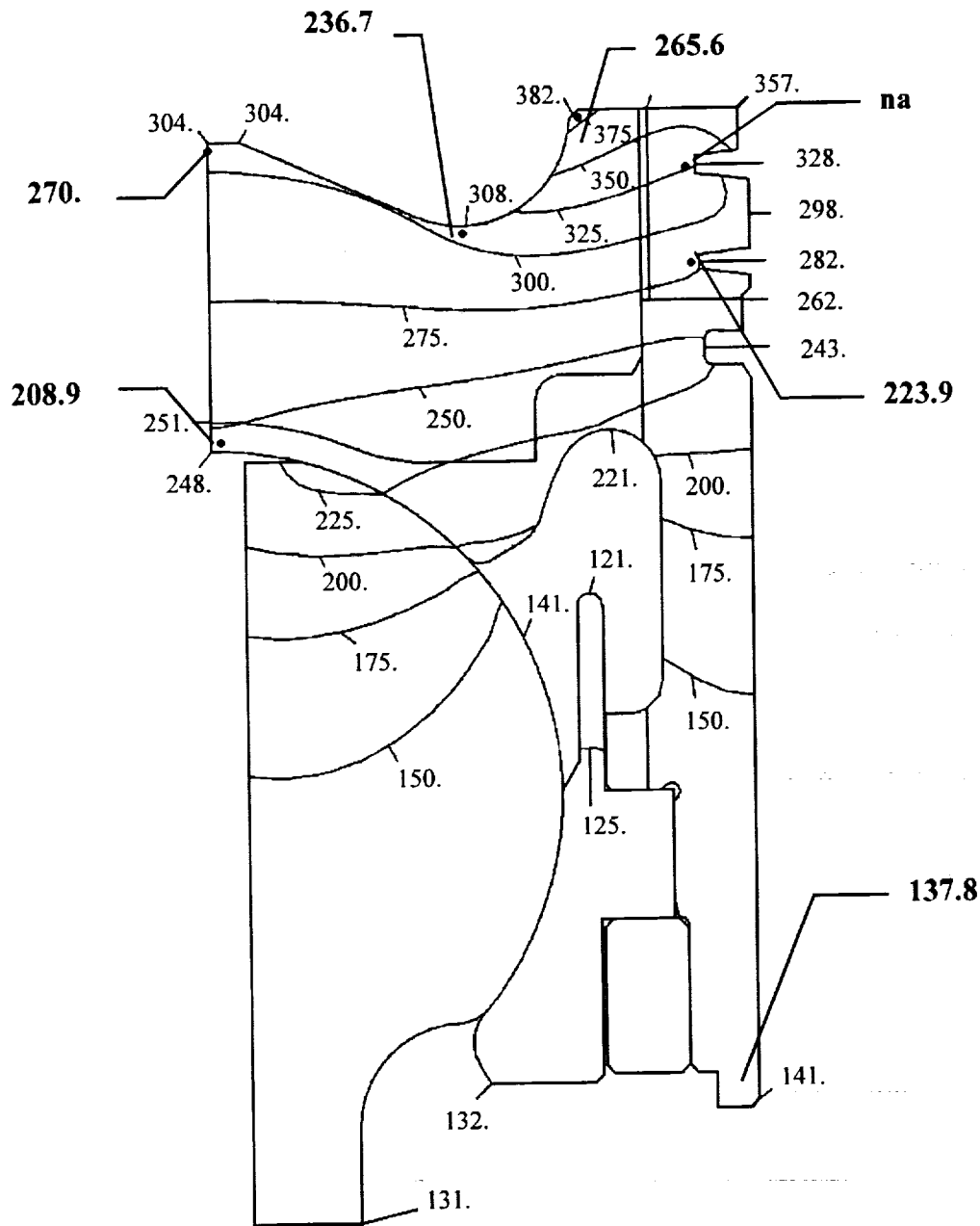


**Figure 3.1.14:** Modeled temperatures (°C) versus measured temperatures comparison.

Initial observation reveals that all of the measured temperatures, except at bottom skirt, are significantly cooler than those predicted by the FE analysis. The primary contribution to the difference in measured versus modeled temperatures is probably due to the differences in the achieved engine operating condition and the LE-55 operating condition - particularly the leaner air-fuel ratio run during the engine test. The leaner air-fuel ratio would have a tendency to cool the piston. This is confirmed by the bottom skirt thermocouple location where the measured



temperature matched very well with the modeled temperature. This thermocouple location is farthest from any crown cooling induced by the presence of excess combustion air.

The measured spherical joint piston data remains useful, however. Boundary conditions for the actual engine operating conditions can be input into the FE analysis. The FE analysis can then be rerun to determine how well the recalibrated model spherical joint piston temperatures match actual engine operating temperatures. An exercise to match the measured engine data to a recalibrated FE model was not attempted before the end of the contract.

### 3.1.7 Design for Manufacture

The spherical joint piston concept design consists of several precision machined components. It should be noted that precision machined parts in the piston design result in higher overall cost of the piston assembly. Several design refinements are presented which reduce the number of precision machined parts and lead to a reduction in the ultimate cost of the piston assembly.

A major design refinement would be to machine the complete piston from a single casting. This approach would incorporate the holder ring within the monolithic piston casting and would completely eliminate the need for the threaded ring. The proposed one-piece spherical joint piston design is shown in Figure 3.1.15.

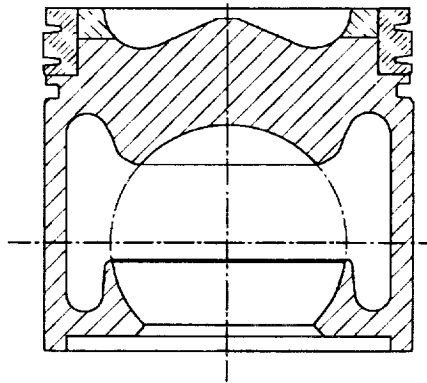


**Figure 3.1.15:** Proposed one-piece spherical joint piston design.

The internal casting cavity could be formed by a sand core. The core could be easily removed from the casting through the large underside opening. Core techniques are currently available which would allow the piston to be squeeze cast.

An alternative to the one-piece spherical joint piston is to use two simpler castings – a crown casting and a skirt casting. The castings would be welded together somewhere in the thin walled skirt area. This approach would allow substitution of a material with a relatively low coefficient of thermal expansion for the skirt.

The piston and connecting rod should be viewed as a system. Typically, in a system, as the complexity of one component is reduced the complexity of an associated component increases. In the case of the one-piece piston, as the piston design is simplified the complexity of the connecting rod design increases in order to facilitate assembly of the two components.

Consider the amount of bearing area required for satisfactory operation of the small end of the connecting rod. First, there is the upper bearing surface which transmits the combustion load into the shank of the connecting rod. Second, there is the lower bearing surface which bears the inertia load of the piston. The lower bearing surface can be made much smaller than the upper bearing surface since the inertia loads are small in comparison to the combustion loads. Relatively small side loads require no separate bearing surface.

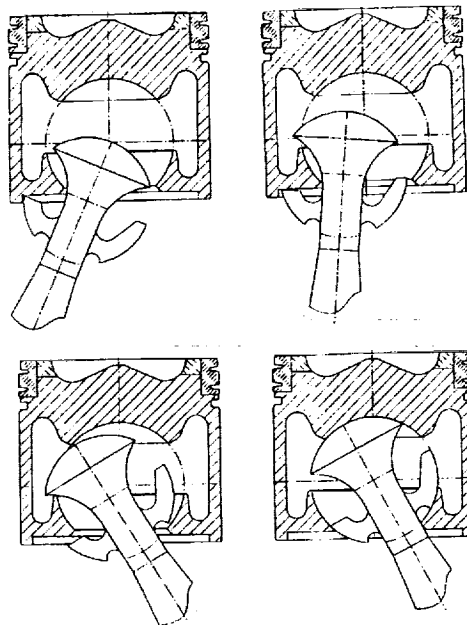


**Figure 3.1.16:** Proposed connecting rod installation for the one-piece spherical joint piston.

Combining the bearing area requirements with the need for low assembly weight, a modified sphere design results for the small end of the connecting rod which is similar in appearance to an apple core. An important advantage of this design is that its horizontal width is smaller than the diameter of the original sphere. With careful removal of material from the small end sphere, and after finding a procedure for connecting rod inclination and movement, the small end sphere (apple core) can be introduced through the bottom opening of the piston even though the bottom opening diameter is only 72.5% of the full sphere diameter (Figure 3.1.16). The fact that the connecting rod's inclination in an engine is limited to  $\pm 18.1^\circ$  ( $r/l = 0.31$ ) ensures satisfactory connection between the piston and connecting rod once assembled.

There is one restriction with respect to the cross section of the connecting rod in the vicinity of the small end. To allow maximum inclination of the connecting rod during assembly while maintaining sufficient load bearing area the shank cross section has to have an elliptical shape with the major axis of the ellipse in the direction of the crankshaft. Physical models of the one piece spherical joint piston and apple core connecting rod have been built. Assembly and disassembly of the piston and connecting rod is easily accomplished and repeatable.

In production, the one-piece piston would be squeeze cast. The connecting rod would be forged and the piston bearing surfaces of the single point turned to desired specifications. Under fully established production, the cost of the piston and connecting rod assembly is anticipated to be comparable to competing alternative piston designs.

### **3.1.8 Conclusions - Spherical Joint Piston**

- A spherical joint piston has been developed through the point of proof-of-concept to withstand the increased thermal and mechanical loads present at the LE-55 operating conditions. The fiber reinforced aluminum piston provides high mechanical load carrying capabilities. The freely rotating piston allows for uniform thermal growth, which facilitates smaller clearances between the piston and cylinder liner resulting in improved guidance and reduced oil consumption.
- Tests of the spherical joint piston were conducted in a Cummins single cylinder L10 engine. Engine evaluation included no-load motoring tests, low-load engine firing tests and high-load engine firing tests. Maximum sustained peak cylinder pressures were in excess of 24 MPa. One piston completed over 300 hours of general combustion and performance testing; another completed 100 hours of steady state operation followed by 100 hours of transient cycle testing. Each 100 hour test was run with 20.7 MPa peak cylinder pressures at full load.
- Tests were conducted to measure the rotation of the piston in the operating single cylinder engine. The rotation measurements indicate that the existing spherical joint piston design does rotate. However, the piston's rotation is random and unpredictable.
- Piston temperatures were measured on an instrumented, operating spherical joint piston using a telemetry system. Measured piston temperatures were, in general, significantly cooler than predicted temperatures for the same piston locations. Differences in the temperatures were most probably due to differences in the actual and modeled engine operating conditions. Boundary conditions derived from the actual engine operating conditions could be used to recalibrate the spherical joint piston FE model.
- A one-piece spherical joint piston design has been proposed with the intent to reduce the number of components, weight and cost of the concept piston design. The one-piece piston design would eliminate the holder rings and threaded ring found in the original design though the complexity of the connecting rod necessarily increases. Under fully established production, however, the cost of the one-piece piston and connecting rod assembly is anticipated to be competitive with alternative piston designs.

### **3.2 Spherical Joint Connecting Rod**

The ball and socket spherical joint facilitates the design of a shorter piston with high mechanical and thermal load capability. Unlike a conventional wrist pin piston with a hole through the piston skirt, the junction of the spherical joint piston and connecting rod does not interfere with the piston skirt or oil ring. In theory, the center of rotation of the spherical joint piston can be moved closer to the piston's center of mass. This allows for a more stable piston with the possibility of reducing the skirt length and lowering the oil control ring. The axisymmetry of the spherical joint allows piston rotation which promotes a uniform piston temperature distribution resulting in uniform thermal growth. A 16 to 29% larger bearing area than a conventional wrist pin piston along with symmetrical load support means higher cylinder pressure capabilities with the spherical joint.

#### **3.2.1 Baseline Design**

A concept or baseline connecting rod design was developed in Phase I. The concept connecting rod design consisted of an 80 mm sphere mated to the shank of a 1991 Cummins L10 production connecting rod. Prototype connecting rods using this baseline design were rough machined from steel bar stock. The connecting rods were quenched and tempered to 30 HR<sub>C</sub> with the sphere further hardened to 50 HR<sub>C</sub> using a salt dip process. The hardening process was unable to maintain a uniform hardened case depth of 0.5 mm. It was determined that a different means of hardening sphere was needed for the connecting rods to be produced within specification.

Interference between the baseline connecting rod and the piston at 90° before and after top dead center (TDC) became evident once a finite element model (FEM) was created. The location of interference on the connecting rod occurred at the transition between the sphere and the rectangular shank. The size of this sphere transition zone should be kept sufficiently small to avoid interference between the connecting rod and the piston holder rings. To keep the stresses in the sphere transition zone at an acceptable level, the sphere transition zone cross-sectional area should be maximized. It was evident that the geometry of the sphere transition zone would control subsequent spherical joint connecting rod designs.

Detailed design analysis of the ball transition zone was subcontracted to ColTec, Inc. of Columbus, Indiana. ColTec, Inc. used a finite element analysis (FEA) to evaluate stresses and fatigue strength of the baseline and redesigned connecting rods.

#### **3.2.2 Finite Element Analysis**

Cummins provided the geometry data for the baseline design to ColTec, Inc. ColTec, Inc. then developed a 3-D CAD model of a baseline connecting rod and a simplified piston. The CAD model was first used to evaluate the interference between the piston and connecting rod. The maximum amount of interference occurs when the piston is at 90° before and after TDC. At these positions, the angle between the axes of the connecting rod and piston is at its maximum value of 18.1°. A surface model of the baseline rod was rotated 18.1° about the sphere center and then overlaid with a surface model of a simplified piston. An intersection of the surfaces indicated interference between the connecting rod and piston.

The CAD model was further utilized to create a FE model of the connecting rod. The symmetry of the connecting rod was advantageously used by only modeling one quarter of the connecting rod. The initial FE model consisted of the connecting rod geometry from the midpoint of the shank to the top of the ball. This modeling approach reduced the computer analysis time, allowing for quick analyses of the primary region of interest for stresses and fatigue strength – the sphere transition zone. The material properties used in the analysis were those for alloy steel:

- Modulus:  $E = 207 \text{ GPa}$
- Poisson's Ratio:  $\nu = 0.28$

The combustion stroke and the intake stroke were chosen as loading extremes under which to analyze the connecting rod. During the combustion stroke the connecting rod is under compression. The maximum compression loading occurs at TDC under a cylinder pressure of 21 MPa. The cylinder pressure exerts a force of 254 kN on the piston. Accounting for the inertia force of the piston at 1500 rpm, the resultant force which acts on the sphere is 248 kN. This force is distributed uniformly over the top half of the ball and results in a pressure of 52.2 MPa. This pressure was used as the combustion loading in the FE analysis. During the intake stroke the connecting rod pulls the piston downward and is under tension. With the cylinder pressure nearly at ambient level the only loading during the intake stroke is due to piston inertia. The piston inertia force acts uniformly along the underside of the sphere resulting in a pressure of 3.9 MPa. This pressure was used as the intake loading in the FE analysis.

The stresses calculated for the first FE analysis are shown for the combustion stroke and intake stroke in Figures 3.2.1 and 3.2.2, respectively. Note the region with the highest stresses, shown in dark blue and yellow respectively, in both loading cases is the sphere transition zone. The sphere transition zone is also the critical region with regard to fatigue strength. Cummins uses an equivalent fully reversed stress ( $\sigma_e$ ) criterion when evaluating connecting rod fatigue strength.

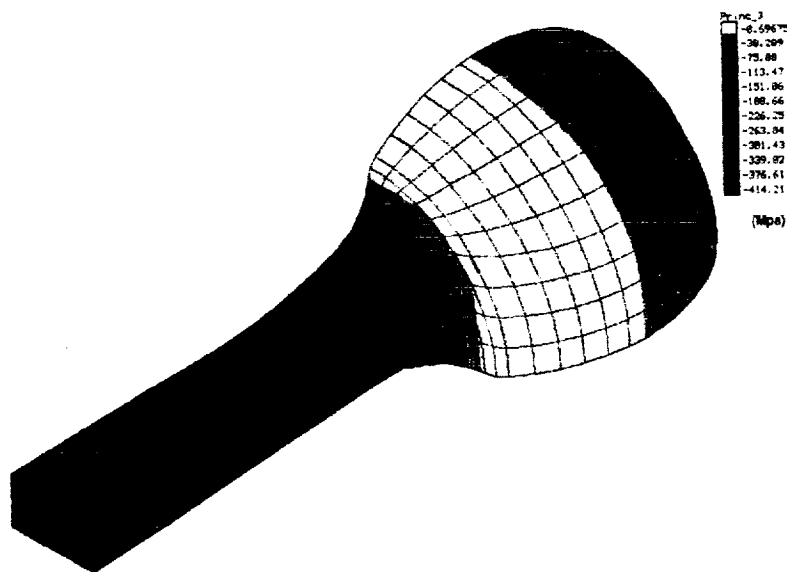


**Figure 3.2.1:** Stress contours for the combustion stroke – baseline connecting rod design.

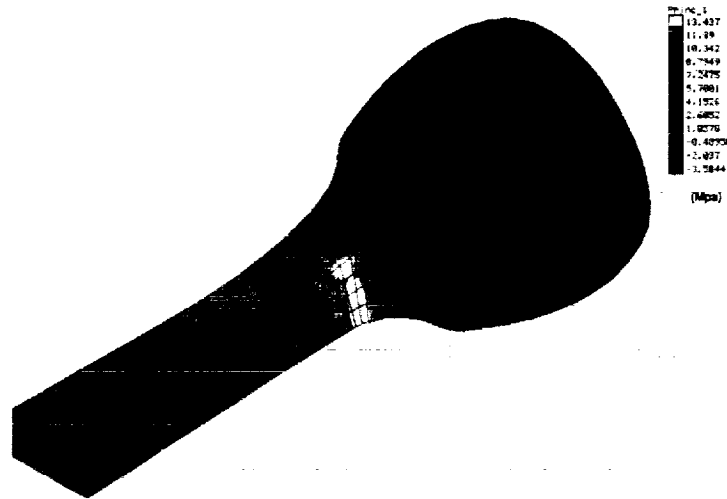


**Figure 3.2.2:** Stress contours for the intake stroke - baseline rod design.

Equivalent fully reversed stress is defined as:

$$\sigma_e = \frac{\sigma_a}{1 - \sigma_m / S_f} \quad 3.2.1$$

$\sigma_a$  - Alternating stress

$\sigma_m$  - Mean stress

$S_f$  - Fatigue strength coefficient for the material

The Cummins equivalent fully reversed stress criterion for connecting rods is:

$$\sigma_e < 152 \text{ MPa}$$

For the baseline design, the FE analysis predicted  $\sigma_e = 189 \text{ MPa}$ . Since the baseline design failed the equivalent fully reversed stress and piston clearance criteria, an alternative design was investigated.

A modified connecting rod design was developed which incorporates an elliptical cross-section shank. The elliptical cross-section chosen allowed for 2 mm clearance with the piston. This clearance was chosen in anticipation of forging die wear and flash line. The FE analysis again showed that the sphere transition zone was the highest stress region. The equivalent fully reversed stress was  $\sigma_e = 183 \text{ MPa}$ . This stress exceeds the criterion established for  $\sigma_e$ . The last option for meeting the  $\sigma_e$  criterion with the elliptical cross-section was to increase the shank's cross-sectional area. Increasing the cross-sectional area would cause an interference between the connecting rod and the piston unless the I.D. of the piston holder rings could be increased. Kolbenschmidt AG was contacted to determine the viability of increasing the holder rings' I.D.

Kolbenschmidt agreed to increase the I.D. from 56 mm to 61 mm since this modification did not negatively impact the bearing capability of the holder rings. The final modified design included an elliptical cross-section shank with sufficient cross-sectional area to meet the  $\sigma_e$  criteria. The equivalent fully reversed stress for this design was  $\sigma_e = 147$  MPa. The stresses calculated for this design are illustrated in Figures 3.2.3 and 3.2.4. A comparison of the stresses for the three designs is presented in Table 3.2.1.

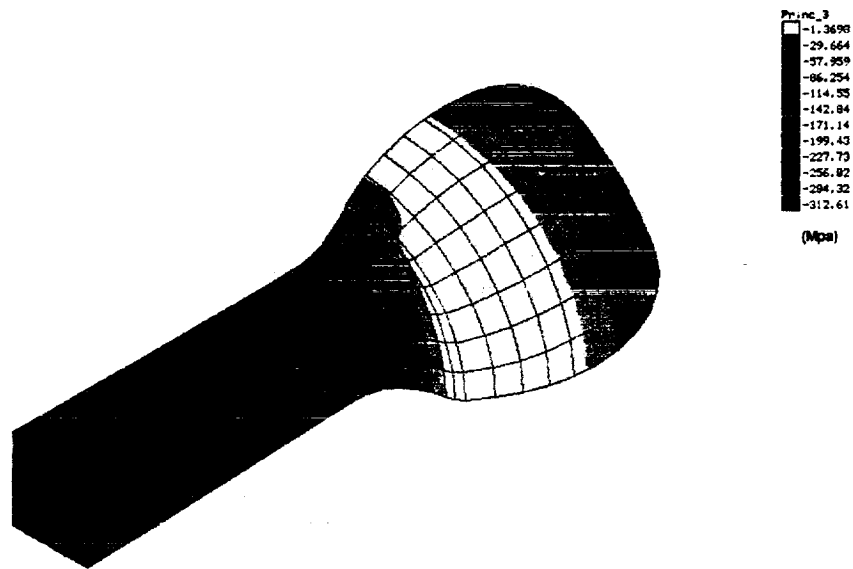


**Figure 3.2.3:** Stress contours for the combustion stroke – initial modified connecting rod design.

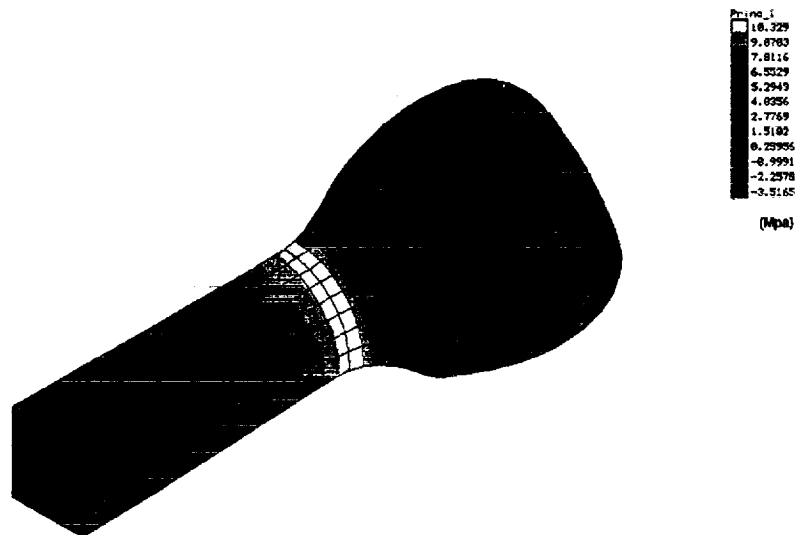


**Figure 3.2.4:** Stress contours for the intake stroke – initial modified connecting rod design.

**Table 3.2.1:** Stress maxima for three connecting rod designs

Design	Combustion (MPa)	Intake (MPa)	$\sigma_e$ (MPa)
Baseline	-414	13.1	189
Elliptical Rod	-400	13.1	183
Elliptical Rod - Increased Cross Section	-312	10.3	147

The final FE analysis of the connecting rod was performed after merging the FE model of the upper connecting rod (sphere to mid-point of shank) with a FE model of the lower rod (mid-point of shank to crank bore – big end). The final FE model is shown in Figure 3.2.5.

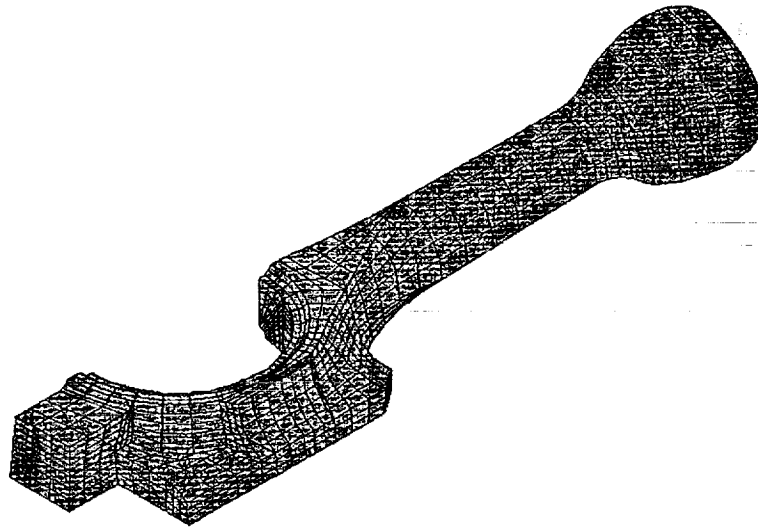


**Figure 3.2.5:** Final finite element model of the spherical joint connecting rod.

The load cases for the final stress analysis included a preload case along with the previous combustion stroke and intake stroke cases. The preload case modeled a bolt load and a crush load. The bolt load is the tensile load which holds the cap onto the big end of the connecting rod. Bolt loading used in this analysis was 86.7 kN. The crush load involves the press fit of the bearing shells inside the crank bore of the big end. The bearing shells are slightly oversized so that as the cap bolts are torqued the bearing shells undergo compression. The crush load is defined by the gap distance, and for this analysis the crush load gap distance used was 0.183 mm.

Results of the preload stress analysis are shown in Figures 3.2.6 and 3.2.7. The figures illustrate regions of high stress near the rear of the big end where the cap bolt seats. High stresses also occur in the region where the tip of the bolt threads into the big end. The maximum stress occurs



in the threaded region and has a value of 391 MPa. This stress is well below the yield strength of 4340 steel (1,380 MPa) and is considered acceptable.

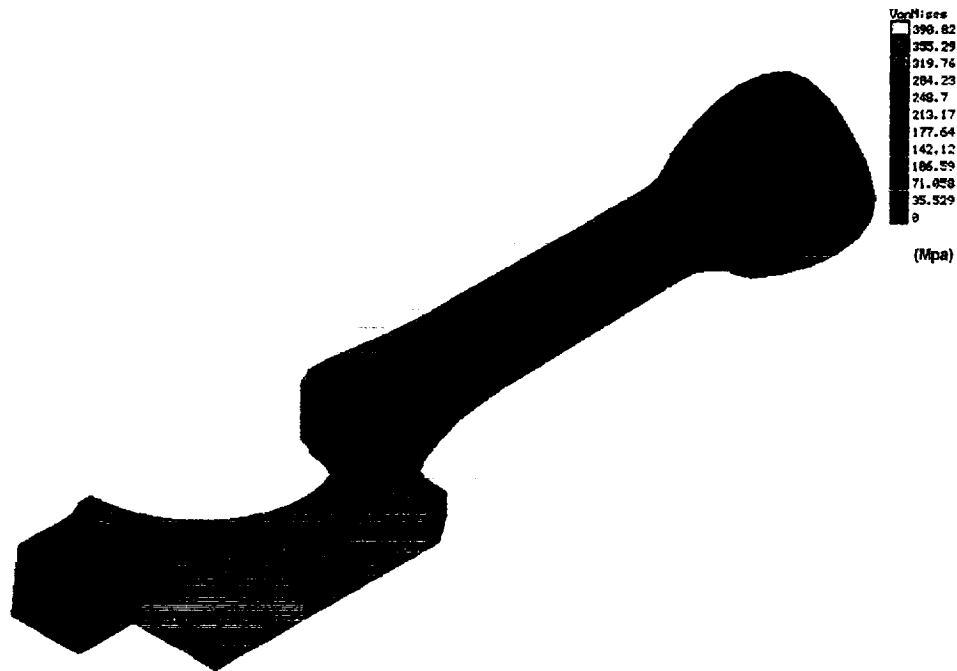


**Figure 3.2.6:** Stress contours for the preloaded case – final modified rod design.

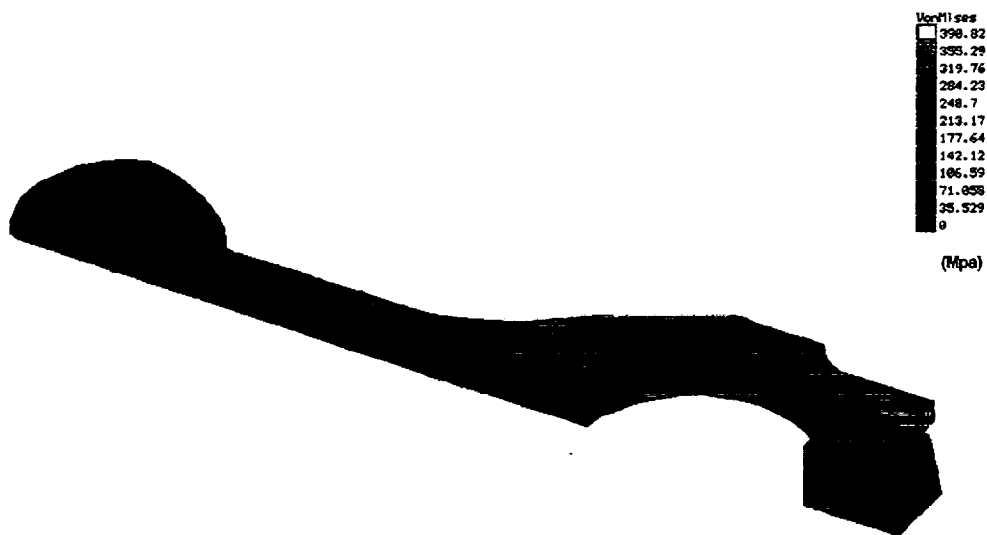


**Figure 3.2.7:** Stress contours for the preloaded case – final modified design viewed from the bearing side.

The stress contours for the combustion loading case are shown in Figures 3.2.8, 3.2.9, 3.2.10, and 3.2.11. The highest stresses occur in the vicinity of the bolts as was the circumstance in the preload case. The bolt region stresses do not vary significantly between the preload and combustion cases indicating that the preload dominates the stresses in the bolt region. The dominance of the preload stress ensures that stresses will not change significantly over time. Therefore, fatigue failures in this region are not a concern. Two high stress areas which were virtually unstressed at preload include the sphere transition zone and the shank at the top of the big end bore. Both of these areas are identified with red contours in Figures 3.2.8 and 3.2.9.

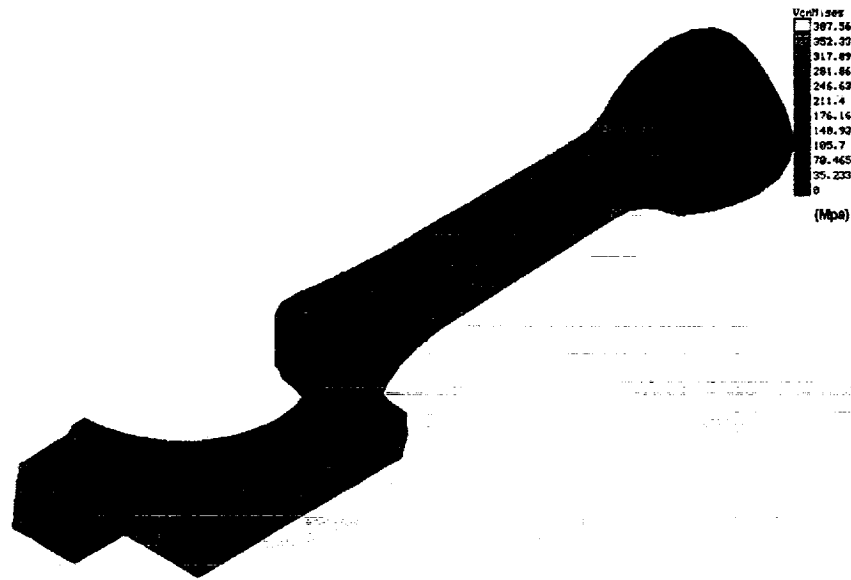


**Figure 3.2.8:** Von Mises stress contours for the combustion stroke – final modified design.

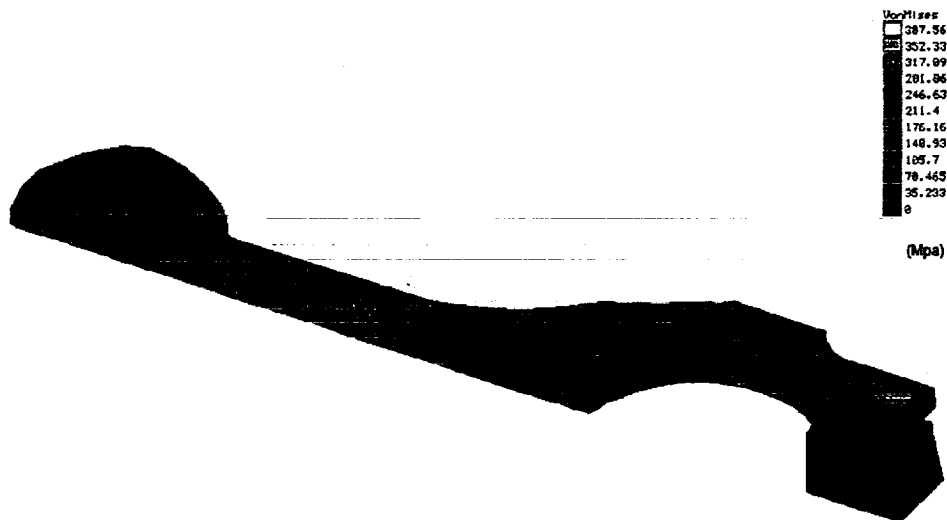


**Figure 3.2.9:** Von Mises stress contours for the combustion stroke – final modified design viewed for the bearing side.

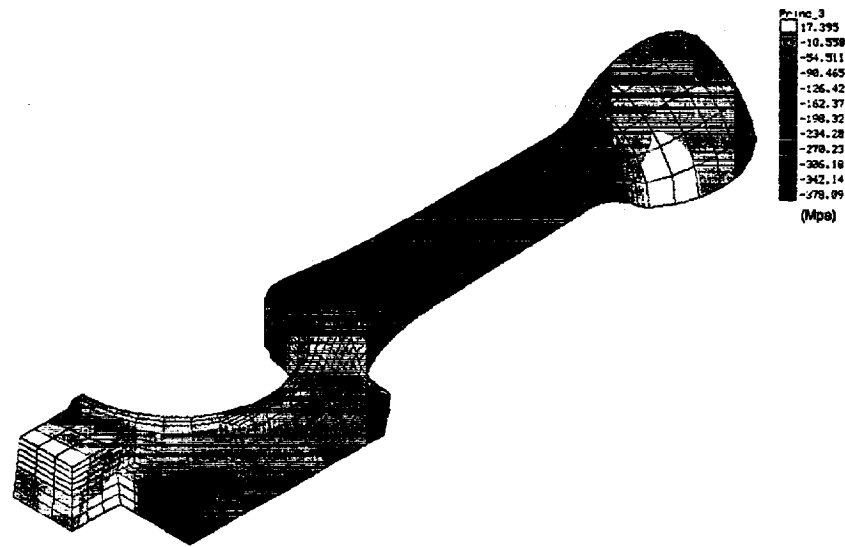


**Figure 3.2.10:** Equivalent fully reversed stress contours for the combustion stroke – final modified design.

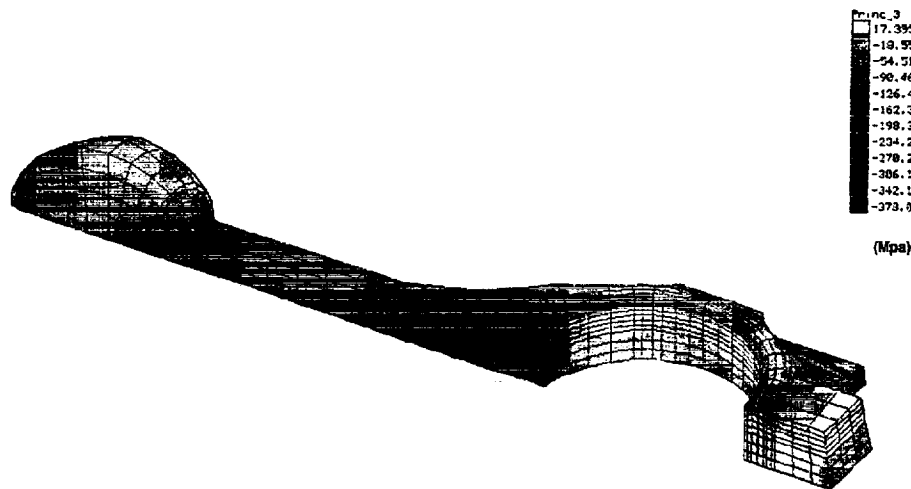


**Figure 3.2.11:** Equivalent fully reversed stress contours for the combustion stroke – final modified design viewed from the bearing side.

The sphere transition zone was expected to be an area of concern with regard to fatigue as was observed in the earlier analysis. Figures 3.2.10 and 3.2.11 show that the top of the shank is in a state of compression. The greatest compressive stress in this zone is 287 MPa. Figures 3.2.10 and 3.2.11 also show that the compressive stresses at the top of the crank bore are not as significant as the stresses at the top of the shank. The maximum compression stress at the top of the bore is 200 MPa. This comparison favors the top of the shank as the critical area for evaluating the design with regard to fatigue.

The stress contours for the intake stroke case are shown in Figures 3.2.12 and 3.2.13. The stress patterns and levels shown in Figure 3.2.12 are similar to those shown in Figure 3.2.6. The maximum tensile stress is 397 MPa. The maximum tensile stress in the shank for the intake stroke is 10 MPa. This stress occurs at the same location where the minimum compressive stress occurs during the combustion stroke. This region is where fatigue is of the greatest concern.

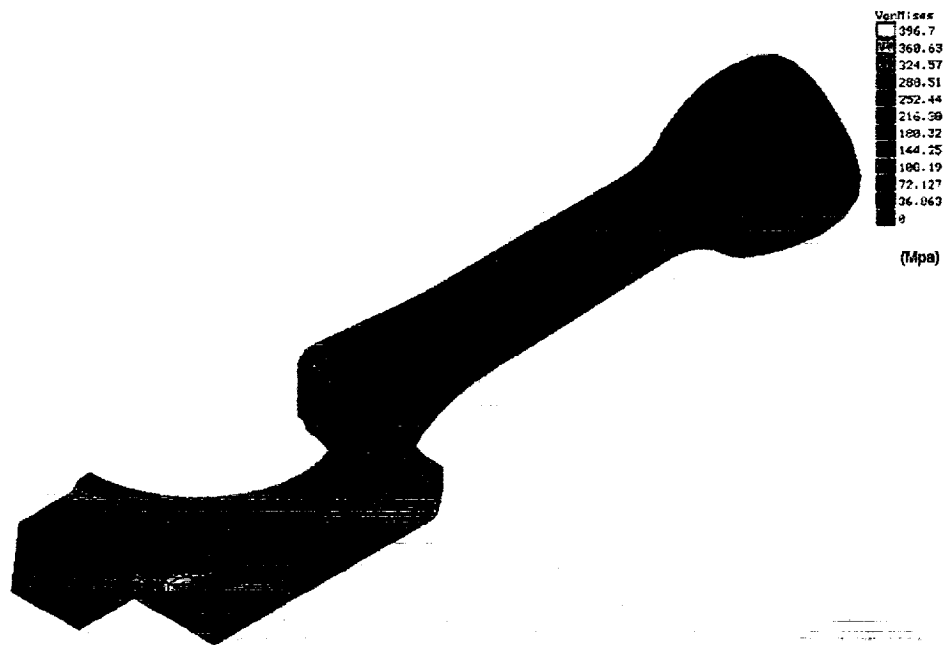


**Figure 3.2.12:** Von Mises stress contours for the intake stroke -- final modified design.

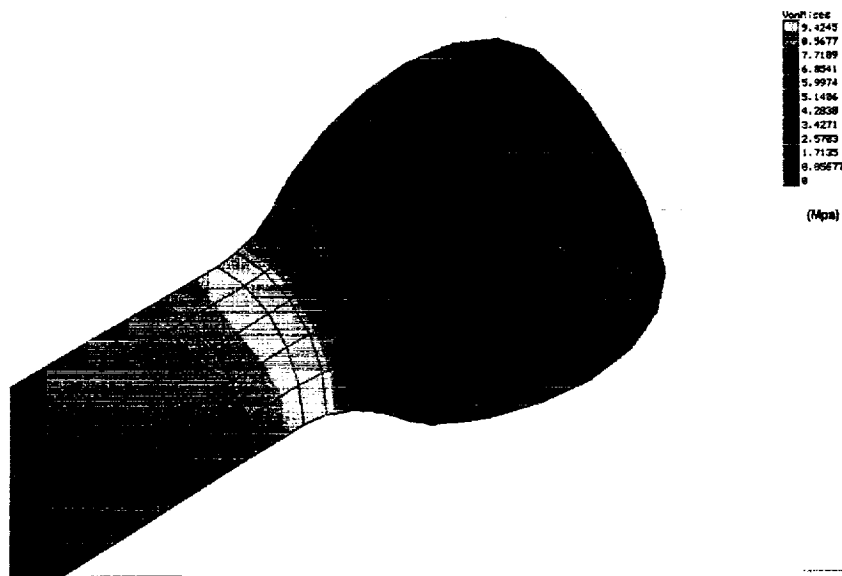


**Figure 3.2.13:** Von Mises stress contours for the intake stroke -- final modified design.

The stress results from the combustion stroke and intake stroke load cases were used to calculate the equivalent fully reversed stress for the complete connecting rod. The stress was calculated to be  $\sigma_e = 136$  MPa. This stress is well below the 152 MPa limit.

Due to the departure of the connecting rod shank cross-section from the standard I-section, a whip stress was calculated. Whip stress results from the bending in the shank as the connecting rod rotates back-and-forth about the piston socket. The maximum bending stress at 2000 rpm occurs 140 mm from the sphere center. This location is at the base of the shank in the transition to the big end. The maximum whip stress was calculated to be 21 MPa. This stress is negligible in comparison to the stresses calculated for the preload case.

Table 3.2.2 summarizes the FE analysis results for the final modified connecting rod. Note that all the predicted stress levels are below their respective recommended limits. Additionally, adequate clearance between the piston and connecting rod has been achieved through a minor modification to the holder ring design.

**Table 3.2.2:** FE analysis stresses and limits in the final modified connecting rod design

Stress Case	Preload Yield (MPa)	Whip Yield (MPa)	Equivalent Fully Reversed Fatigue (MPa)
Final Modified Design	391	21	136
Recommended Limit	1,389	1,389	152

### 3.2.3 Machining Development

Machining of the prototype connecting rods was done by C&A Tool Engineering, Inc. of Churubusco, Indiana. C&A Tool was selected after an exhaustive search for machine shops capable of meeting the demanding surface finish requirements for the sphere end of the rod.

C&A Tool used 3-D CAD wireframe information provided by ColTec, Inc. to program their CNC machining stations. A qualification connecting rod was machined from aluminum using the CNC program. The aluminum half-cut connecting rod was submitted to Cummins Metrology for inspection. The results from the dimensional qualification of the aluminum half-cut connecting rod were positive.

The connecting rods were machined from E4340H alloy steel. E4340H is an electric furnace (E) alloy with deep hardenability (H). This alloy was chosen for its resistance to fatigue and impact failure. The E4340H alloy also provides a long service life primarily due to its low phosphorus and sulfur limits. The elemental composition of E4340H is given in Table 3.2.3

**Table 3.2.3:** Connecting rod E4340H alloy steel chemistry

Element	C	Mn	P	S	Si	Ni	Cr	Mo	Fe
Percent	0.37	0.60	0.025	0.025	0.15	1.55	0.65	0.20	
Composition	to	to	max.	max.	to	to	to	to	Balance
Limits	0.44	0.95			0.30	2.00	0.95	0.30	

Machining of the connecting rods involved several processes. The first process was to rough mill the connecting rods. The connecting rods were then heat treated to increase their hardness from 93 HR<sub>B</sub> as received to 24 HR<sub>C</sub>. The connecting rods were then finish milled and rough ground. The sphere end of the connecting rod was also rough ground at this point. After rough grinding the sphere end of the connecting rod it was necessary to bring the sphere's hardness up to that of a standard piston pin – 50 HR<sub>C</sub>. Heat treating the sphere required care to avoid hardness "bleed" into the sphere transition zone. Hardness bleed into the transition zone can result in residual stresses. As discussed in the finite element analysis, minimizing the stresses in the sphere transition zone is critical for connecting rod fatigue life.

Hardening the sphere was accomplished with a custom fabricated induction heating coil. The connecting rods were addressed with the coil while they were spun at 1600 rpm. Spinning the connecting rods held the hardness case depth to 0.5 mm and eliminated hardness bleed. After induction hardening the connecting rods underwent a cryogenic treat process. This process involved exposing the ball to cryogenic temperatures with the affect of promoting the transformation of austenite phase in the hardened case to martensite phase. Cryogenic treatment was used to control dimensional variability (self growth) in the sphere after the finish grind.

The last machining process involved finish grinding the sphere end of the connecting rods. The surface finish of the sphere was held to the equivalent requirements for a conventional piston pin. The surface finish requirements and the achieved surface finish are summarized in Table 3.2.4.

**Table 3.2.4:** Summary of sphere surface finish

Parameter	Requirement	Achieved
Roughness, R <sub>a</sub>	≤ 0.102 μm	0.02 μm
Peak-to-Valley, R <sub>tm</sub>	0.5 μm @ 76 μm cutoff	0.12 μm
Bearing Area, T <sub>pl</sub>	≥ 60% @ 0.25 μm	85%

### 3.2.4 Fabrication and Testing

C&A Tool Engineering, Inc. was given approval to proceed with fabrication of ten spherical joint connecting rods. The connecting rods were to be machined to the design proposed by ColTec, Inc. with a 1.1 mm width reduction at the big end. The width reduction was proposed as a result of a statistical analysis of the stackup clearances between the spherical joint connecting rod and

other engine structures. The analysis recommended a 0.55 mm reduction on each side of the rod at the big end.

In this spherical joint piston design there is no access for piston cooling nozzles to supply oil to the undercrown. Supplying lubricating and cooling oil to the piston was accomplished by incorporating several drillings within the connecting rod. as shown in Figure 3.2.14, a feeder drilling was placed between the oil supply at the big end bearing and the center of the base of the connecting rod shank. A main drilling was then placed between the base of the connecting rod and the center of the sphere. At the sphere, the drilling was separated into three branches – the main branch proceeds to the top of the sphere while two lateral branches proceed to the left and right of the vertical center-line of the sphere. The main branch supplies lubricating oil to the sphere/piston bearing interface. The lateral branches supply cooling oil to the piston cooling gallery and are angled such that the oil stream clears the top of the holder rings throughout the entire engine cycle. The lateral drillings are positioned within a plane parallel to the engine crankshaft center-line.

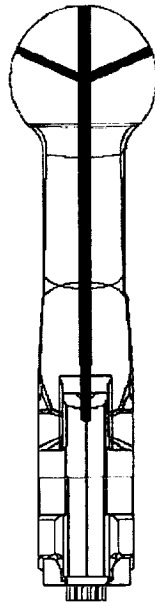


**Figure 3.2.14:** Connecting rod oil drillings.

Production big end connecting rod bearing halves were modified with oil slots in order to increase the oil flow to the connecting rod oil drilling. The bearing modifications are shown in Figure 3.2.15. As shown in Figure 3.2.15, an oil slot was placed along the entire inner diameter of the lower bearing half while the slot was cut only to the oil drilling on the short side of the inner diameter on the upper bearing half. The oil slot was not cut along the entire inner diameter of the upper bearing half in order to maximize the bearing area in the high load region.



**Figure 3.2.15:** Slotted connecting rod big end bearings.

Six connecting rods had been finish milled when one of the rods cracked in the sphere transition zone. It was determined that the failure was due to a quench crack that was present in the original bar stock billet. Ultrasound was used to analyze the quench crack. However, this method could not be used to locate quench cracks, only to confirm their presence. No other method for finding quench cracks in bar stock billets could be found. To ensure the integrity of the uncracked rods, the rod spheres were induction hardened as per plan, including the cryogenic treat process. None of these connecting rods cracked. Since the connecting rods did not crack during the high stress cryogenic treat process, it was confidently assumed that quench cracks did not exist in the remaining connecting rods. The connecting rod spheres were then finish ground.

Ten spherical joint connecting rods were fabricated and found to be in agreement with most dimensional specifications. One problem found in the first connecting rod delivered was the minimum and maximum ball to shank transition radii were smaller and larger than specified, respectively. This situation was remedied on the remaining connecting rods. Figure 3.2.16 is a photograph of a finished connecting rod.

Initial assembly of the spherical joint connecting rod and piston resulted in binding of the piston and connecting rod (see 3.1.4 **Spherical Joint Piston - Assembly and Engine Testing**). Using a marking compound during assembly trials it was discovered that the contact area between the piston and connecting rod was not as designed and resulted in binding. Location and concentricity of the piston saddle and holder rings with respect to the piston skirt, and location of the sphere with respect to the crank bore are critical parameters that must be controlled.

As stated previously, the initial motoring tests of the spherical joint piston/connecting rod assembly resulted in galling between the piston holder rings and the sphere of the connecting rod. Several modifications were made to the holder rings to address the galling (see 3.1.4 **Spherical Joint Piston - Assembly and Engine Testing**). In addition to the holder ring modifications, a modification was made to the connecting rod to further reduce the potential for galling.



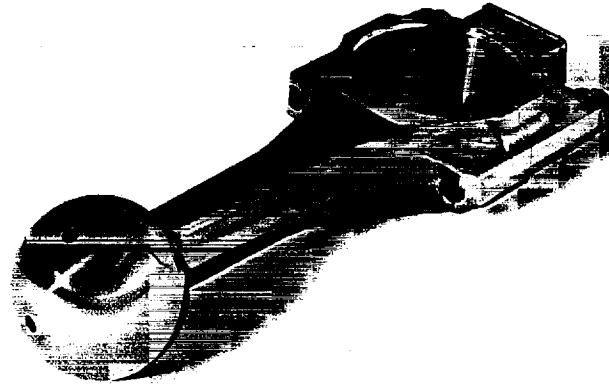


**Figure 3.2.16:** Final design (finished) of the spherical joint connecting rod.

The modification to the connecting rod involved increasing the radius of the transition between the sphere and the connecting rod shank. By increasing the radius, the potential for this connecting rod feature to plow into the bearing surface of the holder rings was minimized. As already noted, modifications to the connecting rod and holder rings enabled successful operation of the spherical joint connecting rod/piston assembly in a firing single cylinder research engine.

### **3.2.5 Conclusions - Spherical Joint Connecting Rod**

- The spherical joint connecting rod design provides 16 to 29% greater bearing area than the traditional wrist pin rod and piston.
- The final connecting rod design incorporates an elliptical cross-section shank with sufficient cross-sectional area to meet Cummins equivalent fully reversed stress criterion for connecting rod of  $\sigma_e = 152$  MPa. The elliptical cross-section shank was necessary to provide adequate operational clearance between the connecting rod and piston holder rings.
- Due to the departure of the connecting rod shank cross-section from the standard I-section a whip stress was calculated. Maximum whip stress was determined to be 21 MPa. The magnitude of the whip stress was negligible in comparison to other stresses within the connecting rod.
- A spin induction hardening process was developed to bring the hardness of the rod sphere up to an acceptable 50 HR<sub>C</sub>. The hardening process maintained a uniform 0.5 mm case depth.
- The case hardened sphere was subjected to cryogenic temperatures to promote the transformation of austenite phase in the hardened case to martensite phase. The cryogenic treatment was used to control dimensional variability in the sphere after finish grind.
- The form and finish requirements of the connecting rod sphere were met and surpassed on the final grind of the ten connecting rods machined for engine test.
- The spherical joint connecting rod was successfully tested in a single cylinder research engine after minor machining modifications were made to reduce the potential for sphere galling against the piston holder rings.

### **3.3 Spherical Joint Piston Telemetry**

The spherical joint piston design represents a major departure from piston designs currently used in on-highway, heavy duty diesel engine applications. Extensive finite element (FE) analysis of the spherical joint piston was conducted during the initial stages of design. In order to verify the results of the FE analysis it is necessary to make measurements on a piston operating under in-cylinder conditions which define the input boundary conditions. A new piston telemetry system was developed to meet the special measurement requirements of a rotating spherical joint piston operating under extreme in-cylinder conditions.

In the past, instrumented conventional pistons have been used in conjunction with flexible lead wires supported by a mechanical 'grasshopper' linkage. In this manner, electrical signals were transmitted from the reciprocating piston inside an operating engine to data acquisition equipment outside the engine. The spherical joint piston differs from a conventional wrist pin piston in that the spherical joint piston is free to rotate about the cylinder bore axis. A mechanical linkage would restrain the spherical joint piston's rotation thus seriously compromising the validity of the measurements. In addition, mechanical linkages typically require extensive engine modifications and have a relatively short operating life due to wire fatigue at the linkage flexure points.

Although short range telemetry has been previously used for piston measurements [Ref 2] [Ref 3] [Ref 4] [Ref 5], wider use of such telemetry systems has been restricted by the problems associated with providing a simple and reliable source of electrical power. Batteries are subject to durability and maximum operating temperature limitations and impose a severe weight penalty. Inductive power transfer systems, though potentially effective, require major engine modifications. At least one researcher has successfully generated electrical power on a reciprocating piston using an inertial generator [Ref 2], but at power levels insufficient to activate most conventional telemetry systems or transducers.

In this effort, a piston-mounted electrical power generator which utilizes the relative motion between the piston and the cylinder liner wall was developed to overcome the limitations of currently available telemetry power supplies. The power generator was developed in parallel with the spherical joint piston and has subsequently been used in conjunction with a custom FM telemetry system to measure spherical joint piston operating temperatures.

#### **3.3.1 Design Specifications**

Real time temperature measurement and dynamic strain measurement were the primary design requirements for the telemetry system. The signal conditioning requirements for temperature measurement are quite different from the requirements for dynamic strain measurement. Two similar but distinct telemetry systems would be required for the two measurements.

An in-house survey of potential piston telemetry users was conducted in order to identify the major attributes desirable in a telemetry system regardless of specific application. The desired attributes were then translated into specific design goals for the spherical joint telemetry system and its associated power supply, as shown in Table 3.3.1. Additional measurement and environmental specifications were drawn up and are summarized in Table 3.3.2.

**Table 3.3.1:** Telemetry system design goals

Design Goal	Measure
Minimum engine modifications	No cylinder block or other base engine modifications
Applicable to various measurement parameters and transducer types	Could be adapted to measure acceleration, displacement, pressure, etc.
Integral power source	Continuous operation not limited by power source
Applicable across engine families	Package size compatible with smallest piston
Impose no speed or temperature constraints upon engine operation	Operation from low idle to maximum overspeed, at piston skirt temperature
Non-intrusive	No significant change in heat flow or load paths
Applicable in field	Installation and removal by component substitution, with no permanent engine modifications

**Table 3.3.2:** Telemetry measurement and environmental specifications

Parameter	Temperature System	Strain System
Number of Channels	7 or 15	1, 4 or 7
Scan Rate (per channel, user selectable)	2 to 200 sec	2 to 200 sec
Frequency Response		
Single Channel	-	20 kHz
Multi-Channel	-	2.5 kHz
Measurement Range	20 to 600°C	± 2500 µε
Measurement Accuracy	± 3°C	± 25 µε
Power Consumption (max)	15 mA @ 9 VDC	
Operating Temperature Range	20 to 130°C	
Operating Speed Range	600 to 2300 rpm	
Maximum Acceleration	6000 m/s/s	

The spherical joint piston's geometry requires that the telemetry system module be designed in the shape of an annulus. The module package design is shown as-mounted on a spherical joint piston in Figure 3.3.1. The module consists of two submodules – a telemetry submodule and a power generator submodule. The telemetry submodule which includes signal conditioning circuitry, a multiplexer and a transmitter occupies a 240° annulus sector. The power generator submodule occupies the remaining 120° sector.

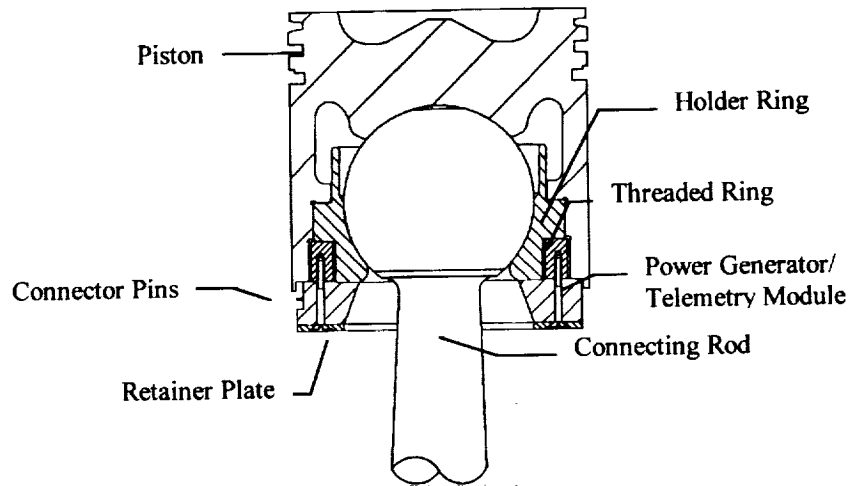


**Figure 3.3.1:** Telemetry system module packaging for the spherical joint piston.

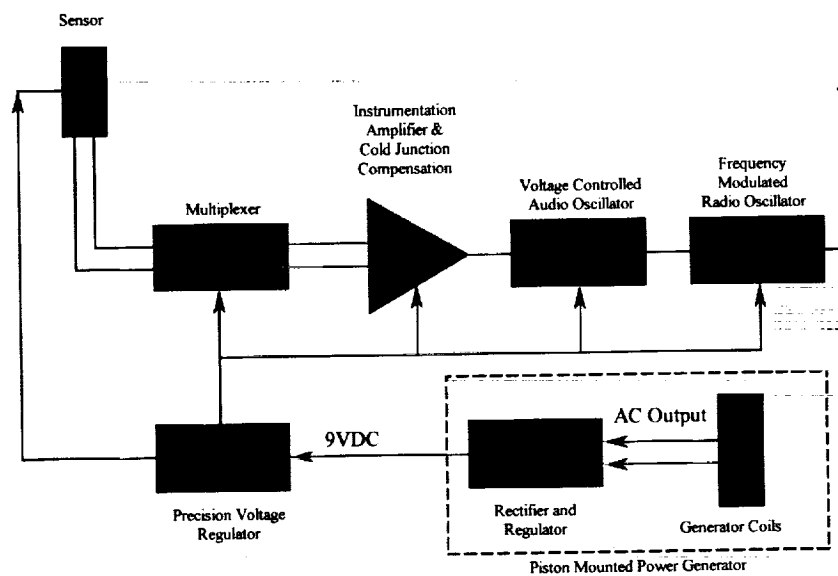


**Figure 3.3.2:** Piston mounted temperature telemetry module functional block diagram.

A functional block diagram of the temperature module is shown in Figure 3.3.2. The diagram consists of a proprietary power generator submodule (lower right) and a telemetry submodule employing existing and proven signal conditioning and FM-FM radio technology. An antenna is mounted in the engine oil pan (not shown). A cable connects the antenna to a receiver and demodulator external to the engine.

A review of commercially available telemetry systems revealed no one system embodied all the user specified attributes. A number of systems had the required measurement capabilities.

However, none of the systems had the means to generate electrical power while meeting all the environmental, duration and minimum-modification constraints. In order to meet the piston telemetry system design requirements, a novel power generator was developed in-house. Development of the in-house power generator is presented in the following section.

### 3.3.2 Power Generator

Development of the power generator included evaluation of existing concepts, paper studies of new concepts, initial experimental work, detailed analysis and modeling, rig evaluation and motoring engine rig tests. To meet the telemetry system design goals and specifications, the required power generator had to be capable of providing a continuous regulated output of 15 mA at 9VDC under all anticipated engine operating conditions. The power generator had to be compact and have minimal effect on temperature or loading distributions within in-cylinder components. The generator had to require minimum engine modifications for installation and be applicable for field measurements in customer engines. Though the telemetry system was intended for use in an operating engine, a means for providing power to the temperature telemetry system with the engine stopped was required to measure thermal transients after engine shutdown.

CONCEPT – The key to developing a viable power generator was seen as being able to harness a small portion of the abundant thermal or mechanical energy available within an engine and convert it into electrical energy. This reasoning led to the concept of taking advantage of the relative motion between the piston and cylinder liner as the basis of a linear generator using the arrangement schematically shown in Figure 3.3.3. In Figure 3.3.3, a coil ① is wound around a permanent magnet core ② and mounted on the underside of the piston. The magnet has pole pieces ③ which extend out to the cylinder liner wall. The cylinder liner wall is machined at a location below the surface swept by the piston rings to produce annular or arcuate grooves ④ with spacing equal to that of the magnet pole pieces. The grooves are backfilled with a flame sprayed application of a low permeability material. The cylinder bore is then finish machined and honed to produce a surface finish similar to that of a production cylinder liner. The result is a zone on the cylinder liner wall with alternating bands of ferromagnetic material (parent cylinder liner) and non-ferromagnetic material.

As the piston travels through its stroke, the magnetic circuit formed by the coil assembly and adjacent cylinder liner wall is periodically interrupted by the low permeability bands. The resulting change in magnetic flux ( $\delta\phi/\delta\tau$ ) generates an electromotive force (emf) in the coil. The output is rectified and regulated to provide the required DC voltage. The linear velocity of the coil varies over each engine cycle. With the variation of piston linear velocity the change in magnetic flux in the coil and the passing frequency of the magnetic bands in the cylinder liner wall also vary. The resulting voltage waveform is thus modulated in both frequency and amplitude as shown in Figure 3.3.4.

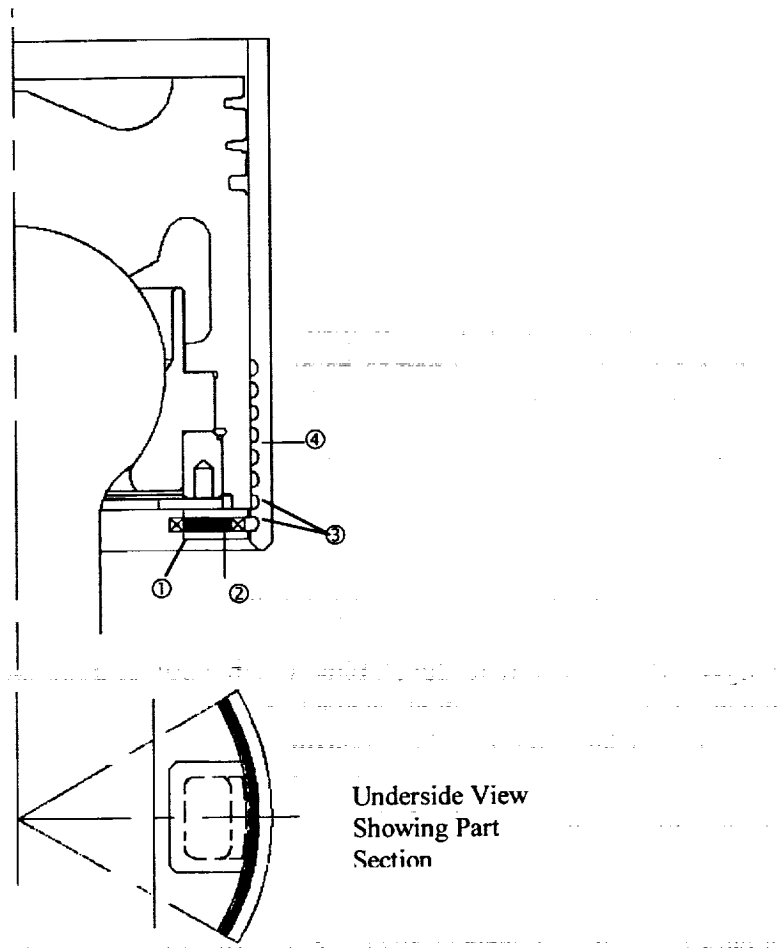


**Figure 3.3.3:** Schematic of linear power generator.

The power generator relies for its operation upon relative motion between the piston and cylinder liner and therefore cannot directly power the telemetry system with the engine stopped. However, the power generator design lends itself to the use of a stationary primary winding located at the base of the cylinder liner in order to induce a voltage in the generator coil while the coil is not reciprocating. The generator coil would necessarily have to be aligned with the stationary primary coil. This can be accomplished by barring over the engine to position the piston. In this manner, the telemetry system can also be used to measure piston temperature or strain transients immediately after engine shutdown.

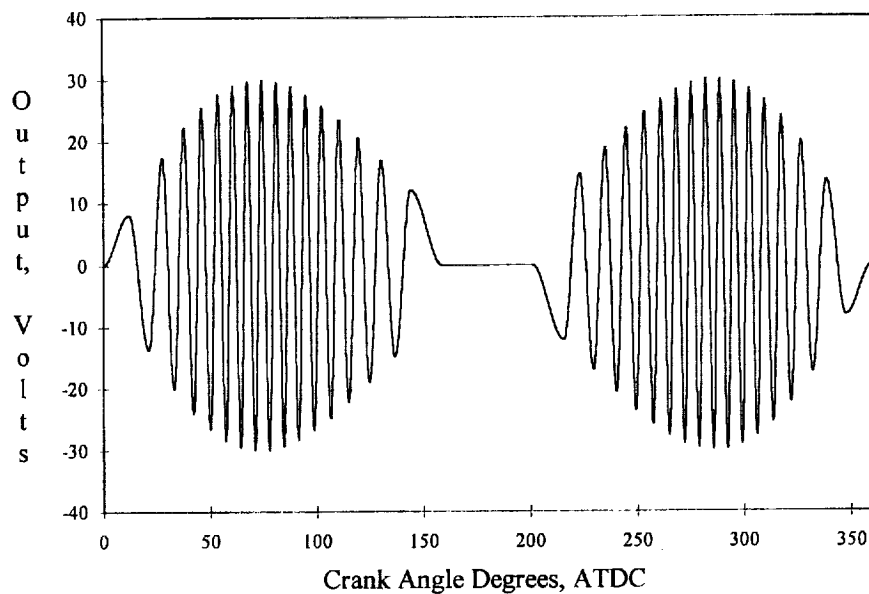


**Figure 3.3.4:** Calculated power generator voltage waveform.

**DESIGN ANALYSIS** – An analytical model of the power generator was constructed to assist in design optimization. Principle parameters incorporated into the analytical model were engine geometry, magnet material properties and dimensions, the number of coil turns, pole piece material properties and construction, air gap dimensions, cylinder liner groove spacing and non-ferromagnetic material properties.

Slider-crank geometry was used to calculate the instantaneous piston velocity throughout a complete engine cycle. The piston velocity was used to determine the instantaneous rate of change of flux in the magnetic circuit as a function of engine crank angle. The magnetic circuit was modeled to determine appropriate coil assembly dimensions for different permanent magnet materials and to estimate the corresponding total change in magnetic flux, operating load line and resultant induced voltage in the coil. With consideration to mechanical and thermal characteristics, a magnet material was selected on the basis of this analysis. The material properties of the magnet material were then incorporated into a more detailed analytical model for optimization of the coil assembly geometry. Power generator module packaging constraints required the adoption of two smaller coil assemblies connected in series. However, subsequent testing indicated that only one of the smaller coils is sufficient for all engine speeds above low idle (nominally between 600 and 700 rpm) provided that operating clearance between the coil and the cylinder liner wall is tightly controlled.

A major design consideration for the rectifier and regulator circuit was electrical energy management at low and high engine speeds. At low engine speeds the circuit must extract the maximum amount of energy from voltage pulses with successively decreasing amplitude. These pulses occur during piston deceleration at the end of each stroke. At high engine speeds the

circuit must dissipate excess generated power. A compromise of these conflicting requirements was accomplished by optimizing the rectifier and regulator circuit for low engine speeds. The rectifier circuit was then designed to dissipate the excess power generated at high engine speeds. To aid in regulator circuit development, the voltage waveform predicted by the analytical model was digitized and used as the control signal for a power amplifier driven through an impedance matching stage to give an output characteristic similar to that predicted for the power generator itself.

### 3.3.3 Rig Test and Validation

Much of the early telemetry system development work was conducted using the rotating test rig. Extensive testing was also performed in a motored, single cylinder engine test rig to simulate the conditions in a running engine while still allowing easy access to the piston for monitoring the power generator output. Description of the telemetry development work performed using each test rig follows.

ROTATING TEST RIG – The operating principle of the linear power generator was initially demonstrated using a lathe which doubled as a rotating test rig. A simple rotating analogy of the power generator was built. The analogy consisted of a section of a cast iron cylinder liner with axial grooves machined into its outer surface as shown in Figure 3.3.5. The cylinder liner section was spun in the lathe with a suitable power generator coil assembly mounted within close proximity. Early test results were very encouraging. One prototype configuration generated over 15V RMS across a 600Ω load at an equivalent engine speed of 2200 rpm. The rotating rig was used extensively during subsequent development of the power generator.



**Figure 3.3.5:** Cast iron cylinder liner with axial grooves in the O.D. as used in the lathe (rotating) test rig.



The rotating test rig was also used to assist with the selection of non-ferromagnetic groove backfill materials, to assist with the definition of the optimum groove depth and to assist with verification of the analytical model used to screen magnet materials and coil geometries. A typical plot of electrical output versus test rig rotational speed and total coil turns is shown in Figure 3.3.6. Although the test rig did not permit the generation of the precise waveform anticipated in an operating engine, it did allow most of the important design parameters to be explored quickly and effectively. For determination of sensitivity to groove depth, for example, sample cylinder liners were externally grooved, flame sprayed with various low permeability materials and then lathe turned to successively smaller diameters before each evaluation on the rotating test rig.

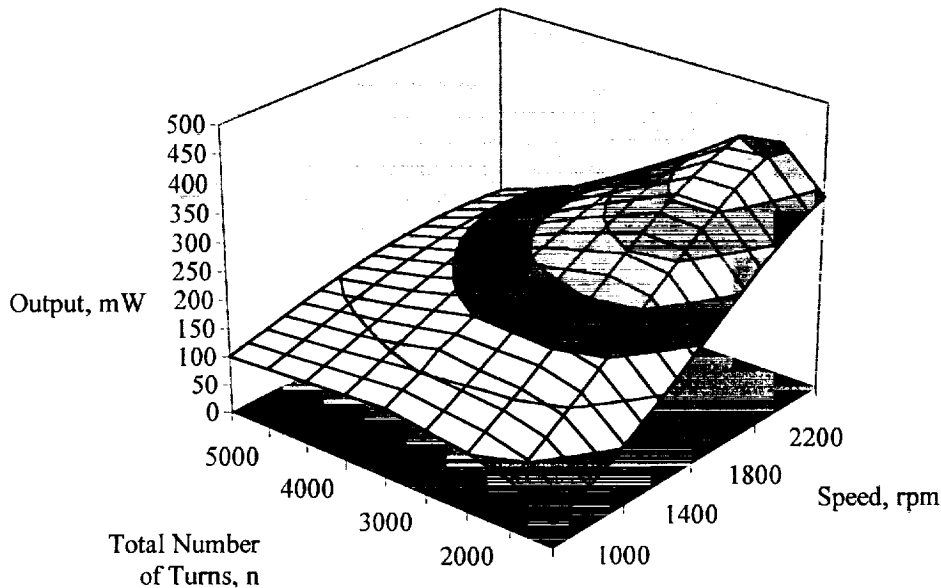


**Figure 3.3.6:** Plot of power generator output versus rig rotational speed and total number of coil turns.

ENGINE MOTORING TEST RIG – After design optimization and module packaging were completed, the emphasis of the test work switched to demonstrating the ability of the power generator and telemetry submodules to operate for extended periods under environmental conditions similar to those found in an operating engine. System evaluations were conducted on a engine motoring test rig shown in Figure 3.3.7. This rig incorporated a single cylinder L10 engine (SCE L10). The SCE L10 was motored by a 26 kW, variable speed DC drive. Dry-sump lubrication was provided by an external oil cart equipped with heaters capable of maintaining oil temperatures up to 122°C.

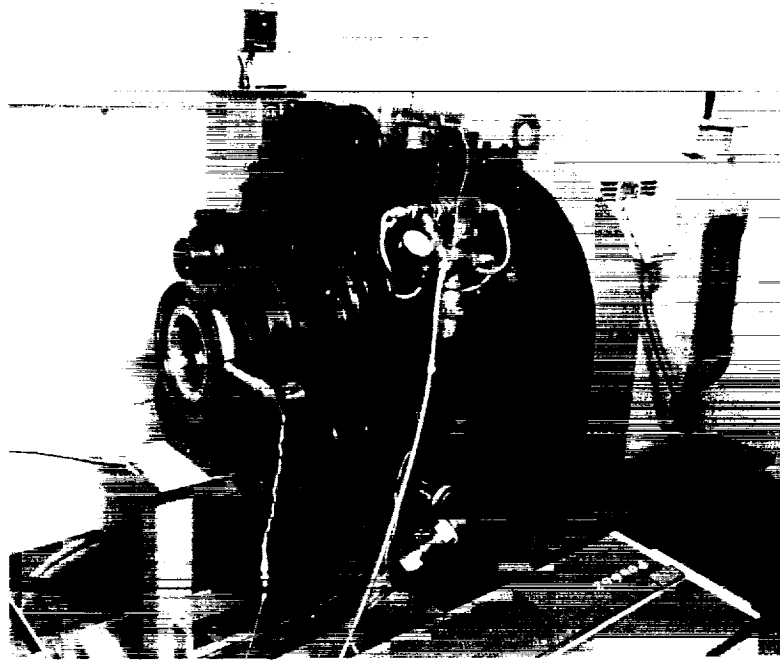


**Figure 3.3.7:** Single cylinder engine motoring test rig.

The initial power generator submodules tested were secured to the base of a modified, conventional production articulated piston. A linear commutator system was mounted to the piston crown as shown in Figure 3.3.8.

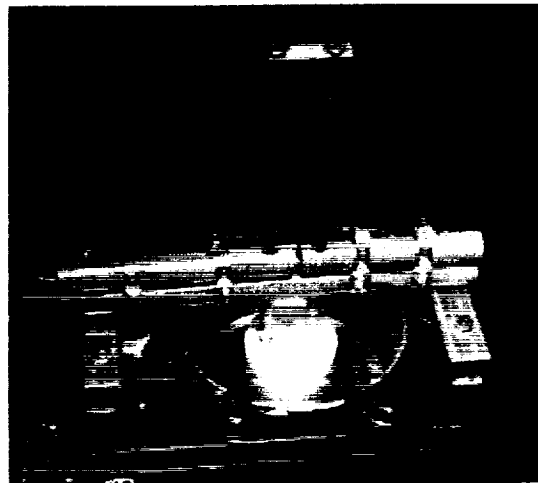


**Figure 3.3.8:** Linear commutator system on motoring engine test rig.

The linear commutator consisted of two insulated brass rods extending up through a cylinder bore sized hole in a cover plate fitted in place of the cylinder head. Carbon brushes were brought in contact with the brass rods and were connected to an external electrical load. Output from the loaded reciprocating power generator submodule could therefore be easily measured. The commutator was also used to supply activation current to the piston mounted telemetry submodule for operation of the submodule independent of the power generator submodule.

Evaluation of both the power generator submodule and the telemetry submodule mounted on a spherical joint piston was also performed on the engine motoring test rig. The telemetry system was successfully operated with temperature signals being transmitted at engine speeds from as low as 400 rpm to the maximum test rig speed of 2100 rpm. A total of 100 hours of extended high speed motored engine rig testing with oil sump temperatures as high as 122°C were completed. The temperature telemetry system has been successfully demonstrated on engine firing tests in a single cylinder engine (spherical joint piston) and in multi-cylinder engines (both conventional, production monoblock and articulated pistons).

#### **3.3.4 Conclusions - Spherical Joint Piston Telemetry**

- A new piston telemetry system which utilizes the relative motion between the piston and the cylinder liner wall has been developed to meet the special measurement requirements of a rotating spherical joint piston. The telemetry system consists of a piston mounted signal multiplexer and transmitter. A patented, piston mounted power generator operates in conjunction with a modified cylinder liner to power the system. The system is robust having high inertia load capability and high environmental temperature operating capability.
- A single cylinder engine motoring test rig was used to evaluate the telemetry system. Piston temperature signals were transmitted over a range of motoring speeds from 400 rpm to 2100 rpm. Over 100 hours of extended high speed testing with oil sump temperatures up to 122°C were completed.
- The use of this telemetry system is not restricted to measuring piston temperatures and dynamic strains. Efforts are underway to use the telemetry system to make inter ring gas pressure measurements as well as piston ring motion measurements. In addition, the telemetry submodule has been repotted for use on a connecting rod to measure bearing temperatures as well as connecting rod dynamic strains.
- The use of the telemetry system has grown beyond advanced piston, research applications (spherical joint piston development) to current product development applications. The system has been successfully used to study the effect of engine fueling parameters on piston crown thermal loading in a production multi-cylinder engine. The flexibility of this telemetry system allows for piston measurements where the physical restrictions of certain engine cylinder blocks previously made such measurements impossible. The potential uses for this flexible and capable telemetry system are just beginning to be explored.

### 3.4 Alternative Piston Designs

The spherical joint piston was a major departure from current heavy duty diesel engine piston experience. As a contingency plan, a conventional articulated piston was investigated. A piston made from nickel aluminide material and a piston made from titanium aluminide material were pursued. The substitution of these materials in the articulated piston design yielded pistons with higher strength and thermal fatigue resistance than steel pistons at LE 55 operating conditions.

#### 3.4.1 Nickel Aluminide Crown for Articulated Piston

The nickel aluminide family of alloys possesses many properties favorable to piston design. In particular, nickel aluminide ( $\text{Ni}_3\text{Al}$ ) has a high yield strength which increases with increasing temperature. Figure 3.4.1 is a plot of specific strength versus temperature which illustrates this characteristic. The IC-221M nickel aluminide alloy was chosen as a candidate material for the piston crown application. The percent composition by weight for the various elements in the alloy is given in Table 3.4.1.

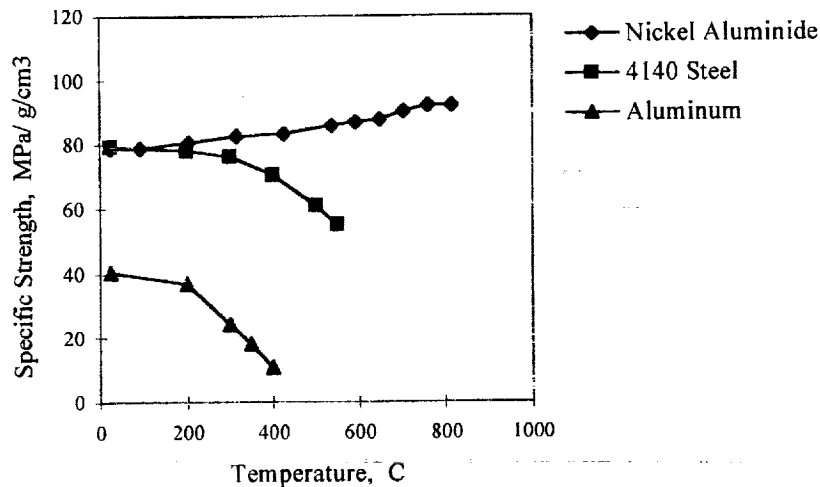


**Figure 3.4.1:** Comparison of specific strength versus temperature for nickel aluminide, 4140 steel and aluminum.

**Table 3.4.1:** Percentage composition by weight of nickel aluminide alloy IC-221M

Element	Al	Cr	Zr	B	Ni
% Composition	8.5	7.8	1.7	0.02	balance

Six  $\text{Ni}_3\text{Al}$  piston crowns were cast by Precision Castparts Corporation using six different techniques to optimize the investment casting parameters. After qualification by Cummins metallurgy staff, six additional piston crowns were cast using the optimized parameters.

The piston crown castings were finish machined by Kolbenschmidt AG in Germany. Kolbenschmidt's initial machining efforts using tungsten carbide cutting tools resulted in tool breakage. The fracture of with the tungsten carbide cutting tools was eliminated by resorting to tool steel cutting tools. However, the wear rate on the tool steel cutting tools was very high.

Due to the large grain structure and ductility of the nickel aluminide material, Kolbenschmidt AG was unable to hold the surface finish requirements for the piston ring grooves by machining. Ring groove circumferential waviness and chatter were difficult to control. After a concerted effort to grind the groove surfaces to finish specifications, the piston crown most closely meeting those specifications was placed on a 50 hour test in the single cylinder research engine.

The piston was first run-in for 20 hours at light load (68 N-m, 1500 rpm and 25:1 A/F, 8.3 MPa PCP). Initial blow-by was higher than normal (1 kPa versus < 0.25 kPa). The high blow-by was not unexpected due to the circumferential waviness and chatter in the ring groove surfaces. After the 20 hour run-in period, the load on the engine was increase to 136 N-m (12.4 MPa). The blow-by remained relatively constant at 1 kPa. The load was then increased to 203 N-m (15.2 MPa). Blow-by increased to 2 kPa. The increase in blow-by was believed due to the inability of the rings to properly seat against the surface of the ring grooves. Therefore, the load was reduced to 136 N-m for the remainder of the 50 hour test to maintain blow-by at reasonable levels.

Post-test engine tear down revealed that the nickel aluminide piston had scuffed. The scuff included the piston crown (primarily the second land) and the piston skirt. All three piston rings had stuck. At this point the investigation with regard to the nickel aluminide material was suspended in favor of investigating titanium aluminide as a piston crown material.

### 3.4.2 Titanium Aluminide Crown for Articulated Piston

Titanium aluminide (TiAl) was chosen for evaluation as a piston crown material based on its low density (about half that of steel) and superior specific strength when compared to nickel aluminide, steel and aluminum. The room temperature specific strength of titanium aluminide is much greater than nickel aluminide as shown in Figure 3.4.2.

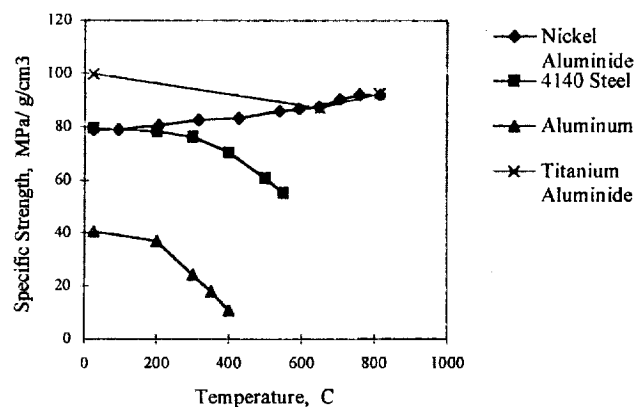


**Figure 3.4.2:** Comparison of specific strength versus temperature for titanium aluminide, nickel aluminide, 4140 steel and aluminum.

As temperature increases, the specific strength of titanium aluminide decreases to a level equivalent to the specific strength of nickel aluminide. At ~650°C, the specific strength of titanium aluminide recovers to match the specific strength of nickel aluminide and increases with increasing temperature. The percent composition by weight for the various elements in the titanium aluminide used in this investigation is presented in Table 3.4.2.

**Table 3.4.2:** Percentage composition by weight of titanium aluminide alloy

Element	Al	Cr	Fe	Nb	Ti	Balance
% Composition	32.5	2.5	0.03	4.6	60.3	0.07

Casting of the titanium aluminide piston crowns was also done by Precision Castparts Corporation. Casting tooling for the titanium aluminide piston crowns was developed by modifying the tooling used for the nickel aluminide piston crowns. Several casting runs were made to minimize porosity in the titanium aluminide casting. Once the casting parameters for the titanium aluminide material were optimized ten castings were made suitable for finish machining.

Karl Schmidt UNISIA, Inc. (the U.S. subsidiary to Kolbenschmidt AG) was responsible for finish machining the titanium aluminide piston crowns. The titanium aluminide material proved to be very difficult to machine due to its extreme hardness. The approach taken to finish machine the titanium aluminide piston crowns was to use a electro-discharge machining (EDM) process. EDM was used to form the combustion bowl, initial cut the piston ring grooves and to cut the piston pin bores. The piston ring grooves and second land were finish ground. Finished titanium aluminide piston crowns were not available for engine test. Issues with regard to narrow piston ring groove widths could not be resolved by the end of the program. Therefore, no titanium aluminide piston crowns were tested in the single cylinder research engine.

### Conclusions - Alternative Piston Designs

- Nickel aluminide piston crowns were cast and finish machined. The nickel aluminide alloy IC-221M used in this investigation had a very large grain structure and was very ductile when cut. The alloy caused high tool wear rates and was very difficult to machine to specified surface finish requirements.
- One nickel aluminide piston crown was tested for 50 hours in the single cylinder research engine. Post-test tear down inspection revealed that the piston had scuffed. The scuff was most likely due to the suboptimal piston ring groove surface finish characteristics (waviness and chatter). All three rings on the scuffed piston had stuck.
- Titanium aluminide piston crowns were cast and finish machined. The titanium aluminide alloy used in this investigation was very hard and required an EDM process to cut the piston bowl, initial cut the piston ring grooves and to cut the piston pin bores.
- Due to issues with regard to narrow piston ring groove widths, no titanium aluminide piston crowns were tested in the single cylinder research engine.

### **3.5 Steel Compression Rings**

Piston rings are critical to the advanced power cylinder. The primary functions of piston rings are to seal combustion from the crankcase and to seal lubricating oil from the combustion chamber. Control of oil consumption is critical to meeting current and future particulate emission regulations. Higher cylinder pressure requires improved top ring performance in both sealing and structural durability. High BMEP levels also raise temperatures and thermal loads on the rings. At these high loads and temperatures the current ductile iron top ring with an electroplated chromium coating is not sufficient. New materials and designs are required for the top ring to maintain its durability.

Much of the piston ring development was concentrated on the top piston ring due to the higher thermal and pressure loads the ring must tolerate. The ring design criteria included improving the fatigue strength compared to the current cast iron top ring in the Cummins L10 engine, without sacrificing conformability to the cylinder bore. The piston ring that was developed is a reduced cross section ring made of 440B stainless steel with gas nitrided flanks and a ceramic face coating. The reduction in ring cross section is necessary to maintain conformability due to the higher elastic modulus of the steel ring material.

The process of designing the ring began with the selection of a base material that would withstand the severe LE-55 operating condition. The properties of the ring were evaluated through its high temperature fatigue and tribological properties. Compliance of the ring to cylinder wall irregularities has been shown to improve the ring performance. Choosing the correct ring geometry plays an important role in the compliance of a ring. The face coating was also examined. With the proper face coating, it was conceivable that both ring and liner wear could be reduced. Then finally, the experimental work confirms the viability of the advanced ring concepts.

#### **3.5.1 Material Selection**

SAE 9254 steel and stainless steel AISI 440B were chosen as alternatives to ductile iron for the top ring base material. To evaluate the different ring materials, a series of fatigue and wear tests were conducted.

Fatigue testing of plasma coated and chrome plated rings is one of the standard tests performed in the evaluation of new coatings and base materials. The three major ring features tested were the base material, keystone angle, and coating process.

The fatigue test machine used holds four rings and is enclosed in an oven. Rings are prepared for fatigue testing by drilling two small holes in the rings at 90° and 270°. Rings are placed between the static and dynamic side of the machine. They are then compressed to their designed diameter, introducing closure stress. Rings are deflected further by an eccentric cam, introducing alternating or dynamic stress. Finally, the sample temperature is raised by the furnace, introducing thermal stress. Rings are cycled at a preset frequency. As each ring fractures its failure cycle is registered automatically by a computer. The test is only stopped when all rings are fractured or 10<sup>6</sup> cycles are obtained. Frequency, temperature, and breakage cycles are stored by the computer.

The results of the fatigue test are shown in Table 3.5.1. From the table it can be seen that the endurance limit of AISI 440B increases as the ring temperature increases. This increase in the fatigue strength is due to the strengthening effect of strain aging of steels at elevated temperatures. Cast irons have similar behavior, but not as pronounced. The highly alloyed steels which contain more than 10% Chromium, have increased fatigue strength at high temperatures.

**Table 3.5.1:** Endurance limit data (mm) from the fatigue tests on different materials and coatings

Part Number	Material	Coating	Keystone Angle (°)	Temperature (°C)			
				38	260	316	371
XC05501	440B	Plasma	10	-	10.16	-	12.70
89902	Iron	Chrome	10	5.21	6.35	6.35	7.62
C5524	Iron	Plasma	7.75	12.70	10.16	7.62	7.62
C5456	Iron	Chrome	7.75	7.62	7.62	6.35	7.62

A comparison of rings 89902 and C5456, in Table 3.5.1, shows that keystone angle differences do not have a significant effect on fatigue strength at the higher temperatures. The coating process has little effect on the fatigue life of the ring at the higher temperature as seen by the comparison of C5524 and C5456. The most significant comparison is made between C5524 and XC05501. At 260°C both rings had accumulated  $10^6$  cycles with cyclic deflection of 10.16 mm. At 371°C the 440B sample was cycled 12.70 mm in comparison to the 7.62 mm deflection for ductile iron. This indicates that the rings made of AISI 440B stainless steel have higher fatigue strength than ductile iron rings at elevated temperatures. The steel rings tested were not gas nitrided. A nitriding process is expected to either increase or have no effect on the fatigue strength of steel.

Another evaluation for the ring base material is the wear rate between the side of the ring and the ring groove. Side wear testing is done by simulating ring motion within the ring groove with a Cameron Plint test rig. Using this rig it is possible to measure wear rate and establish surface interaction mechanisms of ring and groove materials. The results are used in ranking the side wear resistance of the candidate ring materials. Rings fabricated from ductile iron (K-28), SAE 9254 steel, and nitrided 440B stainless steel were tested. For each ring, three groove materials were tested. These materials were full Niresist, SAE 4140 steel, and aluminum impregnated chip Niresist (partial Niresist). The effect of surface finish was examined for the nitrided 440B ring material. Ground samples were prepared to a surface finish of  $R_a = 0.6 \mu\text{m}$  with a SiC 80 grit wheel prior to the nitriding process. Polishing of the nitrided surface finish was improved to  $R_a = 0.1 \mu\text{m}$ . During hand polishing, the brittle 0.010 mm thick white layer formed in the nitriding process was removed.

Combining the wear test results for each material, Table 3.5.2 and Figure 3.5.1 show the average wear coefficient for each ring and groove material. As expected, both ring and groove material wear rates increased in sooted oil. Table 3.5.2 shows that the nitrided 440B ring material has a lower wear rate than K28 ductile iron and SAE 9254 steel in sooted oil. The partial Niresist



groove material showed the highest rate of wear in sooted oil.

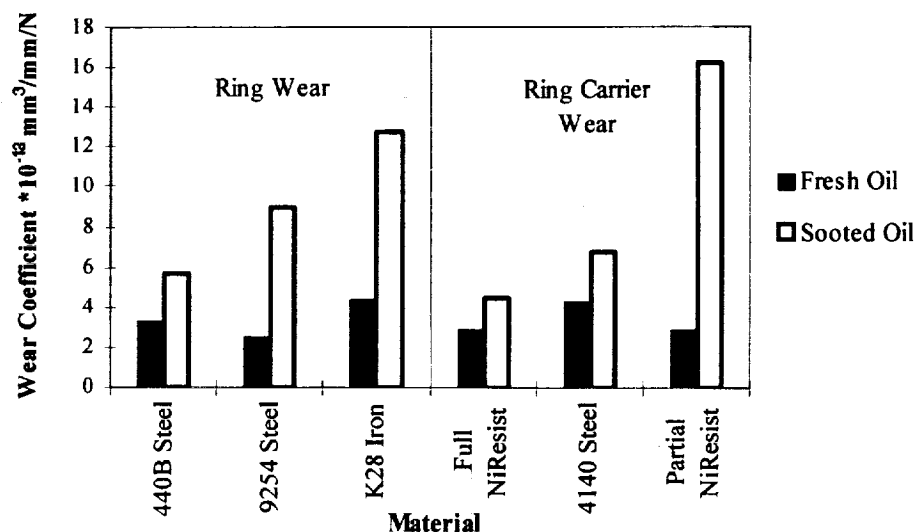


**Figure 3.5.1:** Ring and ring carrier wear coefficients in fresh and sooted oils for various ring and ring carrier materials.

It is worth noting in Table 3.5.2 that the SAE 9254 ring tested against Niresist has slightly lower ring wear than the polished nitrided ring. However, in all cases, the total system wear (ring and groove) is lower for nitrided 440B than SAE 9254. The steel rings showed the lowest ring and groove wear in fresh oil when tested against the partial Niresist groove material.

The wear rate of the materials alone does not reveal the total history of surface interactions. Surfaces must be examined and characterized by Scanning Electron Microscopy and X-ray Elemental Mapping. The most significant wear mechanisms were adhesive, abrasive, delamination, corrosion, and surface fatigue.

Wear of the Niresist groove material surface revealed surface corrosion and signs of abrasive wear when the mating surface is the SAE 9254 ring material. In comparison, nitrided 440B rings tested on the Niresist showed no sign of abrasive wear or any other wear mechanism. The Niresist did show signs of delamination and contact fatigue. The contact fatigue wear is contributed to higher Hertzian contact pressure. This could be due to the higher modulus of elasticity in the nitrided layer compared to the base metal.

**Table 3.5.2:** Wear rate coefficient in  $\text{mm}^3/\text{N}\cdot\text{mm} \times 10^{10}$  for various ring and ring groove materials in fresh and sooted oils

Ring Material	Groove Material	Fresh Oil		Sooted Oil	
		Ring Wear	Groove Wear	Ring Wear	Groove Wear
K28	Full Niresist	0.66	2.3	4.6	4.2
K28	Partial Niresist	7.0	7.0	30.0	26.0
K28	SAE 4140	2.5	6.5	8.2	3.6
SAE 9254	Full Niresist	0.3	6.7	1.8	8.6
SAE 9254	Partial Niresist	0.2	0.3	7.0	20.0
SAE 9254	SAE 4140	0.2	7.0	2.5	14.0
Nitrided 440B	Full Niresist	0.7	5.0	1.3	10.0
Polished Nitrided 440B	Full Niresist	1.3	6.0	3.5	4.0
Polished Nitrided 440B	Partial Niresist	0.75	2.0	4.0	10.0
Polished Nitrided 440B	SAE 4140	4.4	5.0	2.5	10.0

SAE 4140 groove material suffered from moderate abrasive wear and plastic deformation when it was tested against SAE 9254. The SAE 9254 surface showed moderated signs of abrasion. In contrast, the nitrided 440B ring material shows low abrasive wear against SAE 4140. In this case, the groove material exhibited most of the wear symptoms such as mild plastic deformation and abrasion.

The problems are more severe for the partial Niresist groove material than SAE 4140. This groove material, tested against SAE 9254, suffered delamination from the contact stresses and mild abrasion. The mating SAE 9254 surface showed minor signs of corrosion. The test of partial Niresist against nitrided 440B did not fare any better. Both surfaces suffered from mild to severe abrasion with fracture occurring on the groove material. Back scattered images of worn partial Niresist showed cracking in the Fe/Ni phase. In the aluminum phase, delamination of the material occurs.

### 3.5.2 Ring Geometry

Steel was considered as a base material in the previous sections. However, steel has a higher modulus of elasticity than the standard ductile iron rings. As a result, a steel ring will be less conformable to variations in the cylinder wall than an iron ring with the same cross section. If the ring does not conform well to the cylinder wall oil consumption will increase. The steel ring can

be made more conformable by reducing the radial width. As a result, the steel ring was designed with a reduced cross section as shown in Figure 3.5.2. The piston ring that was developed is a reduced cross section ring made of stainless steel with gas nitrided flanks and a ceramic face coating. Selection of the ceramic face coating is discussed in the next section.

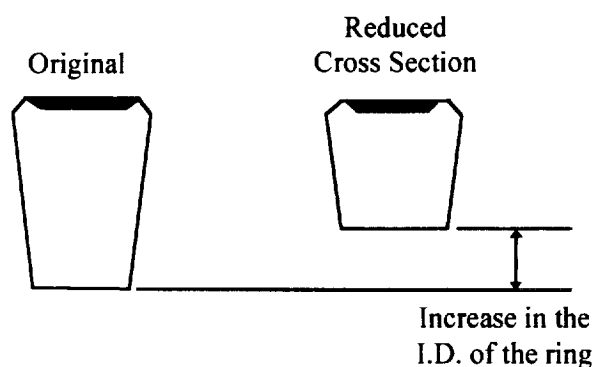


**Figure 3.5.2:** Cross section comparison for a standard and reduced cross section top compression ring.

### 3.5.3 Face Coating Selection

Three thermal sprayed coatings were developed. A metallic coating of Iron-Moly, a ceramic coating of Chrome Oxide, and a Cermet coating of NiCr Chrome Carbide were considered. The metallic and ceramic coatings were plasma sprayed while a high velocity oxygen fuel (HVOF) technique was used to spray the Cermet powder. The ceramic Chrome Oxide top coat required a bond coat, and four different bond coats were examined.

Coating properties measured were hardness, chemistry, oxides, percentage of porosity, unmelted particles, and relative adhesion. Results from these tests are shown in Table 3.5.3.

**Table 3.5.3:** Results from the physical property tests conducted on various ring coatings and bond coats

Face Coating	Bond Coating	Twist Test (°)	Hardness (DPH)	Porosity (%)
Iron/Moly	-	48	680-720	< 5
Chrome/Oxide	None	38	1225-1400+	< 5
Chrome/Oxide	NiChrome-Sph	72	-	-
Chrome/Oxide	NiChrome-Frag	68	-	-
Chrome/Oxide	Ni <sub>3</sub> Al	70	-	-
Chrome/Oxide	NiCrAlY	70	-	-
Chrome Carbide	-	45	745	< 5

A twist test was employed to determine the relative adhesion strength of the top coatings and the bond coatings. In this test, one ring tip was held stationary while the opposite tip was twisted in a perpendicular plane to the ring. From Table 3.5.3, it can be seen that without the bond coat the Chrome Oxide coating failed at a twist angle of  $38^{\circ}$ . Bond coats increased the twist angle to as much as  $72^{\circ}$ .

The Iron-Molybdenum coating had an average bulk hardness of 650-DPH-300 with some hardness phases as high as 710-DPH-300. Molybdenum dispersion in the coating was determined to be uniform and multiple iron-molybdenum carbon phases exist in the coating. Coating oxidation is more apparent at the rails than in other places in the groove. It was observed that less oxide banding occurs at the center of the groove than in other sections of the ring.

The Chrome Oxide cross sectional average hardness ranged from 1225 to greater than 1400-DPH-300. These differences in hardness were due to different enthalpies used in the plasma spraying process. Higher enthalpy sprays produced a harder top coat. Coating porosities were between 1% and 5% and no visible unmelted Chromium Oxide was observed in the cross section. All of the ceramic powders were sprayed from one powder lot.

Spherical and irregular shaped Nichrome powders were used to produce bond coatings. The finer spherical powder oxidized more readily than the irregular shaped powder during the plasma spray process. This effect was insignificant since there were excessive unmelted particles produced by the irregular powder.  $\text{NiCrAlY}$  and  $\text{Ni}_3\text{Al}$  bond coatings showed the highest resistance to oxidation during the plasma spray process; however, oxidation caused no significant change in the maximum twist angle.

The average bulk hardness of the Chromium Carbide coating was 745-DPH-300 with the lowest hardness at the rail (700-DPH-300). This coating had the highest hardness at the center of the groove (780-DPH-300).

The Cameron Plint wear tester was also used to evaluate the top coats. In this case coated rings were tested against segments of a honed liner. The wear results are summarized in Figure 3.5.3. The chromium plated face coating wore substantially more than all the other coatings. In addition, cylinder wear induced by the electroplated chromium was higher than the thermally sprayed coatings. The Iron-Molybdenum metallic coating showed higher face wear than the chromium carbide Cermet and chromium oxide ceramic coatings, but induced the lowest liner wear of all the coatings.

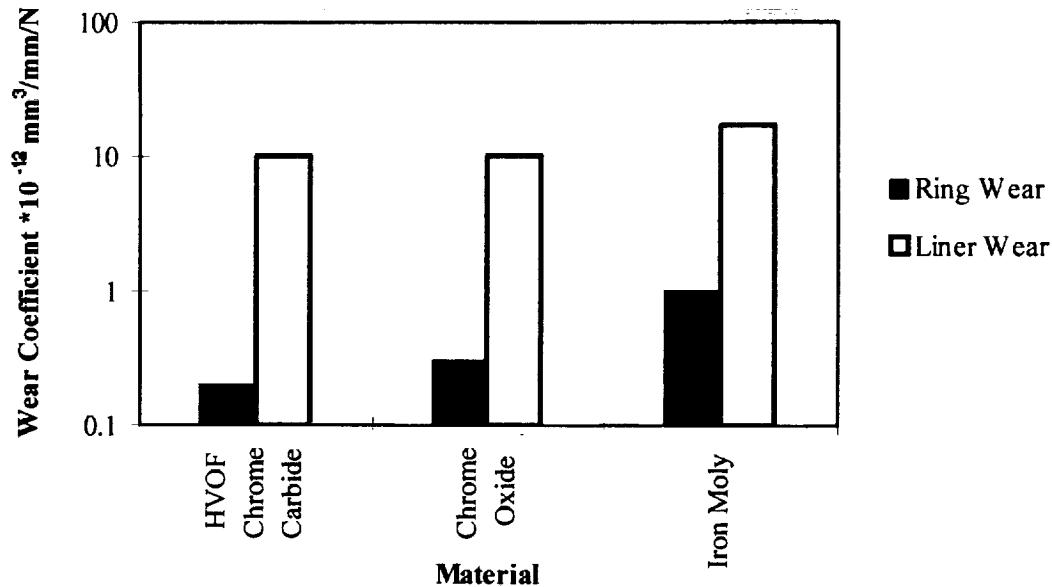


**Figure 3.5.3:** Ring and cylinder liner wear coefficients for various ring materials and ring coatings.

### 3.5.4 Conclusions - Steel Compression Rings

- The 440B stainless steel is the best candidate for the base ring material because of its high fatigue strength and improved tribological properties.
- The polished nitrided 440B is the best choice of ring material for reduced wear.
- The Full Niresist groove material has the best tribological characteristics of the three groove materials tested.
- In fresh oil the partial Niresist had the lowest wear rate of all candidates with steel rings.
- For a steel ring it is necessary to reduce the cross section to maintain the conformability of the ring.
- NiCrAlY is a good bond coat for the Chrome Oxide top coat due to its superior oxidation resistance.

### 3.5.5 Engine Testing of Steel Compression Rings

#### 3.5.5.1 Oil Consumption - Reduced Cross Section Steel Rings

Initial tests were performed on a single cylinder engine. Both reduced and full cross section steel rings were tested. The results showed a large (34%) and statistically significant (90% confidence) reduction in oil consumption with steel rings over the ductile iron rings (Table 3.5.4). There was no statistical difference between the full and reduced cross section rings. The first ring had no twist and the second rings had a positive twist.

These single cylinder engine tests were followed by a full six cylinder engine test. The tests showed a large reduction in oil consumption with the steel ring. The reduction is quantified in Table 3.5.4.

**Table 3.5.4:** Oil consumption results comparing steel and ductile iron rings in a single cylinder engine

	Nominal Oil Consumption	Standard Deviation.
Ductile Iron	1.0	0.26
Reduced Cross section Steel	0.28	0.10
Full Cross section Steel	0.43	-

There has been no mechanism that has been verified to explain the reduction in oil consumption observed with the steel rings. However, the ductile iron baseline comparison was with old style rings that had not been optimized for oil consumption. In the following tests, comparisons were made with the optimum ductile iron ring configuration.

### 3.5.5.2 Description of Full Cross Section Steel Rings Tested

The rings used in the work were made at the Cummins Piston Ring Division. They were made with a 9254 steel substrate with a High Velocity Oxygen Fuel (HVOF) sprayed Chrome Carbide Moly (CCM) top coat. The rings were standard size (not reduced cross section). The top ring had no twist and the second ring was positive twist. The twist of the rings is different from the current ring configuration. The current rings have a positive twist top ring and negative twist second ring, which had been optimized for good oil consumption.

### 3.5.5.3 Summary of Results - Full Cross Section Steel Rings

The following tests were performed.

1. Tests for oil consumption (1800 rpm, overload)
2. 500 hour Torque Peak Endurance (split test, 1200 rpm, overload) - Durability
3. 500 hour Cold Flush Thermal Shutdown (cyclic test) - Durability
4. 650 hour Torque Peak Endurance (1200 rpm, overload) - Durability
5. 130 hour Exhaust Gas Recirculation (split test, 1800 rpm) - Durability

#### 3.5.5.3.1 Oil Consumption

- Oil consumption and blowby were higher with the steel rings than with production rings.
- Steel rings did not show the same ring motion as production rings (shown by the carbon on the top side of the rings) due to the different twist of the steel rings.

#### **3.5.5.3.2 Coating Durability**

- No apparent loss in the functionality of the top rings were observed in the abuse tests. The exception being one scuffed cylinder due to excessive dust.
- The percent of the face worn was less than what would be expected from a standard chrome ring. In split tests the wear of the ring face was significantly less than the chrome.
- Some signs of coating distress or cracking was observed in the Cold Flush Thermal Shutdown and Torque Peak Endurance tests. These areas of distress were only found on two rings and were very small in size.

#### **3.5.5.3.3 Metallurgical Evaluation**

- The HVOF Chrome Carbide Moly top coating displayed, in general, acceptable surface wear characteristics with respect to its integrity (porosity), wear scar size and uniformity and durability (chipping, flaking, and/or cracking).
- Microstructurally, the Chrome Carbide Moly coating displayed acceptable properties with respect to its bulk and individual phase hardness, individual phase size, shape, and distribution and bond adherence to the steel substrate.
- Chemical analysis of the coating, using energy dispersive (EDS) techniques, showed a very wide range of elemental compositions, between ring sets/lots, of the Chrome Carbide Moly coating.
- Metallurgically, the piston ring substrate material (steel) displayed acceptable properties respect to its hardness, microstructure, and chemical composition.

#### **3.5.5.3.4 Conclusions - Engine Testing**

- Steel rings were shown to be durable in the engine tests.
- The advanced HVOF Chrome Carbide Moly face coating was also durable and had less wear than the standard Chrome coating. However, small signs of distress were observed in the most abusive test which requires further investigation.
- Metallurgically, the advanced steel rings and coatings showed acceptable properties.

### 3.6 Thermal Barrier Coatings

Thermal barrier coatings were initially investigated for "adiabatic" diesel engines due to first law thermodynamic predictions of significant fuel economy improvements, reduction in heat rejection, and the potential to increase power density of the diesel engine. Cummins Engine Company, Inc. conducted extensive evaluation of existing thermal barrier coatings using the Cummins V903 diesel engine. These initial exploratory efforts were conducted using duplex coatings consisting of a NiCrAlY bond coating and a yttria stabilized zirconia top layer. Total coating thickness was on the order of 1.5 mm with the bond coating thickness of approximately 0.1 mm. These investigations conducted in the early 1980's revealed that the existing thermal barrier coatings were insufficient to survive short duration tests in a high output diesel engine (1.38 MPa brake mean effective pressures (BMEP)) [Ref 6]. Extensive trial and error development efforts conducted at that time using plasma sprayed zirconia coatings did not result in acceptable or reproducible coating lives.

Efforts sponsored by the DOE/NASA, Tank Automotive Command (TACOM), and Cummins internal funds in the mid 1980's focused on understanding the stresses in the thermal barrier coatings with a goal of significantly improving the life of the coatings in diesel engines. Approximately two orders of magnitude in thermal barrier coating life improvements were necessary for utilization of the coatings in advanced diesel engines.

The DOE/NASA program [Ref 7] had an objective to develop zirconia based thermal barrier coatings with a thermal conductance of  $410 \text{ W/m}^2\text{-K}$  which could survive 100 hours of operation in a research single cylinder engine. The engine chosen for this program was the Cummins V903 direct injection diesel engine with a 140 mm bore and 120 mm stroke. The V-8 engine was rated at 360 kW at 2100 rpm for the turbocharged configuration. The geometric compression ratio chosen for this work was 13.5:1, and the peak cylinder pressure was limited to a maximum of 13.8 MPa.

Extensive diesel engine cycle simulation and finite element analysis of the coatings were conducted to understand the effects of a coating on diesel engine performance and the stress state in the coating and underlying metal substructure. The TACOM programs [Ref 8] expanded the effort initiated with DOE to develop improved thermal barrier coatings which could survive the high cylinder pressures and thermal loads projected for military applications.

An engineered coatings approach was used in the DOE program which consisted of using existing databases augmented where necessary by the collection of additional data, modeling of stresses in the coatings by finite element techniques, and extensive rig and engine tests. Cummins and United Technologies Research Center cooperated on this program to modify thick thermal barrier coatings developed for turbine tip seals for diesel applications.



### 3.6.1 Coating Development for Diesel Engines

#### 3.6.1.1 Modeling

Diesel engine performance modeling was conducted which projected that the maximum benefits of the thermal barrier coatings were obtained by applying the coatings to the piston and cylinder head surfaces. The effects of the coatings on valves and cylinder liners were not projected to result in significant fuel economy improvements. Therefore, research efforts on the DOE/NASA and TACOM programs concentrated on cylinder head and piston coating development. With the insulation levels defined by the coating thermal conductance, diesel engine performance models predicted that the in-cylinder heat rejection would be reduced by 38% and that the fuel economy would be improved by 2% for a turbocharged engine and 3% for a turbocompound version of the engine.

United Technologies Research Center (UTRC) used one-dimensional thermal-structural modeling to select preferred coating systems for spray fabrication trials and rig tests. A one-dimensional thermal-structural model was established to predict both the temperature gradients across layer interfaces of candidate coating systems and overall coating state-of-stress at maximum operating conditions. Predicted temperatures from the thermal analysis were used to predict stresses within the coating systems at a diesel engine maximum operating condition. The modeling indicated that single layer coatings systems were in compression at the top of the coating and in tension at the bond/substrate interface [Ref 9]. Previous single layer coatings have been shown to delaminate in the zirconia coating in this tensile region above the bond coating.

It was determined that multilayer coatings, consisting of multiple layers of ceramic metal mixtures with a top coating of ceramic, reduce in-plane tensile stresses in the ceramic top layers. Figure 3.6.1 shows that the thermal stresses were significantly less than the measured coating strength. The coating was in compression at the top surface which was 2.5 mm from the bond coating-ceramic coating interface. Metal substrates were also analyzed and it was determined that substrate yielding should not be expected. Additionally, thermal modeling indicated that the metal temperatures were insufficient to result in bond coating oxidation in the short time that engine coating delamination was experienced in previous engine tests.

Two dimensional finite element modeling using the cycle average boundary conditions also suggested that a multilayer thermal barrier coating could survive engine conditions. Efforts concentrated on the understanding of a 2.5 mm multilayer coating. This coating consisted of mechanical mixtures of CoCrAlY and zirconia fully stabilized by yttria. The 2.5 mm coating consisted of 0.5 mm layer of 40% zirconia/ 60% CoCrAlY, followed by a 0.5 mm 85% zirconia/ 15% CoCrAlY layer, followed by a 1.5 mm thick 100% zirconia layer. The zirconia layer was approximately 85% dense. Processing conditions were developed to generate residual stresses in the thermal barrier coatings by controlling the substrate temperature during the deposition process.

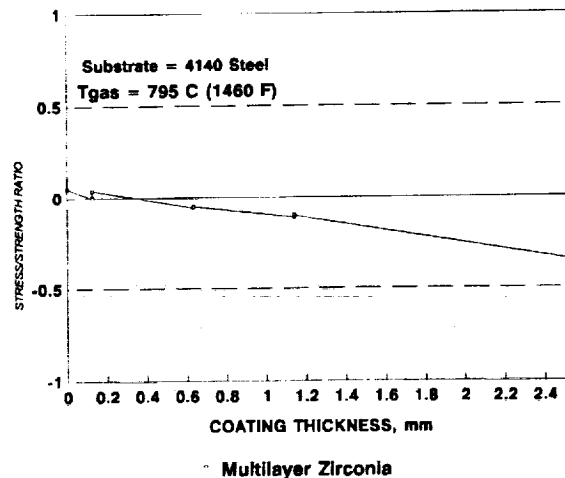


**Figure 3.6.1:** Coating strength to stress ratio through the thickness of a multilayer zirconia based coating.

It is also important to consider thermal transients when designing with ceramic materials. The low thermal diffusivity of the ceramics causes their temperatures to quickly respond to changes in operating environment while the temperatures of the base materials respond much more slowly. This thermal response behavior causes significantly different temperature and thermal stress profiles to be encountered under transient operation than those observed at steady-state.

The first thermal transient considered was a sudden cooling of the combustion face. Calculations were made at steady-state for conditions representative of full load operation at rated speed. At time zero, the in-cylinder conditions were suddenly changed to those representative of no-load conditions. The resulting transient spatial thermal response within the coating is summarized in Figure 3.6.2, where the surface temperature drops rapidly while the interior temperature reacts more slowly. With increasing time, the coating temperature decreases. The predicted thermal stresses in the coating are shown in Figure 3.6.3. The trend shows a relaxation of the compressive stress at the surface with increasing time. This relaxation results in a slight reduction in the tensile stress experienced in the bond coat adjacent to the substrate. Cycle-to-cycle transients and rapid heating of the coating were also modeled.

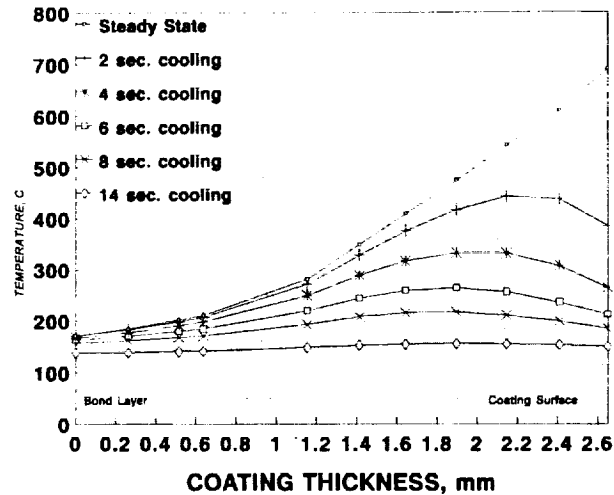


**Figure 3.6.2:** Coating temperature changes during cooling from steady state engine conditions.

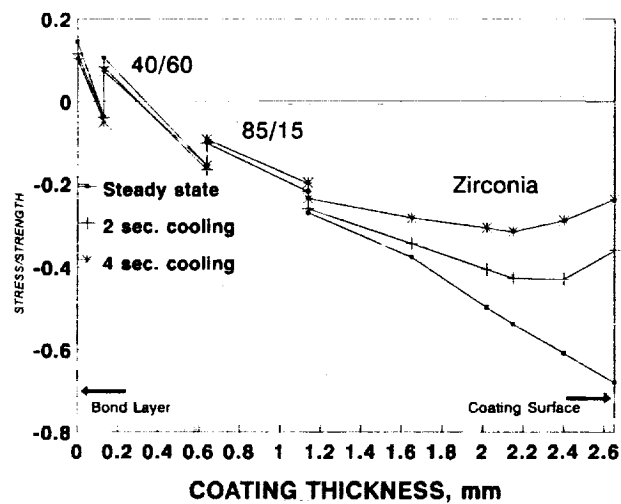


**Figure 3.6.3:** Estimated stresses in a multilayer zirconia based coating during cooling.

It was determined through transient analysis using a simple finite element model that:

1. Temperature and stress profiles under transient conditions were found to be significantly different than those at steady-state.
2. Engine load changes, though resulting in a change in stress profiles, were not predicted to result in coating failure for the cases considered.
3. Firing cycle transients resulted in a predicted surface temperature swing of 225°C, and an increase compressive stresses in the surface layers of the coating. These compressive stresses were predicted to be less than 0.13 mm into the coating.

### 3.6.1.2 Spray Fabrication and Rig Tests

UTRC developed a spray fabrication technique to define material properties most representative of actual coating material. Flat-plate substrates were attached to a rotating holding fixture in areas representing the piston crown diameter. Heat was applied to the panels through the use of small propane torches mounted on a ring that surrounded the base plate. A thermocouple placed on the backside of the substrates provided the processing temperature and allowed for manual adjustment of the propane to maintain the desired prestress temperature through the spray run. The actual robot motion control and spray processing parameters used to coat the piston crowns were used to coat the substrates. Test specimens were fabricated from the substrates in locations indicative of the crown rim and center dome areas of the piston. This approach was needed to verify uniformity of properties across the crown diameter.

Based on preliminary one-dimensional transient analysis performed by Cummins for the baseline multilayer-layer coating on ductile iron, the rig thermal cycle was targeted to achieve a maximum surface temperature of approximately 675-730°C with a maximum thermal gradient across the coating of approximately 480-537°C at a seven second time point into the cycle.

Test rig conditions were calibrated using the baseline multilayer-layer coating system on a nickel-based superalloy test panel that had been instrumented with embedded thermocouples. A test cycle which closely reflects the predicted diesel engine thermal environment was created with a maximum thermal gradient across the coating of approximately 510°C in seven seconds and a top surface temperature of 675°C. Two additional test cycles representing maximum thermal gradients of 555°C and 705°C respectively were used to further screen thermal strain capability at higher temperatures.

Ductile iron test panels with the baseline multilayer coating system were sprayed at both a medium fabrication temperature and a medium (hybrid) fabrication temperature which incorporated a temperature spike through the bond coat region. These panels were then exposed to the same thermal cyclic test conditions. The panel sprayed at the medium fabrication temperature was initially tested and survived the 510°C thermal gradient. Examination of the panel after five cycles yielded no visible damage. The panel was then subjected to the more severe 555°C and 705°C thermal gradients. No damage occurred after the 555°C cycle. However, after the 705°C cycle, the coating showed moderate cracking at the 40/60 zirconia/CoCrAlY to 85/15 zirconia/CoCrAlY interface.

The panel fabricated at the medium (hybrid) prestress temperature profile was exposed to the 705°C thermal gradient and showed minimum cracking sensitivity. These test results showed the superior strain capacity of the baseline multilayer coating system fabricated with the medium (hybrid) fabrication temperature control.

A prototype plasma spray facility with the capabilities needed to continuously apply multilayered thermal barrier coatings was set up to coat Cummins V903 and L10 piston crowns and single cylinder heads [Ref 9]. The facility was equipped with a six-axis articulating robot to provide gun motion control. Part holding fixturing for all diesel engine components was developed for both simulations and actual hardware. The fixturing for the piston crown incorporated a flame shroud

to provide the capability of heating the piston crown substrate during the spray processing to control fabrication temperature. A powder feed delivery system was used to provide continuous feed rate control during coating deposition. This powder system had the capability to deliver four coating materials sequentially.

Spray process parameters to produce zirconia-based thermal barrier coatings on V903 piston crowns and cylinder heads were developed by translating UTRC's experience in producing turbine seal coatings on curved duct segments. Fundamental issues addressed included prestressing technology and special processing techniques needed to coat each of the specific diesel engine components.

Initial processing efforts focused on developing robotic control software for the plasma gun motion. Applying the coating system across the piston crown diameter proved to be difficult and variable due to the complex bowl geometry. Simulated piston crowns were machined and used to assess the magnitude of the coating thickness variation across the actual piston crown contour. A combination of single-layer and multilayer coating systems were sprayed on the simulated crown. The simulation was then sectioned and polished for metallographic examination of the thickness variation of the individual layers, particularly in the bowl area of the crown. From thickness measurements it could be seen that the deposition was not efficient in areas away from the 90° spray angle. By moving the plasma gun in a circular arc across the piston diameter and including a gun rotation into the wall area resulted in the highest degree of thickness, microstructure and properties uniformity across the crown diameter. Baseline robotic control parameters such as speeds and program increments were determined empirically by conducting a series of coating trials on piston crown simulations.

### **3.6.2 Engine Evaluation**

Single cylinder engine tests confirmed that the multilayer thermal barrier coatings exhibited lives approximately an order of magnitude greater than the duplex thermal barrier coatings. These multilayer zirconia based coatings achieved the DOE/NASA contractual goals of 100 hours at rated engine conditions and approximately 1.38 MPa brake mean effective pressure (BMEP), while meeting the thermal conductance goals of 408 W/m<sup>2</sup>-K. However, engine fuel economy was not improved and coating life capability was marginal. Further evaluation of similar multilayer zirconia coatings in a commercial L10 engine revealed that the coatings could survive steady state operation at 1.38 MPa BMEP. However, cyclic tests resulted in coating deterioration and coating loss. Further confounding was the observation that the zirconia coatings had open crack patterns at the surface of the coating while finite element stress calculations predicted the coating to be in compression for the input boundary conditions. Additional improvements in coating life and capability were required for the technology to be commercially viable.

TACOM sponsored efforts concentrated on the engine evaluation of thermal barrier coatings on an articulated steel piston in a multicylinder L10 engine to further define coating durability at higher brake mean effective pressures, 1.83 MPa. Initial tests at steady state operation confirmed that multilayer zirconia coatings would survive steady state operation for 200+ hours. Cyclic tests were conducted between high idle and full power conditions. Coating loss was experienced

in these cyclic tests. Further coating evaluation focused on the evaluation of the coating in cyclic tests which were conducted for 75 hours followed by removal of the cylinder head. Various zirconia multilayer coating strategies were evaluated including varying residual stresses, using partially stabilized zirconia instead of fully stabilized zirconia, varying plasma gun power, and other coating changes. These modifications had essentially no measurable effect on the coating life.

Contrary to intuition and predicted stresses, a mullite based multilayer coating was tested. Mullite was selected due to this materials lower thermal expansion and higher thermal conductivity compared to zirconia coatings. The mullite based coatings had significantly improved performance as compared to the zirconia based coatings as shown in Figure 3.6.4. Diesel engine evaluation of zirconia and mullite based coatings demonstrated that the mullite coatings significantly outperform the zirconia coatings in steady state and cyclic engine tests. In multiple engine builds, the mullite multilayer coatings survived transient conditions that extensively damaged zirconia based coatings.

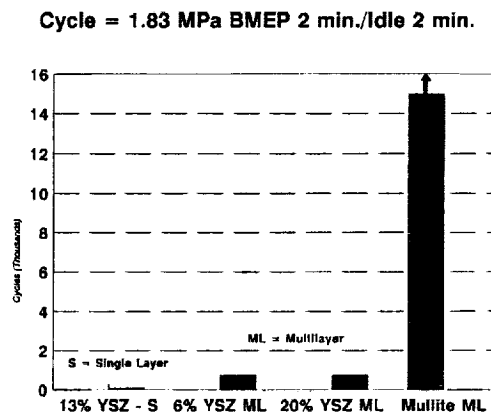


**Figure 3.6.4:** Lifetime Improvements in thermal barrier coatings in cyclic diesel engine tests.

### 3.6.3 Nondestructive Evaluation

Although state-of-the-art plasma control systems and robotics have been used to deposit thermal barrier coatings, minor errors in plasma gun manipulation, concentric powder feed and plasma alignment and slight changes in coating deposition rates can alter the coating structure and coating performance. Since the thermal barrier coatings are applied individually to the pistons and limited production studies have been conducted, a reliable inspection process is required for the coatings. At the period of time that the coatings were being developed, Cummins initiated efforts with Wayne State University to apply infrared imaging techniques to investigate and understand the coating appearance before and after engine test. Thermal wave imaging was found to offer significant advantages, including speed of data collection and user friendly interpretation of the images [Ref 10]. Destructive evaluation of the coatings confirmed that delaminations or coating

inconsistencies were detected by the thermal wave imaging technique. Infrared imaging is currently used to inspect the thermal barrier coating prior to and after engine evaluation at Cummins. This nondestructive evaluation technique has led into new areas of research and has confirmed several hypotheses. One of which was that the center portion of the piston is difficult to coat and in selected cases was delaminated in the region prior to engine evaluation. Another hypothesis was that peak temperatures were critical in defining coating life.

#### **3.6.4 Coating Crack Initiation**

As a gradual increase in coating durability was realized, the coating life was still inadequate for many advanced diesel applications. A critical factor missing in many investigations was the understanding of the crack initiation and propagation mechanisms in thermal barrier coatings. Purdue University and Cummins began an investigation to determine the mechanisms responsible for surface crack initiation at conditions that simulate the engine thermal loading conditions in a diesel engine [Ref 11] [Ref 12] [Ref 13].

A simple experiment was designed to simulate the boundary conditions imposed during diesel engine combustion. In direct injection diesel engines, combustion of the fuel results in localized high heat flux regions on the piston and cylinder head. These areas of high heat flux concentration correlate with coating damage observed during diesel engine evaluation of thermal barrier coatings. Previous analytical modeling had predicted that the thermal barrier coating was in compression through all engine operating conditions. This resulted in a paradox, since crack opening due to tensile stresses was observed in thermal barrier coatings. To understand the observations from diesel engine tests, an experiment was designed as a two dimensional representation of the diesel engine combustion. An advantage of this specimen design was that during crack formation, the depth of the surface crack and the presence of interface cracks could be determined by low power optical inspection. The specimens consisted of multilayer beam specimens with a concentrated heat flux in the center of the sample. The experiments and analysis were conducted on three specimen configurations.

The concentrated heat flux region was created by high powered infrared lamps. Temperature measurements were recorded at multiple points on the coating surface and the substrate. Tests were conducted by heating the specimen by turning the lamps on at full power and then maintaining a steady state temperature for two hours. A two hour test time was used in order to allow the surface stresses to equilibrate. At the end of the test, the specimen was cooled to room temperature under natural convective cooling.

In order to develop an understanding of the stress distribution in the specimens, analytical models of the specimens were developed using the finite element method. The magnitude of the in-plane stress in the top layer governed the formation of the surface crack. The temperatures and the stresses were calculated in four discrete steps.

1. The residual stresses were calculated by assuming a uniform stress free temperature of 618°C which approximates the manufacturing temperature used in the coating deposition for the test specimens.

2. The thermal stresses were calculated at steady state temperatures based on measurements of the heat flux generated by the lamps.
3. Stress relaxation was allowed to occur for a two hour period.
4. The specimen was uniformly cooled back to room temperature.

The stress relaxation of the zirconia was estimated using a strain gauge mounted to the bottom of the substrate to measure the strain change as a function of time during steady state heating.

Experimental measurements showed that the temperature of the coating surfaces reached approximately 870°C for a thick zirconia specimen and 760°C for a comparable mullite coating thickness. The stress relaxation was modeled [Ref 14] as  $\epsilon = A\sigma^n$  where  $A = 4.03 \cdot 10^{-19}$  and  $n = 1.59$  for zirconia at 870°C and  $A = 2.98 \cdot 10^{-17}$  and  $n = 1.1$  for mullite at 760°C. Surface crack formation was observed in the thicker zirconia specimen, but was not observed in the thick mullite. Crack formation started at the zirconia surface, thus indicating that a tensile stress at the surface governs crack initiation behavior. In order to understand the thermal crack initiation behavior in the zirconia, the stress distributions were calculated analytically. The stress in the thick zirconia coating is in compression of 200 MPa near the surface. During the heating of the zirconia surface, the zirconia coating surface reaches a much higher temperature than the underlying metal surface. The result of this thermal gradient is that the zirconia coating expands more than the underlying metal which results in a large calculated compressive stress in the ceramic coating. However, at the higher temperatures, stress relaxation locally reduces the magnitude of the compressive stress. This stress relaxation results in a local tensile residual stress in the coating at room temperature. This operational induced residual tensile stress is sufficient to crack the zirconia coatings.

The model suggests that the stress relaxation properties should be reduced to extend the service life of the coating. Since stress relaxation is highly temperature and material dependent, analysis was conducted for a mullite coating. The model predicts the temperatures were not sufficient to induce cracking for the lower temperature and different mechanical properties of mullite.

### 3.6.5 Emissions and Engine Fuel Economy

An extensive data set of engine performance measurements have been made comparing a single cylinder diesel engine using steel articulated pistons with an insulated coating of yttria stabilized zirconia or mullite [Ref 15]. Measurements made on back-to-back single cylinder tests included cylinder pressure, brake torque, NO<sub>x</sub>, unburned HC, and particulate as a function of timing at four speed-load operating conditions. The effect on heat transfer of insulated pistons was determined based on indicated fuel consumption versus centroid of heat release curves. Engine performance using the zirconia coated piston was measured to have 1 - 3% higher indicated and brake specific fuel consumption in comparison to the baseline, as shown in Figure 3.6.5. The difference between the two pistons was greatest at the most advanced injection timings.



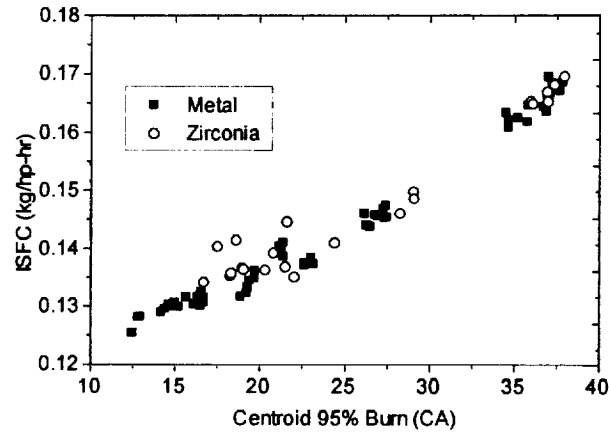


**Figure 3.6.5:** Comparison of metal and zirconia coated pistons at 1800 rpm and rated load. Indicated specific fuel consumption (ISFC) versus centroid of area where 95% of heat release has occurred.

The mullite coated pistons displayed a fuel consumption increase which was as much as 8% at advanced timings, as shown in Figure 3.6.6. Heat release was slightly extended for the zirconia pistons and extended even longer on the mullite pistons.

Error analysis of the measurement methods showed an uncertainty of  $\pm 3\%$  in the indicated specific fuel consumption and  $\pm 2$  crank degrees in the centroid could be expected for this set of measurements. The data was therefore inconclusive on the effect of insulation on heat transfer for the zirconia coated pistons, but the mullite coated pistons displayed a measurable reduction in indicated mean effective pressure which was judged to be caused by increased heat transfer.

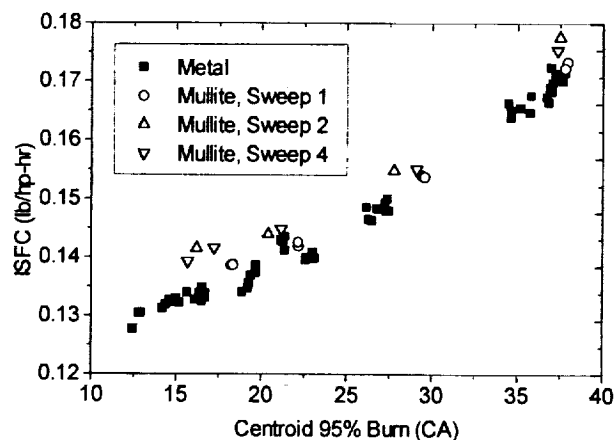


**Figure 3.6.6:** Comparison of metal and mullite coated pistons at 1800 rpm and rated load. Sweeps refer to specific timing sweeps when data was collected.

Emissions for the insulated pistons showed similar  $\text{NO}_x$  particulate trade-off curves at retarded timings, but the particulate increased at advanced timings on the mullite coated pistons. The zirconia coated pistons displaced a slight increase in particulate and  $\text{NO}_x$  at advanced timings as shown in Figure 3.6.7.

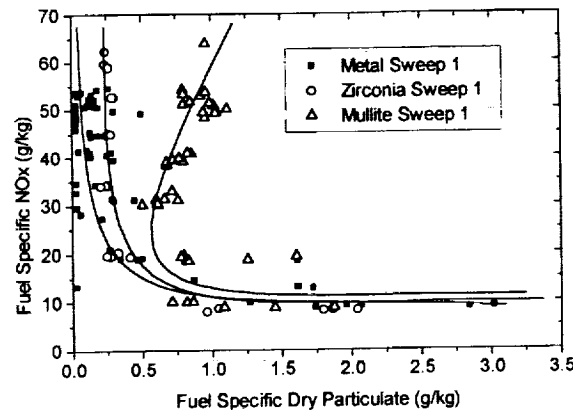


**Figure 3.6.7:** Fuel specific  $\text{NO}_x$  and particulate trade-off curve for metal, zirconia, and mullite coated pistons at 1800 rpm and part load conditions.

### 3.6.6 Conclusions - Thermal Barrier Coatings

- Thermal barrier coating life has been significantly enhanced by understanding the mechanisms that control the coating life. Initial diesel cycle average boundary conditions did not adequately represent the thermal loading applied to the thermal barrier coating.
- Nondestructive evaluation based on the infrared imaging technique was instrumental in understanding the thermal barrier coating structure as deposited and after engine evaluation. Thermal wave imaging confirmed that some coatings were delaminated prior to engine evaluation. This technique also confirmed that local thermal gradients tied to the diesel combustion process were resulting in localized damage. This information led to the development of a low thermal expansion mullite based coating system [Ref 16] which had better thermal fatigue resistance than the zirconia coatings.
- Use of robust thermal barrier coatings permitted the engine fuel economy and emissions data collection which was not complicated by combustion chamber changes due to coating loss.
- Engine fuel economy and emissions performance improvements were not realized for the state-of-the-art diesel engines evaluated. Metal temperatures underneath the coatings have been shown to be reduced which impacts thermal fatigue life of these components.

### **3.7 *Insulated Cylinder Head***

The thermal input to the cylinder head when subjected to the abusive LE-55 operating condition demanded a new design with greater thermal fatigue resistance. The cylinder head must withstand the high thermal loading without compromising reliability or durability. The approach in developing the cylinder head was to use high alloy gray cast iron material for the bulk of the head with high temperature materials in critical areas. The cylinder head concept utilized strategic oil cooling which eliminated water as the cooling medium. The intake and exhaust ports were insulated to minimize heat transfer between the gases flowing through the ports and the cylinder head. A high temperature alloy combustion face insert was designed to increase the resistance to thermal fatigue in the valve bridge region of the cylinder head. Based on a finite element analysis of this overall concept, the cylinder head had essentially infinite thermal fatigue life at the thermally abusive LE-55 operating condition.

A specific design objective for the cylinder head was to retain the use of gray cast iron where possible, while substantially improving the thermal fatigue life compared to the current L10 head design, even with the high thermal loading imposed by the LE-55 engine configuration. The cylinder head design retained the valve, injector, and capscrew locations of the production L10 cylinder head.

A decision was made to cool the head as required in order to reduce the thermal gradients during operation. With such minimal cooling, it was determined that the coolant passages would operate at higher surface temperatures than appropriate for conventional glycol and water mixtures. While glycol alone could be used, the decision was made to use the engine oil as the head cooling fluid. Cooling was focused in the critical valve bridge areas using oil drillings. The substitution of oil drillings for water cooling jackets increased the volume within the head so that aerodynamic improvements could be made to the intake and exhaust ports, even with ceramic insulating port liners. Figure 3.7.1 illustrates the various design features of the cylinder head.

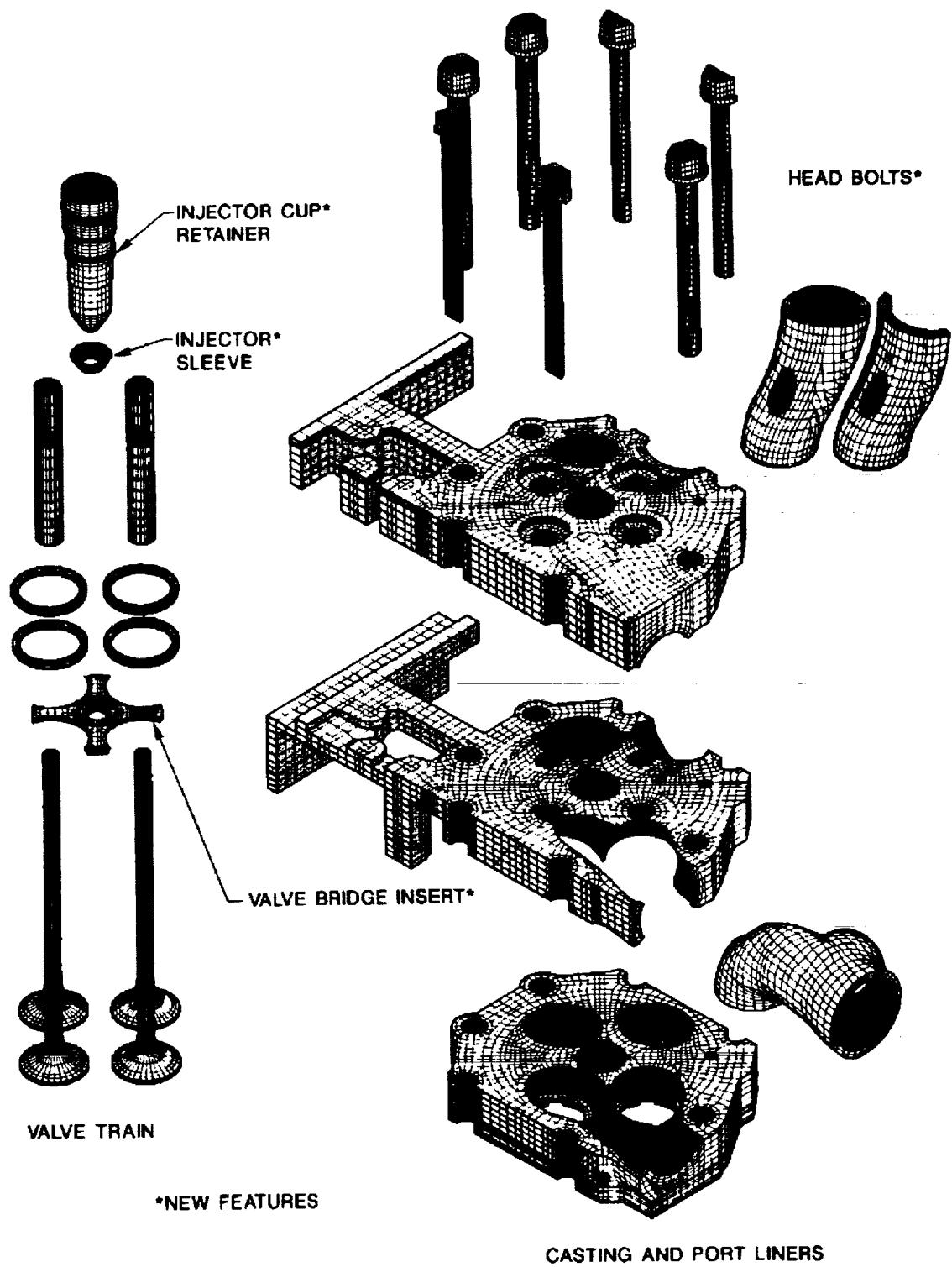


**Figure 3.7.1:** Finite element mesh of the LE-55 cylinder head.

### 3.7.1 Strategic Oil Cooling

In order to effectively utilize engine oil as the cooling fluid, heat transfer improvement devices called turbulators were developed to enhance heat transfer within the oil drillings. Turbulators enhance heat transfer through primarily three mechanisms. First, turbulators increase swirl in the oil which increases the velocity at the wall, and therefore heat transfer. Second, turbulators cause a break up and reformation of the fluid boundary layer which increases heat transfer by reducing the thickness of the boundary layer. Finally, the turbulators add surface area to the cooling passage which also increases heat transfer. One disadvantage of turbulators is that the pumping power to achieve a given flow rate is increased.

Bench tests were performed to determine an optimum turbulator design. Eleven types of turbulators were constructed and tested. The turbulator types consisted of twisted sheet metal, springs, tapped threads, roughened surfaces, and variations of these. The results of these bench tests are illustrated in Figures 3.7.2 and 3.7.3. Figure 3.7.2 shows the performance of the baseline oil passage and various turbulator designs from a heat transfer standpoint. Figure 3.7.3 compares the baseline and turbulator designs based on their restriction to oil flow. The choice for the final turbulator design was a compromise between the turbulator with the greatest improvement in heat transfer coefficient and the smallest pressure drop across the passage.

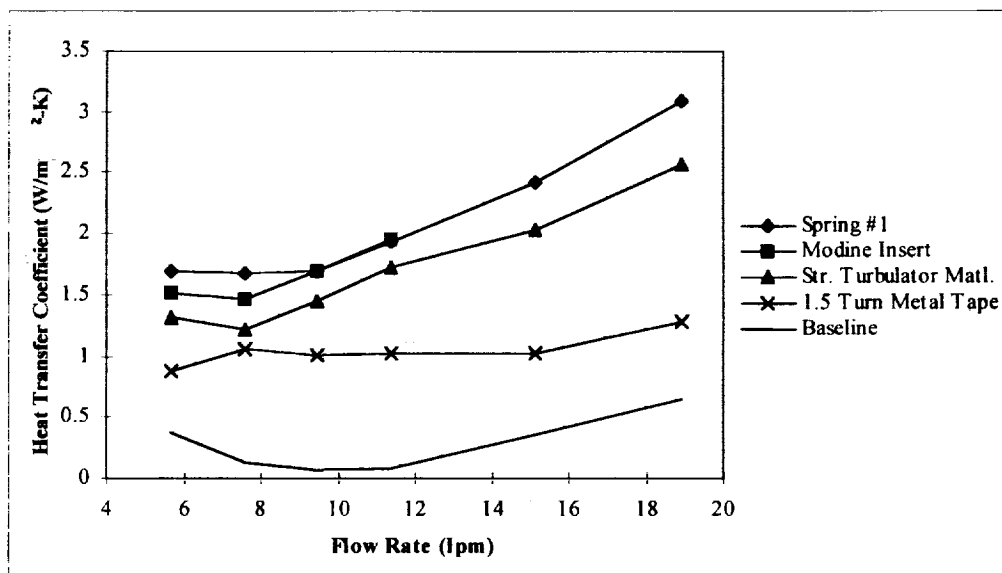


**Figure 3.7.2:** Experimental convection coefficient versus flow rate for various turbulator designs.

Based on this investigation it was determined that changing the surface finish from a smooth to rough surface did not necessarily enhance heat transfer. In fact, a threaded surface resulted in local stagnation of flow and inhibited heat transfer. It was determined that the best turbulator design was a coiled wire (Spring #1) insert from both a pressure drop and a heat transfer

standpoint. With the coiled wire insert, the convection coefficient could be increased by at least a factor of four over the baseline case.

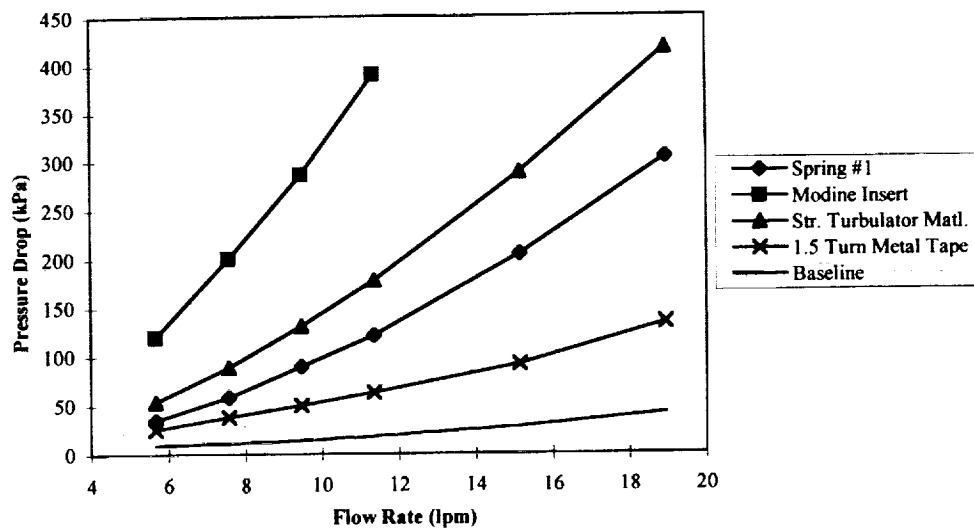


**Figure 3.7.3:** Experimental pressure drop versus flow rate for various turbulator designs.

### 3.7.2 Combustion Face Insert

To reduce heat rejection and improve combustion face fatigue resistance, a dual approach was taken. The central portion of the combustion face contains a nickel aluminide insert which thermally isolates the gray iron in the injector and valve bridge regions. A discussion on the material properties of nickel aluminide can be found in section 3.4 - **Alternative Piston Designs**. The insert was free to thermally expand without causing undue stress in the valve bridges. The remaining combustion face outside of the insert was designed to have a plasma sprayed ceramic thermal barrier coating

### 3.7.3 Finite Element Analysis

A finite element (FE) analysis of the cylinder head was conducted to determine the thermal effects of insulation design strategies and to evaluate the thermal and mechanical stresses generated within the cylinder head. The insulation strategies considered were ceramic port insulation, a superalloy valve bridge insert and a thermal barrier coating sprayed onto the combustion face. To accurately model actual engine conditions, the cylinder liner, cylinder block, and valve assembly were included in the finite element mesh (FEM). Figure 3.7.1 and 3.7.4 illustrate the model used in this analysis. Figure 3.7.1 is a sectioned view of the cylinder head which shows the inner structure. Figure 3.7.5 illustrates the various boundary conditions used for the structural analysis of the cylinder head. Figure 3.7.6 shows the finite element model surfaces which had forced convection boundary conditions imposed upon them.

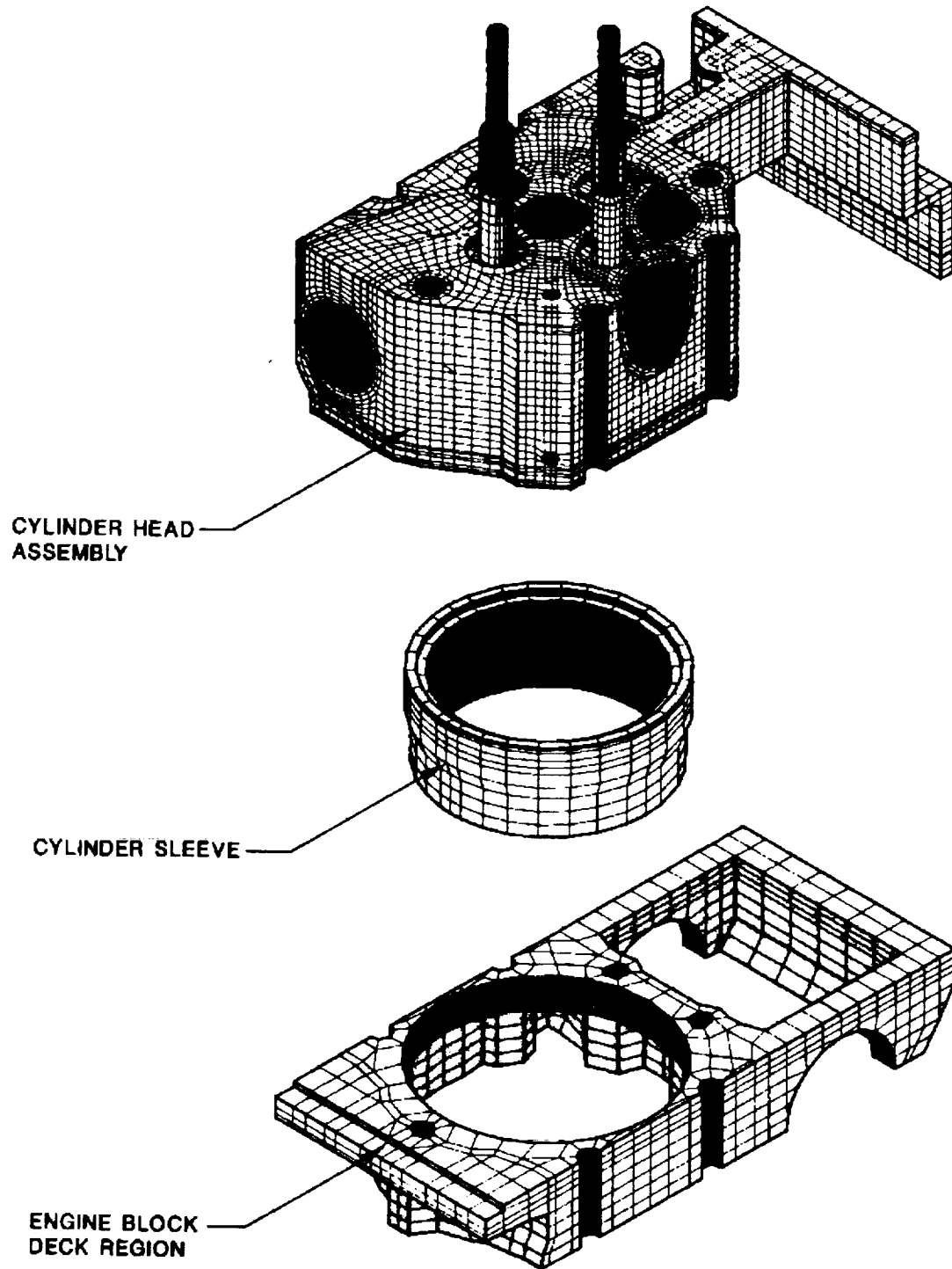


**Figure 3.7.4:** Finite element mesh of the NASA cylinder head, cylinder liner, and engine block.

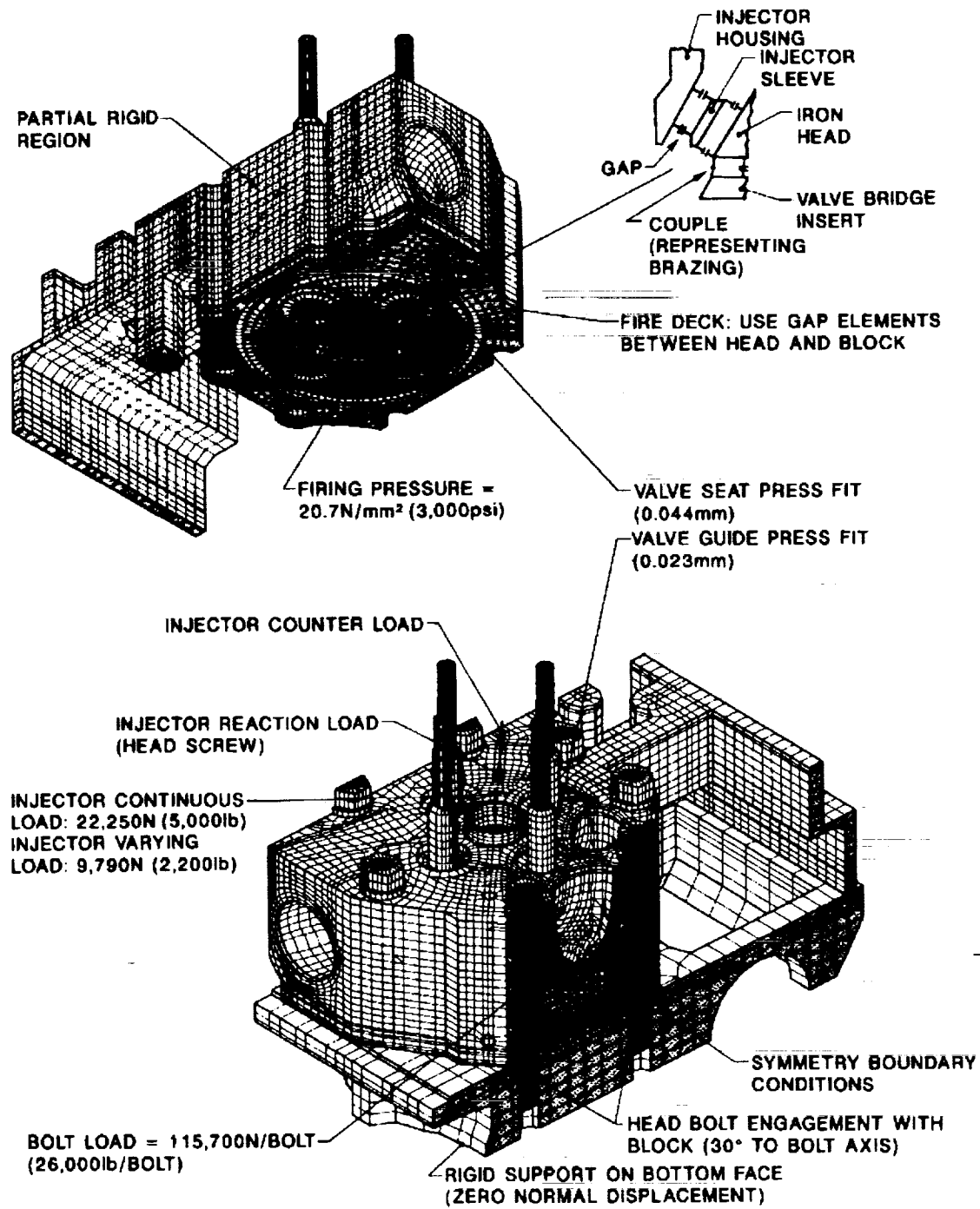


**Figure 3.7.5:** Structural boundary conditions used in the NASA cylinder head FE analysis.



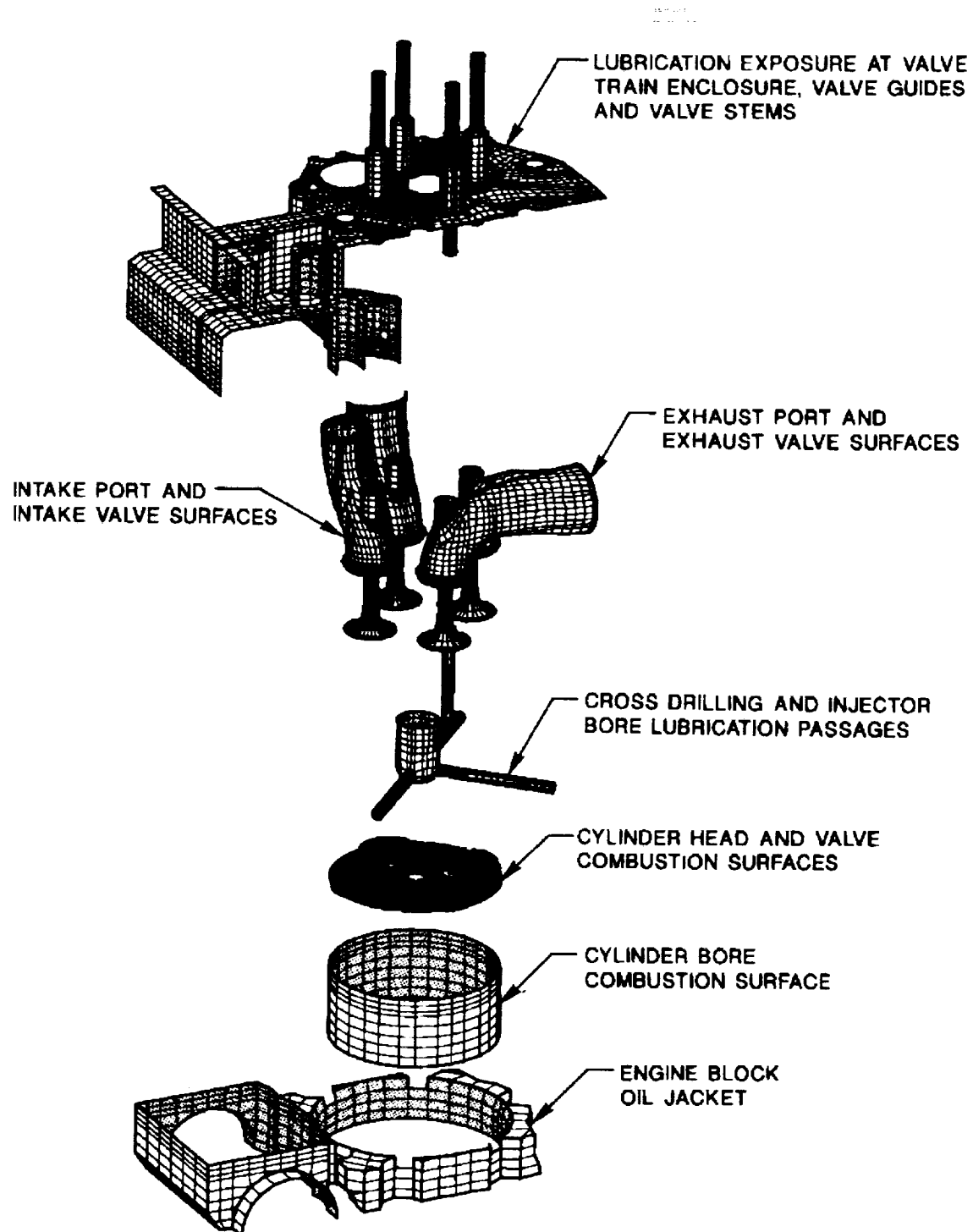


**Figure 3.7.6:** Convective boundary conditions used in the NASA cylinder head FE analysis.

The model was used to revise specific design details, and to predict the relative thermal fatigue life of the various designs options. Figure 3.7.7 summarizes the results of the thermal analysis for various design options. Shown in the figure is the percent reduction in metal temperature as compared to the baseline case. The baseline head is an uninsulated cast iron configuration with unturbulated focused oil cooling. The conclusions from the thermal analysis are that, compared to the baseline cylinder head configuration, insulating both the intake and exhaust ports significantly reduces the thermal gradients above the valve bridge cooling passages. The ceramic ports, however, have no effect on the valve bridge and injector seat temperatures. The ceramic thermal barrier coating on the combustion surface does reduce the parent metal temperature, however, the resulting temperature, 540°C, is still unacceptable. Increasing the valve bridge cooling by a factor of three also has an effect on combustion face metal temperatures, but even with these features, the valve bridge insert is required to obtain adequate protection for the cast iron.

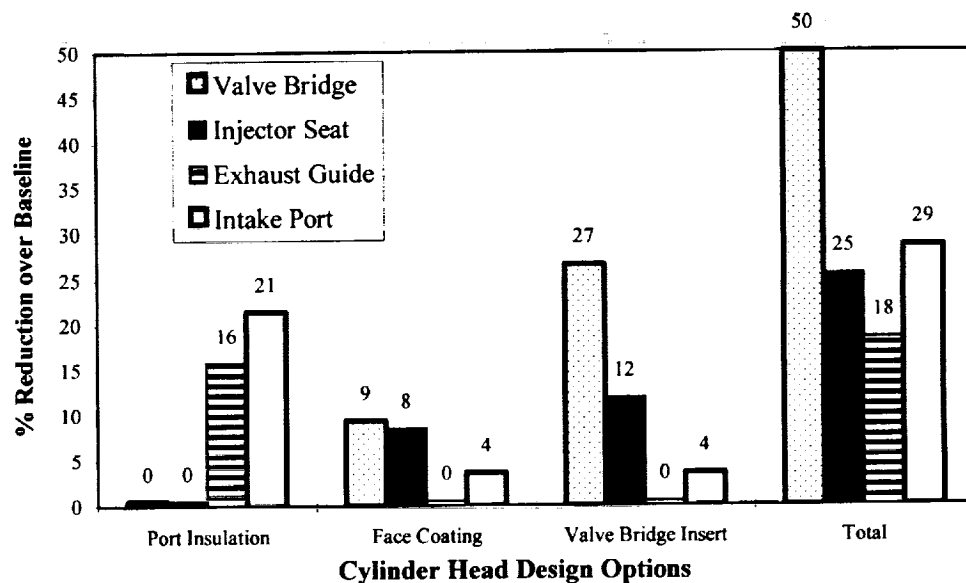


**Figure 3.7.7:** Percent reduction in metal temperature as compared to the baseline cylinder head for various insulating design options.

Use of the valve bridge insert reduces parent metal temperature by 105°C to 420°C, acceptable for gray cast iron. Figures 3.7.8 and 3.7.9 show the finite element model results for the fully insulated cylinder head at full load conditions. Figure 3.7.9 shows the effect the valve bridge insert has on metal temperatures. Large temperature gradients across the valve bridge insert and port liners show their effectiveness in reducing the gray cast iron metal temperatures.

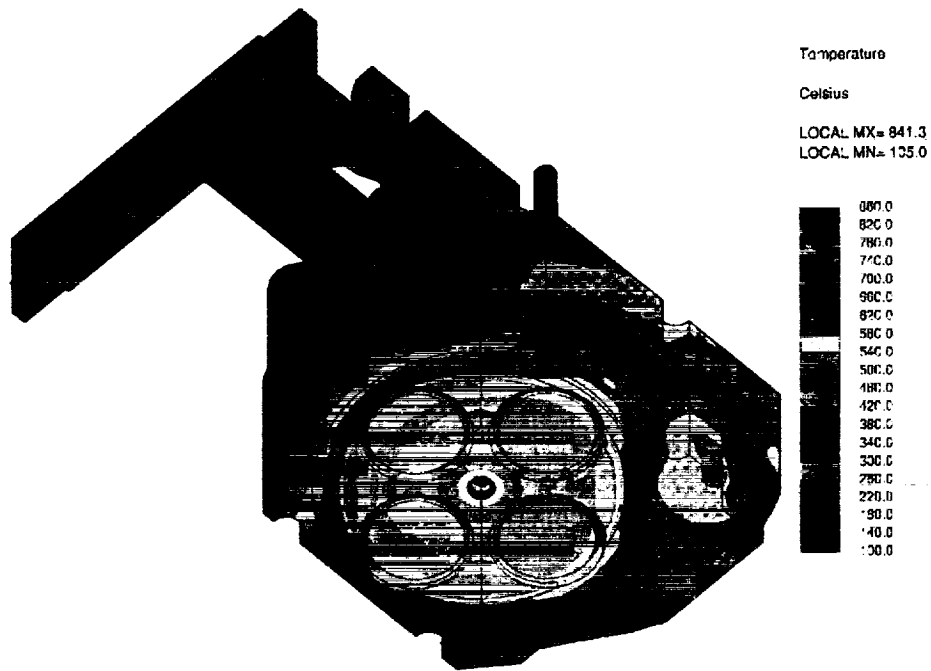


**Figure 3.7.8:** Steady state FE temperature analysis of the fully insulated NASA cylinder head at 1500 rpm and full load (355 kW).

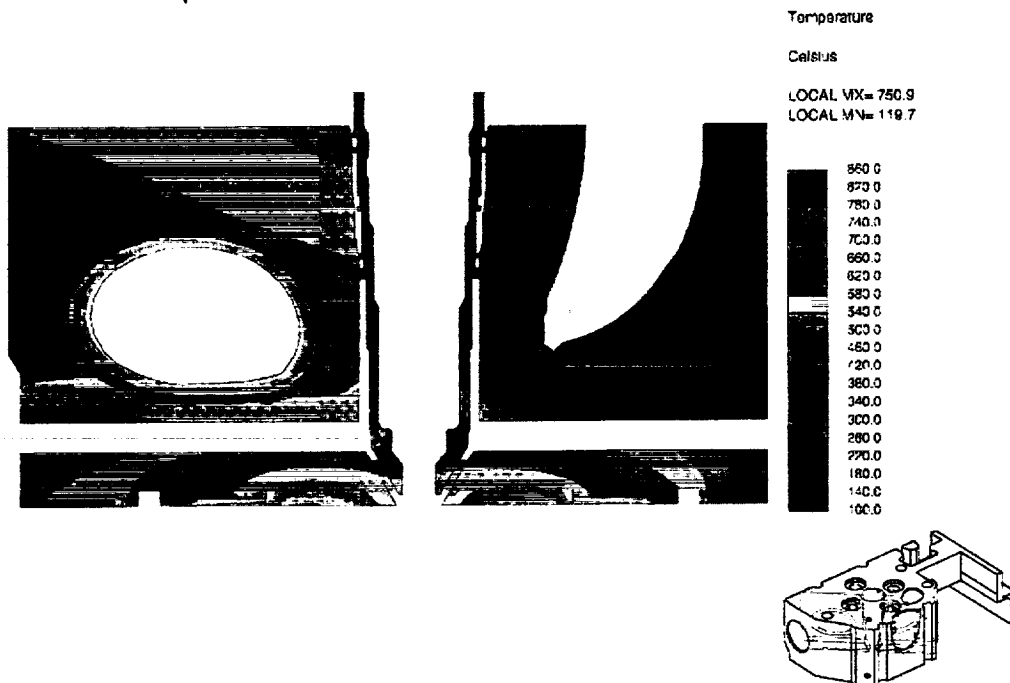


**Figure 3.7.9:** Steady state FE temperature analysis of the fully insulated NASA cylinder head at 1500 rpm and full load (355 kW) – sectioned view.

### 3.7.4 Port Liner Development

Previous work at Cummins has shown that insulating the exhaust ports can substantially lower cylinder head temperatures and therefore increase thermal fatigue resistance. In addition, it is desirable to have a low intake air temperature to improve charge air density and minimize the demands on the turbocharger compressor. Since it is desirable to operate the cylinder head at high temperatures, to minimize cooling needs the cylinder head design includes ceramic insulated intake ports to reduce heat transfer to the intake air. The port liners were designed to be readily made by a ceramic slip casting process. The exterior of the port liner is covered with a porous compliant layer designed to crush and absorb the casting stresses.

The ceramic materials selected for port development were aluminum titanate and sodium-zirconium-phosphate (NZP). Both of these ceramic materials have low thermal conductivity and excellent thermal shock resistance based on their low thermal expansion characteristics. The aluminum titanate ports were provided by Coors Ceramics Co. and the NZP ports were provided by Ceramtec, Inc. Prior to this program, the NZP material had not been formed by slip casting. A materials property study concluded that modified aluminum titanate and NZP have sufficient strength and stability to withstand the cylinder head operating conditions. Various properties of the ceramics are given in Table 3.7.1.

**Table 3.7.1:** Properties of materials used in ceramic port development

Material	Young's Modulus (GPa)	Flexural Strength (MPa)	Thermal Conductivity (W/m-K)	Thermal Expansion Coefficient ( $10^{-6}/^{\circ}\text{C}$ )
Aluminum Titanate	50	30	1.6	1.5 <sup>†</sup>
NZP	80	70	1.0	0.3

<sup>†</sup> Average coefficient for heating cycle - 20 to 1000°C

Initial work on insulating ports involved direct replacement of the cast iron geometry with aluminum titanate ceramic port liners. This created ceramic shapes which were not optimized for survival during casting. The design of the cylinder head had to be modified to account for the properties of the ceramics and allow for port shapes with rounded surfaces and smooth transitions with a minimum of angles and sharp corners. The design included insulation for both intake and exhaust ports

### 3.7.5 Casting Development

Successful cylinder head castings with ceramic ports are highly dependent on the performance of the compliant layer in absorbing the stresses generated during the casting process. The compliant layer is designed to be of low density and high porosity. These characteristics allow the compliant layer to crush and absorb the stresses that are created during the cooling and compression of the gray iron. Initial development of NZP involved casting an intake port in gray iron in a crucible

without a compliant layer to determine if the base NZP material had any basic advantages over the modified aluminum titanate. Results of this crucible casting trial indicate that the NZP material cannot withstand the compressive and tensile stresses generated in a complex port shape without a compliant layer. This result is similar to previous experience with aluminum titanate ports. Development of a compliant layer became crucial for successful casting of ceramic port liners. Ceramtec was able to fabricate NZP ports with a compliant layer. However, these ports were considered too friable to be used in casting. Additional ports made from NZP were supplied with an improved compliant layer and were used in the first NZP cylinder head casting trial. Aluminum titanate ports fabricated with a foamed aluminum titanate compliant layer were used for their first casting trial. These initial casting trials resulted in excessive spalling and cracking of both types of ceramic ports. A total of five castings were poured for the initial port development. Three castings were made with all aluminum titanate ports and two were made with an NZP intake port, an aluminum titanate intake port, and an aluminum titanate exhaust port. Modifications to the compliant layer and to the casting process itself were made after each trial. Compliant layer modifications included changes to the density, porosity, and thickness, as well as application of Fiberfrax<sup>®</sup> felt to critical areas. The aluminum titanate ports showed improvement through each subsequent casting trial, and intake ports were successfully cast on the fifth trial. The NZP ports displayed extensive network cracking in both casting trials. It was determined that extensive development of the NZP material would be required for successful castings. For this reason, development of NZP as a port material was discontinued on this program.

The next set of casting trials consisted of three cylinder heads with aluminum titanate ports. Initially, one cylinder head was cast to determine the effect of minor geometry changes in the port design on the success of ceramic castings. Inspection showed that the ceramic exhaust port had sustained a severe crack. The final two heads poured used ports with improved geometry and modified compliant layers. Inspection of these heads immediately after removal from the sand mold revealed no cracks in the ceramic ports. The temperature of the casting at this point was estimated to be 150°C. Just prior to bead blasting, a ceramic exhaust port in one of the heads cracked. The remaining cylinder head survived bead blasting and initial grinding before a crack in the exhaust port was discovered. The temperature of the casting when the crack was discovered was 40°C.

Additional modifications to the port geometry and compliant layers resulted in the successful casting of two cylinder heads with aluminum titanate intake and exhaust ports. Changes to the port geometry included a larger radius of curvature in the section joining the two legs of the exhaust port and the removal of the holes used for the valve guide passages. The valve guide passages must now be cut into the ports using ultrasonic machining after successful metal casting. The change to the compliant layer that resulted in the successful castings was the addition of compliant material to the ends of the ports.

### **3.7.6 Port Flow Testing**

Elimination of the water cooling jackets in the cylinder head created space so the intake and exhaust ports could be more aerodynamically designed. The goal in redesigning the ports was to increase effective flow area and decrease swirl as compared to a production L10 cylinder head. The intake and exhaust ports were redesigned using CAD surfacing techniques. Core plug molds

were produced directly from the CAD file to reduce production time and eliminate possible errors in fabrication. In order to test the effect of the port geometry changes, a plastic cylinder head model was made using these core plugs.

The cylinder head port flow box was tested on an air flow rig. Effective flow area through the intake and exhaust ports and swirl in the combustion chamber were measured at various valve lifts. This data was then compared to port flow tests done on a production L10 cylinder head. The redesigned intake and exhaust ports showed significant improvement in effective flow area at all valve lifts. Effective flow area versus valve lift for the standard L10 and LE-55 cylinder head are illustrated in Figure 3.7.10. Since the L10 combustion was optimized around a quiescent combustion chamber, another goal of the port redesign was to maintain or decrease the swirl level. The redesigned cylinder head maintained lower swirl levels than the production L10 head at all valve lifts. The redesigned cylinder head has improved the port flow characteristics over the production L10 head.

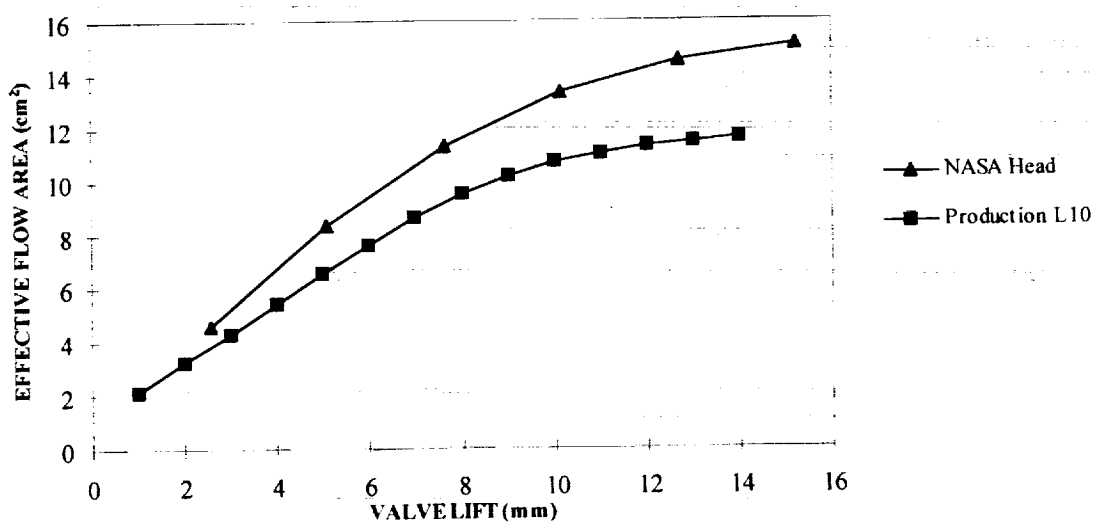


**Figure 3.7.10:** Effective flow area versus valve lift comparison for the L10 and LE-55 cylinder heads.

### 3.7.7 Engine Testing - Port Liners

Sequential engine testing of an uninsulated and otherwise identical port insulated cylinder head was performed to determine the effectiveness of the insulation on reducing metal temperatures. Engine tests at conditions similar to those used in the finite element analyses were performed in a effort to validate the model. Engine performance data was also collected to quantify the effects of intake and exhaust port insulation on engine performance.

A single cylinder research engine was used for evaluation of the LE-55 cylinder head. Achieving precise operating conditions and quantifying these conditions required extensive instrumentation of the single cylinder engine. Each cylinder head was instrumented with five thermocouples for measuring metal temperatures. Two thermocouples were located 9 mm above the combustion

face in the exhaust-exhaust and intake-exhaust valve bridge region. Two additional thermocouples were placed 27 mm from the combustion face, above the oil drillings. The fifth thermocouple was located above the exhaust port. Exhaust gas temperatures were measured with a sheathed E-type thermocouple and a fast response thermocouple. The temperature, pressure, and flow rate of the lubrication oil, cylinder head coolant oil, intake air, and diesel fuel were measured. High speed cylinder pressure data were collected to determine the gross indicated mean effective pressure (GIMEP) and apparent heat release rate (AHRR). An injector needle lift sensor was used to monitor the start of fuel injection. The use of this instrumentation allowed for precise control and monitoring of the engine operation.

To reduce the error associated with the test measurements, an average of ten individual data points was used to define each condition. Each of the individual data points represents the average of 120 samples recorded during a two minute fuel reading. Standard deviations were calculated based on the individual data points for each operating condition.

The boundary conditions used for the FE analysis of the cylinder head were designed to simulate the LE-55 operating condition. The recipe for this operating condition specifies a number of critical engine operating parameters. A summary of the ideal operating conditions for the recipe and the conditions achieved during the testing are presented in Table 3.7.2.

**Table 3.7.2:** LE-55 engine recipe and actual test conditions

Parameter	LE-55 Recipe	Test Conditions
GISFC (g/gikW-hr)	167.9	175.5
Engine speed (rpm)	1500	1500
Peak cylinder pressure (MPa)	19.3	17.2
Air-fuel ratio	30:1	30:1
Compression ratio	17.3:1	17.1:1
Intake manifold temperature (K)	283	316.5

The single cylinder research engine presents a challenge when evaluating engine performance characteristics since the single cylinder engine did not have a turbocharger. Without a turbocharger, evaluating the benefits of exhaust port insulation was difficult since the extra energy available in the higher temperature exhaust gas does not provide higher boost pressure. Additionally, if the engine operating conditions are set up using constant air and fuel mass flow rates as was typically done, then the benefits of intake port insulation are not fully realized in the typical engine performance measures. To address the fact that no turbocharger was present, the exhaust gas temperature was measured to determine if there was an increase in temperature due to the exhaust port insulation. To evaluate the effects of intake port insulation on engine breathing, a constant air pressure was supplied to the intake manifold. By supplying a constant intake manifold pressure, the differences in air mass flow rate and volumetric efficiency could be used as a means of determining the effects of intake port insulation.

Metal temperature data for the uninsulated and insulated cylinder heads were collected at a number of GIMEP levels. GIMEP levels ranged for 900 kPa at an air-fuel ratio of 30:1 up to 2.7 MPa at and air-fuel ratio of 25:1.

At critical high temperature locations, above the exhaust port for example, insulation reduced metal temperatures by as much as 80 K as shown in Figure 3.7.11. At the exhaust-exhaust valve bridge, temperatures were reduced by as much as 11 K. Below the exhaust port, temperature reductions ranged from 13 K to 40 K across the operating range. Figures 3.7.12 and 3.7.12 illustrate the temperature reductions. Figures 3.7.11 through 3.7.13 represent data recorded at an engine speed of 1500 rpm and an air-fuel ratio of 30:1. Temperature reductions were similar at 1200 rpm and 1800 rpm and were more pronounced at air-fuel ratios of 25:1.

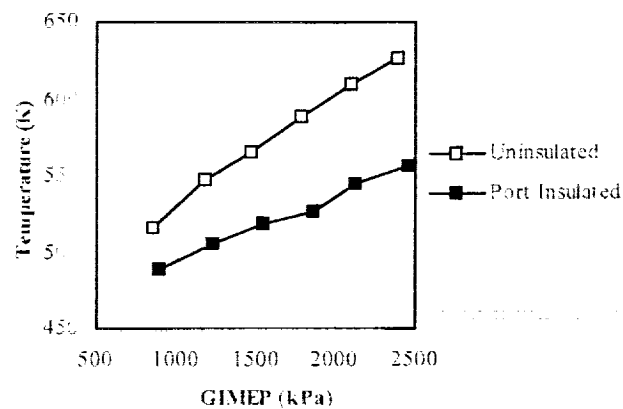


**Figure 3.7.11:** Metal temperatures measured above the exhaust port with and without ceramic insulation.

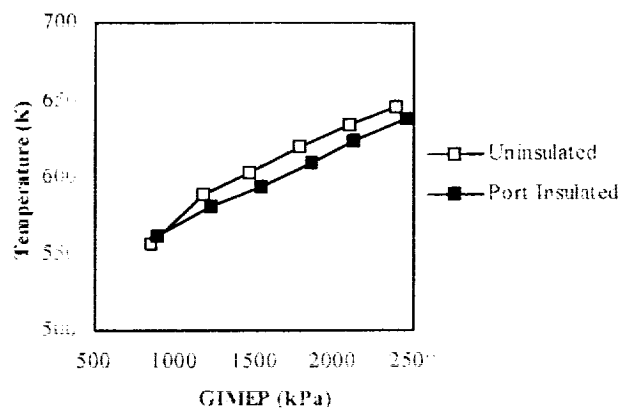


**Figure 3.7.12:** Metal temperatures measured at the exhaust-exhaust valve bridge with and without ceramic insulation.



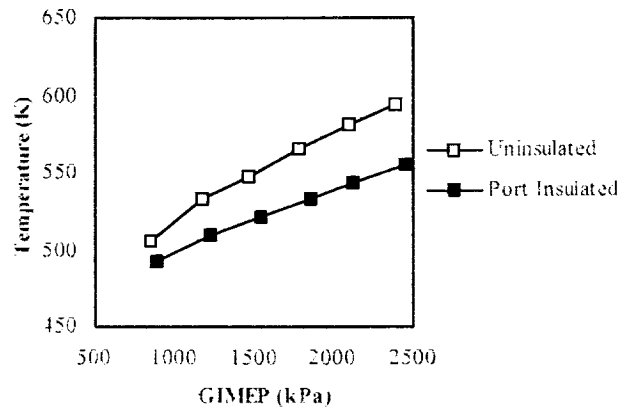


**Figure 3.7.13:** Metal temperatures measured below the exhaust port with and without ceramic insulation.

Temperature results at the LE-55 operating condition were compared to the temperatures predicted by the FE analysis. Table 3.7.3 quantitatively compares the results. Some of the discrepancies between the model and the test results can be attributed to differences in the cylinder head configuration. The primary difference between the model and the cylinder head was the oil drilling configuration. The FE model and cylinder designed were originally constructed with only three oil cross drillings, leaving out the fourth drilling above the intake-intake valve bridge. Further analysis of oil flow around the injector dictated that a smaller drilling above the intake-intake valve bridge was necessary to prevent flow stagnation.

**Table 3.7.3:** Cylinder head temperature reduction comparison

Location	FE Predicted Reduction	Engine Test Observed Reduction
Above exhaust port	60- 80 K	62 K
Exhaust-exhaust valve bridge	0 - 10 K	11 K
Below exhaust port	40 -60 K	32 K

The engine performance data gathered on the uninsulated and port insulated cylinder heads were used to determine how port insulation affects specific fuel consumption, volumetric efficiency and exhaust gas temperature. The gross indicated specific fuel consumption (GISFC) was used for comparison rather than the brake specific fuel consumption (BSFC) since the engine tests were performed on a single cylinder engine. On single cylinder engines where the oil pump, fuel pump, and other accessory drives are removed, brake quantities become unrealistic measures of engine

performance. The volumetric efficiency was measured relative to the intake manifold conditions using the formula:

$$\eta_v = \frac{2 m_a}{\rho_{a,i} V_d N} \quad 3.7.1$$

where,

- $m_a$  = Air mass flow
- $\rho_{a,i}$  = Intake manifold air density
- $V_d$  = Displaced volume
- $N$  = Engine speed

Volumetric efficiency is a key indicator of cylinder head performance since it is a measure of how efficiently air is pumped through the engine. Exhaust gas temperature was measured to determine how exhaust port insulation might affect turbocharger operation and thus engine performance.

A reduction in specific fuel consumption (GISFC) of 1 to 4% was observed with the port insulated cylinder head. The observed fuel consumption (GISFC) at an engine speed of 1500 rpm and an air-fuel ration of 30:1 is plotted versus GIMEP in Figure 3.7.14. The error bars in Figures 3.7.14 and 3.7.15 represent one standard deviation. Measured fuel consumption at 1500 rpm increased as the air-fuel ratio decreased to 25:1 as shown in Figure 3.7.15. Reductions in fuel consumption at 1200 rpm and 1800 rpm due to port insulation were similar to those observed at 1500 rpm. The specific fuel consumption measured at the LE-55 operating condition was 175.5 g/gkW-hr. This was within 4.5% of the fuel consumption target. The fuel economy benefits observed with port insulation were encouraging.

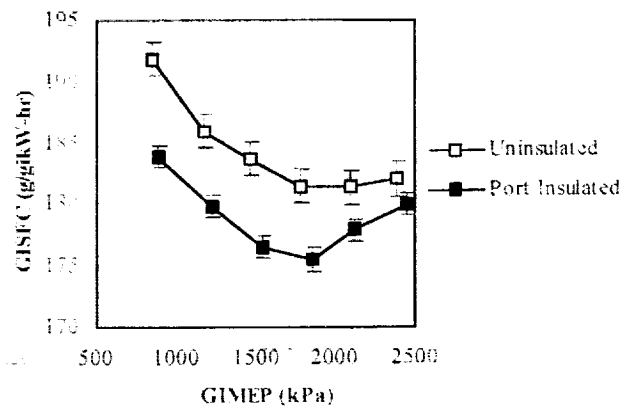


**Figure 3.7.14:** Specific fuel consumption comparison, 1500 rpm, 30:1 air-fuel ratio.

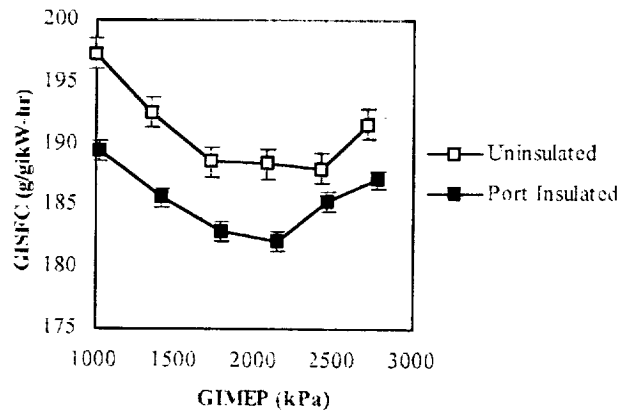


**Figure 3.7.15:** Specific fuel consumption measured at 1500 rpm, 25:1 air-fuel ratio, with and without port insulation.

Volumetric efficiency increased by 1 to 3% for the port insulated cylinder head. Figure 3.7.16 illustrates the volumetric efficiency increase due to port insulation at an engine speed of 1500 rpm and an air-fuel ratio of 25:1. Volumetric efficiency gains were similar at 1200 rpm and 1800 rpm and were slightly greater at 30:1 air-fuel ratio. Figure 3.7.17 is a plot of volumetric efficiency versus GIMEP at an engine speed of 1800 rpm and an air-fuel ratio of 30:1. The increase in volumetric efficiency realized with the insulated cylinder head suggests that the ceramic intake ports reduced the reheating of the charge air, however, a direct measurement of the air temperature before and after the port could not be made.

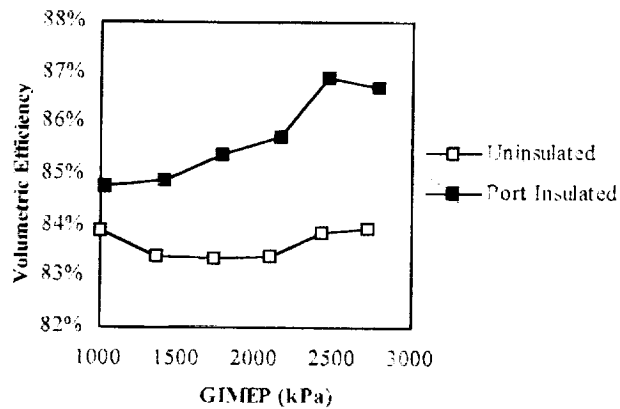


**Figure 3.7.16:** Volumetric efficiency measured at 1500 rpm, 25:1 air-fuel ratio, with and without insulation.

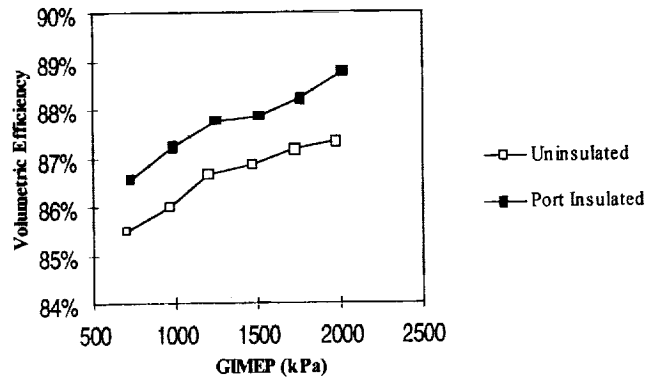


**Figure 3.7.17:** Volumetric efficiency measured at 1800 rpm, 30:1 air-fuel ratio, with and without insulation.

Exhaust port insulation increased the exhaust gas temperature across the range of GIMEP levels and engine speeds tested, as shown in Figure 3.7.18. At the LE-55 operating condition the exhaust gas temperature increased 34 K. Figure 3.7.18 is an example of the increase in exhaust gas temperature at an engine speed of 1800 rpm and air-fuel ratio of 25:1. The increase in energy in the exhaust gas is a direct result of the exhaust port insulation. The extra energy in the exhaust gases would have otherwise been transferred to the cylinder head and lost to the coolant. This additional energy could be used by the turbocharger to provide increased intake boost, however, the single cylinder engine used for evaluation could not be equipped with a turbocharger. Additional testing on a multi-cylinder engine with a turbocharger would fully define the benefits of exhaust port insulation.

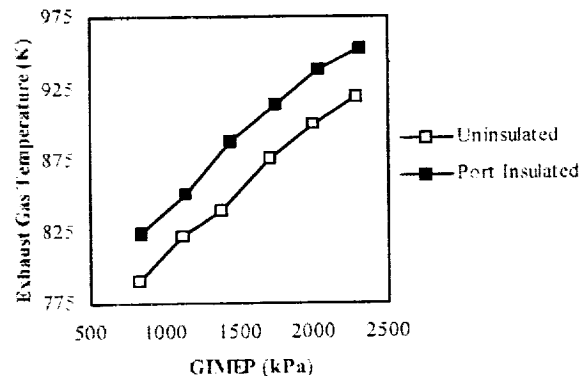


**Figure 3.7.18:** Exhaust gas temperature measured at 1800 rpm, 25:1 air-fuel ratio, with and without insulation.

### 3.7.8 Engine Testing - Oil Drilling Turbulators

A large amount of heat is produced in a diesel engine. The heat will accumulate in the cylinder head where it can have damaging effects including valve bridge cracking. By installing coiled wire turbulators in strategic locations, heat can be transferred from the cylinder head to the oil coolant.

Increased heat transfer to the oil coolant keeps the valve bridges and injector cavity cooler which in turn decreases the metal temperatures in the cylinder head. Reduced metal temperatures result in increased thermal fatigue life and engine durability.

The coiled spring were sized using the following two equations:

$$d = 50Re^{(0.875)}D \quad 3.7.2$$

$$P = 10d \quad 3.7.3$$

Equation 3.7.2 was used to determine the wire diameter for the turbulator. In Equation 3.7.2,  $D$  is the diameter of the oil drilling and  $Re$  is the Reynold's number. The diameter of the drilling ( $D$ ) was 6 mm or 4 mm. The Reynold's number was dependent on individual drilling flow rates and drilling characteristics. Equation 3.7.3 was used to determine the pitch of the turbulator which was ten times the diameter of the coiled spring wire ( $d$ ).

Turbulators were placed in the cylinder oil supply drilling and three oil drain drillings. The turbulators ran the length from each drilling entrance to the injector bore. Each turbulator was stretched and placed inside the respective oil drilling. Afterwards, the turbulator was allowed to expand and firmly press against the oil drilling wall.

To properly evaluate the effects of turbulators on cylinder head metal temperatures extensive instrumentation was employed on the single cylinder research engine. Five thermocouples were located in the cylinder head: one above the exhaust port, one above the oil drilling but below the exhaust port, 27 mm above the combustion face, one in the exhaust-exhaust valve bridge, 9 mm above the combustion face, one above the oil drilling on the intake side, and one below the oil drilling in the intake-exhaust valve bridge, 9 mm above the combustion face. The single cylinder research engine conditions run for the turbulator evaluation are shown in Table 3.7.4.

**Table 3.7.4:** Engine conditions run during evaluation of oil drilling turbulators

Parameter	Setpoint
Engine Speed	1500 rpm
Injection timing (TVC)	28°
Intake manifold temperature	43°C
Fuel in temperature	40°C
Oil rifle temperature	116°C
Cylinder block coolant out temperature	91°C
Cylinder block coolant flow rate	39.3 lpm
Cylinder head coolant flow rate	12.5 lpm

The turbulators reduced cylinder head metal temperatures in each of the five thermocouple locations. The temperatures of turbulated and nonturbulated cylinder heads are shown in Figures

3.7.19 through 3.1.28 for each of the thermocouple locations at each air-fuel ratio. As can be seen from Figures 3.7.21 and 3.7.22 for the location above the oil drilling but below the exhaust port, 27 mm above the combustion face and Figures 3.7.23 and 3.7.24 for the exhaust-exhaust valve bridge location, 9 mm above the combustion face, these locations showed the greatest temperature reduction. At an air-fuel ratio of 25:1, these locations had an average temperature reduction of 15% and 14%, respectively. At an air-fuel ratio of 30:1, these same locations had an average temperature reduction of 13% (see Figures 3.7.29 and 3.7.30 along with Figures 3.7.21 through 3.7.24). The location above the exhaust port had the smallest temperature change at both air-fuel ratios: a 1.5% reduction at 25:1 and a 0.7% reduction at 30:1 (see Figures 3.7.29 and 3.7.30 along with Figures 3.7.19 and 3.7.20). The small temperature reduction above the exhaust port was expected since this location was a large distance from the turbulated oil drilling. The location above the oil drilling on the intake side and the location below the oil drilling in the intake-exhaust valve bridge, 9 mm above the combustion face showed a minimal temperature reduction at both air-fuel ratios (see Figures 3.7.29 and 3.7.30 along with Figures 3.7.25 through 3.7.28).

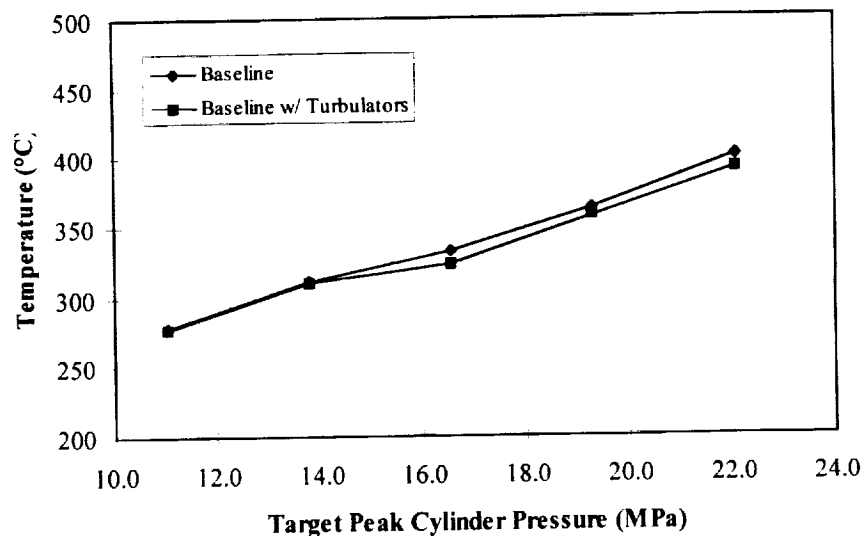


**Figure 3.7.19:** Metal temperatures above the exhaust port, with and without turbulators, 25:1 air-fuel ratio.

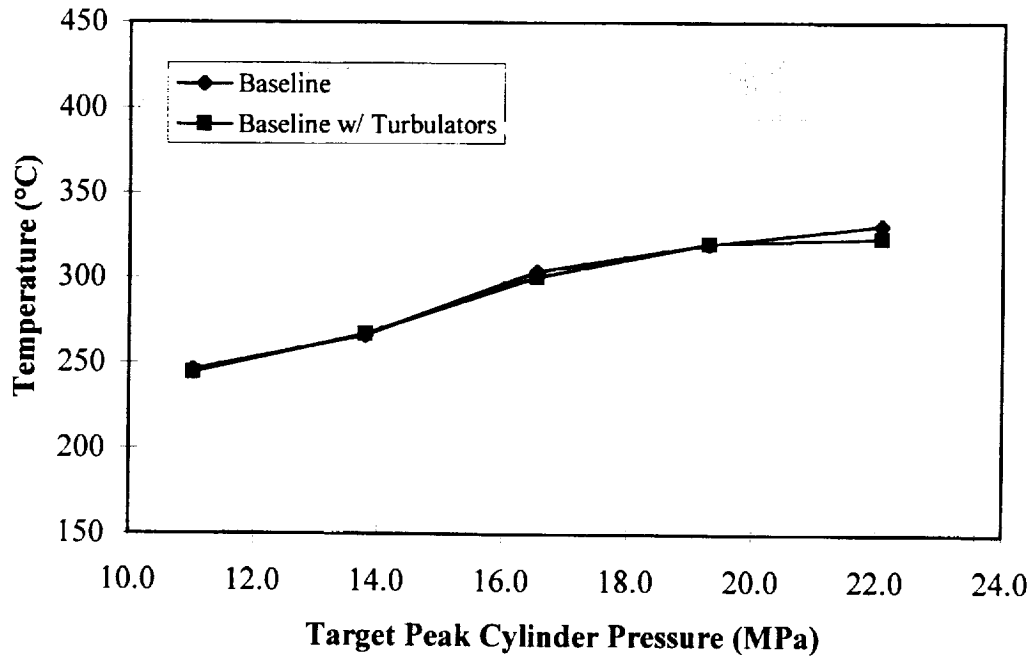


**Figure 3.7.20:** Metal temperatures above the exhaust port, with and without turbulators, 30:1 air-fuel ratio.

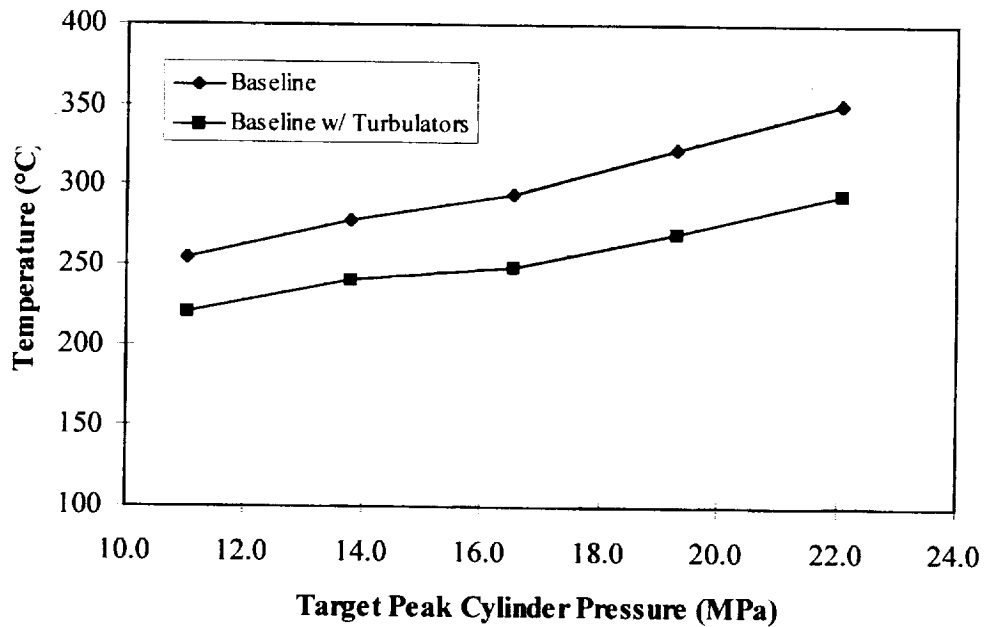


**Figure 3.7.21:** Metal temperatures below the exhaust port, above the oil drilling, 27 mm above the combustion surface, with and without turbulators, 25:1 air-fuel ratio.

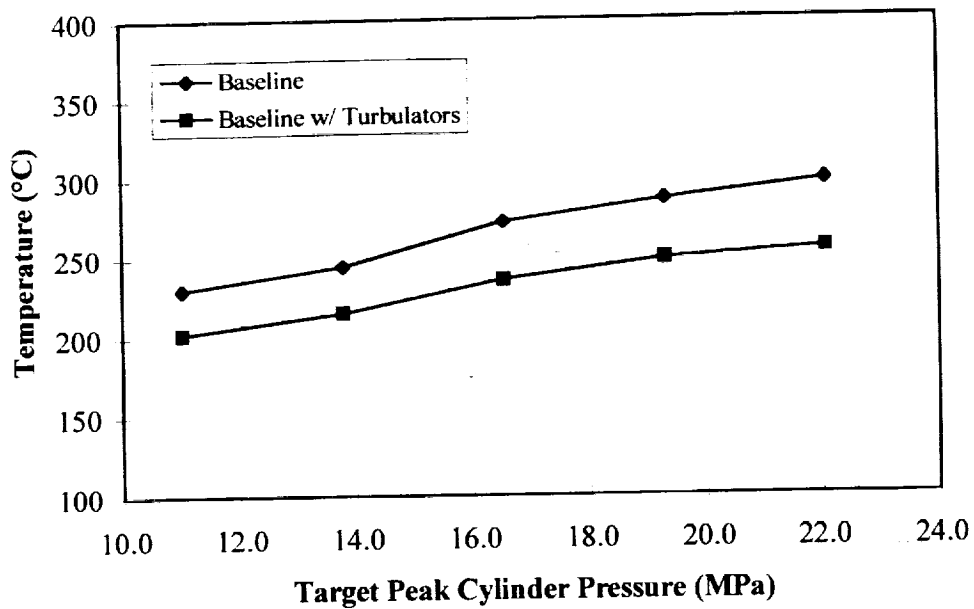


**Figure 3.7.22:** Metal temperatures below the exhaust port, above the oil drilling, 27 mm above the combustion surface, with and without turbulators, 30:1 air-fuel ratio.

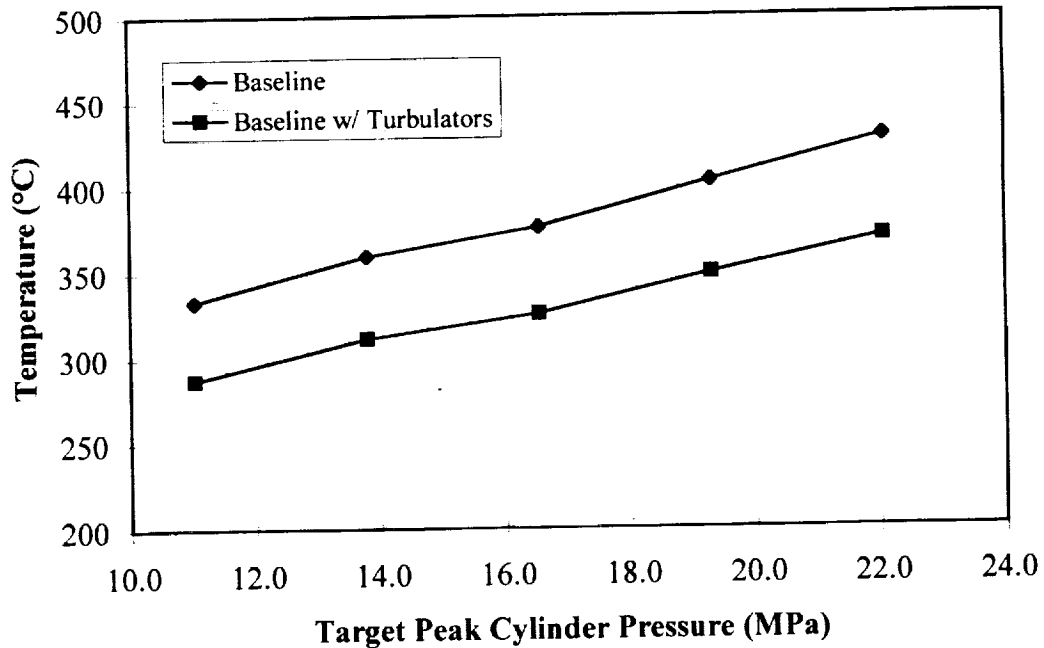


**Figure 3.7.23:** Metal temperatures at the exhaust-exhaust valve bridge, 9 mm above the combustion face, with and without turbulators, 25:1 air-fuel ratio.



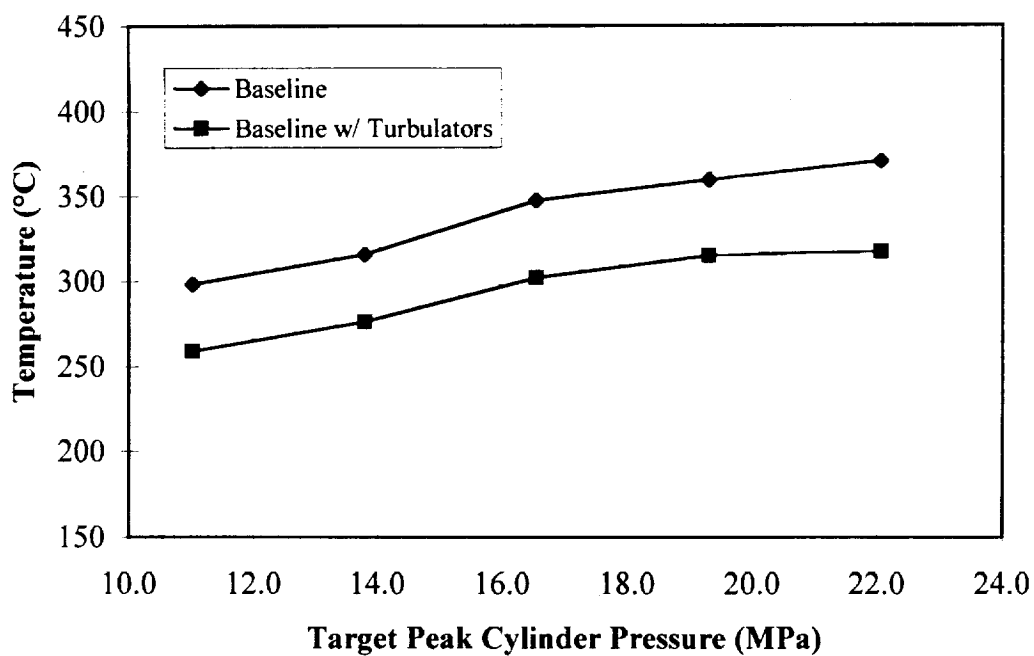


**Figure 3.7.24:** Metal temperatures at the exhaust-exhaust valve bridge, 9 mm above the combustion face, with and without turbulators, 30:1 air-fuel ratio.

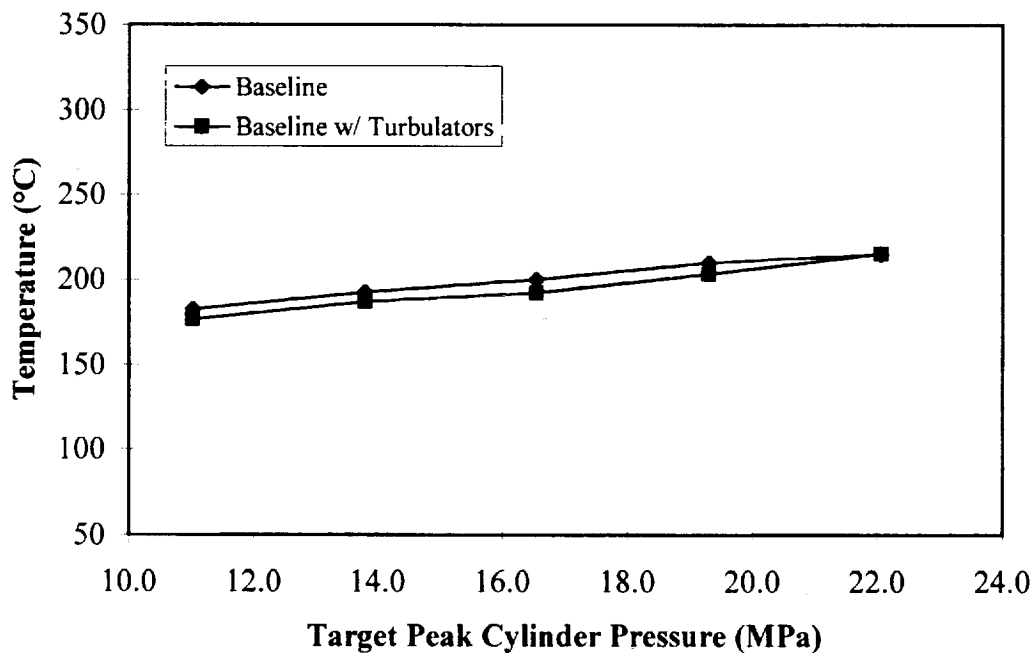


**Figure 3.7.25:** Metal temperatures above the oil drilling, intake side, with and without turbulators, 25:1 air-fuel ratio.

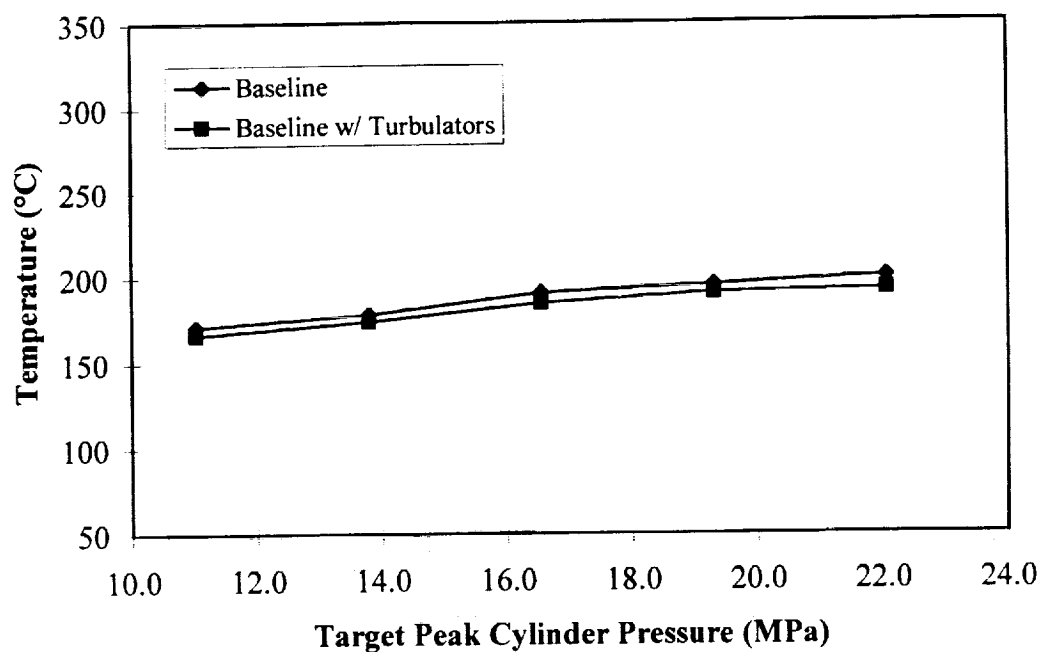


**Figure 3.7.26:** Metal temperatures above the oil drilling, intake side, with and without turbulators, 30:1 air-fuel ratio.

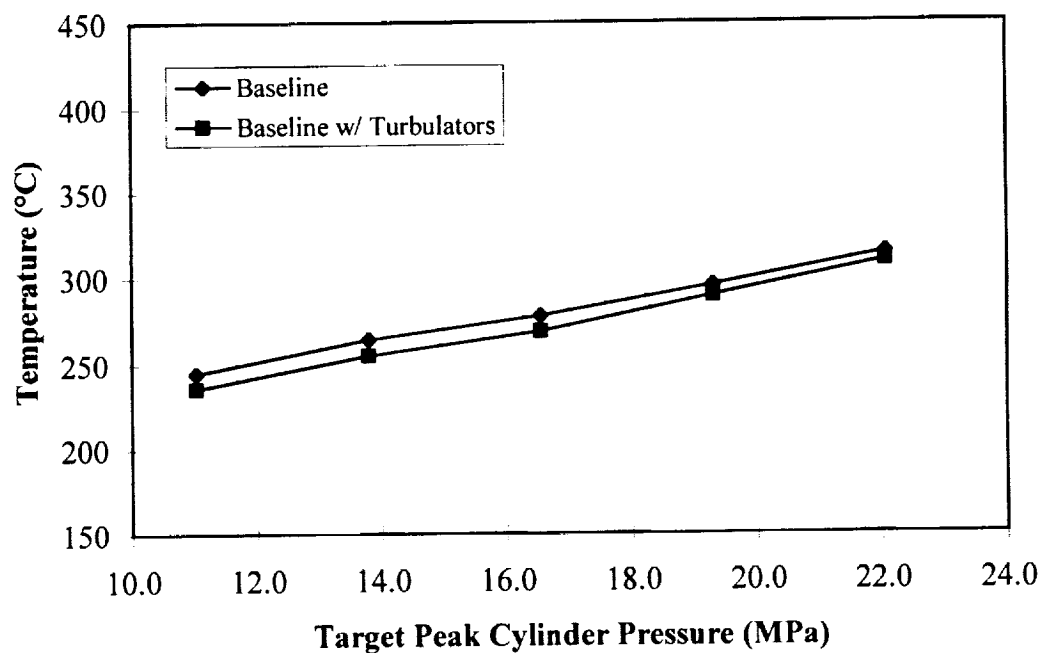


**Figure 3.7.27:** Metal temperatures 9 mm above the combustion surface, intake-exhaust valve bridge side, with and without turbulators, 25:1 air-fuel ratio.

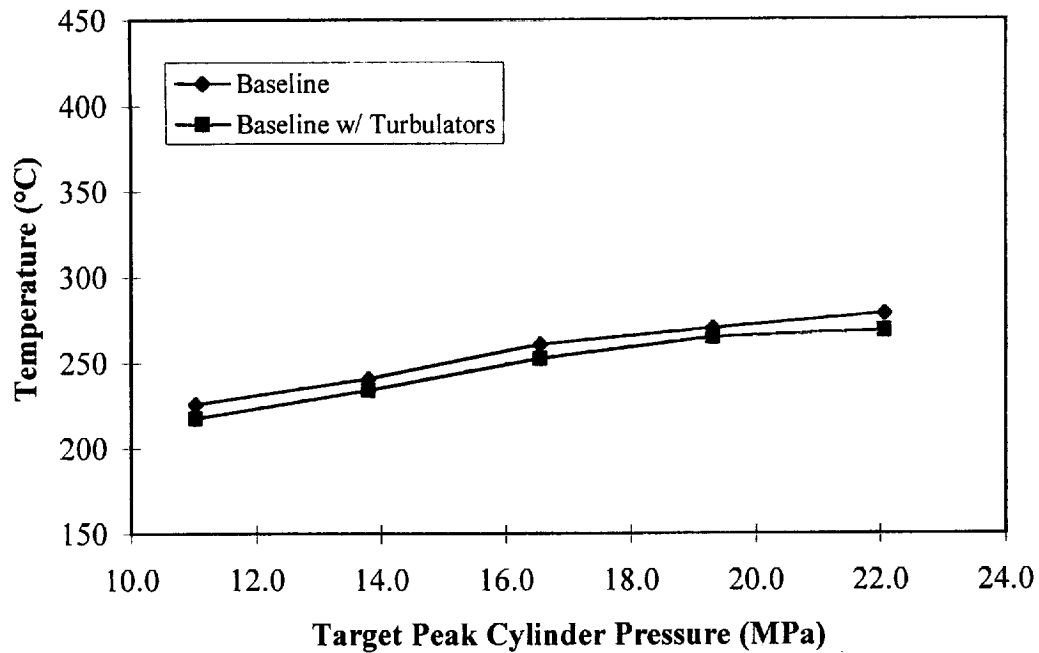


**Figure 3.7.28:** Metal temperatures 9 mm above the combustion surface, intake-exhaust valve bridge side, with and without turbulators, 30:1 air-fuel ratio.

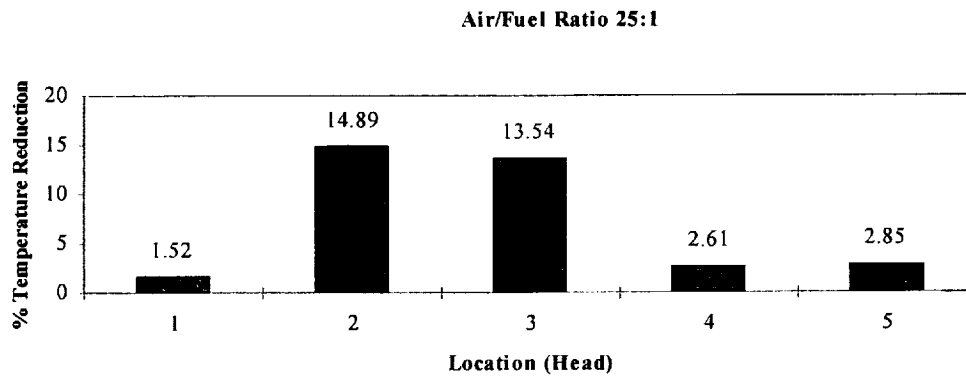


**Figure 3.7.29:** Percent temperature reduction at head thermocouple location, 25:1 air-fuel ratio.

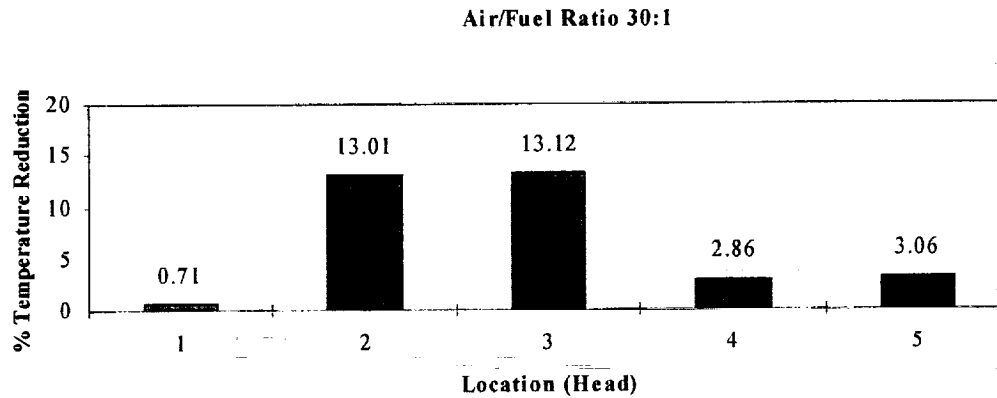


**Figure 3.7.30:** Percent temperature reduction at head thermocouple location, 30:1 air-fuel ratio.

When the turbulators were removed from the cylinder head after engine test, no oil coking was evident in the oil drillings or on the turbulators. However, two turbulators had been partially forced out of their drillings (the turbulators located at the outlets which drain into the cam box). Based on this observation, larger turbulators or machined turbulators should be considered to prevent this occurrence.

### 3.7.9 Conclusions - Insulated Cylinder Head

- A finite element analysis (FEA) of the insulated LE-55 cylinder head predicted a maximum metal temperature of 420°C at the thermally abusive LE-55 operating point.
- The FEA performed on the LE-55 cylinder head predicted infinite thermal fatigue life at the LE-55 operating condition point.
- Improvements in the intake and exhaust port designs resulted in a 20% increase in effective flow area with swirl levels cut in half.
- Ceramic intake and exhaust ports fabricated from aluminum titanate were successfully cast into a grey iron cylinder head.
- Engine performance data collected on a single cylinder research engine suggested that a 1 to 4% fuel consumption reduction is possible through the use of ceramic port insulation. The benefits of ceramic port insulation are shown in Table 3.7.5.

**Table 3.7.5:** Benefits of ceramic port insulation

Benefit	Observed Value	Percent Benefit
Reduced metal temperature above exhaust port	62 K	10.5%
Reduced fuel consumption GISFC	2 - 8 g/gikW-hr	1 - 4%
Increased volumetric efficiency	0 - 3.7%	0 -4.3%
Increased exhaust gas temperature	16 - 48 K	2 - 5%

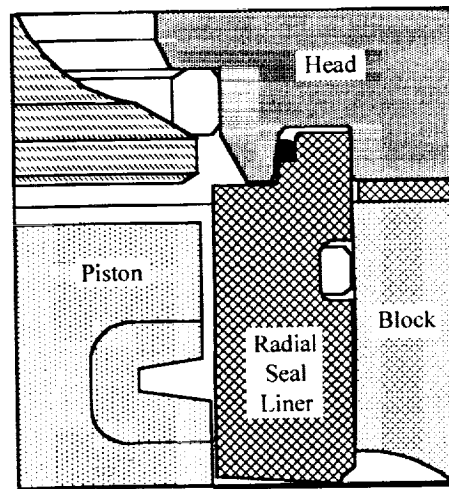
- Coiled spring turbulators inserted into the valve bridge cross drillings significantly reduced metal temperatures in an oil cooled cylinder head.
- The greatest cylinder head metal temperature reductions occurred above and below the exhaust-exhaust oil drilling. The average unturbulated temperature above the exhaust-exhaust oil drilling of 300°C was reduced by 15% at an air-fuel ratio of 25:1 with turbulators. At an air-fuel ratio of 30:1, the average temperature of 266°C was reduced by 13%. The average unturbulated temperature below the exhaust-exhaust oil drilling of 380°C was reduced by 14% at an air-fuel ratio of 25:1 with turbulators. At an air-fuel ratio of 30:1, the average temperature of 338°C was reduced by 13%.
- Due to the large distance between the oil drillings and the thermocouple above the exhaust port, the use of turbulators resulted in the smallest temperature reduction above the exhaust port. The average unturbulated temperature of 337°C was reduced by 2% at an air-fuel ratio of 25:1. At an air-fuel ratio of 30:1, the average temperature of 293°C was reduced by 1%.
- The temperature reduction due to the use of the oil drilling turbulator enhances the thermal fatigue life of the LE-55 cylinder head.

### 3.8 Radial Combustion Seal Cylinder Liner

A successful cylinder liner design is one that simply and reliably seals combustion pressure while retaining bore integrity for minimal oil consumption. The cylinder liner concept for the LE-55 engine incorporates oil cooling of the block as well as a radial combustion sealing strategy.

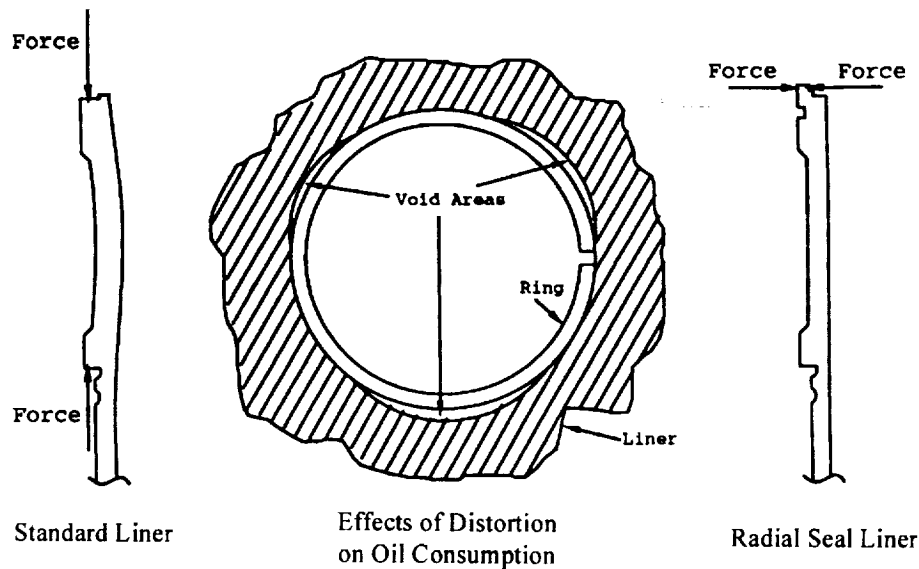
Apart from housing the cylinder kit, the cylinder liner plays an important role in controlling oil consumption. Large axial clamping forces necessary to seal a conventional cylinder cause bore distortion. Distortion in the cylinder liner bore can be detrimental to oil consumption. To counter bore distortion, a unique cylinder liner sealing concept was designed to transform the axial clamping loads to radial clamping loads.

Figure 3.8.1 illustrates the radial combustion seal cylinder liner design. The radial combustion seal design involves a top-extended cylinder liner, a grooved cylinder head, and a standard cylinder head gasket fire ring. The I.D. of the cylinder head groove is machined with a 5° taper (the groove is wider at its opening than at its bottom). When the cylinder head is placed upon the top-extended cylinder liner, the chamfer in the cylinder head groove radially forces the fire ring against the cylinder liner. The resulting combustion seal has large radial clamping forces and significantly reduced axial forces. Additionally, the radial combustion seal is augmented by cylinder pressures which work to force the fire ring into the tapered cylinder head groove. Therefore, combustion sealing is actually improved as cylinder pressure increases.



**Figure 3.8.1:** Radial combustion seal cylinder liner concept.

Figure 3.8.2 illustrates the difference in force distribution between a 1991 Cummins L10 combustion seal and the radial combustion seal. The objective of the radial combustion seal is to confine the radial clamping forces to a small region at the top of the cylinder liner. Theoretically, if the axial loads on the cylinder liner are reduced, bore distortions will be reduced, and oil consumption control will be enhanced. To verify this hypothesis, a series of tests were performed to measure cylinder liner distortion on cylinder liners installed in an engine block.



**Figure 3.8.2:** Standard cylinder liner versus radial combustion seal cylinder liner force comparison and their effects on bore distortion.

### 3.8.1 Bore Distortion Testing

An Incometer was used to measure bore distortion of the cylinder liner. The Incometer is capable of making bore measurements at different levels along the cylinder axis and at different angles around the cylinder bore. From the Incometer measurements it is possible to determine actual bore distortion and calculate an average or RMS distortion over all or part of the cylinder liner.

In previous bore distortion tests a torque plate was used in place of the cylinder head. Holes were bored through the plate to allow the Incometer to be installed from above. For this investigation, however, a cylinder head was used instead of a torque plate since it was thought that the torque plate could not truly duplicate the complicated clamping loads of a cylinder head. A holding fixture was fabricated to support the Incometer from the crankshaft main bearing journals with the engine block inverted. In this way, it was possible to have the cylinder head and main bearing caps in place and torqued to specification while making measurements with the Incometer.

A statistical design of experiments was used to identify the effects of various factors on bore distortion. Three different head bolt clamp loads were tested: 100%, 75%, and 50% load. The effects of the fire ring were also included by testing with two different diameter fire rings and no fire ring. Two cylinder heads were tested, the 1991 Cummins L10 cylinder head modified for a single cylinder engine and the LE-55 cylinder head. There was concern that there may be an interaction between the dowel in the cylinder block used to locate the cylinder head and the radial combustion seal cylinder liner which also acts as a dowel for the cylinder head. As a result, tests were made with and without the cylinder block dowel.

The bore distortion testing served a dual purpose. Primarily, the tests were used to compare the distortions of the radial combustion seal cylinder liner to that of the 1991 Cummins L10 cylinder

liner. Secondly, the tests were used to investigate the root causes of cylinder liner distortion. Identifying the root causes required an examination of the magnitude and order of the distortions.

Figure 3.8.3 shows the RMS distortion in the upper half of the two cylinder liners investigated. It can be seen that the distortion of both cylinder liners is much greater with the cylinder head torqued onto the engine block than without. The radial combustion seal cylinder liner and the conventional cylinder liner have nearly the same magnitude of distortion in the upper half of the cylinder liner with the cylinder head bolted on.

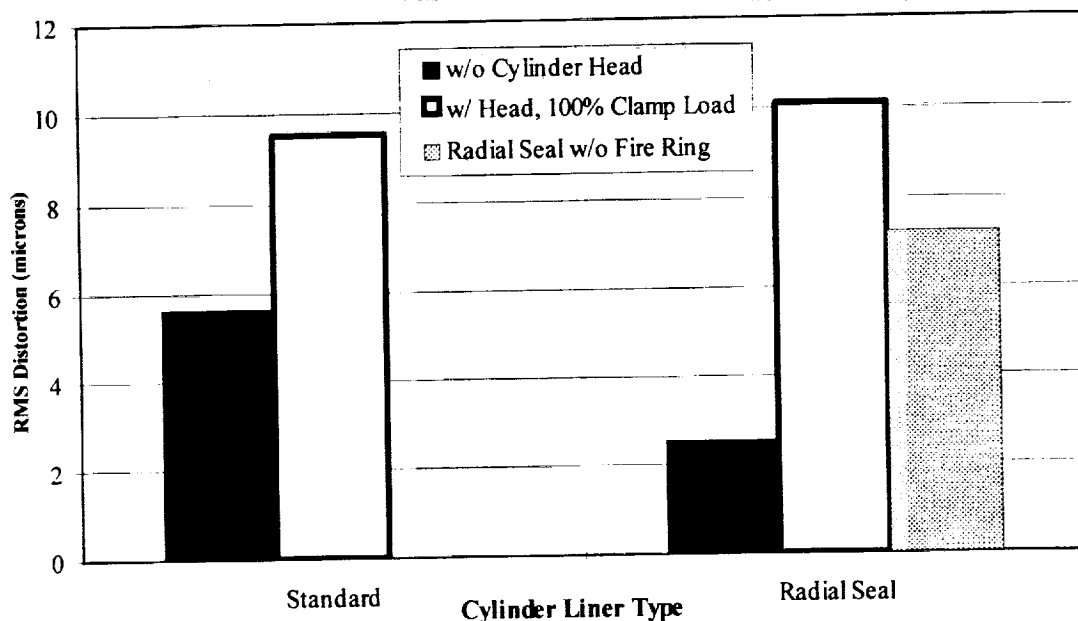


**Figure 3.8.3:** RMS distortion comparison between a 1991 Cummins L10 cylinder liner and a radial combustion seal cylinder liner at the upper region of the bore.

The primary contact surface between the cylinder head and the radial combustion seal cylinder liner is through the fire ring. Other locations where the cylinder liner contacts the cylinder head and cylinder block are "slip" fits and are not intended to cause distortion. As shown in Figure 3.8.3, however, the bore of the radial combustion seal cylinder liner distorts when the cylinder head is bolted down without the fire ring. This distortion indicates an interaction between the liner and block or head other than through the fire ring.

The most significant difference between the 1991 Cummins L10 cylinder liner and the radial combustion seal cylinder liner is the RMS distortion in the lower half of the cylinder liner. The radial combustion seal cylinder liner has significantly more distortion than the 1991 Cummins L10 cylinder liner, as shown in Figure 3.8.4. In this case, however, the distortions of the radial combustion seal cylinder liner without the fire ring are about the same as the case without the cylinder head. The interaction between the cylinder head or cylinder block and the cylinder liner



that was observed in the upper portion of the cylinder liner is not observed in the lower portion of the cylinder liner.

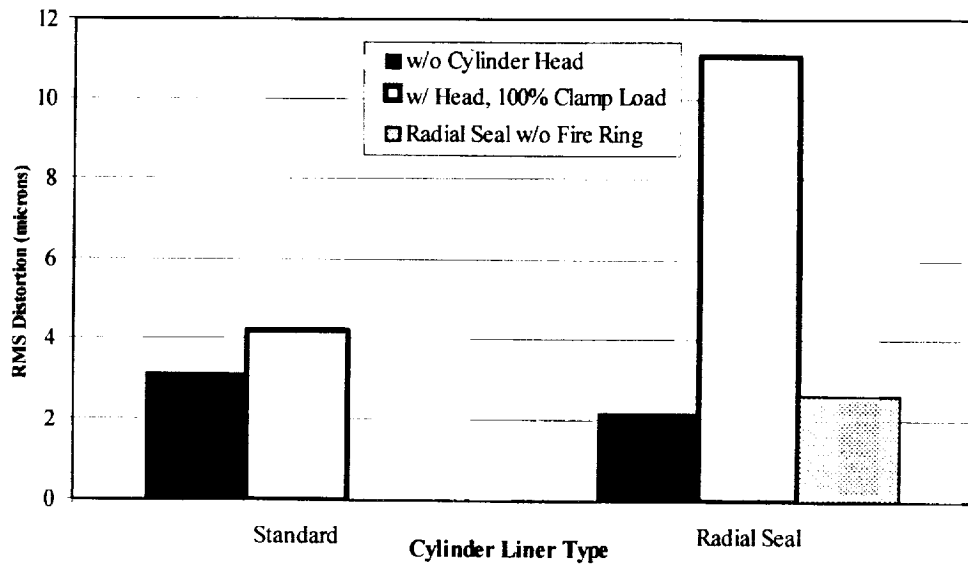


**Figure 3.8.4:** RMS distortion comparison between a 1991 Cummins L10 cylinder liner and a radial combustion seal cylinder liner at the lower region of the bore.

Based on the statistical test matrix, the largest contributor to the distortion of the lower half of the radial combustion seal cylinder liner is due to the fire ring. In fact, without the fire ring, the lower distortion is equivalent to the distortion without the cylinder head (Figure 3.8.4). It can be concluded from these tests that the interaction between the fire-ring and the cylinder head and cylinder liner causes the distortion at the top of the cylinder liner to be transmitted to the lower half of the radial combustion seal cylinder liner.

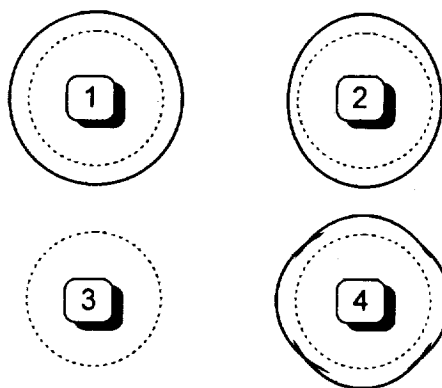


**Figure 3.8.5:** Harmonic orders of distortion.

The harmonic order of the distortions (Figure 3.8.5) in the 1991 Cummins L10 and the radial combustion seal cylinder liner were also characterized to assess the effect of the radial combustion seal cylinder liner. The software for the Incometer incorporates a Fourier analysis to determine the magnitude of each mode of distortion. It was found that the lower order distortions (modes 0-5) show no statistically significant difference between the 1991 Cummins L10 and radial combustion seal cylinder liner. However, at the higher orders (modes 6-8) there is a significant difference. The 1991 Cummins L10 cylinder liner has larger distortions of the higher order than the radial combustion seal cylinder liner. Piston rings cannot conform to the higher order distortions as well as they are able to conform to the lower order distortions. This nonconformity may cause greater oil consumption with the 1991 Cummins L10 cylinder liner than with the radial combustion seal cylinder liner.

Results from this analysis indicate that the overall magnitude of distortions in the radial seal liner will not be lower than the 1991 Cummins L10 cylinder liner. However, the harmonic order of the distortions will be lower. Since the ring can conform better to lower order harmonics in the cylinder liner, a benefit in oil consumption might be expected.

### **3.8.2 Sealability Testing**

The concept behind the radial seal cylinder liner allows for lower clamping loads to maintain similar sealing characteristics. Sealability tests were performed to help understand how the axial clamping load affected the sealing characteristics of the radial seal cylinder liner.

Sealability testing work was carried out at Fel-Pro. Two fixtures were constructed. One fixture simulated the cylinder block and held the cylinder liner, while the other fixture was comprised of a plate with a machined groove to simulate the cylinder head. A dummy piston was used to seal the gases and a mass flow transducer was used to monitor air leakage. The radial seal cylinder liner was mounted in the fixtures. An MTS machine was used to load the cylinder head fixture. In this manner it was possible to vary the load on the cylinder head, simulating different torque loads on the cylinder head bolts. It was also possible to vibrate the cylinder head fixture to simulate dynamic loads. For all tests the cylinder was pressurized to 13.8 MPa with nitrogen gas. Tests were run at both ambient and elevated (150°C) temperatures.

The fire ring in the 1991 Cummins L10 cylinder head gaskets requires approximately 700 kN/m to seal combustion pressures. Sealability tests showed the radial combustion seal could seal effectively down to clamping loads as low as 263 kN/m. At 175 and 219 kN/m substantial leakage was observed. The monitoring period for all of the tests was between 15 minutes and 1 hour. Testing at 150°C showed no gas leakage with clamp loads of 263 kN/m. These results indicate the use of the radial combustion seal cylinder liner requires 60% lower clamping loads to achieve static sealing characteristics similar to the 1991 Cummins L10 cylinder liner.

The concept behind the radial combustion seal cylinder liner is to seal the combustion gases with the wire fire ring. There should be no direct contact between the cylinder head and the cylinder liner, except through the fire ring. It was desired to determine whether the sealing action was due to the fire ring or inadvertent contact between the cylinder head and cylinder liner. The sealability test fixture was assembled without the fire ring and pressurized. The leak rate observed without

the fire ring was high for all clamping loads tested. This indicated that the seal is accomplished through the fire ring.

Dynamic sealability tests were also performed at room temperature and at 150 °C. In these tests, the cylinder head fixture was vibrated by 0.017 to 0.018 mm at 16 and 32 Hertz. The cylinder head was loaded to a clamping load of 350 kN/m (approximately 150 kN) and the cylinder pressurized to 13.8 MPa. No gas leakage was observed during these tests.

Results of the sealability testing showed no gas leaks in the static and dynamic tests at ambient and elevated temperatures. Based on these tests it was believed that the radial combustion seal cylinder liner would be able to seal combustion pressures in an operating engine at bolt loads 50% less (350 kN/m) than the 1991 Cummins L10 cylinder liner.

### 3.8.3 Cooling Jacket Heat Transfer Enhancement

Using engine oil as a cooling medium for the cylinder liner presented challenges due to the thermal property differences between oil and water. Oil has a higher specific heat than water, is more viscous than water and operates at a higher temperature than water. These characteristics make using oil as a coolant more difficult.

As with the cylinder head, increasing heat transfer from the cylinder liner to the cooling oil in the cylinder block was examined. Unlike the cylinder head oil drillings, the water jacket on the 1991 Cummins L10 cylinder liner would not allow for flow turbulence. To enhance the heat transfer within the water jacket, performance of extended heat transfer surfaces or fins was investigated.

Cylinder liners were prepared for bench testing by machining separate heat transfer fin geometries (small circumferential, larger circumferential, small axial and large axial) into their respective cooling jackets. Of the heat transfer fin geometries evaluated, the greatest increase in heat transfer was demonstrated with the large axial fins. Figure 3.8.6 compares the heat transfer coefficients for different geometries. Large axial fins increased heat transfer by a factor of 1.7.

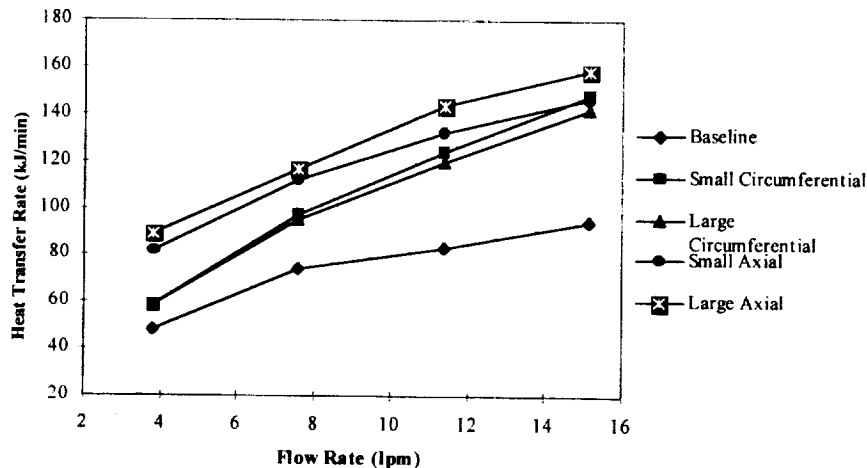


**Figure 3.8.6:** Heat transfer rate comparison for cylinder liner heat transfer enhancements.

After bench testing, the cylinder liner with the large axial, water jacket heat transfer fins were placed on test in the single cylinder L10 engine (SCE L10). Extensive instrumentation was employed on the SCE L10. The cylinder liners were instrumented with 12 thermocouples each for measuring metal temperatures. The thermocouples were placed at three axial locations: first ring top reversal, second ring top reversal and first ring bottom reversal. Four thermocouples were installed at each axial location and space 90° apart around the circumference of the cylinder liner. Thermocouple locations are illustrated in Figure 3.8.7.

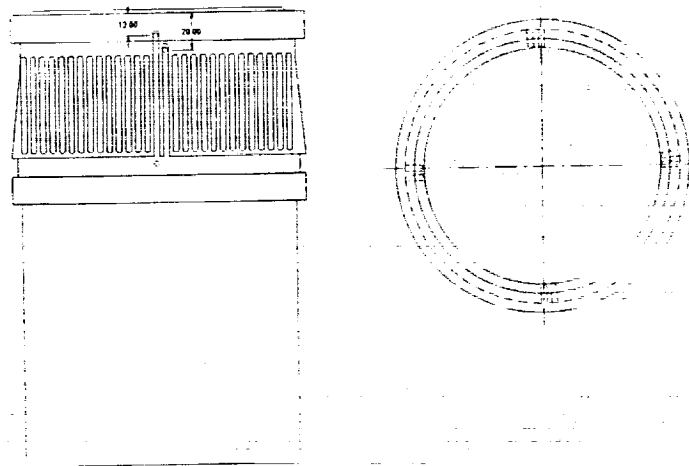


**Figure 3.8.7:** Thermocouple locations on the cylinder liner with large axial cooling jacket fins. All dimensions in millimeters.

Finned and standard cylinder liners were evaluated in SCE L10 tests. The effect of two coolants (50/50 ethylene glycol - water mixture and 15W-40 oil) and coolant flow rate on cylinder liner metal temperatures was also investigated. To properly evaluate the effects of the heat transfer fins, several engine operating parameters were held constant as shown in Table 3.8.1.

**Table 3.8.1:** Engine operating parameters held constant for cylinder liner heat transfer fin evaluation

Parameter	Setpoint
Engine Speed	1500 rpm
Injection timing (TVC)	28°
Intake manifold temperature	43°C
Fuel in temperature	40°C
Oil rifle temperature	116°C
Cylinder block coolant out temperature	91°C - 50/50 glycol / 116°C - oil
Cylinder block coolant flow rate	39.3 lpm
Cylinder head coolant flow rate	12.5 lpm

Two air-fuel ratios were run: 25:1 and 30:1. In order to obtain the average temperature at each peak cylinder pressure and air-fuel ratio, the four thermocouples at each axial location on the cylinder liner were averaged together.

High speed cylinder pressure data were collected to determine gross indicated mean effective pressure (GIMEP) and heat release. A needle lift sensor was used to monitor the start of fuel injection. This instrumentation allowed for precise control and monitoring of engine operation.

Test results showed at first ring top reversal and an air fuel ratio of 25:1 that heat transfer fins reduce the cylinder liner temperature by an average of 10% with the 50/50 glycol coolant and by a average of 7% with oil as coolant as shown in Figure 3.8.8. At an air-fuel ratio of 30:1, heat transfer fins reduced the cylinder liner temperature by an average of 8% with the 50/50 glycol coolant and by an average of 7% with oil as coolant as shown in Figure 3.8.9.

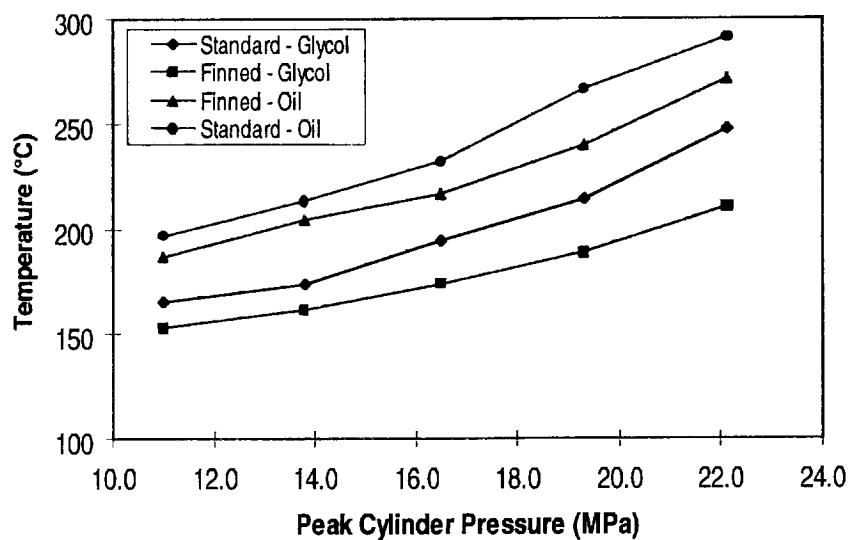


**Figure 3.8.8:** Cylinder liner temperatures at first ring top reversal, 25:1 air-fuel ratio.

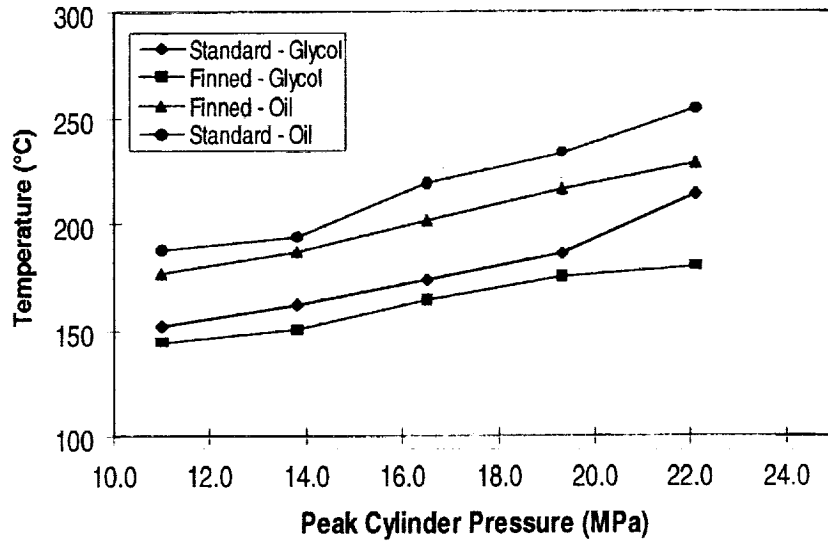


**Figure 3.8.9:** Cylinder liner temperatures at first ring top reversal, 30:1 air-fuel ratio.

At second ring top reversal and an air-fuel ratio of 25:1, heat transfer fins reduced the cylinder liner temperature by an average of 12% with 50/50 glycol as coolant and by an average of 3% with oil as coolant as shown in Figure 3.8.10. At an air-fuel ratio of 30:1, heat transfer fins reduced the cylinder liner temperature by an average of 9% with 50/50 glycol as coolant and by an average of 4% with oil as coolant as shown in Figure 3.8.11.

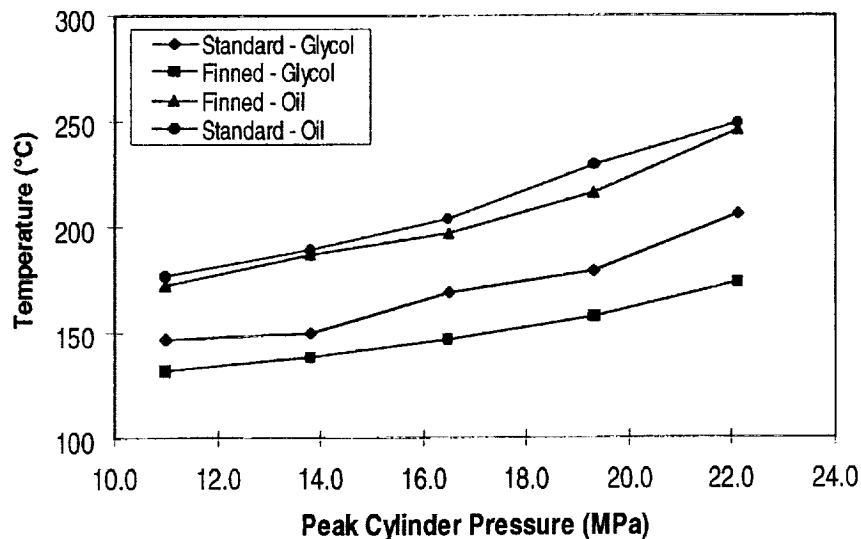


**Figure 3.8.10:** Cylinder liner temperatures at second ring top reversal, 25:1 air-fuel ratio.

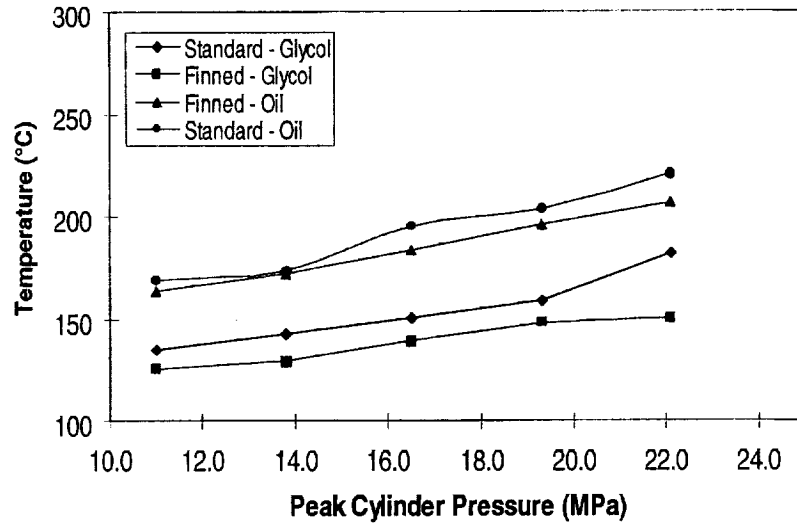


**Figure 3.8.11:** Cylinder liner temperatures at second ring top reversal, 30:1 air-fuel ratio.

At first ring bottom reversal and an air-fuel ratio of 25:1, heat transfer fins reduced the cylinder liner temperature by an average of 7% with 50/50 glycol as coolant. However, heat transfer fins increased the cylinder liner temperature by an average of 6% with oil as coolant as shown in Figure 3.8.12. At an air-fuel ratio of 30:1, heat transfer fins reduced the cylinder liner temperature by an average of 6% with 50/50 glycol as coolant. However, heat transfer fins increased the cylinder liner temperature by an average of 5% with oil as coolant as shown in Figure 3.8.13. It is possible that the fins affected the oil coolant flow at the first ring bottom reversal location causing the temperature increase.

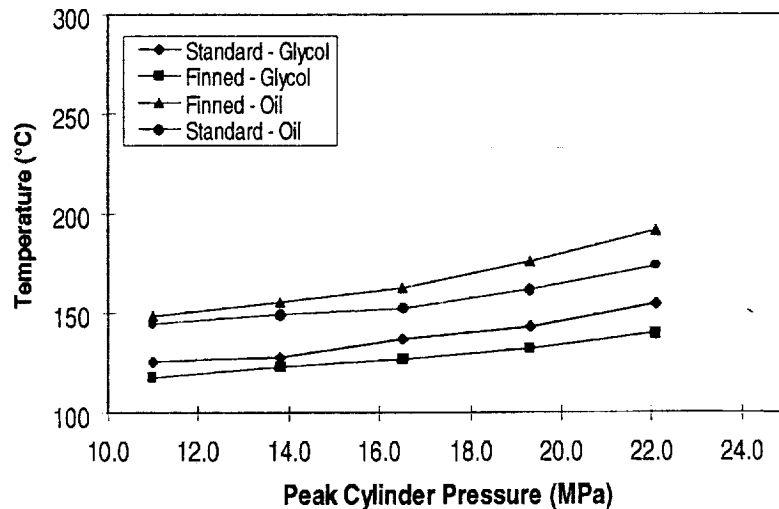


**Figure 3.8.12:** Cylinder liner temperatures at first ring bottom reversal, 25:1 air-fuel ratio.

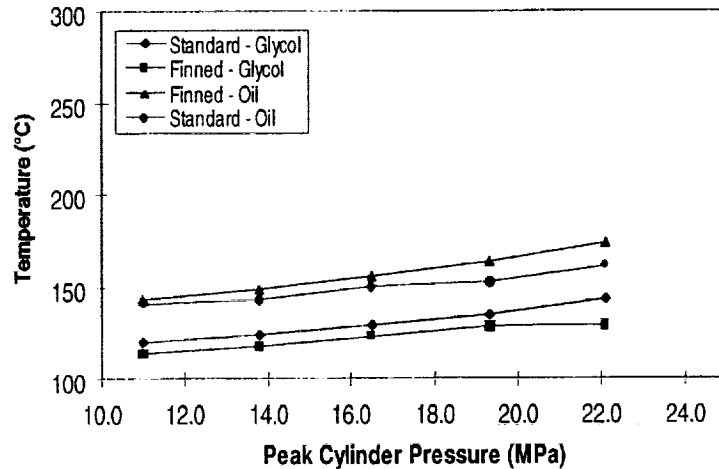


**Figure 3.8.13:** Cylinder liner temperatures at first ring bottom reversal, 30:1 air-fuel ratio.

At first ring top reversal, heat transfer fins reduced the cylinder temperature by an average of 9% with 50/50 glycol as coolant and by an average of 7% with oil as coolant. At second ring top reversal, heat transfer fins reduced the cylinder liner temperature by an average of 11% with 50/50 glycol as coolant and by an average of 4% with oil as coolant. At first ring bottom reversal, heat transfer fins reduced the cylinder liner temperature by an average of 7% with 50/50 glycol as coolant but increased the cylinder liner temperature by an average of 6% with oil as coolant. Averaging all measured locations, heat transfer fins reduced the cylinder liner temperature by an average of 9% with 50/50 glycol as coolant and 2% with oil as coolant.

The effects of oil flow rate on cylinder liner temperatures are shown in Figures 3.8.14 through 3.8.19. All temperature measurements for the figures were taken at an air-fuel ratio of 25:1

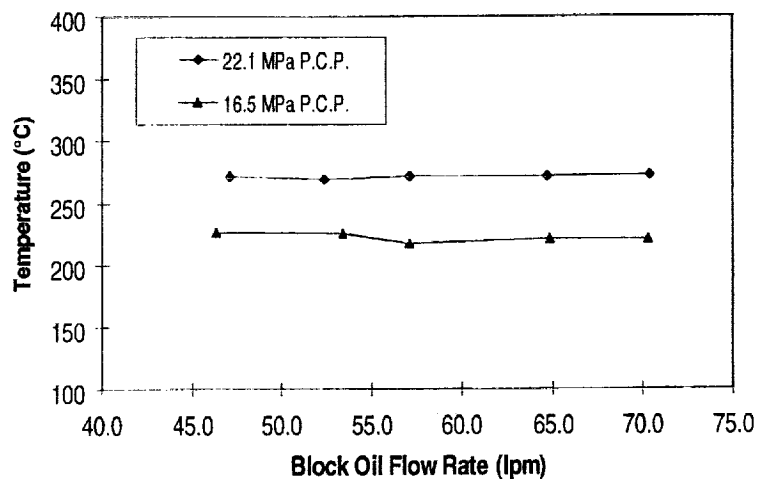


**Figure 3.8.14:** Finned cylinder liner temperatures at first ring top reversal versus coolant oil flow rate, 25:1 air-fuel ratio.



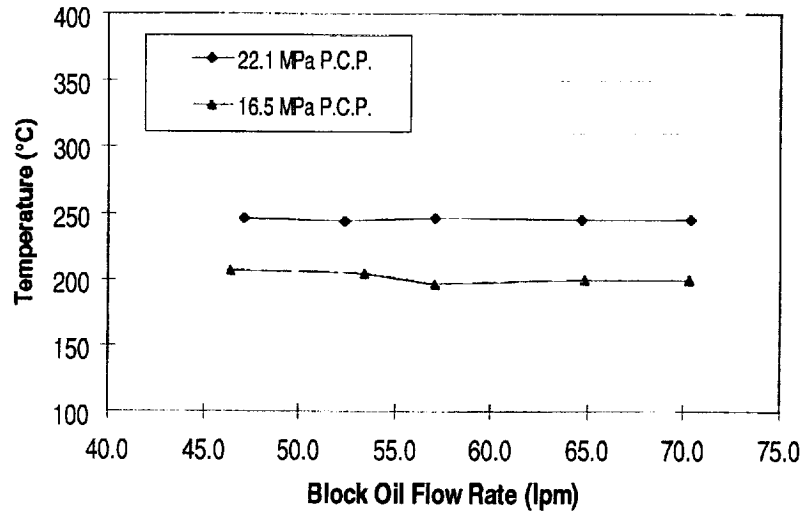


**Figure 3.8.15:** Finned cylinder liner temperatures at second ring top reversal versus coolant oil flow rate, 25:1 air-fuel ratio.

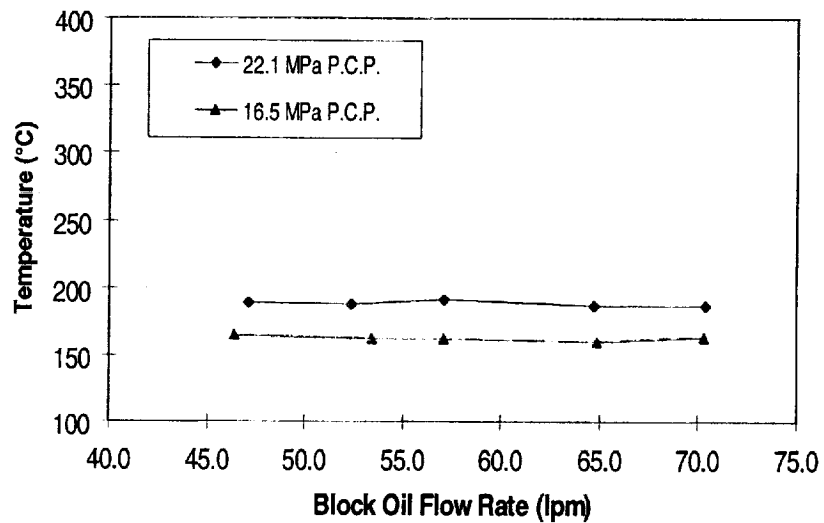


**Figure 3.8.16:** Finned cylinder liner temperatures at first ring bottom reversal versus coolant oil flow rate, 25:1 air-fuel ratio.

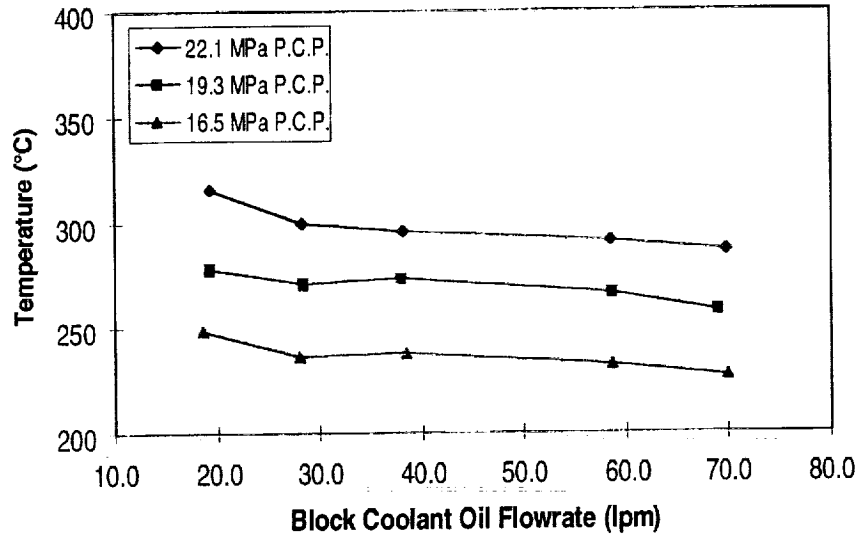


**Figure 3.8.17:** Standard cylinder liner temperatures at first ring top reversal versus coolant oil flow rate, 25:1 air-fuel ratio.

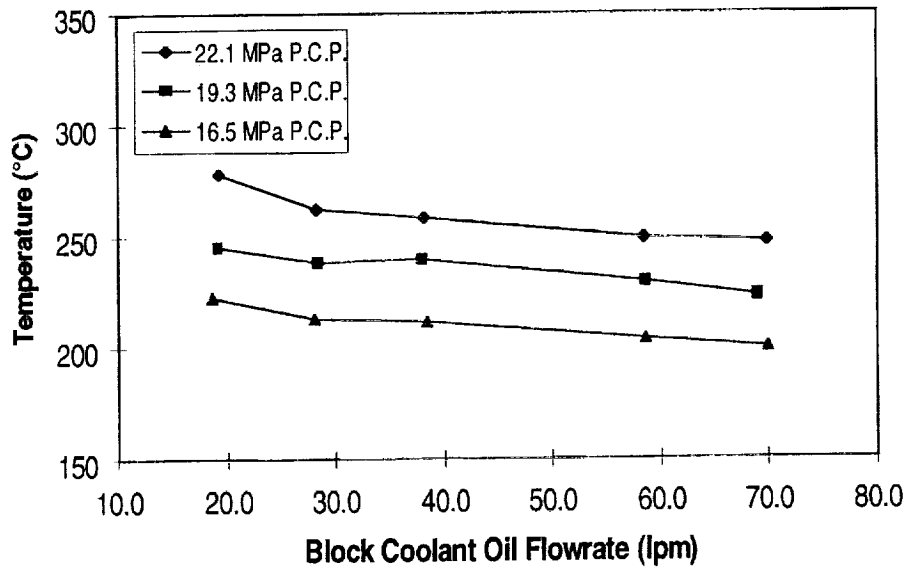


**Figure 3.8.18:** Standard cylinder liner temperatures at second ring top reversal versus coolant oil flow rate, 25:1 air-fuel ratio.

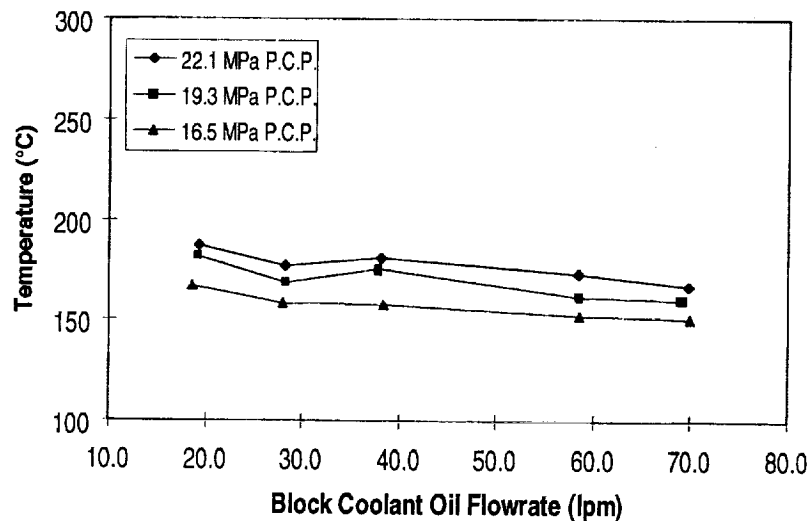


**Figure 3.8.19:** Standard cylinder liner temperatures at first ring bottom reversal versus coolant oil flow rate, 25:1 air-fuel ratio.

### 3.8.4 Conclusions - Radial Combustion Seal Cylinder Liner

- The radial combustion seal cylinder liner had bore distortion in the upper half of the cylinder liner that are similar to the 1991 Cummins L10 cylinder liner. The radial combustion seal cylinder liner had larger distortion than the 1991 Cummins L10 cylinder liner in the lower half of the cylinder liner.
- The distortion in the radial combustion seal cylinder liner were of a lower harmonic order than in the 1991 Cummins L10 cylinder liner. The lower order harmonic distortions in the radial combustion seal cylinder liner might help to reduce oil consumption.
- Sealability tests predicted that the radial combustion seal cylinder liner would effectively seal combustion pressures at 50% lower bolt loads than the 1991 Cummins L10 cylinder liner. Lower bolt loads could result in lower bore distortion.
- The use of large axial heat transfer fins increased the heat transfer to the coolant by 1.7 times.
- A cylinder liner with large axial heat transfer fins machined into the cooling jacket region showed marked metal temperature reduction over a cylinder liner with no heat transfer fins. The fins reduced cylinder liner temperatures by an average of 9% with 50/50 glycol as coolant (91°C) and 7% with oil as coolant (116°C) at the first ring top reversal location. At the second ring top reversal location, heat transfer fins had an average temperature reduction of 11% with 50/50 glycol as coolant (91°C) and 4% with oil as coolant (116°C). Heat transfer fins had an average temperature reduction of 7% with 50/50 glycol as coolant (91°C) at the top ring reversal location. Heat transfer fins increased cylinder liner temperatures by an average of 6% with oil as coolant (116°C) at the top ring bottom reversal location.
- Oil coolant flow rate had a minimal effect on temperature reduction with the finned cylinder liner. However, with the cylinder liner with no fins, increasing the oil coolant flow rate from 19 lpm to 28 lpm resulted in temperature reductions of 4%, 4% and 6% at the first ring top reversal, the second ring top reversal and the first ring bottom reversal locations, respectively.

### 3.9 Alternative Combustion Seals

With increasing demands on engine performance, engine components are required to have greater durability and to perform under more stressful conditions. Alternative combustion seals were investigated to determine their capability to handle high peak cylinder pressures and temperatures. With reliable and durable combustion seals, engine performance and longevity can be increased.

#### 3.9.1 C-Ring Seal and Omega Seal

As an alternative to the radial combustion seal (See Section 3.8 **Radial Combustion Seal Cylinder Liner**) two active combustion seal designs were evaluated: a C-Ring combustion seal and an Omega combustion seal. Figures 3.9.1 and 3.9.2 illustrate the geometry of the C-Ring combustion seal and the Omega combustion seal, respectively.

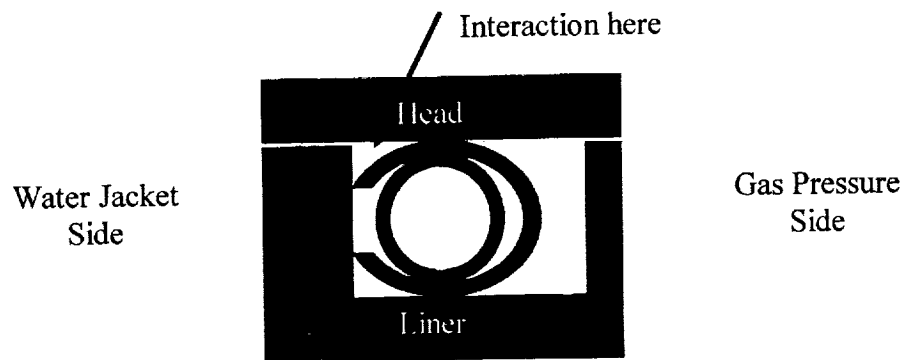


**Figure 3.9.1:** Installed C-Ring combustion seal geometry.

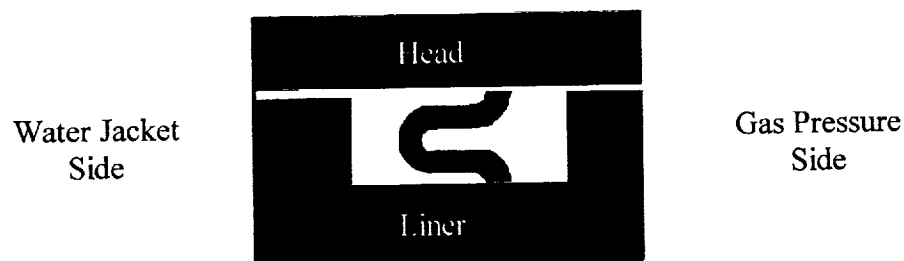


**Figure 3.9.2:** Installed Omega combustion seal geometry.

The characteristic of an active combustion seal is any movement by the cylinder head will cause a corresponding movement by the combustion seal. The C-Ring combustion seal seals by the spring action of the seal geometry. The Omega combustion seal seals by the spring action of the seal geometry and is augmented by in-cylinder gas pressure. Both seals were design to crush down 14% when installed in an engine. Table 3.9.1 lists other pertinent data with regard to each combustion seal.

**Table 3.9.1: C-Ring and Omega combustion seal data**

	C-Ring Seal	Omega Ring Seal
Manufacturer	Advanced Products	Parker-O-Seal Division
Jacket Material	Alloy 718	Inconel 718
Coating	Nickel	Soft nickel
Spring Material	Alloy X-750	na
O.D.	139.7 mm	137.2 mm

### 3.9.2 Assembly and Engine Test

The seals were evaluated over steady state and thermal cycle tests in a single cylinder research engine. Steady state tests were performed at 20.7 MPa peak cylinder pressure at an air-fuel ratio of 30:1. The thermal cycle tests consisted of operating the engine at the steady state point for three minutes and at a no-load point for three minutes for a six minute cycle. A minimum of four hours of steady state testing and a minimum of 16 hours of thermal cycle testing (160 cycles) were required to pass the evaluation. Tests were conducted with standard head bolt torques (217 N-m +90°) and reduced head bolt torques (217 N-m and 136 N-m).

Since it was unknown how the C-Ring combustion seal would perform at reduced head bolt torques, testing was started at standard head bolt torques (217 N-m +90°) and progressed to reduced head bolt torques. Rough calculations were performed to determine the lowest theoretical head bolt torque where the clamping load would equal the gas pressure force. The formula used to calculate clamping load from head bolt torque was:

$$\text{Clamping Load} = 0.2 \times \text{torque} \times d_{\text{bolt}} \quad 3.9.1$$

where  $d_{\text{bolt}}$  is the bolt diameter.

At a head bolt torque of 136 N-m, the clamping load on the cylinder head just exceeded the gas pressure force at 22.1 MPa peak cylinder pressure. Testing of the Omega combustion seal was started at a reduced head bolt torque of 136 N-m.

In steady state tests, the C-Ring combustion seal satisfactorily performed at head bolt torques of 217 N-m +90° and 217 N-m. At a head bolt torque of 136 N-m, the C-Ring combustion seal leaked. During thermal cycle testing, the C-Ring combustion seal performed well at the standard head bolt torque of 217 N-m +90°. However, at 217 N-m, the C-Ring combustion seal leaked. The C-Ring was not thermal cycle tested at 136 N-m as shown in Table 3.9.2.

**Table 3.9.2:** Test results of C-Ring combustion seal - 20.7 MPa peak cylinder pressure

Head Bolt Load	Steady State	Thermal Cycle
136 N-m	Seal leak	Not tested
217 N-m	✓	Seal leak
217 N-m +90°	✓	✓

The Omega combustion seal performed adequately in steady state tests at a reduced head bolt torque of 136 N-m. Since the Omega combustion seal did not leak at this head bolt torque, the seal was not tested at 217 N-m nor 217 N-m +90°. In thermal cycle tests, the Omega combustion seal leaked after 3.4 hours at a head bolt torque of 136 N-m. However, the Omega combustion seal satisfactorily performed during thermal cycle tests at a head bolt torque of 217 N-m. Therefore, the Omega combustion seal was not tested at 217 N-m +90° as shown in Table 3.9.3.

**Table 3.9.3:** Test results of Omega combustion seal - 20.7 MPa peak cylinder pressure

Head Bolt Load	Steady State	Thermal Cycle
136 N-m	✓	Seal leak
217 N-m	Not tested	✓
217 N-m +90°	Not tested	Not tested

### 3.9.3 Conclusions - Alternative Combustion Seals

- The Omega combustion ring performed well at a reduced head bolt torque of 136 N-m in steady state tests. The seal leaked at 136 N-m head bolt torque during thermal cycle tests. The Omega combustion seal satisfactorily performed during a 16 hour thermal cycle test at a reduced head bolt torque of 217 N-m.
- The C-Ring combustion seal leaked at a reduced head bolt torque of 136 N-m during steady state tests. The seal also leaked at a reduced head bolt torque of 217 N-m during thermal cycle tests. The C-Ring combustion seal performed satisfactorily at the standard head bolt torque (217 N-m +90°).
- It was thought that the C-Ring combustion seal failed before the Omega combustion seal due to the manner in which the C-Ring is seated into the groove (gland) in the cylinder liner. When the C-Ring combustion seal was installed into the cylinder liner groove, it fit quite snugly around the O.D. of the cylinder liner groove. It is possible that the interaction between the ends of the seal gap and the groove O.D. restricted the seal's ability to flex and remain resilient. When the cylinder head was torqued down and the seal crushed, the forces between the cylinder liner groove O.D. and the C-Ring may have increased. It was hypothesized that during engine operation the aforementioned forces would further increase as the seal heated up and expanded into the cylinder liner groove.

### **3.10 Powdered Metal Cylinder Liner**

Friction and wear are important issues in cylinder liner design. For the LE-55 concept engine, various powdered metal (PM) cylinder liner materials were examined for their tribological properties. The powdered metal material can improve the wear characteristics and reduce friction which should help the cylinder kit achieve and withstand the conditions imposed by the operating requirements of the LE-55.

The evaluation of PM materials concentrated on identifying materials for use in cost-effective, high durability cylinder liners as part of an optimized tribological system. The PM technology lends itself to optimizing a cylinder liner that will meet many different physical requirements. The goal of this test program was to find a material that would give an order of magnitude reduction in piston ring and cylinder liner wear compared to conventional materials (electroplated hard chromium rings and pearlitic grey cast iron liners). Also, the material should maintain a low friction coefficient.

#### **3.10.1 Material Selection**

PM cylinder liners are made from blend of metal powders that optimize mechanical and tribological properties. The process and methods of using a cold isostatic dry bag press for producing cylinder liners has been in the development for about ten years. The powders are compacted into the final shape and sintered. After sintering the cylinder liners are thermally or isostatically sized to give as accurate a shape as possible.

It is well known that PM materials have porosity. The shape, size and amount of pores can be controlled by the type of powder, compaction pressure, sintering procedure and type of alloying elements. The pore system can serve as a natural reservoir for the lubricant oil. This will serve to retain oil on the cylinder walls for engine startup. In many of the PM materials available for cylinder liners it is possible to have different solid lubricants in the pore system. This has the potential of reducing friction and minimizing metal-to-metal contact. This becomes most important when there is no oil or very thin layer of oils at piston top dead center.

One of the PM cylinder materials examined, TS56, has a fine pearlite matrix with a micro hardness of 250 to 350 MHV 0.10. The structure is strengthened by phosphorus and copper in solid solution. In comparison to high phosphorus gray cast iron, PM materials do not form free steadite. The mechanical properties are superior to gray cast iron, especially tensile strength, yield strength and modulus of elasticity. TS56 can be used where reduced cost is important.

A TS62 material containing alloying materials Ni and Mo was examined in order to build a high strength and wear resistance matrix. This material contains a structure of martensite, pearlite and bainite. The tensile strength is approximately 650 MPa and the modulus of elasticity is over 146,000 MPa. This material can contain solid lubricant to help lower friction.

TS29, a high efficiency PM material with higher surface hardness and stiffness, was also studied. The tribological properties of TS29 are superior to those of TS56 and TS62. The structure of TS29 consists of a fine pearlite strengthened with alloying metals. A high alloyed carbide

containing structure is embedded in the pearlite which gives TS 29 excellent high temperature wear properties. TS29 can be fabricated with different solid lubricants depending on the application. Table 3.10.1 lists a comparison of the PM materials tested.

**Table 3.10.1:** Comparison of mechanical properties of gray cast iron, TS29, TS56 and TS62 cylinder liner materials. Values listed are typical for the materials studied

Material	Density (g/cm <sup>3</sup> )	Tensile Strength (MPa)	Elongation (%)	Modulus of Elasticity (MPa)	Macro Hardness (HV10)	Micro Hardness (HV0.1)
Gray Iron	7.2	300	<1	100,000	210	
TS56	6.9	600	1.2	140,000	170	250-350
TS62	6.9	650	1.5	140,000	195	250-500
TS29	6.8	550	1	130,000	210	300-500

Microstructures of the PM materials were obtained from the suppliers. All the materials investigated were largely pearlitic. However, the TS62 and TS29 grades contained some martensite. The TS56 material contained grain boundary carbide/phosphide networks. The TS29 grade, a mixture of 20% M2 tool steel with an iron based powder, contained regions of essentially unalloyed M2 tool steel with a fine carbide dispersion (primarily WC). One of the differences between the PM materials and the cast irons was the lower carbon content, typically 1%, of the former. Thus, PM materials contained much less free graphite than the cast irons. The chemical composition of various cylinder liner materials is listed in Table 3.10.2.

**Table 3.10.2:** Percent composition by weight for gray cast iron and various PM cylinder liner materials

Material	C	Si	Mn	P	S	Cu	Ni	Mo	Cr	V	Other
Gray Iron	3.2 to 5.5	1.8 to 2.6	0.5 to 0.8	0.15 max	0.1 max	0 to 1.0	0 to 0.5	0 to 0.5	0.2 to 0.8		
TS56	1.1			0.45							
TS62	0.9		0.6		0.4	1.6	4.0	0.5			
TS62-1	0.9		0.6		0.4			1.0			
TS29	1.4	0.06	0.7		0.4	2.0		1.0	0.8	0.4	W: 1.3
TS29-6	1.2		0.6		1.0	0.4					M2A 1203: 20
TS29-7	1.2		0.6		1.0	0.4					M2: 20



### 3.10.2 Wear Testing

Wear tests were performed on a Cameron Plint reciprocating wear tester. The test conditions were chosen to represent the ring/cylinder liner engine environment near to the top ring reversal position. Liner samples were tested against one of the advanced piston ring coatings, a High Velocity Oxy-Fuel Chrome Carbide/Nichrome coating. The test time was six hours and the normal load was 225 N. The lubricant (CE/SF 15W-40) was dripped onto the samples at a rate of one drip every ten seconds. Fresh oil was used with the system heated to 200°C and 350°C. Sooted oil was tested at 200°C.

Common practice in the diesel and automotive industries is to apply a thin coating of manganese phosphate (Lubrite) to cylinder liners to facilitate break-in of the engine. The Lubrite process was not applied to the cylinder liner materials investigated. All data reported here refer to uncoated cylinder liner samples.

The results of the wear tests are shown in Figures 3.10.1, 3.10.2 and 3.10.3. Figure 3.10.1 shows normalized average cylinder liner wear for each condition and material tested. It can be seen that the PM materials reduced wear by more than 50%. The best PM candidate (TS29-6) showed wear less than 10% of the standard gray iron cylinder liner. The measured ring wear was about the same for all the PM candidates as shown in Figure 3.10.2. Figure 3.10.3 shows a small decrease in friction with the powder metal materials.

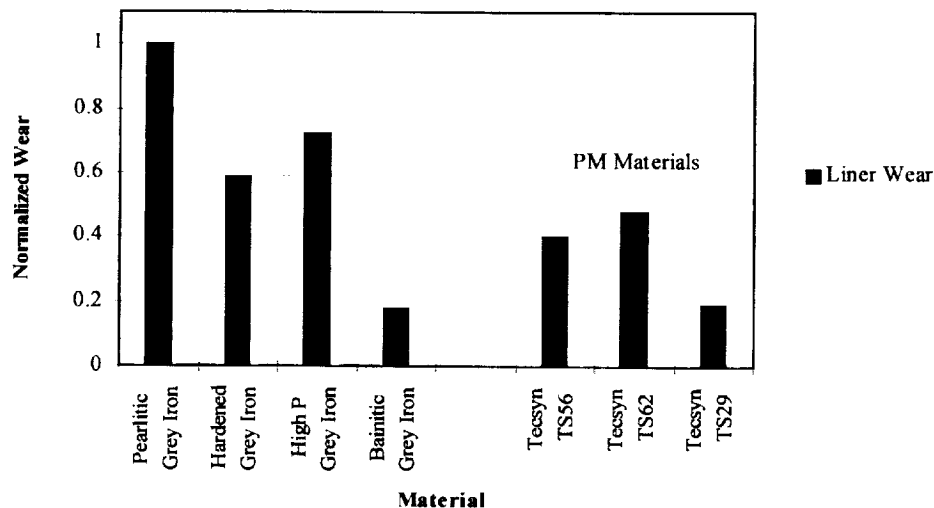


**Figure 3.10.1:** Normalized average wear for various cylinder liner materials.

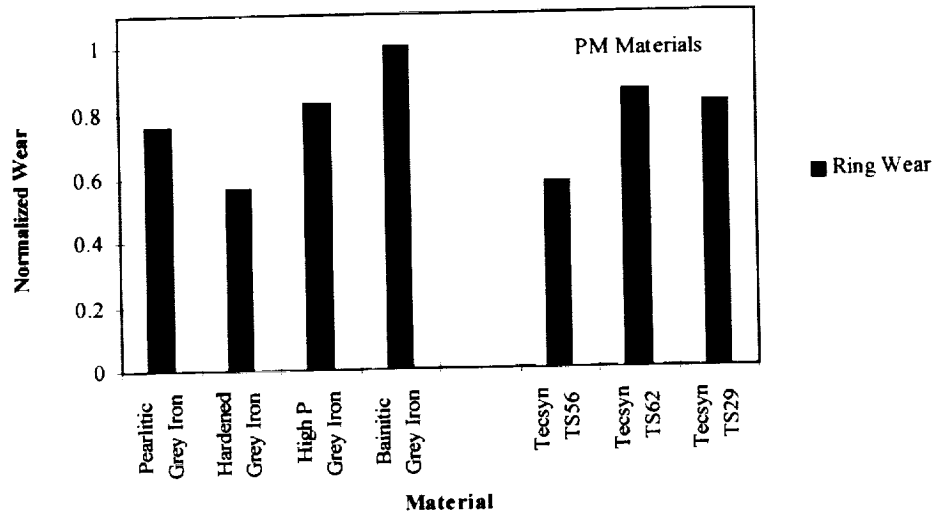


**Figure 3.10.2:** Normalized average ring wear tested against various cylinder liner materials.

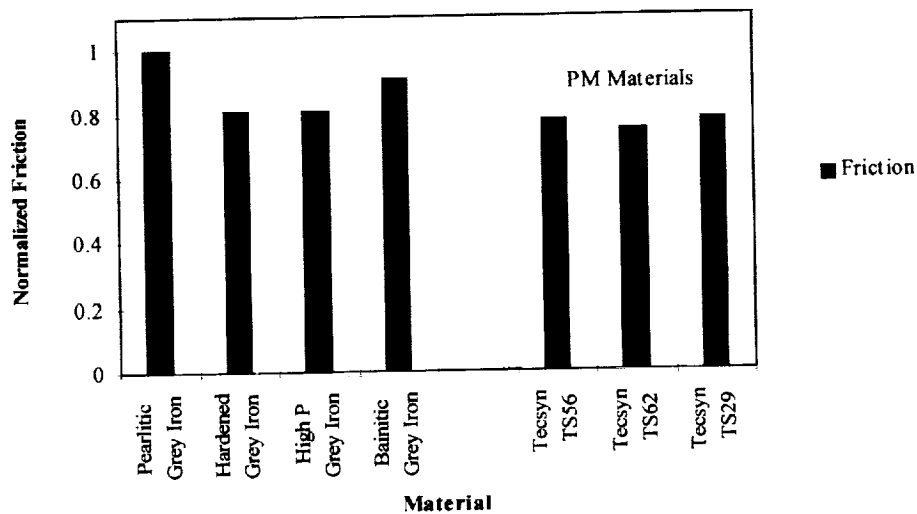


**Figure 3.10.3:** Normalized average friction for various cylinder liner materials.

Figures 3.10.4, 3.10.5, and 3.10.6 illustrate the effects of oil conditions on ring wear coefficients for various cylinder liner materials. As shown in Figure 3.10.4, the powdered metal cylinder liner materials have little effect on wear in fresh oil at 200°C. Wear test were also conducted on various cylinder liner materials in fresh oil at 350°C and sooted oil at 200°C. The results from these tests are illustrated in Figures 3.10.5 and 3.10.6.

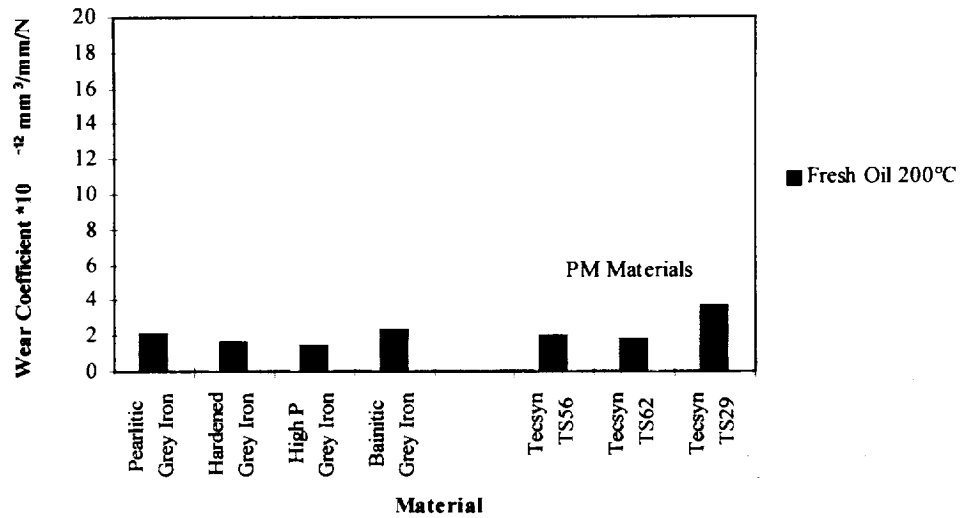


**Figure 3.10.4:** Ring wear coefficient for various cylinder liner materials in fresh oil at 200°C. Rings coated with HVOF Cr<sub>3</sub>C<sub>2</sub> - 20% NiCr.

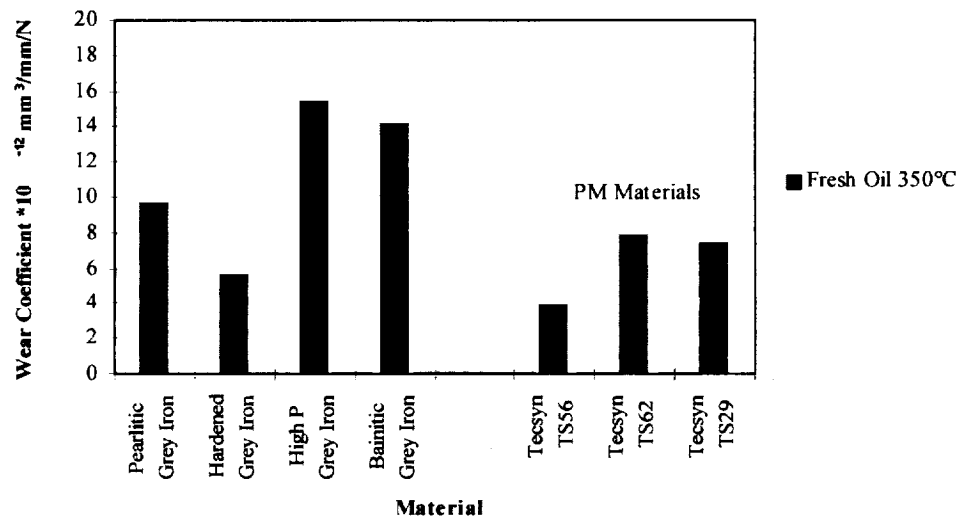


**Figure 3.10.5:** Ring wear coefficient for various cylinder liner materials in fresh oil at 350°C. Rings coated with HVOF Cr<sub>3</sub>C<sub>2</sub> - 20% NiCr.

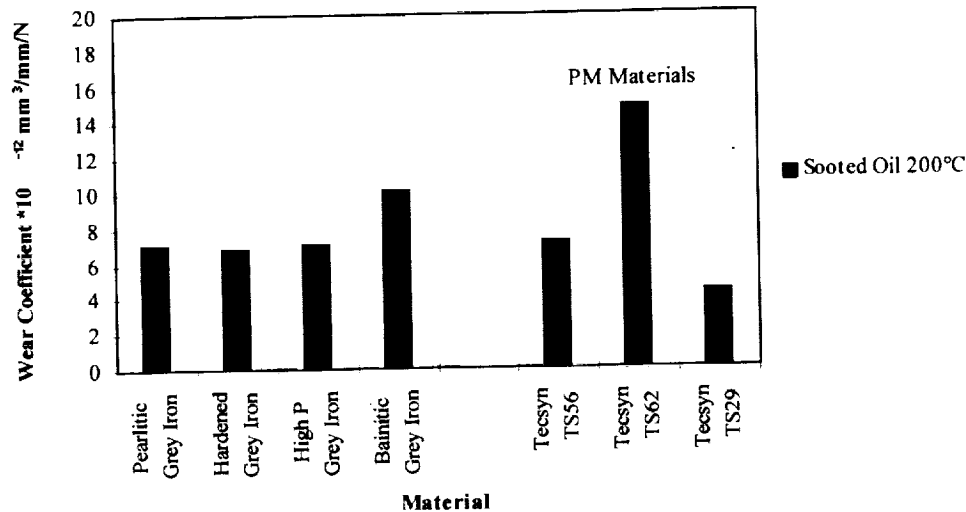


**Figure 3.10.6:** Ring wear coefficient for various cylinder liner materials in sooted oil at 200°C. Rings coated with HVOF Cr<sub>3</sub>C<sub>2</sub> - 20% NiCr.

### 3.10.3 Wear Surfaces

The 350°C fresh oil tests resulted in cylinder liner wear surfaces covered with oil deposits and surface films which largely obscured the microstructural features. The appearance of the wear scars clearly indicated that the liner wear mechanism at high temperatures is dominated by corrosive mechanisms such as oxidation and reaction with lubrication additives.

The wear scar from the baseline pearlitic gray iron liners in fresh oil showed a substantial amount of pitting and possible evidence of corrosive wear, either by oxidation or reaction with lubricant anti-wear additives. There was no abrasive wear normally evidenced by ploughed wear grooves running parallel to the sliding direction. Delamination around the graphite flakes was visible as lifting of thin layers of metal.

With high-soot oil the gray iron wear surface showed substantial abrasion. Pitting and surface films were visible in some areas. However, much of the surface appeared to be clean. It is believed that the anti-wear additives in the sooted oil were less active than in the fresh oil due to reactions with the soot and oxidative depletion of the additives.

A fresh oil wear scar on the TS56 sample was dominated by abrasive wear grooves with little evidence of chemical attack. Wear rates were lower than for the pearlitic gray cast iron cylinder liner. Abrasion was still the dominant wear mechanism with high-soot oil, although etched pearlite colonies were resolved in the wear surface, indicating some chemical attack.

A fresh oil wear scar on the TS62 sample showed evidence of abrasive wear, although wear grooves were less deep than the TS56 material. Evidence of pitting was also observed. With

high-soot oil, the wear scar showed abrasion (again, less than for material TS56) and etching of pearlite colonies indicating corrosive wear.

The TS29 material showed a mixture of pitting and deep abrasion marks on the fresh oil lubricated wear surface. M2 tool steel regions did not appear pitted.

#### **3.10.4 Conclusions - Powered Metal Cylinder Liner**

- The best powdered metal (PM) material studied was TS29-6. This material showed the largest decrease in wear and a small improvement in friction. The standard TS29 material also performed well.
- Cylinder liner wear mechanisms were dominated by two processes – chemical attack or reaction with oil additives, and abrasion.
- The cost of the PM cylinder liner, estimated at mature production volumes, is anticipated to be 50% greater than the current bainitic gray cast iron cylinder liner.

### 3.11 System Demonstration Testing

The final task for Phase IV of the program was to run a steady state test and a transient cycle test with all the developed in-cylinder components installed in the single cylinder research engine (SCE L10). The in-cylinder components to be evaluated in these tests were:

- Spherical joint piston and connecting rod
- Reduced cross-section steel top ring
- Iron second and steel oil ring
- Strategically oil cooled cylinder head
- Oil drilling turbulator inserts
- Radial combustion seal cylinder liner with cooling jacket heat transfer fins

#### 3.11.1 Engine Test Matrices

The program requirement for the Cummins In-Cylinder Components program was that the steady state test and thermal cycle test be run for 100 hours each at the LE-55 operating point. Engine operating parameters for each 100 hour test are shown in Table 3.11.1. All engine operating parameters were to be held constant for the steady state test. The thermal cycle test, however, involved cycling the fueling between full load and high idle on a 3 minute interval so that a complete cycle would comprise 6 minutes. The 6 minute cycle length allowed for 10 cycles per hour or 1000 cycles in 100 hours.

**Table 3.11.1:** 100 hour Steady State and Thermal Cycle engine parameters for System Demonstration Testing

Test:	Steady State	Thermal Cycle
Duration	100 hours	100 hours
Engine speed	1500 rpm	1500 rpm
Air-Fuel ratio:	30:1	30:1 (full load)
Peak cylinder pressure	20.7 MPa	20.7 MPa (full load)
Engine coolant	15W-40 Oil	15W-40 Oil
Coolant temperature	110°C	110°C

A separate single cylinder research engine was built up for each test. During the engine build for the steady state test the cylinder head port insulation was found to be damaged. An uninsulated cylinder head was substituted. All other in-cylinder components for these builds were as listed above.

The single cylinder research engine built up for the steady state test was placed on test on Monday, July 31, 1995. The engine accumulated 24 hours at the LE-55 steady state test conditions by Friday, August 4, 1995. Continuous (around the clock) engine testing was initiated

on Monday, August 7, 1995. Seventy-eight hours at the LE-55 steady state conditions were accumulated continuously on the engine through the first shift on Thursday, August 10, 1995. Total test time at the LE-55 steady state conditions was 102 hours.

A check of the peak cylinder pressures for the LE-55 steady state conditions was conducted at the conclusion of the test. The cylinder head was removed from the engine and a cylinder pressure transducer was installed. Removal of the cylinder head permitted visual inspection of the cylinder head combustion face, the piston crown and the cylinder liner. The hardware appeared to be in excellent condition. The spherical joint piston could still be rotated by hand. Post test check of the cylinder pressure showed that the engine had been operating with peak cylinder pressures in excess of 20.7 MPa.

The second single cylinder research engine built up for the thermal cycle test was placed on test on Wednesday, August 30, 1995. The engine ran continuously for approximately 50 hours before being shutdown for an extended holiday weekend. After test restart, the single cylinder research engine ran continuously until the end of test. The engine test was completed on Thursday, September 7, 1995. A total of 103.5 test hours were accumulated at the thermal cycle conditions resulting in 1021 cycles.

### **3.11.2 Post Test Analysis**

The in-cylinder components (piston, connecting rod, piston rings, cylinder liner and cylinder head) evaluated in the 100 hour thermal cycle test were the same as those tested in the 100 hour steady state test. Post thermal cycle test observations of the hardware follow.

SPHERICAL JOINT PISTON – The piston did not exhibit any signs of abrasive skirt-to-cylinder liner wear. The piston was free to rotate on the connecting rod ball without any binding.

The piston did not appear to have rotated during the tests as evidenced by discrete spray plume burn spots on the combustion bowl rim. A small dent in the flat of the combustion bowl cone was observed indicating a possible impact with the injector nozzle tip. The rings appeared to be in good condition.

A detailed analysis of the spherical joint piston was provided by Kolbenschmidt AG.

The skirt diameter may be somewhat too large in the upper part. There is distinctive wear down to the bottom of the lathe cut grooves. To reduce this wear it may be helpful to remove the short skirt oil drain grooves thus enhancing the size of the skirt pads which run undisturbed. The end of the skirt appears to be in poor condition. On one side, at the height of the threaded ring, there is much skirt wear. It appears that the threaded ring thermally expanded and forced the skirt out and thus enlarged the skirt diameter. The diameter of the oil drain holes in the threaded ring could be enlarged to increase the oil change rate in the piston with the expectation that piston and skirt temperatures will be reduced. For the next piston design iteration it is suggested that a redesigned skirt barrel profile be incorporated.

The first and second rings appear to have run very hot. The first ring appears to be slightly overheated in the vicinity of the ring gap. The ring land between the first and second ring is too small in diameter resulting in the deposition of hard carbon which has polished the cylinder liner.

SPHERICAL JOINT CONNECTING ROD – The connecting rod appeared to be in excellent condition. The spherical joint did not have any significant end play between the connecting rod and piston. The connecting rod could be moved freely and smoothly within the piston socket. However, it was observed that the holder rings could rotate within the socket by moving the connecting rod. The situation with the holder rings indicated that the threaded ring torque had relaxed during engine test. The big end connecting rod bearings were in excellent condition with much of the original top layer bearing material still present.

CYLINDER LINER – The cylinder liner appeared to be in excellent condition. No excessive wear in the cylinder liner bore surface was observed. A raised section of carbon built up above the top ring reversal location was noted. The heat transfer fins located in the cylinder liner cooling jacket were clean and free of oil deposits.

CYLINDER HEAD – The cylinder head tested was the original design iteration with only three valve bridge drillings: two intake-exhaust and one exhaust-exhaust. The redesigned cylinder head has four oil bridge drillings. The cylinder head was in excellent condition. The combustion seal fire ring was severely crushed by the radial combustion seal cylinder liner due to an excessive interference fit. One of the oil drilling turbulators had moved due to cooling oil supply pressure and flow.

### **3.11.3 Conclusion - System Demonstration Testing**

- The in-cylinder components including a spherical joint piston, a spherical joint connecting rod, a reduced cross-section steel top ring, an iron second ring, a steel oil ring, a strategically oil cooled cylinder head, oil drilling turbulator inserts and a radial combustion seal cylinder liner with cooling jacket heat transfer fins, have been successfully evaluated in a single cylinder research engine. The in-cylinder components completed 100 hours of steady state test and 100 hours of thermal cycle test at the LE-55 operating conditions.
- Issues with the durability of the cylinder head port insulation require additional manufacturing development.
- Issues with the spherical joint piston skirt profile, second ring land diameter and piston temperature control require additional design iteration.
- Issues with combustion seal fire ring crushing due to suboptimal interference fit between the cylinder head and cylinder liner require additional design iteration.
- Issues with the fixing of oil drilling turbulator inserts within the oil drilling require additional design iteration.
- Design proof-of-concept of the components developed on the Cummins In-Cylinder Components program has been successfully demonstrated.



### **3.12 *Effects of Insulation on Performance and In-Cylinder Heat Transfer***

#### **3.12.1 Experimental Measurements on the Effects of Piston Insulation**

For years, the use of insulated components to reduce in-cylinder heat transfer has been investigated as a means of improving engine performance by increasing thermal efficiency, increasing exhaust gas energy and reducing or eliminating cooling requirements. Studies on the anticipated benefits to fuel consumption through insulation produced estimates ranging from 3 to 20% as reported by investigators such as Morel et al. [Ref 17] and Bryzik and Kamo [Ref 18]. In testing insulated engines, experimental findings have been mixed and, at best, below the level of the benefits anticipated. Woshni et al. [Ref 19] and Furuhashi and Enomoto [Ref 20] tested insulated components and concluded the opposite of the desired heat transfer reduction occurred. Woshni et al. concluded heat transfer increased as wall temperatures rose above 600 K. This conclusion was confusing in light of experiments by Morel et al. [Ref 21] [Ref 22] [Ref 23] and Assanis [Ref 24] which showed a decrease in heat transfer to the cylinder head of insulated engines. Many other studies followed, most of which measured worse fuel consumption using insulation while some measured an improvement.

Little progress has been made in explaining the conflicting results and in determining the physical explanation behind the data. The intent of this work was to obtain a large data set using careful measurement techniques to determine the effect of insulation on in-cylinder heat transfer. The data were to be repeated in order to show and understand the scatter and uncertainty of back-to-back data from one engine build to the next. The large data set was to be used to put prior work, which includes smaller sets of data, into perspective.

##### **3.12.1.1 Experimental Set-Up**

A performance comparison among coated and uncoated pistons was made by exchanging pistons in the single cylinder L10 engine (SCE L10). The SCE L10 was equipped with an electronic, closed nozzle, unit fuel injector. Cooling water, lubricating oil, fuel and combustion air were temperature controlled and supplied to the engine by auxiliary systems within the engine test cell. Combustion air and fuel flow rates and temperatures were controlled to specific values.

Two coatings were tested on separate pistons: yttria stabilized zirconia and mullite. Yttria stabilized zirconia has been used extensively in insulated engine experiments but shows poor durability in extended tests. Mullite is less insulating than yttria stabilized zirconia. However, the mullite coating is more durable and has survived the engine tests reported here.

Steel articulated piston crowns were prepared to receive the multi-layer coatings by machining 1.52 mm of material from the piston bowl and crown. The coatings were then sprayed to a depth of 2.0 mm. Each coating was preceded with a bond coat which has a coefficient of thermal expansion between that of the metal and the sprayed coating [Ref 25]. The sprayed coatings were then ground back to the original piston dimensions. By preparing the spray coated pistons in this manner the compression ratio of the uncoated piston was maintained.

The baseline engine test matrix consisted of injection timing sweeps at 1200 and 1800 rpm with full load and part load operating points as shown in Table 3.12.1. The timing sweeps were used to characterize indicated fuel consumption (ISFC) as a function of injection timing or centroid of heat release. The ISFC as used in this paper was determined based on the cylinder pressure during the closed portion of the engine cycle (4-stroke). Therefore, the ISFC used in this paper represents the gross indicated specific fuel consumption (GISFC).

**Table 3.12.1:** Test matrix for back-to-back engine tests

Speed	Load	Timing
1200	Part	10 Injection Timings
	3.5 kg/hr fuel 86.2 kg/hr air	-12 ~ 11 cad Start of Combustion
1200	Full	5 Injection Timings
	7.08 kg/hr fuel 143 kg/hr air	-8 ~ 3 cad Start of Combustion
1800	Part	11 Injection Timings
	5.4 kg/hr fuel 181.4 kg/hr air	-17 ~ 12 cad Start of Combustion
1800	Full	7 Injection Timings
	7.94 kg/hr fuel 231 kg/hr air	-8 ~ 10 cad Start of Combustion

Combustion air and fuel flow rates were held constant at each operating condition shown in Table 3.12.1. This meant, in the case where the cylinder charge air was heated more during the intake process, a higher intake pressure was needed to supply the same combustion air flow rate.

Start of injection and injection duration were controlled electronically by a solenoid valve within the injector. The injector timing valve closure (TVC) signal was used as a nominal value to match start of injection between data sets. Injector push tube loads were also collected on a crank angle resolved basis to measure injection uniformity. Injector push tube load results showed injection at the same TVC produced repeatable timing for the start of injection.

Cylinder pressure was measured with a water cooled AVL-QC32C piezoelectric quartz pressure transducer. The shaft encoder used was capable of 0.5 crank angle resolution. One hundred (100) cycles of cylinder pressure data were ensemble averaged for use within the heat release analysis.

Several timing sweeps were run with the uncoated pistons followed by the coated pistons. As shown in Table 3.12.2, the coated pistons were not run at all the operating points. This test matrix design was used since it was believed additional information would not be gained from the operating points/material combinations not run. In total, over 300 data points were taken in an effort to obtain enough data to observe the repeatability and accuracy of the measurements.

**Table 3.12.2:** Piston coatings and the number of timing sweeps at each speed and load

Piston Coating	1200 rpm Part Load	1200 rpm Full Load	1800 rpm Part Load	1800 rpm Full Load
Uncoated	2	2	4	3
Zirconia	1	0	2	2
Mullite	0	0	4	2

### 3.12.1.2 Experimental Method

The coated and uncoated pistons were compared from two perspectives. One perspective involved a direct comparison of performance characteristics such as fuel consumption and emissions. The other perspective involved a comparison of heat transfer characteristics. A comparison of performance parameters provided information on the effect of the coated pistons if they were used to replace uncoated pistons in an existing engine. However, this comparison does not provide information on whether an engine with the coated pistons could be optimized to a condition of improved performance. Heat transfer, however, is a more fundamental characteristic which, if decreased, should lead to better performance characteristics for a given optimized combustion system. Both the overall performance and heat transfer characteristics of the coated pistons must be considered simultaneously in order to determine if there are benefits to the overall combustion system. For example, the benefit of reduced heat transfer must not outweigh a cost to exhaust emissions.

Engine performance was compared by measuring brake specific fuel consumption, nitrogen oxides ( $\text{NO}_x$ ), particulate and unburned hydrocarbons. In-cylinder heat transfer was evaluated using a thermodynamic first law energy balance over the closed portion of the combustion cycle. The approach taken to evaluate the heat transfer can be explained by considering the injection timing sweep generated by an engine cycle simulation computer program as shown in Figure 3.12.1. The solid line in Figure 3.12.1 represents a typical timing sweep where ISFC is plotted as a function of the centroid of heat release. Note that ISFC decreases as timing is retarded until a minimum is reached just to the right of top dead center (TDC) near three crank angle degrees (cad). For ideal combustion (no heat transfer) the minimum would occur at TDC because the closer the fuel is burned to TDC the higher the effective expansion ratio resulting in maximum thermal efficiency.

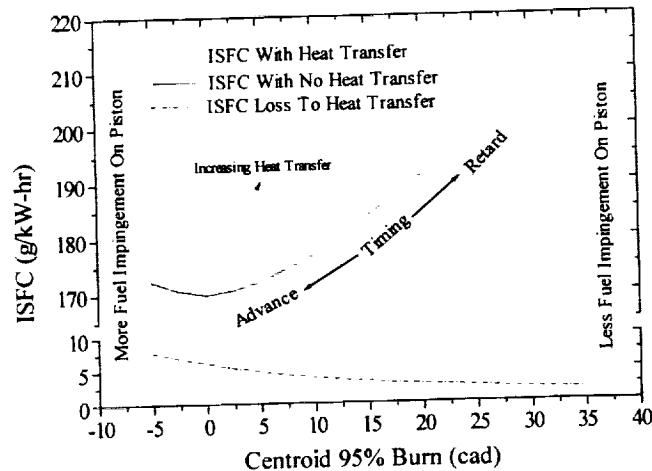


**Figure 3.12.1:** Typical ISFC versus centroid curve for a diesel engine.

The dashed curve in Figure 3.12.1 represents a timing sweep with heat transfer included. With heat transfer the ISFC curve shifts up and to the right. The upward shift is necessary but not sufficient to indicate increased heat transfer. As timing is advanced, heat transfer increases due to longer residence times for the hot burned gases. Heat transfer shifts the minimum toward more retarded timings. The magnitude of the shift in the minimum is an indication of the quantity of heat transfer.

An increase in the duration of heat release can also cause the curve to shift upward due to fuel which burns at the same centroid but further from TDC, resulting in higher fuel consumption. The increased duration also tends to increase the total heat transfer because the duration of the combustion event is longer, allowing more time for radiation. A z-axis comprising combustion duration might then be imagined for Figure 3.12.1 which would show an increase in ISFC as the duration of the combustion event increases. This defines a surface above which instantaneous heat transfer increases and below which instantaneous heat transfer decreases.

In this set of experiments, timing sweeps were run to create ISFC versus heat release centroid curves. The data were repeated after engine rebuilds to determine the uncertainty associated with the best fit line through the data points. This approach was found to match the error analysis well. Heat transfer characteristics were then compared by considering the location of the minima and degree of shift in the curves. This technique allowed the observation of a trend to be established using data which involved multiple operating conditions instead of a comparison at a single operating point.

Combustion air and fuel flow rates and temperatures, engine speed, and injection pressure can all affect combustion duration and, in turn, influence the heat transfer. In this set of experiments it was decided to hold the combustion air and fuel flow rates and temperatures constant, thereby fixing the mass flow into the cylinder. The consequences of holding the mass flow constant was that pressure in the cylinder at intake valve closing had to shift to the value necessary to obtain the

desired flow. Injector push tube loads were monitored to assure the injection pressure and duration were maintained constant and repeatable.

### 3.12.1.3 Error Analysis

The data presented here and in many studies done on insulated components rely heavily on the accuracy of the ISFC and heat release centroid calculations. Therefore, the accuracy of the experimental measurements must be understood in order to determine how closely the differences in test results using coated and uncoated pistons can be resolved. The ISFC is calculated from the integrated pressure versus volume history of the combustion event. Errors in the cylinder pressure measurement and volume calculation can contribute to an error in ISFC. The centroid is determined from the heat release which is also calculated from the pressure/volume relationship. A list of the type of measurement errors associated with the determination of ISFC is presented in Table 3.12.3. Each error type is discussed briefly below.

**PHASING** – Phasing errors result from assigning the cylinder pressure to a given crank angle from which volume is calculated. It is very difficult to phase an optical crank angle encoder to pressure data better than 0.2 cad. Each 0.1 error in crank angle can be shown to result in a 1% error in the calculated ISFC. This error can best be reduced by using the same encoder location for all of the engine tests thereby eliminating the relative error between data points. The error in phasing also affects the centroid calculation since the heat release calculation is dependent on volume. The potential error is significant but smaller, being approximately 0.2 cad error in calculated centroid for each 0.1 cad change in the encoder phasing.

**Table 3.12.3:** Error types associated with ISFC and heat release centroid measurements

Error Type	ISFC	Centroid (cad)
Phasing Error	1% per 0.1 cad	0.2 per 0.1 cad
Initial Pressure	-	0.02-0.04 per mm Hg
Calibration	1%	0.5
Thermal Fatigue	1-3%	1 - 3
Fuel Flow Rate	1 - 3 %	-
Ensemble Average	0.2 - 0.5%	0.1 - 0.2

**INITIAL PRESSURE** – The piezoelectric cylinder pressure transducer is a very linear and accurate measuring device. However, this type of transducer measures relative and not absolute pressures. Therefore, one point on the pressure history must be assigned a value. A common approach is to assign the bottom dead center (BDC) pressure to equal the intake pressure. When running a coated piston, the relationship between intake and BDC pressure may change relative to the uncoated piston resulting in an error in the initial pressure. In these experiments, the initial pressure was selected using an algorithm which searched for a pressure which provided the best fit to a linear regression of the compression line on a  $\ln(\text{pressure})$  versus  $\ln(\text{volume})$  diagram.

This technique may be affected by the different reheat characteristics of the coated and uncoated pistons. However, though assignment of an absolute pressure affects the heat release and centroid calculation it does not affect the calculation of ISFC.

CALIBRATION – It was possible to statically calibrate the cylinder pressure transducer to within 1% of point over the entire cylinder pressure range. This error can be larger, however, if the transducer is not calibrated often or experiences some damage resulting in a change in sensitivity over time.

THERMAL FATIGUE – Thermal fatigue occurs in all piezoelectric transducers and is caused by thermal stresses induced by temperature gradients in the transducer. Thermal fatigue is more readily apparent in a pressure measurement near the end of combustion tending to affect the heat release and therefore the centroid calculations. The main issues are 1) a cylinder pressure transducer's thermal fatigue resistance can change with time; and, 2) the degree of thermal fatigue resistance among transducers may vary even though they are of the same design. A transducer's thermal fatigue resistance is not easily quantified and, therefore, results among different transducers or the same transducer over long periods of time are difficult to compare.

FUEL FLOW – The fuel flow rate was measured with a weigh scale and a timer. The errors involved can be large if the fuel rate measurement system has not reached a steady temperature. There is an inherent potential problem in the fuel measurement, however, since the ensemble averaged cylinder pressure data are taken over a much shorter time period (1 to 10 seconds) than the time period required for the fuel measurement (1 to 3 minutes). If there are any unsteady surges in fuel flow they cannot be detected by the fuel measurement system.

ENSEMBLE AVERAGE – The ensemble average of the cylinder pressure data creates some uncertainty. The numbers shown in Table 3.12.3 and 3.12.4 are for 100 cycle averages. The contribution to the total error is fairly insignificant. As the number of cycles included in the ensemble average is increased beyond 100 the reduction in error is very small.

The uncertainty of measurements for four different error sources is also shown in Table 3.12.4. First, consider the relative error between data taken consecutively with the same setup on a given engine build. Relative errors for phasing, calibration and thermal fatigue are close to zero since there is little change between data points. The only errors left are associated with the fuel flow and ensemble averaging errors with an expected RMS uncertainty of 1.2%. In the case of a typical engine tear down and calibration where the optical encoder is not disturbed but the cylinder pressure transducer is replaced, the calibration and thermal fatigue errors must be included. The expected error in this second case would be 1.7%. In the third case where several measurements are made over time and the cylinder pressure transducer experiences wear and must be replaced, the error due to thermal fatigue becomes more significant. The expected error among data points taken at different times where all the uncertainties must be included, but at the smallest possible level, is close to an RMS sum of  $\pm 3\%$ . Finally, in the fourth case, when the encoder must be replaced and several cylinder pressure transducers are used over long periods of time and a conservative estimate of each error is used, the RMS uncertainty is  $\pm 5\%$  ISFC and  $\pm 3.6$  cad in the heat release centroid.

**Table 3.12.4:** Error sources associated with ISFC and heat release centroid measurements

Error Source	ISFC	Centroid (cad)
Same Set-up	1.2 %	0.6
Tear Down, Calibration	1.7%	1.6
Multiple Sweeps	3%	2.0
Worst Case	5%	3.6

For the data taken in these experiments the expected error is between  $\pm 3$  and  $\pm 5\%$ . Several data sets were taken over a long period of time using several cylinder pressure transducers and two different optical encoders. This suggests that all of the errors need to be included in the estimate. Care was taken to check the cylinder pressure transducers often for thermal fatigue and to correct their calibrations such that the lower of the possible error for each component was expected.

The  $\pm 3\%$  uncertainty should be kept in mind while reviewing the data to be presented. The error analysis identifies a grim reality for ISFC measurements. The ability to resolve differences of less than 3% is marginal and the method is incapable of resolving differences below 1.5%. Most of the ISFC differences measured previously among engines with insulated and uninsulated in-cylinder components have been less than 3% and most of them have relied on cylinder pressure and ISFC measurements to draw conclusions with regard to in-cylinder heat transfer. It is easy to understand why results have been mixed when the measurement capability can so easily produce a greater uncertainty than the differences among the engines being measured.

#### **3.12.1.4 Results**

Results for the baseline uncoated piston over timing sweeps at the four selected speed and load operating conditions are shown in Figures 3.12.2 through 3.12.5. The figures exhibit the expected shape for the ISFC versus centroid curve. Note that at 1200 rpm, torque peak and 1800 rpm, full load, there are no minima. This is due to the fact that the injection timing could not be advanced earlier than the optimum due to peak cylinder pressure limits. Four timing sweeps are shown at 1800 rpm and part load, while two timing sweeps are shown for the remaining operating points. Data from the first timing sweep are shown with solid symbols while the remaining timing sweeps have open symbols. Typically, a timing sweep took several days to complete. The first timing sweep was completed at each speed and load operating point before the second sweep was run.

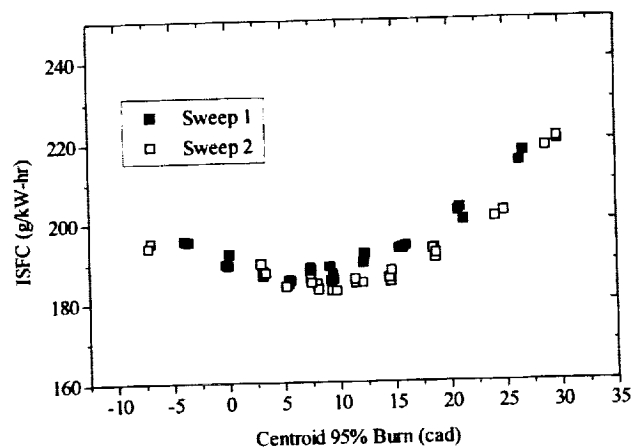


Figure 3.12.2: Two timing sweeps for 1200 rpm, part load using the uncoated piston.

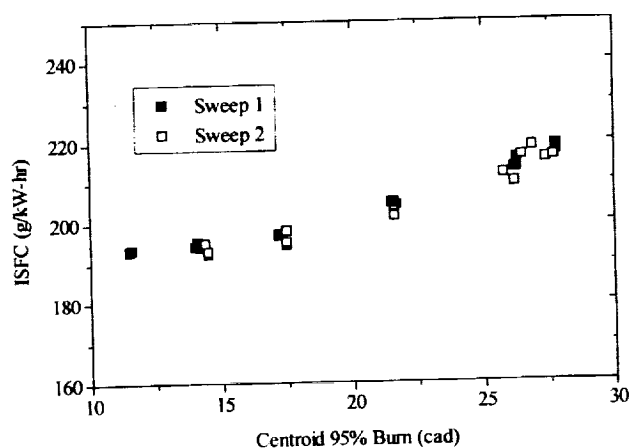


Figure 3.12.3: Two timing sweeps for 1200 rpm, full load using the uncoated piston.

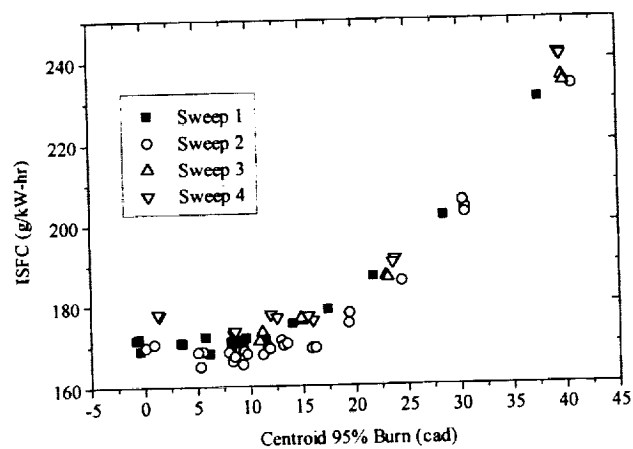
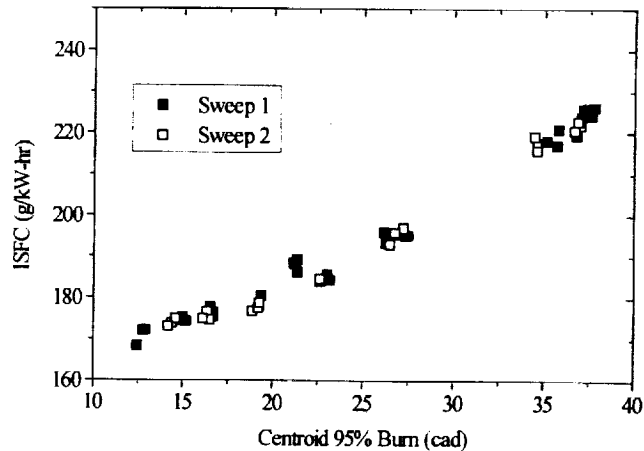


Figure 3.12.4: Four timing sweeps for 1800 rpm, part load using two identical uncoated pistons.





**Figure 3.12.5:** Two timing sweeps for 1800 rpm, full load using the uncoated piston.

The data in Figures 3.12.2 through 3.12.5 show that the repeatability of the ISFC measurement for the same piston was approximately 3%. The part load conditions show more scatter while the full load conditions appear more repeatable. This may be an indication that the fuel measurement system had a better signal-to-noise ratio at the higher flow rates.

For the four timing sweeps shown in Figure 3.12.4 at 1800 rpm, part load, two different pistons were used. The piston was replaced between sweeps 2 and 3 as well as between sweeps 3 and 4. This piston swapping produced relatively large scatter in the data. This observation is important since a piston replacement is necessary in order to compare a coated piston with an uncoated piston. The scatter in the data between the two uncoated pistons indicates how large the differences between the coated and uncoated pistons need to be in order for a measurable difference to be observed.

Data points were often taken in groups of two or three at each timing. Careful examination of the figures shows the points in these groups to be close together. For example, in Figure 3.12.5, the three data points in the upper right corner (open squares) were all taken on the same day at the same injection timing, speed and load. The three data points just to the lower left of the previous data points (solid squares) were also taken on the same day at the same injection timing, speed and load. However, the latter data points were taken several months prior to the first group of data points. The data indicate that, within the same day, the repeatability is within 1 to 1.5% which is expected from the uncertainty of the fuel flow measurement as discussed previously in the error analysis. The scatter from one sweep to the next, however, indicates a larger error in the measurement involving differences in the response of the pressure transducer or transducers over time. The change in heat release centroid indicates thermal fatigue characteristics have changed, as well as a possible change in optical encoder phasing. It can be shown that this shift in the centroid and ISFC can be attributed to the pressure measurement. Figure 3.12.6 shows BSFC versus injection timing (Timing Valve Closed - TVC) at 1800 rpm, part load. Using the measured load on the dynamometer to calculate the BSFC eliminates the effect of the cylinder pressure transducer. The scatter between data points at a given injection timing is greatly reduced,

showing the pressure transducer indicated differences in fuel consumption when there actually were no differences.

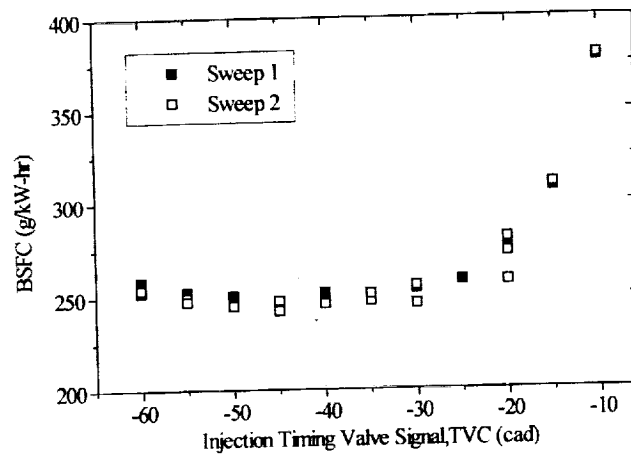


**Figure 3.12.6:** Two timing sweeps for 1800 rpm, part load using the uncoated piston.

Timing sweeps were attempted using the zirconia coated piston after the first two timing sweeps with the uncoated piston were completed at each speed and load. The results for 1800 rpm are shown in Figure 3.12.7 and Figure 3.12.8. At part load, the data for the zirconia coated piston fall within the scatter of the data for the uncoated piston at the retarded timings. As the timing becomes more advanced, the BSFC for the zirconia coated piston appears to be slightly higher than the data for the uncoated piston.

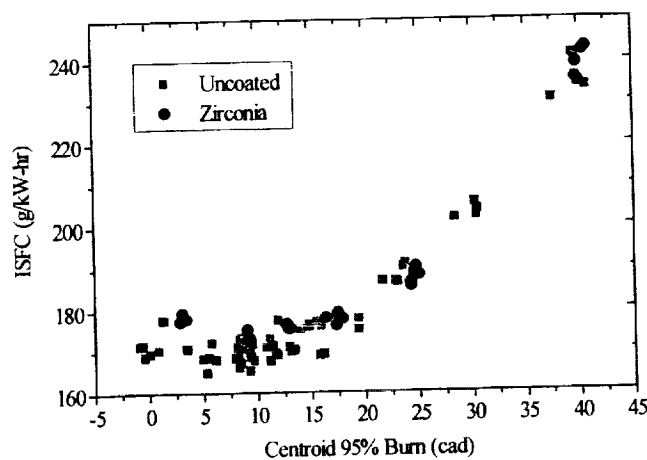


**Figure 3.12.7:** All four uncoated piston and two zirconia coated piston timing sweeps at 1800 rpm, part load

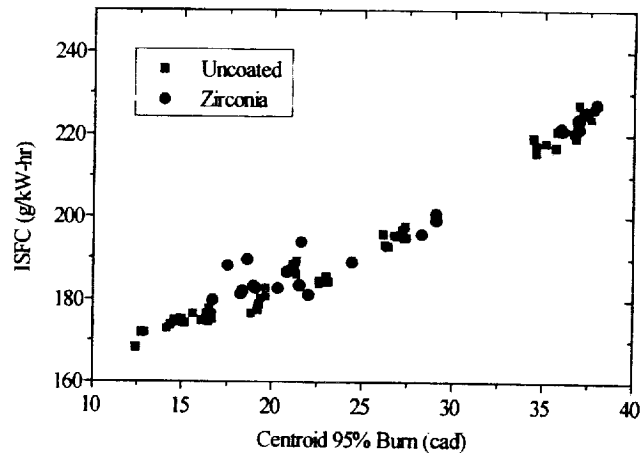


**Figure 3.12.8:** Two uncoated piston and two zirconia coated piston timing sweeps at 1800 rpm, full load.

Repeat of the data at a given injection timing resulted in the grouping of the data points at a given heat release centroid as seen in the figures. The timing sweep for the zirconia coated piston was only done at every other timing point for comparison to the timing sweeps for the uncoated piston. Knowing the data from these groups of points resulted from heat release curves which had the same injection timing, allows for a comparison of the duration of the heat release by comparing the locations of the centroid. Data which shows a retarded centroid for the same injection timing must have a longer burn duration. The burn duration appears to be the same for both pistons at retarded timings but longer at advanced timings for the zirconia coated pistons. This can be seen in the data at the upper right corner where, at retarded timings, the uncoated and zirconia coated pistons have the same centroids at the same injection timing. However, at advanced timings, as seen in the lower left data points, the centroid for the zirconia coated piston has shifted to the right.

In the 1800 rpm, full load data (Figure 3.12.8), the shift in heat release centroid is much larger and occurs at all but the most retarded timing. Three of the data points appear to be at a significantly higher ISFC; approximately 5% higher than the data for the uncoated piston. However, since this ISFC data is 4% higher than the first timing sweep with the zirconia coated piston it is difficult to conclude that the difference compared to the uncoated piston is due to the coating alone.

Two trends appear to be clear in the data. The first trend is the combustion duration tended to increase as injection timing was advanced. The second trend is the difference in ISFC between the coated and uncoated piston also tended to increase as timing was advanced. Since the heat release duration is longer, it is unclear whether the observed increase in ISFC is due to heat transfer. The magnitude of the effect of increasing the heat release duration on ISFC will be explored in **Section 3.12.15 Discussion of Results**.

If only one or two data points were taken at a given injection timing, speed and load the conclusions might be very different. At 1800 rpm, part load and 6 cad centroid, the zirconia coating might appear to have a slightly better ISFC and approximately the same heat release duration. However, at an advanced timing, the zirconia coating would appear to be significantly worse with higher ISFC and longer heat release duration. A timing sweep at 1200 rpm, part load with the zirconia coating showed similar results at retarded timings. Unfortunately, a cylinder pressure transducer failure occurred at advanced timings resulting in the loss of the ISFC data. However, a review of the BSFC data (Figures 3.12.9 and 3.12.10) suggests that the fuel consumption also increased slightly at advanced loads.

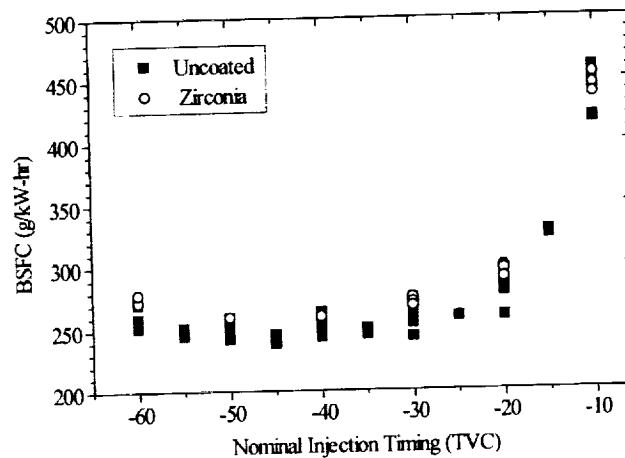


**Figure 3.12.9:** BSFC comparison of uncoated piston and zirconia coated piston timing sweeps at 1800 rpm, part load.

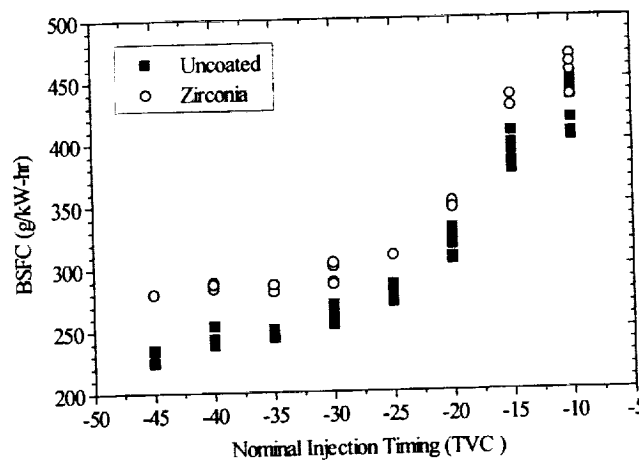


**Figure 3.12.10:** BSFC comparison of uncoated piston and zirconia coated piston timing sweeps at 1800 rpm, full load.

Given the consistency in the data among speeds and loads it was decided to forego further testing on the zirconia coating and to begin testing on the mullite coatings. It was also decided to test the mullite coatings at 1800 rpm only.

Upon measuring the combustion bowl volume of the zirconia coated, mullite coated and uncoated pistons it was determined that the mullite coated bowl was 1 cm<sup>3</sup> larger than the uncoated piston and there was an estimated 1 cm<sup>3</sup> less material around the edges. The difference in bowl volumes was equivalent to a difference of 0.3 in compression ratio between the mullite coated and uncoated pistons. Therefore, sweeps 1 and 2 were run with the piston at a lower compression ratio.

In order to investigate the effect of compression ratio on ISFC results, the piston pin location was systematically changed between selected timing sweeps. The piston pin was raised 0.152 mm between sweeps 2 and 3 to make the coated bowl compression ratio equivalent to the uncoated bowl compression ratio. The piston pin was raised another 0.152 mm between sweeps 3 and 4 in order to make the coated bowl compression ratio greater than the uncoated bowl.

The results are shown in Figures 3.12.11 and 3.12.12. Each of the timing sweeps with mullite coated pistons appears to repeat reasonably well showing little effect of the compression ratio. This is an expected result for such a small change in compression ratio. The timing sweeps with the mullite coated piston show the same characteristics in comparison to the uncoated pistons which were seen with zirconia coated pistons, but the differences are more pronounced. The centroid is shifted to the right for almost all of the data points but is shifted more at the advanced timings. As with the zirconia coated piston, this indicates a longer heat release. The ISFC appears to be significantly higher, particularly at the advanced timings where the ISFC is as much as 8% higher for the mullite coated piston. The data once again match what would be expected if heat transfer were increased. However, there is a degree of uncertainty because the heat release duration is longer.

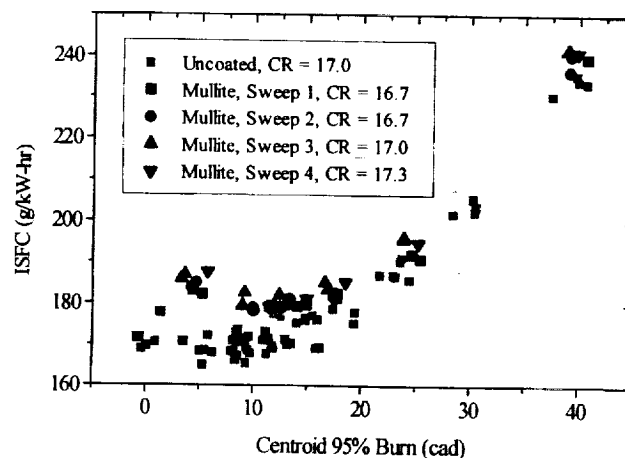


**Figure 3.12.11:** Uncoated piston and four timing sweeps with the mullite coated piston, 1800 rpm, part load.

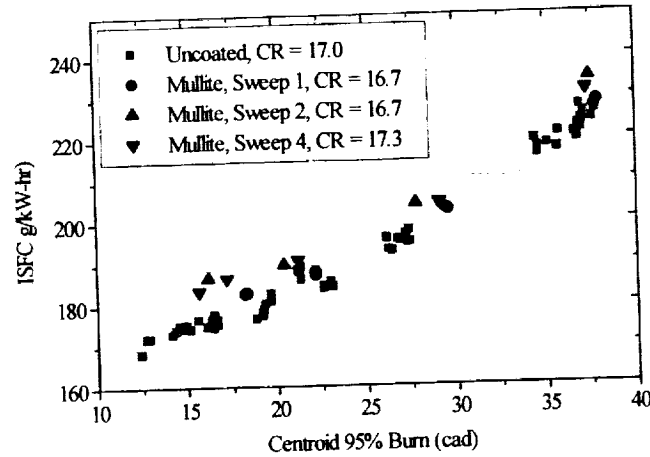


**Figure 3.12.12:** Uncoated piston and mullite coated piston timing sweeps, 1800 rpm, full load.

Results for the BSFC are similar to those for the ISFC as shown in Figures 3.12.13 and 3.12.14. When plotting BSFC versus injection timing, the zirconia coated and mullite coated pistons were higher than the uncoated pistons. This is expected from the longer heat release and shift to later centroids. Heat release rates for the mullite coated and uncoated pistons at three timings and 1800 rpm, part load, are shown in Figure 3.12.15. The heat release for the mullite coated piston begins slightly after the uncoated baseline piston. It has a similar premixed burn but reaches a lower peak and a more drawn out burn during the expansion stroke. The differences are greater between the two pistons at advanced timing, as is seen in the timing sweep plots.

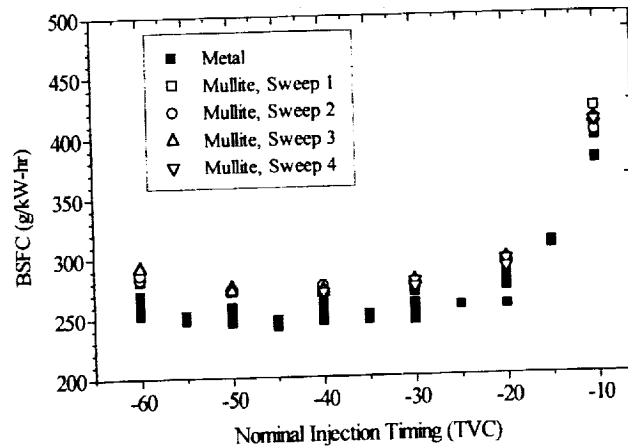


**Figure 3.12.13:** BSFC comparison of uncoated piston and mullite coated piston timing sweeps at 1800 rpm, part load.

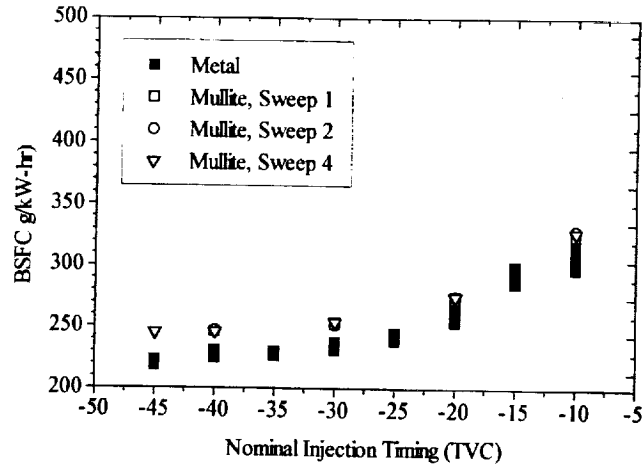


**Figure 3.12.14:** BSFC comparison of uncoated piston and mullite coated piston timing sweeps at 1800 rpm, full load.

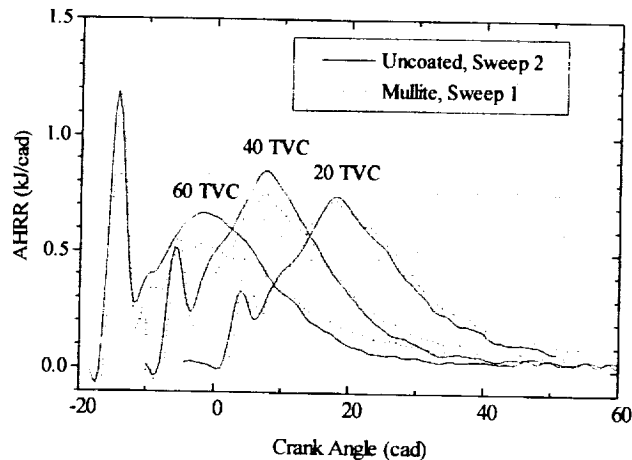


**Figure 3.12.15:** Uncoated piston and mullite coated piston apparent heat release rates, 1800 rpm, full load.

Volumetric efficiency was found to decrease about 1 and 2% for the mullite coated and zirconia coated pistons, respectively. This observation should infer that the trapped gas temperature was higher for the coated pistons. Higher trapped gas temperatures should have led to shorter premixed burn fractions for the coated pistons. As with the heat release rate shown in Figure 3.12.15, this was not the case for the majority of the data at all of the speed, load and timing points. Figure 3.12.16 shows a plot of premixed burn fraction versus TVC timing for the uncoated and zirconia coated pistons. The data show there was no measurable difference in the premixed burn fraction. The reason for this observation is still unclear.

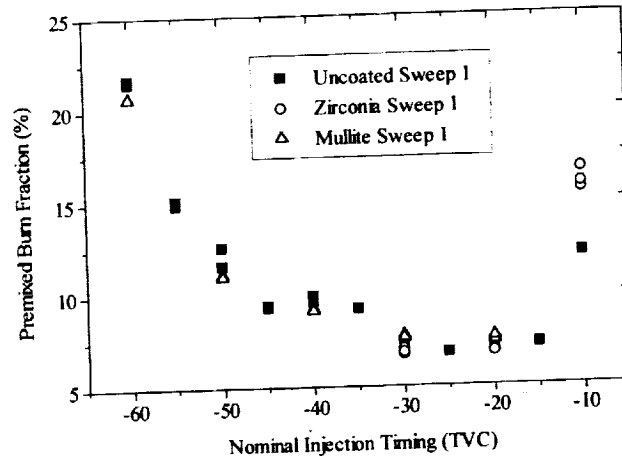


**Figure 3.12.16:** Premixed burn fraction for the three piston coating conditions, 1800 rpm, part load as a function of nominal injection timing (TVC).

A comparison of emissions from the engine running the coated pistons shows the coatings were detrimental to combustion. In Figure 3.12.17, fuel specific  $\text{NO}_x$  is plotted versus dry particulate as calculated from a Bosch smoke measurement and correlation. The data show, once again, there was very little difference between the engines at retarded timings but as timing was advanced the coating produced a greater amount of smoke. The zirconia coating is close to the uncoated piston but displays slightly higher smoke and higher  $\text{NO}_x$  at a given timing. The mullite coated piston shows increasingly worse smoke as injection timing is advanced. This increase in particulate as timing is advanced is normally only seen in engines with uncoated pistons when the fuel is interacting with the piston bowl or combustion chamber walls. It suggests the mullite surface has a detrimental effect on the burning process. This result might also have been anticipated from the shape of the heat release because the end of combustion was slow, which typically aggravates particulate emissions.

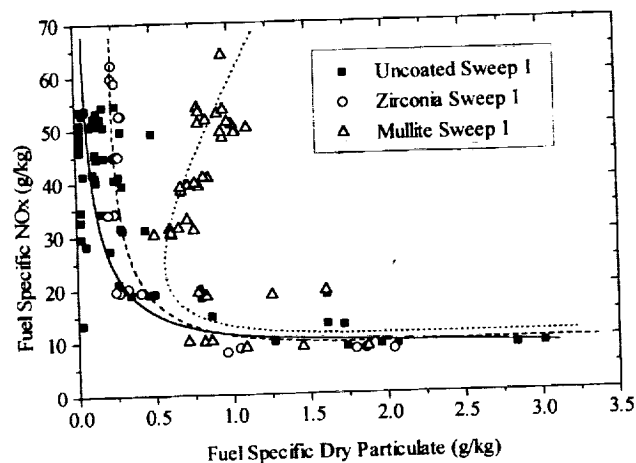


**Figure 3.12.17:** Fuel specific  $\text{NO}_x$ /particulate trade-off curve for the three piston coating conditions, 1800 rpm, part load.



As a final piece of information, it is important to consider the possibility that the injector was not functioning properly while the mullite coated pistons were tested and, therefore, the combustion process was altered. To help monitor injector performance, push tube load was measured with a strain gage. The push tube signals for some of the data points showing differences in combustion are shown in Figure 3.12.18. The figure shows that the push tube load was almost identical from test to test. The difference at the most advanced timings was mostly a constant zero set shift on the strain gage balance. Push tube load was monitored throughout the experiments with similar results. The push tube loads gave no indication the injector was operating differently for the mullite coated or zirconia coated pistons.

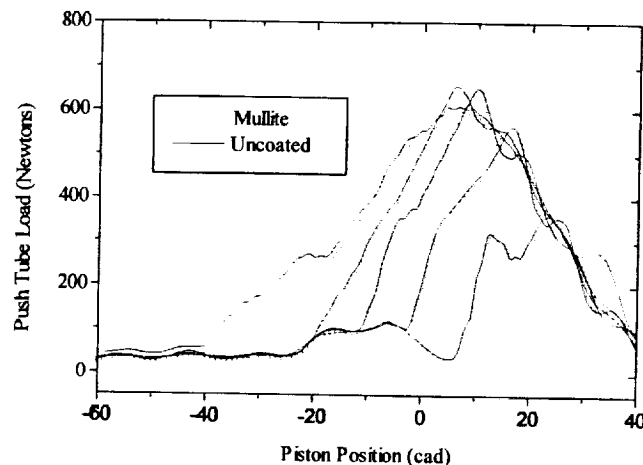


**Figure 3.12.18:** Push tube loads for uncoated piston and mullite coated piston timing sweeps, 1800 rpm, part load. Push tube loads for -10, -20, -30, -40 and -60 TVC.

### 3.12.1.5 Discussion of Results

The data clearly show that for this engine the addition of zirconia and particularly mullite coatings to the pistons had a detrimental effect on engine performance. Indicated and brake specific fuel consumption increased, combustion duration was prolonged, volumetric efficiency decreased, and exhaust emissions degraded. Understanding why performance changed is important in order to determine if the engine can be optimized to take advantage of the changes caused by the piston coatings. The results will be discussed below with some suggestions regarding the cause and some analysis in support of those suggestions.

**INCREASING DURATION** - In all the coated piston tests, combustion duration increased and the increase became larger at advanced injection timings. The fact that advanced injection timing aggravated the combustion problem leads to suggestions as to what the root cause might be.

There are several conditions in the engine different at advanced injection timing than at retarded injection timing. One source of the difference might be the location of the piston relative to the fuel spray. At retarded injection timings the piston is moving away from the fuel spray, thus

decreasing the possibility of fuel or fuel vapor coming in contact with the piston surface. As injection timing is advanced, the fuel spray interacts with the piston to a greater extent.

A simple spray model was used to estimate relative changes in the spray quantity directed toward the piston. The results of the spray model are shown in Figure 3.12.19. As injection timing was retarded to 10 cad aTDC, one third of the fuel was directed toward the cylinder liner above the piston. While the results from the model are only qualitative, the results illustrate that fuel/piston interaction increases at advanced injection timings. One possible cause for the observed differences in ISFC could, therefore, be related to how the fuel burns near the piston surface.

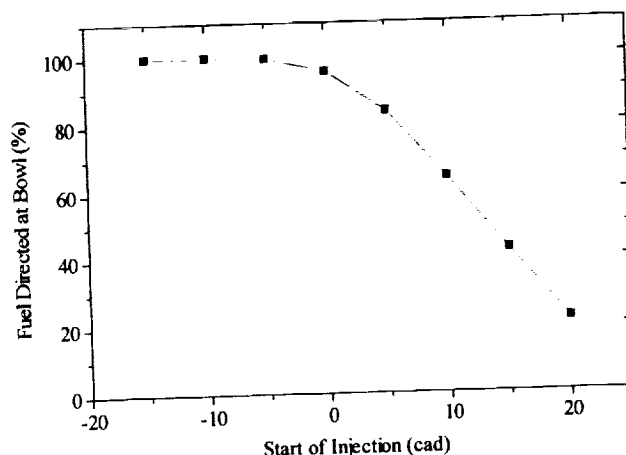


**Figure 3.12.19:** Prediction of the percentage of fuel which could potentially reach the piston or bowl as a function of injection timing.

Another difference which occurs at advanced injection timings involves fluid motion. As the piston ascends on the combustion stroke, gases in the crown region are squished over the rim of the combustion bowl and the swirl motion within the bowl increases. As the piston descends on the expansion stroke, the swirl and squish velocities decrease rapidly. If the surface of the piston coating affects the gas flow the effect would be more dominant at advanced injection timings since at retarded injection timings the gas flow would have already slowed down considerably.

The possible presence of the two phenomena discussed above leads to two hypotheses. The first is fuel becomes trapped within a larger boundary layer or within the porous, rough surface of the piston coating and burns more slowly. The slow burn results in prolonged heat release and increased particulate. The second hypothesis is the rough coating surface causes a more rapid decay in swirl and reduces the mixing of fuel and air. Therefore, the fuel burns more slowly, the heat release is prolonged and, due to decreased mixing and oxidation, particulate increases.

If either hypothesis were accurate then a rough, porous piston having similar thermal properties as the uncoated piston should cause an increase in heat release duration. In order to test the hypotheses, a series of timing sweeps were run over the same test matrix using roughened/porous surface, metal coated pistons. The results from this experiment (see 3.12.2 Experimental

**Measurements on the Effects of Piston Surface Roughness and Porosity)** show the metal coatings' surface roughness and porosity affected the heat release rate in a manner consistent with that observed with the ceramic coated pistons.

**INCREASING ISFC** – In the case of the mullite coated piston, fuel consumption was as much as 8% higher at advanced injection timings. The first task in evaluating this observation is to determine if there has been an increase in heat transfer or a change in combustion rate as described above. Some of the fuel consumption increase can be attributed to a longer heat release duration. However, it appears the increase in fuel consumption was too great for a long heat release duration to be the only contributing factor.

In order to evaluate the effect of an increase in heat release duration on ISFC, a cycle simulation computer program was used. The cycle simulation was first matched to the engine with the uncoated baseline piston by adjusting the heat transfer coefficient to match the cylinder pressure curves over the closed portion of the cycle. The results from the simulation are presented in Figure 3.12.20. In Figure 3.12.20, the cycle simulation is compared to the measured data for several different heat transfer conditions. The uncoated piston simulation point is represented by the open circle located near the minimum fuel consumption point of the uncoated piston timing sweep. The upward pointing triangle represents the same simulation run with the heat release from the mullite coated piston while the remaining model parameters were held constant. The downward pointing triangle represents the cycle simulation run with changes in the shape of the heat release curve. The results show a 1.5% increase in ISFC and a shift in the centroid from 6 to 12 cad. The cycle simulation shows the shape of the heat release alone cannot account for the measured increase in ISFC. At this point the heat transfer coefficient in the cycle simulation was increased by 30% producing the result represented by the downward pointing triangle. The 30% increase in heat transfer in addition to the centroid shift coincides with the results of the mullite coated piston timing sweep. Therefore, the simulation suggests one possible explanation for the test data is an increase in heat transfer of approximately 30% over the cycle.

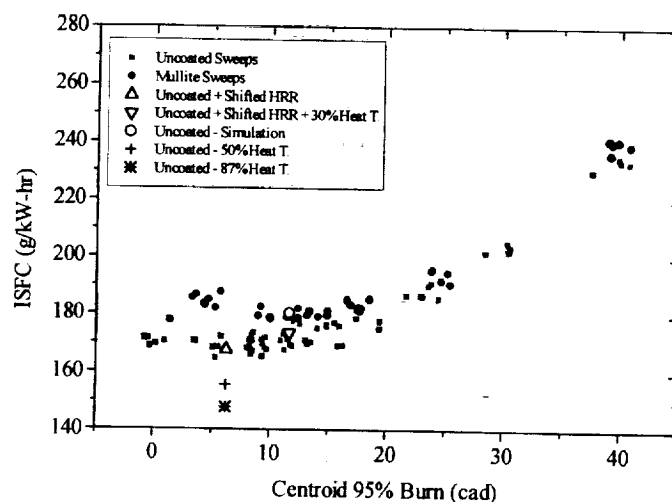


**Figure 3.12.20:** Results of engine simulation analysis on ISFC as a function of heat transfer and heat release shape compared to the measured data.

It is difficult to run the same analysis with the zirconia coated piston data because the difference between the uncoated piston and the zirconia coated piston ISFC was only half as great and near the limits of resolution of the measurement. It would appear, however, the zirconia coated piston exhibited similar behavior but to a lesser degree.

The final two points in Figure 3.12.20 represent the potential reduction in ISFC. The points were simulated with a 50% and an 87% reduction in heat transfer. These values are estimates of the highest possible reduction in heat transfer which could be expected from the thermal properties of the mullite coating and zirconia coating, respectively. The engine could not have done as well as these points suggest because only the pistons were coated and only to a depth of 1.52 mm. However, these data give some idea of the maximum potential benefit of the coatings which, unfortunately, was not realized.

If the thermal properties of the material create higher wall temperatures and more resistance to heat transfer, an observed increase in heat transfer must be the result of an increased film or heat transfer coefficient. It has already been discussed that the piston material can cause a change in the burning rate of the fuel and one possible reason is the surface of the piston affects fluid motion. The surface roughness of the piston may therefore create a higher heat transfer coefficient which offsets the higher wall temperatures. Roughened or porous metal pistons with metal thermal properties would also be expected to display the same behavior.

A second possible cause is an increase in the heat transfer coefficient due to a thinner quench distance between the reaction zone of the flame and the combustion chamber wall. This argument was made by Woshni [Ref 19] and is still a topic of research. As the flame approaches the wall, the reaction zone is at a much higher temperature than the bulk gases. If the flame can get closer to the wall the temperature gradient from the wall to the flame could become higher, even though the wall temperature was higher and the flame temperature is the same. It would appear, at first, that this theory is inconsistent with the measured data in that the mullite piston should have had a cooler surface than the zirconia and yet the mullite appeared to have higher heat transfer. There must, however, be a temperature of maximum heat transfer in Woshni's theory because as the wall temperature continues to increase to the point that the wall and flame are the same, the heat flux must go down. The mullite may therefore be a material which gives the poorest heat transfer characteristics because it heats the surface to a high enough temperature to allow further flame penetration but not high enough to decrease the temperature gradient. More analysis and experimental data are needed in order to confirm this hypothesis but it currently appears to fit the data reasonably well.

Differences in radiative properties of the ceramic and metal materials is another potential explanation for the observed data. Radiation in diesel engines is typically thought to account for 20 to 40 % of the total heat flux. Assuming the difference between the mullite and uncoated piston heat transfer was 30% as suggested by the cycle simulation, it would be difficult to attribute the cause to radiation. Radiation is a potential contributor, but is very difficult to analyze. The radiative properties of the piston material are constantly changing during operation due to deposits. Ceramic coatings are semi-transparent materials, while metal of an uncoated piston is opaque.

Yet another possible reason for the increased heat transfer is fuel or fuel vapor is trapped within the piston pores or between bumps and cracks on the piston surface. As a result, Beardsley and Larson [Ref 26] ran back-to-back piston experiments with sealed ceramic pistons. They reported an improvement in ISFC for their engine only after the sealed pistons were used, while unsealed pistons showed an increase in ISFC. If the porosity of the piston is capable of creating this effect then porous uncoated pistons should also have similar results. This was not the case when porous and roughened metal coated pistons were compared to uncoated production pistons (see 3.12.2 **Experimental Measurements on the Effects of Piston Surface Roughness and Porosity**). The conflicting information suggests more work needs to be done in this area.

Another possible explanation for the increased ISFC is the boundary layer heating theory. During the compression stroke the piston does work on all of the gas within the cylinder. If the gas near the piston is hotter than the gas in the middle of the chamber, it will begin to transfer heat to the wall sooner in the cycle. This can cause higher heat transfer because the near wall temperatures are higher than the bulk gas temperatures. This would seem to be particularly possible when the surface of the piston is rough and porous, trapping the air and heating it up. This heating would be expected not to show up with a metal coated porous or rough piston because the temperature would not be as high at the surface.

In summary, there are several possible explanations for the results, many of which have already been proposed and discussed in previous work. Studies of combustion characteristics using porous and rough metal pistons is expected to help determine whether the changes in combustion can be attributed to surface characteristics or if they are all piston surface temperature related.

#### **3.12.1.6 Conclusions**

- Back-to-back engine experiments comparing uncoated steel crown articulated pistons to separate pistons coated with 1.52 mm of yttria stabilized zirconia or mullite were conducted in order to compare engine performance and heat transfer characteristics.
- The data were taken in timing sweeps at four speed and load operating conditions. The data for the uncoated piston showed a scatter of approximately 3% between timing sweeps.
- Both the zirconia coated and mullite coated pistons showed an increase in heat release duration over the uncoated piston at advanced injection timing. ISFC for the zirconia coated and mullite coated pistons also increased in comparison to the uncoated piston as injection timing was advanced.
- The ISFC for the zirconia coated piston was approximately 3% higher at advanced injection timings. The ISFC for the mullite coated piston was approximately 8% higher at the most advanced timings.
- The difference in ISFC of the uncoated piston and the zirconia coated piston was small enough that an error analysis showed the difference to be of questionable significance, but the increase in ISFC of the mullite coated piston was measurable.
- An analysis of the ISFC increase using computer cycle simulation showed the increase in burn duration was not enough to account for the increase in ISFC. An increase in the heat transfer

### 3.12.2 Experimental Measurements on the Effects of Piston Surface Roughness and Porosity

In an effort to increase the efficiency of internal combustion engines, several researchers have investigated the potential of insulating the combustion chamber walls in order to reduce heat transfer. Such experiments include those conducted by Woshni et al. [Ref 19], Furuhashi [Ref 20], Morel et al. [Ref 22], Assanis et al. [Ref 24], Beardsley and Larson [Ref 26], Mueller [Ref 27], Hay et al. [Ref 28], and Huang and Borman [Ref 29]. A result repeatedly observed from those who reported heat release data from sprayed zirconia coatings was an increase in combustion duration which led to an increase in fuel consumption by reducing the amount of fuel burned near top dead center (TDC). Hay et al. [Ref 28] and Beardsley and Larson [Ref 26] have hypothesized the increase in fuel burning late in the expansion stroke may be attributed to fuel which was trapped in the porous ceramic piston coating. Furthermore, these researchers have hypothesized the surface properties of the ceramic coating may increase the heat transfer coefficient by affecting boundary layer development. If these hypotheses are correct, any porous or rough surfaced piston coating could be expected to similarly affect combustion. The primary difference between a porous metal coated piston and a porous ceramic coated piston would then be the higher surface temperature of the ceramic

Measurements have been made to determine the effect of piston crown surface properties on combustion and engine performance. In this set of experiments, steel crown articulated pistons were fabricated with porous and rough crown surfaces. Three porous surface metal coated pistons and one non porous, rough bond coated piston were compared to an uncoated piston. High speed measurements of cylinder pressure, injector needle lift and injector push tube load were recorded over a matrix of engine speed and load operating conditions. The test matrix matched the matrix previously run comparing ceramic coated pistons (see 3.12.1 **Experimental Measurements on the Effects of Piston Insulation**). Engine performance was evaluated by comparing injection timing sweeps of indicated specific fuel consumption (ISFC) versus the centroid of heat release. With these data, a comparison of the location of the centroid of heat release and the magnitude of the specific fuel consumption was obtained.

#### 3.12.2.1 Experimental Set-Up

A Cummins, L-10, 1.67 liter, single cylinder engine was used for the experiments. This engine was identical to the engine used for previous work with ceramic piston coatings (see 3.12.1 **Experimental Measurements on the Effects of Piston Insulation**). However, engine testing was performed in a different test cell not equipped for emission measurements. Cylinder pressure was measured with a water cooled AVL-QC32C piezoelectric quartz pressure transducer. The shaft encoder used was capable of 0.5 crank angle resolution. One hundred (100) cycles of cylinder pressure data were ensemble averaged for use within the heat release analysis. All heat release information presented is apparent heat release which is the net heat release or combined fuel heat release and energy lost due to heat transfer and blow-by. Injector needle lift was measured to determine the start of injection. Injection pressure was monitored by measuring injector push tube load with a strain gage.

Cooling water, combustion air, and lubricating oil flow and temperature were measured and controlled. Combustion air and fuel flow rates were held constant for each operating point. Fuel

flow rate was measured using a mass balance system. Data, such as lubricating oil and cooling water temperature and pressure, were recorded using a PC-based data acquisition system at a sample rate of 1 Hz.

A test matrix was designed for the four speed and load operating conditions shown in Table 3.12.5. This test matrix matches the matrix previously run using ceramic coated pistons (see 3.12.1 **Experimental Measurements on the Effects of Piston Insulation**). Injection timing sweeps were performed at each operating speed and load in order to define an ISFC versus centroid of heat release curve. The injection timing sweeps contained fewer timing points than the previous test matrix with the ceramic coated pistons and were taken in a slightly different manner. Each point in the injection timing sweep was taken twice – once as timing was advanced and once as timing was retarded. The uncoated piston was evaluated twice – once at the beginning of the test matrix and once after all of the other pistons had been tested. The entire matrix contained approximately 190 operating/injection timing points. A major objective of the matrix design was to collect sufficient data points to verify findings while minimizing the total number of points required so the shaft encoder and cylinder pressure transducer would not have to be replaced due to fatigue. The test design reduced potential errors in the measurements by eliminating the need to reset the shaft encoder phasing. Errors associated with ISFC and centroid of heat release measurements were previously discussed (see 3.12.1 **Experimental Measurements on the Effects of Piston Insulation**).

**Table 3.12.5:** Test matrix for back-to-back engine testing

Speed	Load	Timing
1200	Part	4 Injection Timings
	3.5 kg/hr fuel 86.2 kg/hr air	-21 through -5 cad Start of Combustion
1200	Full	4 Injection Timings
	7.1 kg/hr fuel 143 kg/hr air	-13 through -1 cad Start of Combustion
1800	Part	4 Injection Timings
	5.4 kg/hr fuel 181 kg/hr air	-21 through 0 cad Start of Combustion
1800	Full	4 Injection Timings
	7.9 kg/hr fuel 231 kg/hr air	-14 through 3 cad Start of Combustion

Five articulated, steel crown pistons were used in the engine tests: an uncoated piston (baseline), a rough bond coated, non porous metal (NiCr) coated piston, and three pistons with rough porous

metal coatings. The three porous coated pistons were fabricated with different porosity levels which will be referred to in this paper as high, medium, and low porosity coatings. The operating conditions run with each piston are presented in Table 3.12.6.

**Table 3.12.6:** Number of injection timing sweeps taken at each speed and load with each of the pistons

Piston Coating	1200 rpm Part Load	1200 rpm Full Load	1800 rpm Part Load	1800 rpm Full Load
Uncoated (Baseline)	2	2	2	2
Rough Coating	1	1	1	1
Low Porosity	1	1	1	1
Medium Porosity	1	1	1	1
High Porosity	1	1	1	1

### 3.12.2.2 Experimental Method

Detailed measurements of piston coating porosity and roughness were made and compared to their corresponding engine performance. The piston coating measurements required destructive testing. Therefore, two pistons were sprayed with a coating of each porosity and roughness; one piston was used for engine test and the other piston was used for coating measurements.

Coating porosity measurements were made using a mercury porosimeter. This measurement technique yielded the total open pore volume of the sprayed coating. These data were used to determine approximately how much fuel, air, or air-fuel mixture could possibly be trapped within the open pores of the coating surface.

Coating roughness measurements were made using a FACET™ surface characterization system. The FACET™ system incorporates a scanning electron microscope with an image processor to produce three dimensional topography measurements. For this work, the topography measurements were used to determine the root mean square (RMS) roughness,  $AR_q$ .

For each of the pistons tested, injection timing sweeps were used to create an ISFC versus centroid of heat release curve. The curves were then analyzed for changes relative to the uncoated piston. The example used previously will be repeated here briefly. The illustration of a computer simulated timing sweep was previously presented in Figure 3.12.1. The solid line in Figure 3.12.1 represents a typical timing sweep where ISFC is plotted as a function of the centroid of heat release. Note that ISFC decreases as timing is retarded until a minimum is reached just to the right of top dead center (TDC) near 3 crank angle degree (cad). For ideal



combustion (no heat transfer) the minimum would occur at TDC because the closer the fuel is burned to TDC the higher the effective expansion ratio resulting in maximum thermal efficiency.

The dotted curve in Figure 3.12.1 represents a timing sweep with heat transfer included. With heat transfer the ISFC curve shifts up and to the right. The upward shift is necessary but not sufficient to indicate increased heat transfer. As timing is advanced, heat transfer increases due to longer residence times for the hot burned gases. Heat transfer shifts the minimum toward more retarded timings. The magnitude of the shift in the minimum is an indication of the quantity of heat transfer.

An increase in the duration of heat release can also cause the curve to shift upward due to fuel which burns at the same centroid but further from TDC, resulting in higher fuel consumption. The increased duration tends to increase the total heat transfer because the duration of the combustion event is longer, allowing more time for radiation. A z-axis comprising combustion duration might then be imagined for Figure 3.12.1 which would show an increase in ISFC as the duration of the combustion event increases. This defines a surface above which instantaneous heat transfer increases and below which instantaneous heat transfer decreases. This line of reasoning, along with heat release analysis, were used to evaluate the effects of the various piston surfaces on heat transfer.

Photomicrographs of the low porosity coating and high porosity piston coating cross-sections are shown in Figures 3.12.21 and 3.12.22, respectively. The photomicrographs were taken from the bowl rim area of a piston crown simulation sprayed prior to spraying the test pistons. For all coatings, the porosity decreased near the center of the combustion bowl.



**Figure 3.12.21:** Photomicrograph of the low porosity coating.

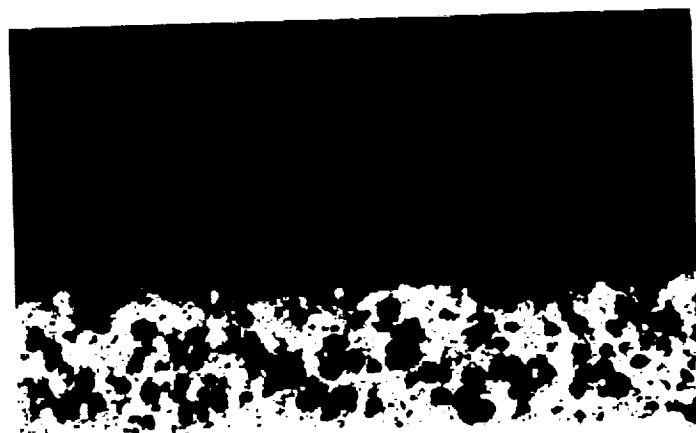


**Figure 3.12.22:** Photomicrograph of the high porosity coating.

Results of the piston coating porosity and roughness measurements are shown in Table 3.12.7. Three measured properties of the coatings are presented. The thickness indicates the depth of the coating on the crown land. The pore volume is the total open pore volume expressed as a percentage of the coating volume (see the Appendix IV for calculation of pore volume). The roughness ( $AR_q$ ) is the RMS average of the measured topography from a mean surface. The properties of particular interest are the pore volume and roughness. The pore volume is a possible storage area for fuel vapor which may prolong the combustion process and increase particulate. The roughness may affect fluid motion, heat transfer and boundary layer development. These properties will be compared with the combustion characteristics produced in the engine to determine their effect on combustion.

**Table 3.12.7:** Piston coating characterization

Piston Coating	Thickness (mm)	Pore Volume (%)	Roughness, ( $AR_q$ , $\mu\text{m}$ )
Uncoated (Baseline)	-	-	na
Rough Bond Coating	0.07	na	29.44
Low Porosity	0.60	29	53.73
Medium Porosity	0.70	46	24.62
High Porosity	0.60	48	44.80

### 3.12.2.3 Results

Test results comparing the uncoated piston with the rough bond coated and high porosity coated piston are shown in Figures 3.12.23 through 3.12.26. The figures describe the ISFC versus centroid of heat release curves at 1200 rpm, part load, 1200 rpm, full load, 1800 rpm, part load, and 1800 rpm, full load, respectively. In Figure 3.12.23, at 1200 rpm, part load, the injection timing sweep was not retarded enough to show the increase in ISFC.

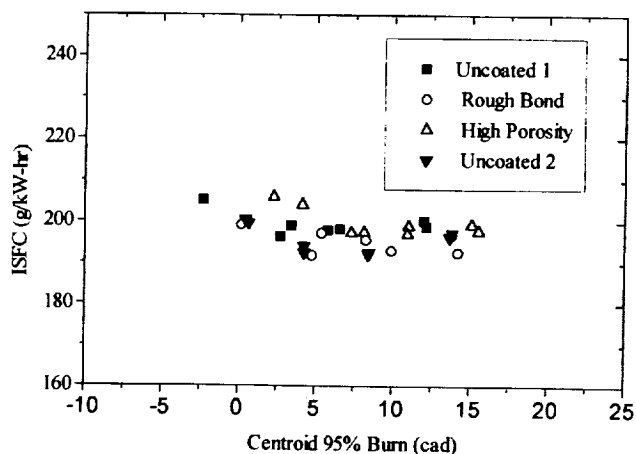


**Figure 3.12.23:** ISFC versus centroid for the uncoated piston, rough bond coating and high porosity coating at 1200 rpm, part load.

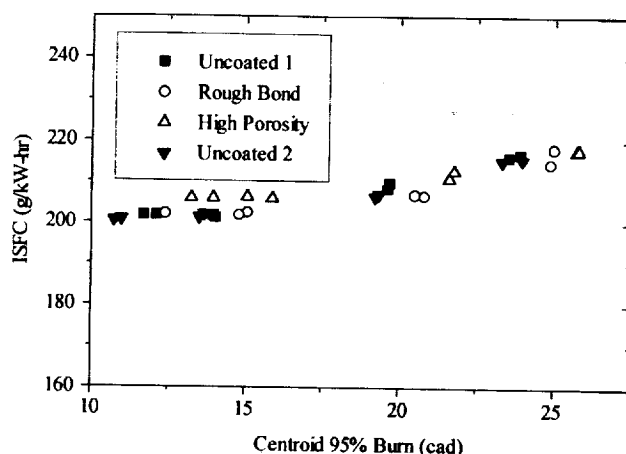


**Figure 3.12.24:** ISFC versus centroid for the uncoated piston, rough bond coating and high porosity coating at 1200 rpm, full load.

In Figure 3.12.26, at 1800 rpm, full load, the data exhibit less scatter. At each operating point, the data at a given injection timing are grouped together and the trend in centroid location and ISFC is clear. All of the points appear to be on the same curve indicating no change in heat transfer rate. However, the high porosity coating data points are shifted the furthest up the curve

to the right indicating a longer burn duration. The rough bond coating data points are positioned between the high porosity coating and the uncoated piston data points. A similar trend can be seen in the 1200 rpm, part load data. However, the trend is not as clear due to the scatter in the data. The scatter in the data is thought to have resulted from the fuel flow measurement which did not repeat well at the lower fuel flow rates. The engine operation was stable at these conditions as evidenced by consistent exhaust temperatures and in-cylinder pressures.

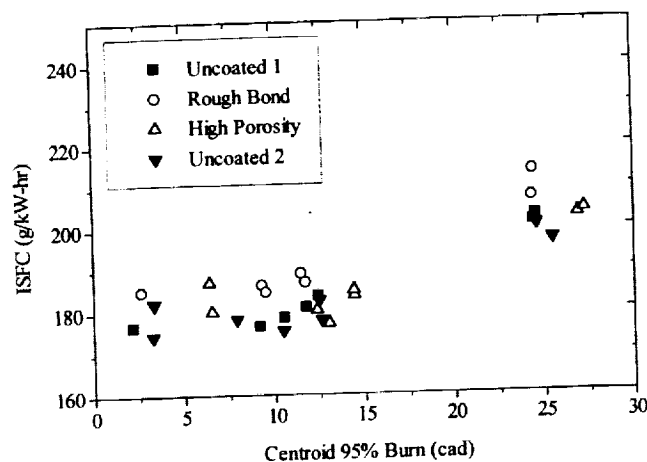


**Figure 3.12.25:** ISFC versus centroid for the uncoated piston, rough bond coating and high porosity coating at 1800 rpm, part load.

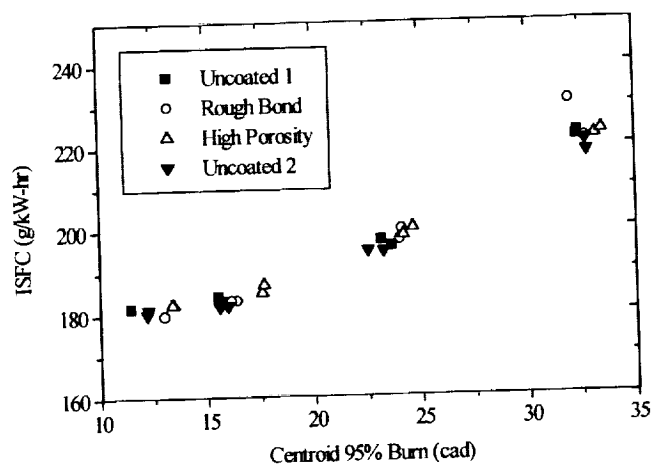


**Figure 3.12.26:** ISFC versus centroid for the uncoated piston, rough bond coating and high porosity coating at 1800 rpm, full load.

In order to see the data more clearly, the figures have been plotted after averaging the data at each injection timing. The results for all four speeds and loads are shown in Figures 3.12.27 through 3.12.28. In each of the figures it can be seen that the centroid of heat release for the high porosity coating is shifted to the right of the uncoated piston. The shift appears larger at the part load conditions where it is between 3 and 5 crank angle degrees while it is between 1 and 3 cad at

the full load conditions. The shift also appears to be independent of injection timing. The magnitude of the shift in centroid of heat release is similar to that observed in engine tests with mullite coated pistons as previously described (see 3.12.1 **Experimental Measurements on the Effects of Piston Insulation**). The rough bond coating also displays a shift in centroid of heat release but to a lesser extent in three out of the four operating conditions.

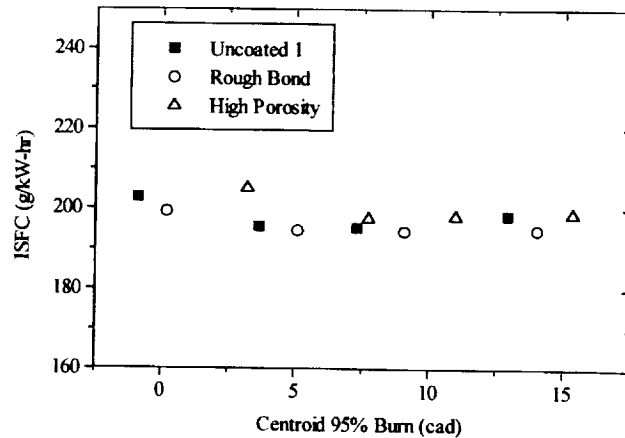


**Figure 3.12.27:** ISFC versus centroid for the uncoated piston, rough bond coating and high porosity coating at 1200 rpm, part load.

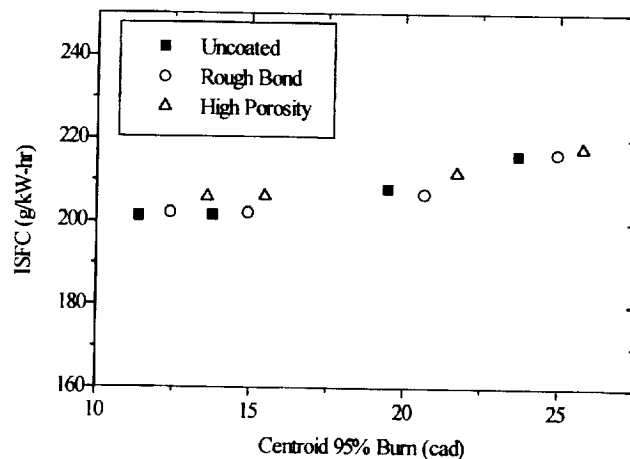


**Figure 3.12.28:** ISFC versus centroid for the uncoated piston, rough bond coating and high porosity coating at 1200 rpm, full load.

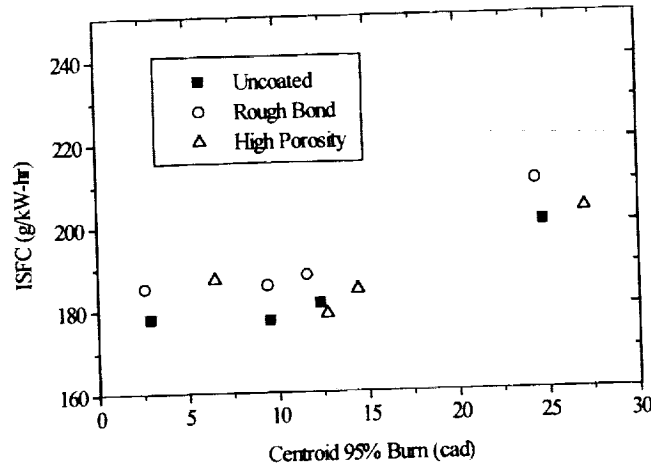


**Figure 3.12.29:** ISFC versus centroid for the uncoated piston, rough bond coating and high porosity coating at 1800 rpm, part load.

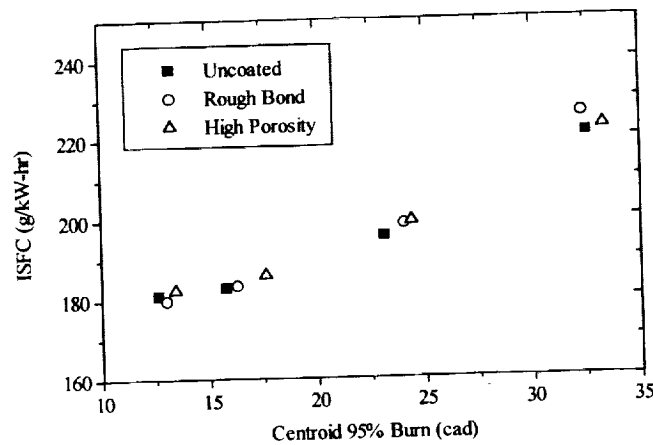


**Figure 3.12.30:** ISFC versus centroid for the uncoated piston, rough bond coating and high porosity coating at 1800 rpm, full load.

At 1800 rpm, part load, the centroid of heat release is not shifted and the ISFC is higher for the rough bond coating. This is inconsistent with the rest of the data set and the data were suspect. BSFC data for the 1800 rpm, part load operating condition are shown in Figure 3.12.31. In Figure 3.12.31, one can see the increase in fuel consumption observed in the ISFC versus centroid of heat release data is not present in the BSFC versus start of injection data. This difference between the ISFC data and BSFC data suggests the cylinder pressure transducer had not been properly operating during the 1800 rpm, part load test. It is possible the cylinder pressure transducer suffered a temporary reduction in coolant flow which affected the transducer's temperature and ultimately its response characteristics.

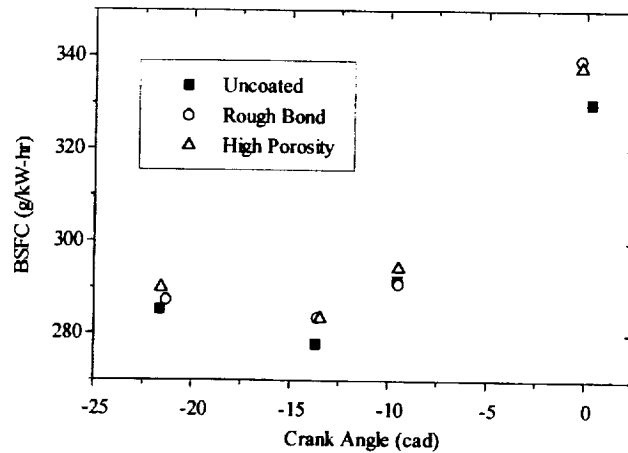


**Figure 3.12.31:** BSFC versus start of injection for the uncoated piston, rough bond coating and high porosity coating at 1800 rpm, part load.

Unstable engine operation was ruled out as the cause of the difference between ISFC data and BSFC data at 1800 rpm, part load. Figure 3.12.31 shows start of injection was very repeatable. The repeatability in the start of injection data was common at all engine speeds and loads tested. The repeatability in the start of injection data confirms the shift in the centroids of heat release observed in all previous data presented was not due to differing injection timing.

Although the data exhibit a shift in the centroid of heat release to later timings, there is little indication the characteristics of the ISFC versus injection timing curve are changed for the porous pistons in comparison to the uncoated pistons. In other words, the effect of the porous pistons is to cause the centroid to be shifted along the baseline ISFC versus centroid of heat release curve but not to create a curve shifted up or down in fuel consumption. The exceptions to this observation are seen at 1800 and 1200 part load at the most advanced injection timing. At these operating points the ISFC appears to be significantly higher (5%) than the baseline curve. Other differences in the ISFC versus centroid of heat release curve are smaller than the anticipated errors of the measurement.

The effect of the piston surfaces can also be identified in the heat release curves, which show how the combustion duration changed for the rough bond coated pistons at 1200 rpm, part load, and 1800 rpm, full load, as shown in Figures 3.12.32 and 3.12.33, respectively. At part load the difference between the pistons is large, while it is very small at rated load. At 1200 rpm, part load, the start of combustion and premixed burn fraction for the three pistons looks almost identical. However, the peak of the diffusion burn is lower on the rough bond coated piston and lower still for the high porosity coated piston. Fuel which is not burned during the peak appears to burn later during the tail of the heat release. At 1800 rpm, full load, the heat release differences are very small but maintain the same trends observed at part load.

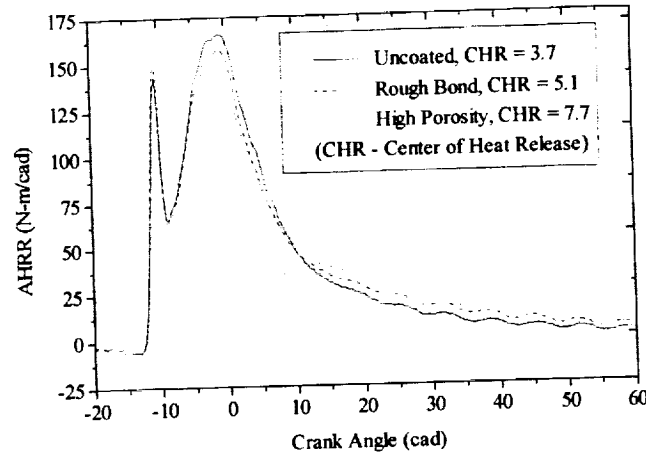


**Figure 3.12.32:** Apparent heat release rates for the uncoated piston, rough bond coating and high porosity coating at 1200 rpm, part load, -15 cad SOI.

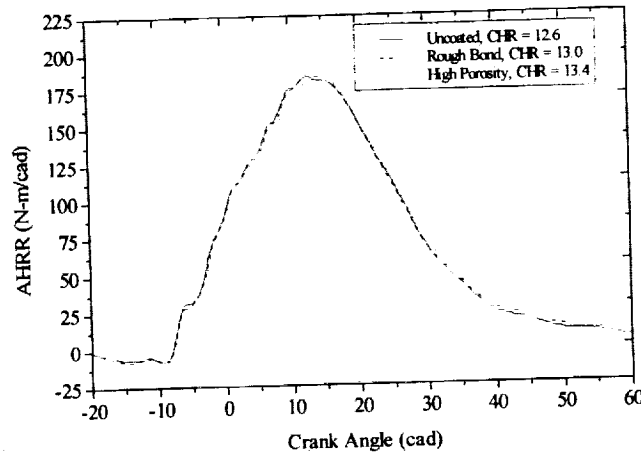


**Figure 3.12.33:** Apparent heat release rates for the uncoated piston, rough bond coating and high porosity coating at 1800 rpm, full load, -15 cad SOI.

The ISFC versus centroid of heat release curves for the three pistons of varying porosity are compared in Figures 3.12.34 and 3.12.35 for 1200 rpm, full load and 1800 rpm, full load, respectively. Both of the injection timing sweeps show no measurable differences among the three porous pistons. All three porosities caused a shift in the centroid of heat release. The shift does not appear to be consistently larger for any one piston in comparison to the others. The same results were observed at the two speeds and loads not shown. After collecting several data points from several pistons the uncertainty of the measurements become more clear. At 1200 rpm it appears that at advanced injection timings the ISFC is slightly higher for the porous pistons, but at 1800 rpm, full load, the injection timing curves of the uncoated and porous coated pistons appear to be the same.



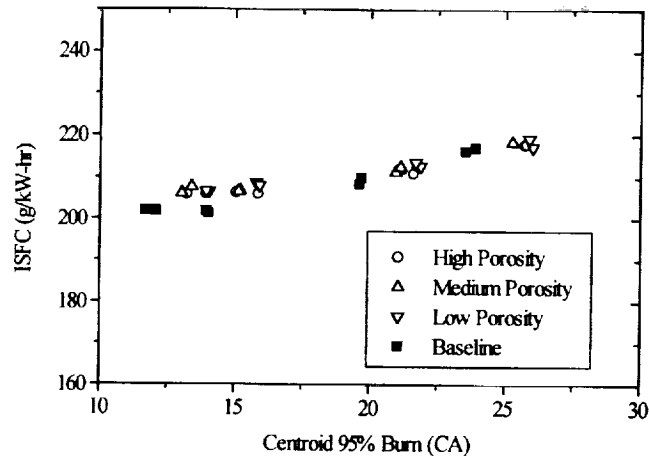


**Figure 3.12.34:** ISFC versus centroid for the high, medium and low porosity coatings at 1200 rpm, full load.

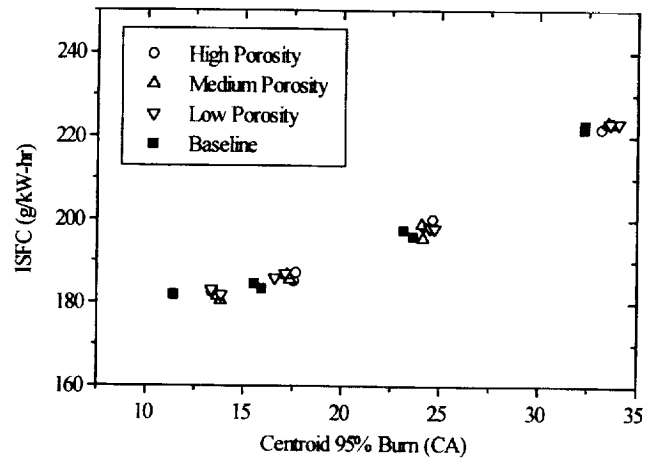


**Figure 3.12.35:** ISFC versus centroid for the high, medium and low porosity coatings at 1800 rpm, full load.

Heat release rates for the porous coated pistons are compared in Figures 3.12.36 and 3.12.37. As was indicated by the centroid of heat release locations, there does not appear to be any measurable differences among the pistons of various porosities on the heat release shape. While small differences occur at one operating condition, they are not consistently seen at others.

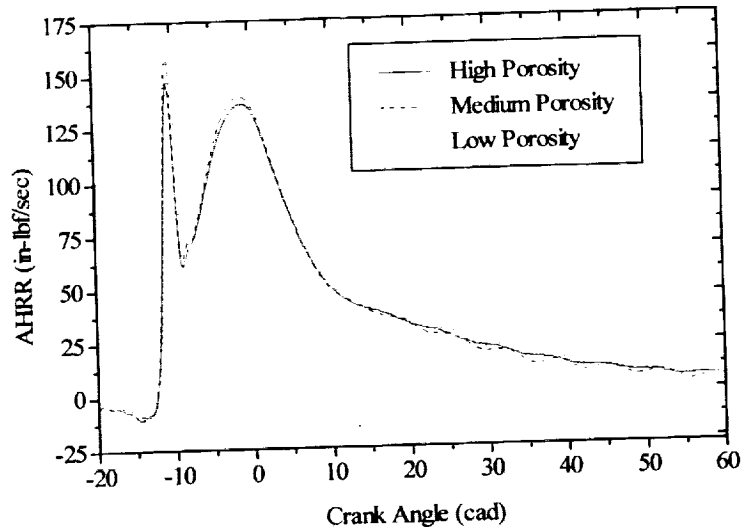


**Figure 3.12.36:** Apparent heat release rates for the high, medium and low porosity coatings at 1200 rpm, part load.

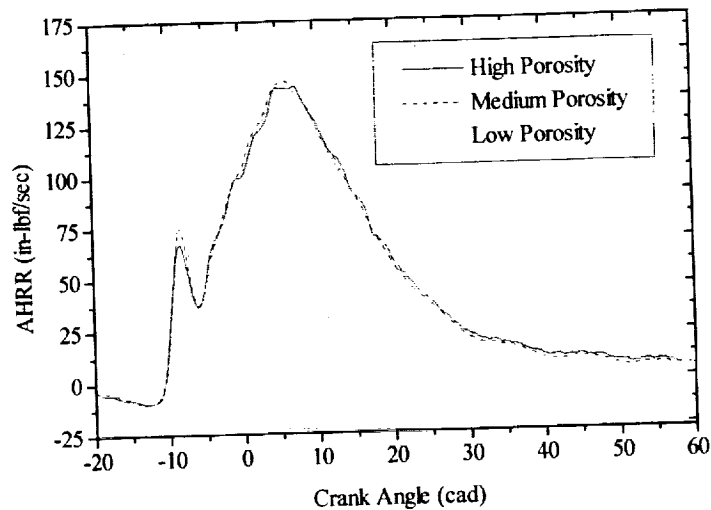


**Figure 3.12.37:** Apparent heat release rates for the high, medium and low porosity coatings at 1800 rpm, part load.

#### 3.12.2.4 Discussion of Results

The results clearly show surface properties can have an effect on the rate of heat release and, therefore, the performance of the engine. The shift in the centroid of heat release for the rough bond coated and porous coated pistons was slightly larger than the shift seen in previous experiments using ceramic coated pistons. Surface roughness alone was sufficient to prolong heat release rates but the porous coated piston, which also had a rough surface, resulted in the most prolonged heat release. Changing the amount of porosity did not appear to affect the heat release.

This would suggest the surface roughness was the more important parameter. However, this conclusion may be premature because of the limited porosity differences.

Due to the reduced rate of combustion, it can be assumed the fuel and air mix more slowly in the case of the porous coated and rough bond coated pistons. Some possible reasons include: fuel trapped within or near the piston surface, reduced bulk gas motion due to an increased friction coefficient, and reduced wall jet velocities due to increased wall friction.

Piston surface temperatures are thought to be high enough in diesel engines that fuel droplets impinging on the surface will experience rapid boiling and heat transfer to the extent the liquid does not touch the surface but rather the fuel vaporizes. This fuel vapor may be forced into the pores of the piston coating by compression and combustion pressures where it is unable to mix with oxygen in the bulk gas. The amount trapped would then depend on the volume of the open pores or the volume trapped in the valleys between the peaks on a roughened piston surface. The mass would depend on the total open pore volume and the piston surface temperature. If this were the case, pistons with ceramic coatings would be expected to trap less fuel than metal pistons of the same porosity and, therefore, the ceramic pistons would have less of an effect on the heat release. This was not the case for the mullite coated piston data previously presented (see 3.12.1 **Experimental Measurements on the Effects of Piston Insulation**) and the porous coated piston data presented here.

The bulk gas flow motion in the cylinder breaks down into small scale turbulence which enhances mixing. Increasing the friction coefficient of the piston surface could have reduced the swirl velocities and, therefore, reduced some of the source of fuel and air mixing. It is difficult to determine if this effect could be large enough without detailed modeling and testing.

The momentum of fuel and entrained air in the injector spray plume creates a vapor/gas jet which may be the dominant source of mixing phenomena at the wall. As the jet splits at the piston surface, momentum may be reduced by the rough or porous surfaces. The decrease in momentum would reduce the penetration of the jet along the piston surface which would lead to a decrease in mixing and heat release.

In any case, the reduction of porosity and surface roughness would appear to be desirable in order to achieve a reduction in heat release rate. An experiment run on polished pistons in a spark ignition engine was performed by Tsutsumi et al. [Ref 30] in which an increase in heat release rate was found. The increase was attributed to a reduction in surface area and heat transfer. Another possible consideration would be an enhancement of turbulent mixing or a decrease in the decay of turbulent mixing which enhanced the flame speed.

In the case of insulated pistons, the temperature near the wall might also have an effect on the wall jet or bulk gas wall velocities. As temperature increases the viscosity of air increases. More viscous air would then mix more slowly and impede the mixing process of the fuel jet.

The data presented here show little indication of an increase in heat transfer. The ISFC versus centroid of heat release curves are shifted slightly or not at all. Considering the primary difference

between the porous coated and mullite coated pistons to be the surface temperature, the higher surface temperatures may be thought to cause the increased ISFC. Surface area was increased considerably for the porous pistons but had little effect on heat transfer. This suggests there is little fluid motion near the wall on the scale of the surface deformations or that little fluid is being exchanged between the porous cavities and the bulk gas.

### 3.12.2.5 Conclusions

- Diesel engine tests were conducted to study piston crown surface effects on combustion and engine performance. Three rough and porous surface metal coated pistons and one non porous, rough surface metal coated piston were compared to an uncoated metal piston. The non porous rough surface piston and the rough surface high porosity piston each shifted the centroid of heat release to more retarded timings when compared to the uncoated piston. The centroid shift was larger at part load conditions and was independent of injection timing. The centroid shift was similar to that seen in previous tests with mullite (ceramic) coated pistons.
- The shift in centroid of heat release was greatest for the rough surface high porosity piston. However, there was little difference in the location of the centroid of heat release among three different porosity coatings. This result suggests surface roughness is the more important parameter.
- The porous and rough piston surfaces caused an increase in heat release duration. As with the shift of centroid of heat release, the heat release duration was longer at part load conditions and was independent of injection timing. The peak of the diffusion burn (apparent heat release) was lower for the rough non porous surface piston and lower still for the rough porous surface piston when compared to the uncoated piston. Fuel which is not burned during the peak appears to burn later during the tail of the heat release. There was little difference in heat release duration and diffusion burn peak among the three porous coated pistons.
- The results of this study indicate piston bowl surface properties such as porosity and roughness can have an effect on the rate of combustion for direct injection diesel engines. The reduction in porosity and roughness of piston coatings appears to be desirable in order to achieve a reduction in heat release rate and a corresponding improvement in engine fuel economy.

### 3.13 Variable Geometry Turbocharger

Transient response of heavy duty automotive diesel engines is highly dependent upon the capabilities of the air handling system. A turbocharger system with a variable nozzle turbine was selected, designed, and constructed for detailed evaluation. An advanced turbocharger control system was also designed and developed to minimize particulate emissions. The complete engine, variable geometry turbine, and control system was tested on the EPA transient cycle. A comparison to current production technology showed approximately 20% reduction in particulate emissions.

Diesel particulate emissions are created primarily when fuel and air are not mixed in the proper proportions. Much effort has been expended by engine manufacturers to improve fuel-air mixing by increasing injection pressures, air-fuel ratios, and air swirl, and by improving combustion chamber geometries. While these approaches can reduce steady state particulate emissions, they are not as effective for controlling transient emissions. During a transient load increase, it is relatively easy to have the fuel system rapidly increase the fuel delivered to the engine. Unfortunately, it is not easy to get the air handling system to rapidly increase the air flow. The following section summarizes work done to identify, design, build and test an advanced air handling system for a heavy duty automotive diesel engine to address the need for rapid transient air handling response.

The objective of this work was to develop the technology to optimize an advanced air handling system for low particulate emissions. The following specific goals were defined.

1. Reduce particulate emissions during the FTP transient cycle by 20%.
2. Reduce transient response time by 20%  
(This goal was modified and will be discussed later).

The engine selected for the project was the Cummins N14 engine with a rating of 460 HP. This was the highest automotive power rating manufactured by Cummins at the time this work was conducted. The logic for choosing this rating was that the total particulate reduction in grams would be largest for this engine. A brief summary of the specifications for this engine is given in Table 3.13.1.

**Table 3.13.1:** Specifications for the VG turbocharger test engine

Model:	Cummins 1994 N14
Fuel system:	Cummins CELECT
Power:	460 bhp @ 1800 rpm
Torque:	23% torque rise @ 1200 rpm
Turbocharger:	Holset twin flow

### 3.13.1 Systems Considered

The typical automotive diesel engine is turbocharged to increase power density and to provide a degree of altitude compensation. The primary object of the turbocharger is to provide an increase in intake manifold air density. There are many other air handling systems besides turbocharging which are capable of increasing intake manifold air density. A short study was conducted to identify the air handling system with the best potential for short term (3-5 years) implementation on heavy duty automotive diesel engines. Supercharging systems were discarded early in the study because they cause unacceptable fuel consumption increases on engines with high duty factors. The three most promising candidate systems involved turbochargers, and are discussed separately below.

The primary difficulty with turbocharging engines for automotive use is the wide range of speeds and loads which are encountered. The turbocharger turbine can be sized to provide the desired compressor power and boost pressure at one operating point. However, off-point operation suffers from either too much or too little boost. Conditions of too much boost pressure are intolerable from engine and turbocharger durability considerations. This forces the manufacturer to settle for a turbocharger-engine match which results in less than the desired boost at several conditions.

Sequential turbocharging is employed on at least one spark ignition automobile engine. This system involves two turbochargers and several control valves. The control valves connect or disconnect the turbochargers from the air handling system as required by the engine operating condition. At low engine speeds, one of the turbochargers is used to provide boost to the engine. When the operator demands additional power, this turbocharger provides additional air until its speed limit is reached. At this point, the second turbocharger is brought on line. Several valves are needed to ensure this process occurs smoothly. For example, one valve must shut off the exhaust gas to the second turbine when the turbine is not needed. The resulting package of two turbochargers and several control valves is substantially larger than a single turbocharger. The sequential turbocharging technique was discarded for this investigation because there are several truck customers who do not have the space in their engine compartment required for installation.

Two other turbocharging systems considered involved variable geometry turbines. The geometry of the turbine nozzle can be varied in such a way as to change the nozzle area. Changing the nozzle area to lower values at low flow rates increases gas velocity and, therefore, turbine speed.

There are two approaches which can be taken to vary the turbine nozzle area. The first method is to design a linkage to pivot each nozzle, thereby varying its angle. As the nozzles are pivoted to aim in a more tangential direction, their exit area becomes smaller, and higher turbine speeds will result from a given flow rate. Unfortunately, there are typically 12-17 nozzles, and all must be designed not to wear or stick over a wide range of operating temperatures.

The second approach to vary the turbine nozzle area is to vary the effective height of the nozzles. The scheme to vary the effective nozzle height is depicted in Figure 3.13.1. The part labeled "Moving Restrictor Plate" has machined slots which exactly match the shape and locations of the nozzles. The plate can then be moved over the nozzles to vary the gas passage height.

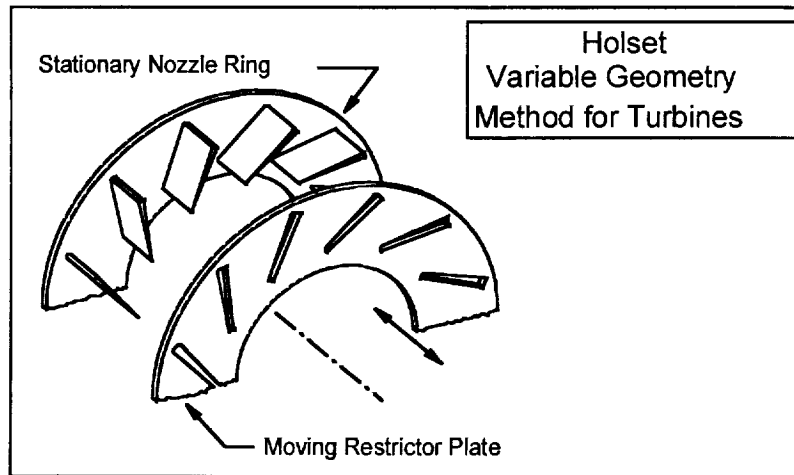


**Figure 3.13.1:** Sketch of scheme used to vary VG turbine nozzle height.

Testing has shown that the method of varying the geometry by changing the passage height will not give quite as good performance at far off-design conditions. However, this method offers only one hot moving part. This appears much more attractive from a viewpoint of long term durability. The moving restrictor plate method was selected for design and hardware development.

### 3.13.2 Turbocharger Design and Bench Test

The variable geometry turbocharger design requirements were as follows.

- Easy access to all connections
- No change in compressor components
- Water cooled bearings
- Must fit in customers' engine compartments (no change in overall size)

A photograph of the unit designed to meet these requirements is shown in Figure 3.13.2. Attached to the lower end of the bracket at the center of the unit is one of the air-operated actuator units used to move the turbine shroud. The addition of this bracket and the actuators did increase the overall size. However, the design was modified until there was no space conflict with other components in most existing customer installations.

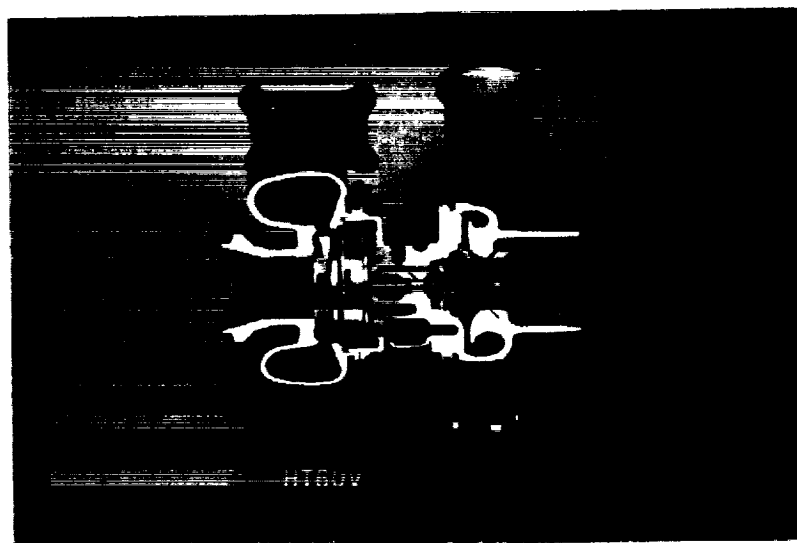


**Figure 3.13.2:** Cutaway of turbocharger with variable geometry turbine.

Figures 3.13.3 and 3.13.4 are close-up photographs showing the restrictor plate in two positions. Figure 3.13.3 shows the plate covering about one half the nozzle width. Figure 3.13.4 show the plate at its fully opened position.

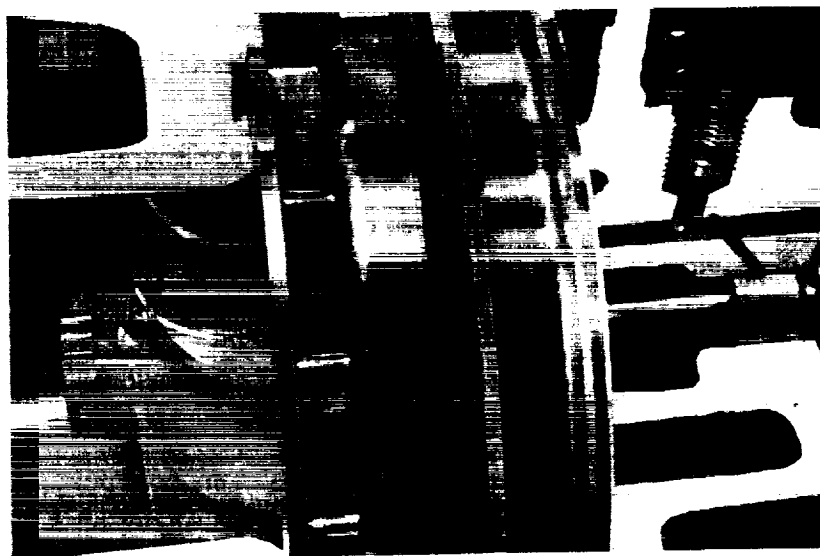


**Figure 3.13.3:** Close-up of partly opened VG turbine nozzles.



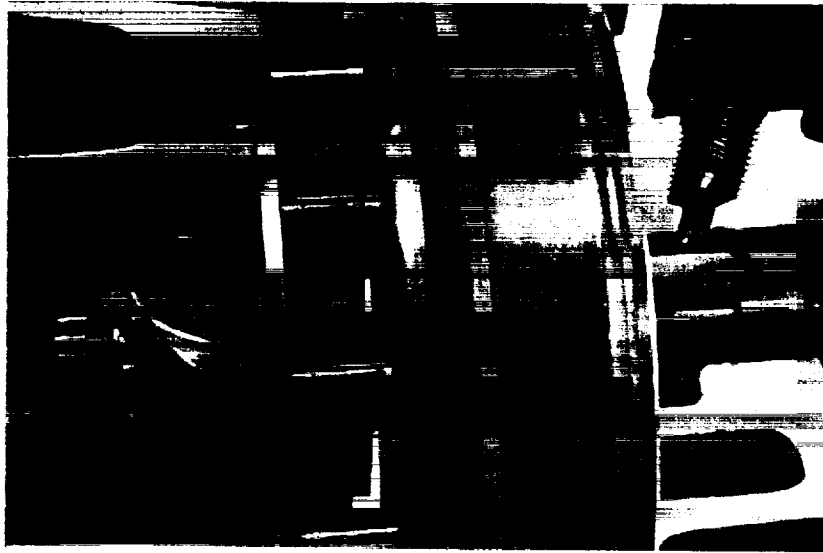


**Figure 3.13.4:** Close-up of fully opened VG turbine nozzles.

A series of performance tests were run with the turbine installed on a steady state gas test stand. The turbine performance was measured with the restrictor adjusted to eight different positions. The data from each of these tests was used to construct a performance map of the turbine. A typical turbine performance map is shown in Figure 3.13.5. The lines which tend to be approximately horizontal were obtained by holding the pressure ratio across the turbine constant and varying the turbine speed. The generally oval lines represent islands of constant total-to-static turbine efficiency.

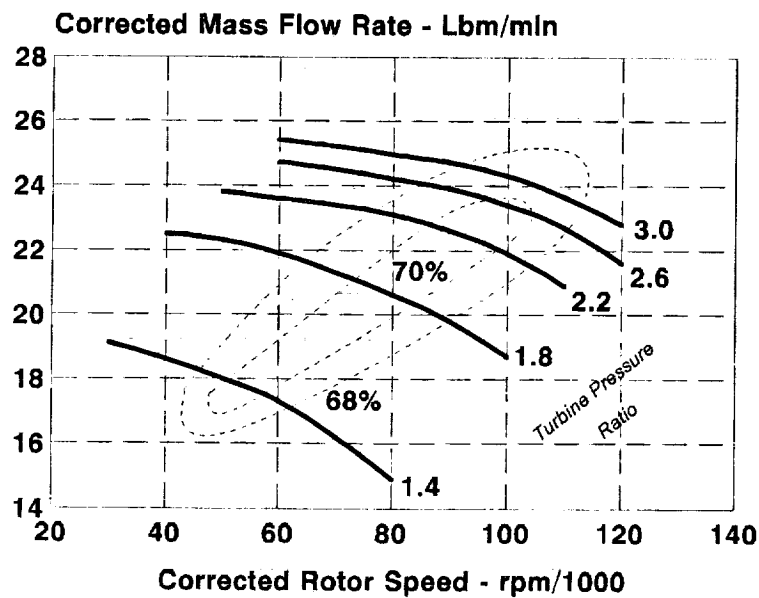


**Figure 3.13.5:** VG turbine performance map at one nozzle opening condition.

The performance of the turbine through a range of nozzle shroud positions is best shown in Figure 3.13.6. For this figure, the efficiency is shown as a function of the adjustable restrictor position with the pressure ratio being held constant at 2.0:1. This figure shows that the turbine efficiency deteriorates at small nozzle areas, but is still acceptable when the mass flow drops to about 50% of the wide open nozzle value.

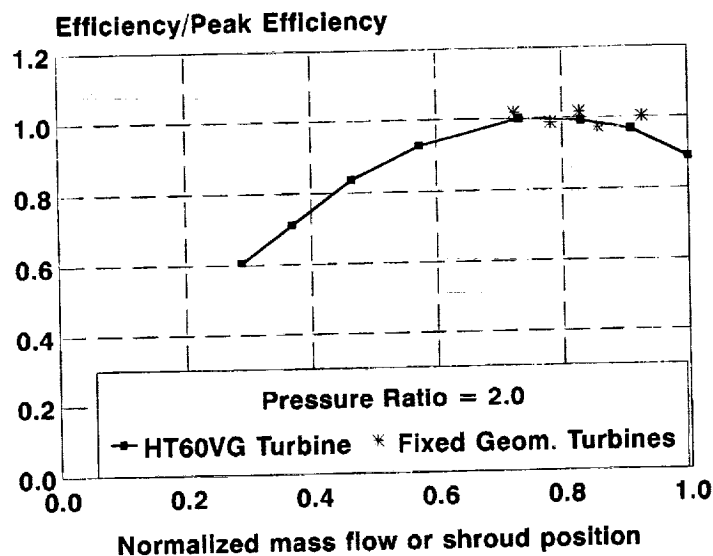


**Figure 3.13.6:** VG turbine performance at 2.0 pressure ratio, peak efficiency and several nozzle openings.

### 3.13.3 Control Strategy and Design

The control strategy development began with a detailed look at what would be required to optimize the variable geometry turbine for best emissions. It was decided that several iterations on the control parameters would be required, and it would be desirable to perform these iterations while the engine was installed in a transient emissions test cell. This meant the control software must be accessible and easily modified between transient test runs. It was decided to use an industrial grade personal computer as the heart of the control development system.

A fixed geometry turbocharger is matched to an engine to negotiate several limits at all combinations of speed, load and ambient conditions. Typical parameters which must be limited are shown in Table 3.13.2.

**Table 3.13.2:** VG turbocharger limiting parameters

Turbine inlet gas temperature
Turbocharger speed
Cylinder pressure
Engine manifold pressure differential

It is very difficult to provide reliable, durable, and inexpensive instrumentation to directly measure all the parameters shown in Table 3.13.2. However, by measuring other parameters, it was possible to develop software routines to compute the parameters shown in Table 3.13.2.

Figure 3.13.7 is a block diagram of the engine system showing the parameters which were measured and computed. The measurements that are made are mostly done in a friendly environment compared to the exhaust system or in-cylinder. The measured quantities are shown in bold type while the computed quantities are shown underlined. This technique reduces the system cost and greatly improves the overall system durability and reliability.

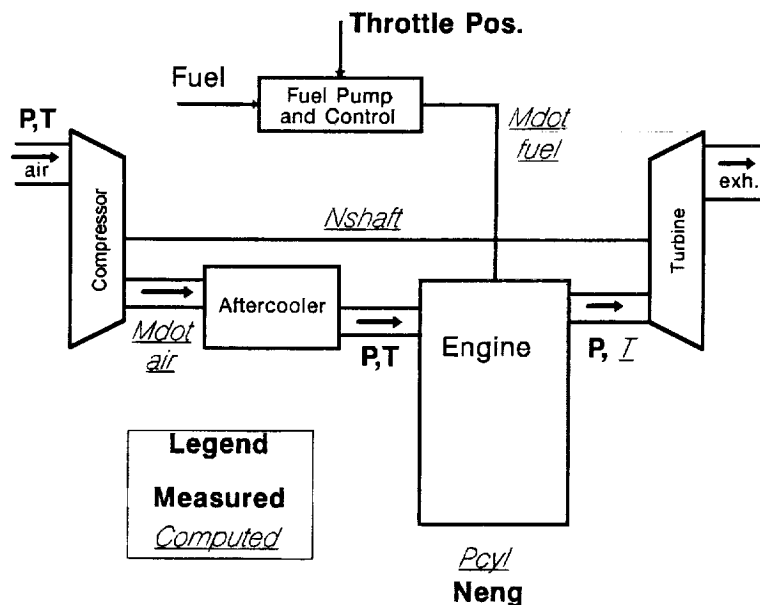


**Figure 3.13.7:** Block diagram of VG turbocharger engine system showing measured and compared parameters.

Under normal operation, the variable geometry control system uses a look-up table method to determine the desired air flow rate. Signals sent to a pressure control valve then cause the turbine nozzle shroud to move to the desired position. The table values can be optimized for any parameter including fuel consumption, emission levels, and transient response. The choice depends on the intended engine market.

The software calculates a number of other parameters which impose constraints on the desired airflow. For example, while trying to achieve a desired airflow rate, the software might sense that the turbocharger speed is about to go over its specified limit. The air flow control algorithm is then overridden by the turbo speed limiter control. Similarly, limits are in place for turbine inlet temperature, engine cylinder pressure, and engine manifold pressure differential.

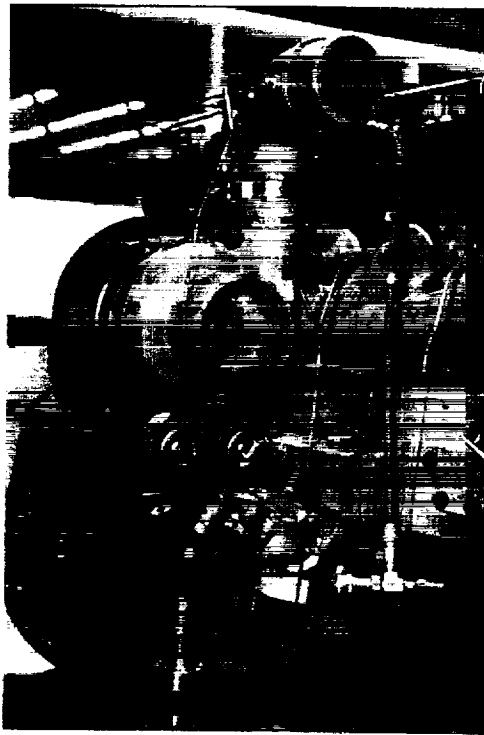
The variable geometry control algorithms run as a subset of programs in a larger controls environment used at the engine test cell. In addition to the industrialized personal computer, the system consists of a variety of signal processing boards, and the required output drivers. The entire system is contained in a portable, air conditioned cabinet which can be placed directly next to the engine within the test cell. The operator's monitor and keyboard are kept in a more friendly environment outside the cell. A photograph of the system is shown in Figure 3.13.8.



**Figure 3.13.8:** VG turbocharger control system

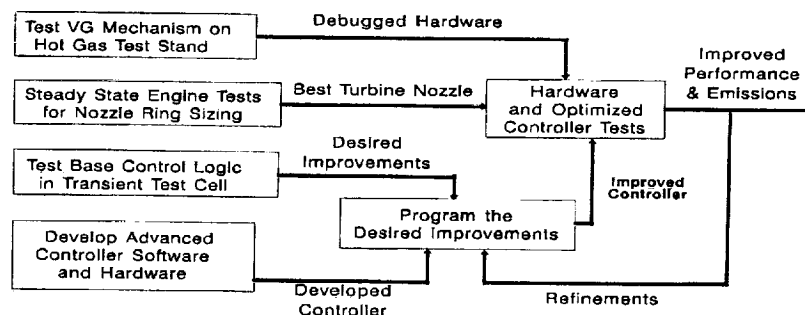
#### **3.13.4 System Testing**

Figure 3.13.9 shows the variable geometry turbocharger installed for testing on the engine. This figure shows how well the actuators were tucked underneath the turbocharger. This design resulted in no significant increase in overall engine envelope size.



**Figure 3.13.9:** VG turbocharger installed for testing on engine.

Testing was best accomplished in three different facilities. A block diagram of the test and development plan is shown in Figure 3.13.10. The hot gas test stand was used to check that the mechanism would not bind or wear during operation. The remaining tests were performed on running engines and are discussed in the following paragraphs.



**Figure 3.13.10:** VG turbocharger system test and development plan.

Much of the development testing was accomplished with the use of a conventional engine test facility with an eddy current dynamometer. It was possible to do some transient test work in this

cell. The eddy-current dynamometer tests were used to explore how to optimize the control system for the EPA transient test facility, which has a fully controllable electric dynamometer.

Figure 3.13.11 shows test results from the eddy-current dynamometer facility. For these tests, the engine speed was held as close as possible to 1200 rpm, and the throttle was snapped open from an idle condition. The original goal was to reduce transient response time by 20% when using a variable geometry turbine. It was decided to amend this goal to a 20% increase in torque output from the engine two seconds after the throttle was snapped open. This gives the same desired result. In addition, the experimental results are subject to much less data scatter.

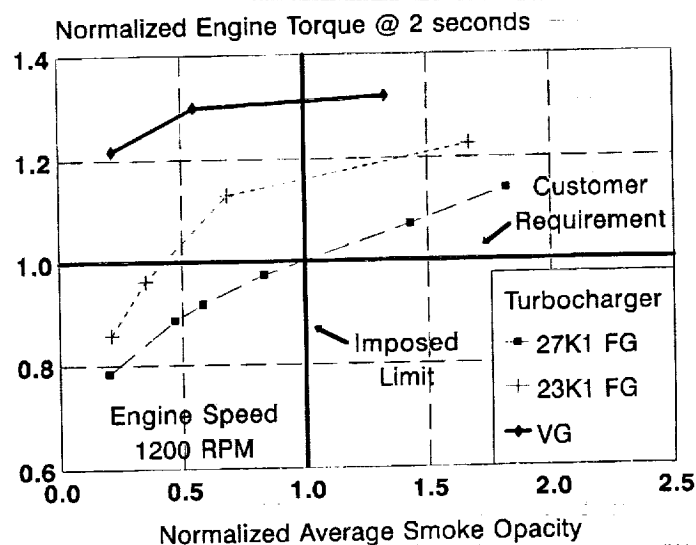


**Figure 3.13.11:** VG turbocharger test results from constant engine speed snap throttle testing.

Figure 3.13.11 contains information comparing the VG turbo test results to desired turbocharger characteristics. The vertical line at a normalized smoke opacity of 1.0 is a normalized average smoke over the two seconds of engine load pickup. This is the level of smoke which the engine emits when it is set up with a fixed geometry turbine and delivers an acceptable level of torque after two seconds. This torque level has been normalized to 1.0 and is the horizontal line labeled "Customer Requirement". An engine set up this way will pass the 1994 EPA transient cycle and will have acceptable "driveability" to a customer.

There is a curved dashed line passing through the intersection of the heavy horizontal and vertical lines. This curved line is labeled "27K1 FG" which signifies that the data on this line were obtained using a particular turbine nozzle size in a fixed geometry turbine. It is possible to adjust the production air-fuel controller to give the various performance levels shown on this line. With this turbine however, it is not possible to improve overall performance, which can only be done by moving both left and up in the figure.

The curved dotted line in Figure 3.13.11 is labeled "23K1 FG". This line shows the performance obtained with another fixed geometry turbine which has a smaller nozzle size. This turbine will

give a combination of both improved torque and reduced smoke. Unfortunately, it may not be possible to use this smaller turbine nozzle on the production engine because the turbocharger speed and the engine cylinder pressures may be too high.

The solid curved line in Figure 3.13.11 was obtained using the variable geometry turbine. This line shows the highest two-second torque levels and the potential for the lowest smoke opacity.

The engine was moved to the FTP transient test cell for final testing. The measured particulate data obtained in the FTP transient test cell were compared to the two-second torque levels obtained earlier to show the performance-emissions tradeoff. The data are presented in Figure 3.13.12. The vertical axis is the same as in Figure 3.13.11, but now the horizontal axis has changed to particulate measured during the 20 minute FTP test cycle. A trend similar to that shown in Figure 3.13.11 is evident. The variable geometry turbine has superior two-second torque, which can be traded off for lower dry particulate. The optimization of the controller was not exhaustive, and further improvements should be possible.

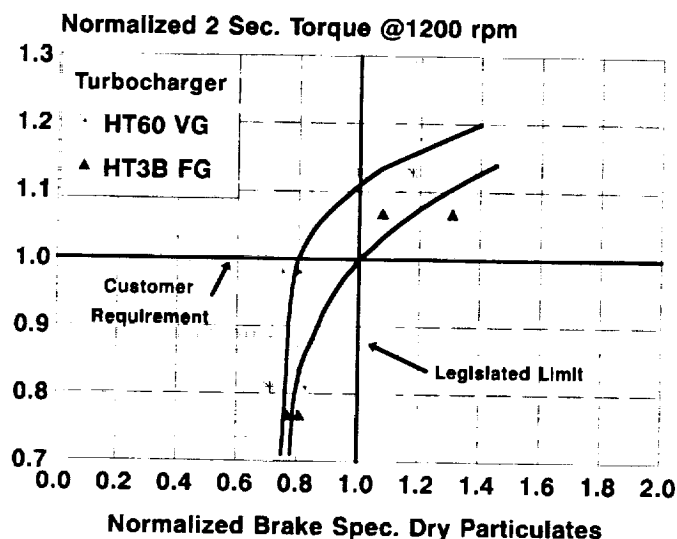


Figure 3.13.12: Results from VG turbocharger system tests on the FTP transient cycle.

### 3.13.5 Conclusions - Variable Geometry Turbocharger

- A variable geometry (VG) turbo can reduce particulate emissions while improving engine transient response.
- The VG turbo successfully reduced particulate emissions by 20%.
- Transient tests fell short of the project goal of 20% improvement in two second transient torque.
- Transient response should be improved with further development of the controller software.

### **3.14 Silicon Carbide Particulate Trap**

The Environmental Protection Agency (EPA) has determined that particulate from diesel powered vehicles represent a potential health hazard. As a result, regulations have been promulgated limiting the allowable amounts of particulate from those vehicles. The 0.1 g/bhp-hr particulate standard that applies to heavy-duty diesels became effective in 1994. Engine manufacturers met those requirements through the use of engine modifications and/or oxidation catalysts. EPA has established more stringent standards for diesel-powered urban buses because of health concerns in densely populated urban areas.

Particulate traps have been shown to significantly reduce carbon particulate emissions from diesel engines. However, current particulate trap systems are expensive and unreliable. Demonstration of a fiber based particulate trap coupled with a novel microwave energy regeneration system which address reliability and cost issues would greatly accelerate the introduction of this filtration technology into diesel engines.

#### **3.14.1 Filter Development**

Filtration of airborne particulate is accomplished by a number of mechanisms. The two dominant means are particle interception and diffusion. Particle interception occurs when the contaminant size is larger than the pores in a filter media which traps the contaminant. The dominant mechanism which affects the efficiency of an air filter is particle diffusion. Particle diffusion is best described by understanding that the path of an individual particle is random and does not follow streamline flow. The path of the particle is then much more likely to intersect the filter structure. When a particle intersects a fiber it is likely to remain trapped on the fiber surface. For example, the home furnace filter is effective in removing pollens and dust in the 10 to 100  $\mu\text{m}$  range even though the spacing in the filter is considerably greater.

An exhaust filter or diesel particulate trap must be designed to remove particles or soot on the order of 0.1 to 1.0  $\mu\text{m}$  in size. Experience with fiber based filter media has shown that fiber based systems are more effective than porous structures such as membranes or ceramic monoliths in terms of the efficiency and particulate capacity.

A microglass filter was used as a 'surrogate' filter element to examine the effects of a fiber filter on trapping efficiency and engine restriction. Microglass is available in a range of fiber diameters and material was chosen that was similar to the commercially available alumina and other ceramic fibers proposed for the particulate filter. Of course, the fiber and binder materials in this surrogate filter were not suitable for the high temperature regeneration.

Selection of a suitable microglass 'surrogate' media was based upon filtration efficiency and restriction. DOP (Di-Octyl Phthalate) smoke, a fine 0.3  $\mu\text{m}$  particle, is commonly used for testing HEPA and ULPA air filters and the particulate size is very close to that of exhaust soot. DOP smoke was used to estimate the efficiency expected in the particulate trap where a target range of 60-80% particulate removal had been established.



The air resistance can be used to calculate the restriction of an ideal filter element at various flows. At the rated horsepower the exhaust flow for the B5.9 liter engine is roughly 400 scfm or 11.3 cmm. An estimate of 0.5 kPa back pressure was calculated for a filter of 2 m<sup>2</sup>. This corresponds to the area that might be packaged in a cylindrical 15 by 15 cm element with a spiral wound design. Filters were then fabricated using 2 m<sup>2</sup> of media in a radial pleated element for testing. The annular elements were 23 cm outside diameter by 15 cm inside diameter and 24 cm in height. The media was supported on both sides by wire screen and consisted of 125, 3.5 cm pleats. This provided an effective area of 2 m<sup>2</sup> for the 'surrogate' samples. When tested at 11.3 cmm the restriction of these elements were 0.7 kPa which is close to the 0.5 kPa estimate.

Filter samples and a housing were tested at on single cylinder L10 (SCE L10) engine which was modified to produce particulate at a high rate, 2 g/bhp-hr or 32.5 grams per hour. While the displacement of the SCE L10 is about 30% of the B5.9 which is a target engine, the particulate generation rate was very close to the 0.2 g/bhp-hr of a 160 bhp B5.9.

The trapping efficiency and back pressure is shown in Figure 3.14.1. As expected, the initial restriction was very low. Restriction after 7 hours was about 25 kPa which has been targeted as the maximum allowable restriction before regeneration. It is expected that the restriction would rise more quickly on a larger engine with higher flow, but the result was encouraging. With the same loading and a three fold increase in flow, the regeneration interval could still be assumed to be greater than two hours. The efficiency began at better than 80%, dropped, then rose to a high of 90% and then declined to about 60% after seven hours. The decrease in efficiency was attributed to leakage at the filter endplates. The test does suggest, however, that the original estimate of 60 to 80% efficiency was reasonable.

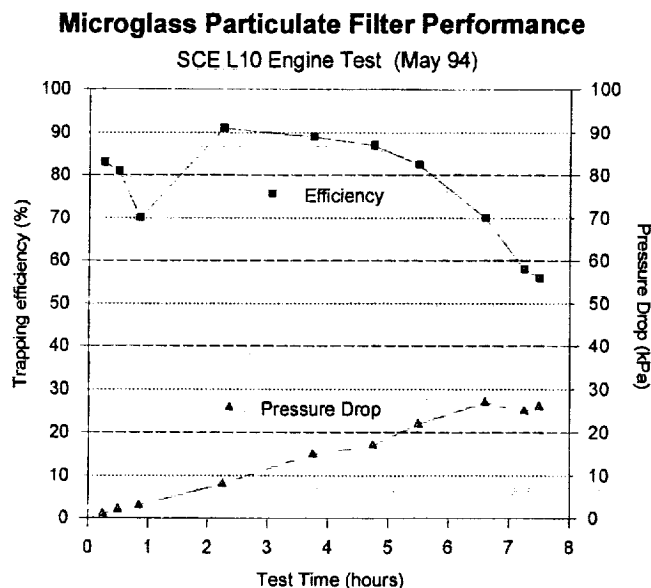


**Figure 3.14.1:** Efficiency and pressure drop versus time for a Microglass filter.

The results of the SCE L10 tests were encouraging and indicate that assumptions about filter performance were reasonable. The physical properties of a filter media to achieve the required performance in an exhaust particulate trap were confirmed during these tests. These physical parameters directed the development of a ceramic paper to be used with chemical vapor infiltration for a regenerable element.

Alumina fiber (ICI Saffil) was chosen to produce filter media for the diesel particulate filter. Information on the properties of silicon carbide coated alumina and its resistance to hot gas environments is known. This composite has demonstrated excellent heating in a microwave. However, unlike the microglass fibers, Saffil is available in a narrow range of products with an average fiber diameter of roughly 3  $\mu\text{m}$ . When the work began to duplicate the properties of the microglass paper with alumina fiber, many fiber samples were not suitable because of the short fiber length. The best results obtained were working with an unmilled bulk version of fiber designated Saffil RF.

Formulation work was accomplished by making small (30.4 cm by 30.4 cm) samples cast in a laboratory hand sheet mold. A fiber formulation was dispersed in water and then drained rapidly through a forming fabric or screen. The wet hand sheet was then blotted to remove excess water and dried on a hot surface. Additional difficulties with Saffil fiber were encountered at this point. Saffil is very weak in both wet web and dry strength and on its own has very high air resistance. In order to increase the permeability of Saffil fiber and add strength, other 'fugitive' fibers were required. Various binder fibers which are highly fibrillated and provide strength through entanglement in the web were examined. Chemicals resins to aid formation and wet strength were also tested. In order for the paper samples to have good 'fired' strength a thermosetting phenolic coating was added to maintain geometry during chemical vapor infiltration (CVI). The unknown affect of the coating on permeability and pore structure raised concerns during the design process.

Candidate samples coated at Oak Ridge National Laboratory received a 1 to 2  $\mu\text{m}$  CVI coating of silicon carbide. It was determined that the coating did not significantly alter the porosity or pore structure of the media. Roughly 20-25% fugitive materials were incorporated to add strength and improve the porosity of the media. The CVI coating effectively replaced the fugitive material producing samples with characteristics similar to the original paper.

Pilot paper machine trials have been conducted on a laboratory machine capable of making continuous Saffil paper. The goal was to produce sufficient amounts of Saffil papers for building filter prototypes. Additions were incorporated with the Saffil fiber to develop the green strength and porosity required for the particulate filter application.

Packaging density of the filter media is a primary concern since the filter must reside within a microwave cavity. The basic filter shape is a cylinder 15.2 cm in diameter and 15.2 cm in length. The construction considered is that of a single face corrugated or pleated media to be spiral wound, Figure 3.14.2. This geometry requires the ceramic paper be either formed into a sinusoidal or pleated arrangement and then alternately sealed between flat layers of material as it is wound.

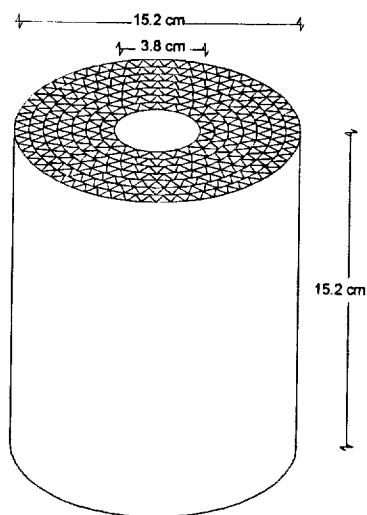


**Figure 3.14.2:** Microwave particulate filter dimensions and geometry

Media properties will affect the ability to produce an element of ideal geometry. The samples, fabricated by Fleetguard, have used the pleated design with triangular cells of approximately 6 mm on each side and a material thickness of 1.6 mm. The estimated area is 1 m<sup>2</sup>. Work is underway to improve the base paper, making it thinner and allowing for smaller pleats or possible fluting. This will give an increase in the packing density of 2 to 3 fold. The immediate goal is to reach the original target of 2 m<sup>2</sup> with 1 mm thick media and a 3 mm pleat.

With the pleated or corrugated configuration, it is necessary to seal the alternating ends of the cells to create a flow path as shown in Figure 3.14.3. Ideally, one edge would be sealed as the pleated and flat sheets are combined and then the opposing end sealed as the element is wound. This requires a sealant that will withstand the chemical vapor processing without opening up the flow path. A sealant composed of milled Saffil, vinyl acetate and powdered phenolic resin has been tested with some success.

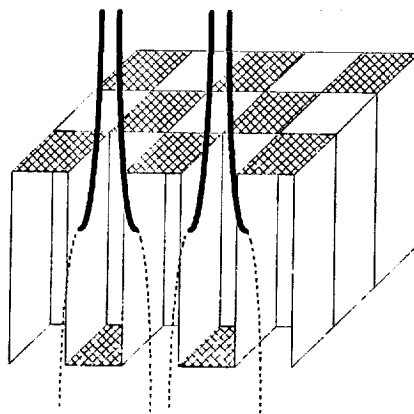


**Figure 3.14.3:** Gas flow through filter media.

The samples fabricated from the pilot machine trials have been submitted to both Oak Ridge National Laboratory and Composite Innovations Corporation. The prototypes to ORNL were somewhat smaller in diameter due to the furnace size limitations. The samples coated by Composite Innovations Corporation were full size. The weight of the full size filter prior to infiltration was approximately 300 grams with sealant. Due to the weight loss of fugitive material in both the media and sealant the finished weight was also approximately 300 grams.

The element mass is much lower than the extruded ceramic traps currently available and provides more rapid heating. The elements are also resilient, although not extremely strong at this point in the development. As completed filters of better geometry become available, strength and durability testing will commence. A Composite Innovations Corporation coated filter is shown in Figure 3.14.4.

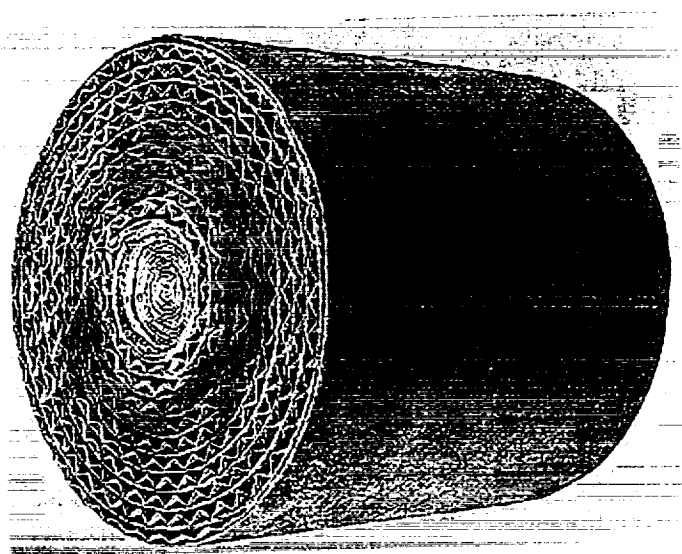


**Figure 3.14.4:** SiC coated alumina fiber filter.

### 3.14.2 Microwave Heating

Several filter prototypes were provided to FM Technologies, Inc. for heating experiments using the cylindrical applicator design. A 2.45 GHz microwave source was used in these experiments. The microwave energy was directed to the applicator using WR284 waveguide and the incident and reflected power were monitored during heating. Thermocouples were placed inside the filter at three positions along the axis of the cylinder to obtain a measure of the axial temperature profile. These thermocouples were inserted through small holes drilled in the cavity wall, thermal insulation, and the filter in such a manner that the thermocouples could be moved in and out to determine the radial temperature profile as well. Figure 3.14.5 shows the positions of the thermocouples and shows the heating data near the top and center of the filter. The filter was

heated to regeneration temperature in less than 5 minutes with only 750 Watts of input microwave power. However, the axial temperature gradient between T1 and T3 exceeded 200 °C.

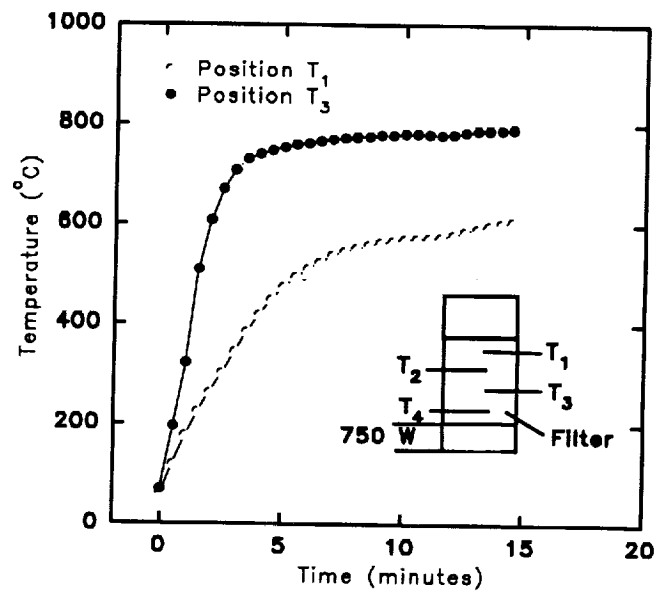


**Figure 3.14.5:** Microwave heating showing large thermal gradient.

The radial temperature gradient was similar in magnitude to the axial gradient. In order to minimize the thermal gradient, a microwave feed system was developed. The heating results using this system, with 750 Watts of input power, are presented in Figure 3.14.6.

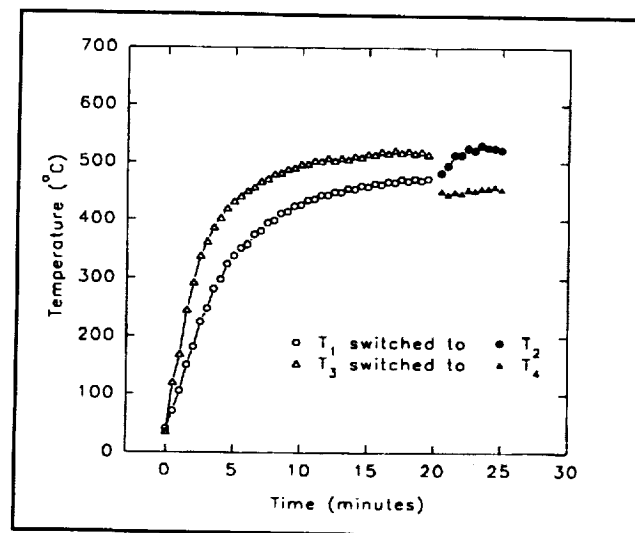


**Figure 3.14.6:** Improved thermal gradient.

The thermocouple locations were the same as indicated previously, but data from all four thermocouples are presented. The heating rate is reduced slightly, but the uniformity of heating is now excellent, with an axial and radial variation of approximately 100°C.

The data shown in Figures 3.14.5 and 3.14.6 were obtained in FMT's laboratory using a microwave applicator that was fabricated from a 17.5 cm outer diameter brass tube. The microwave applicator ends were removable perforated brass plates. The end plates were removed, the prototype filter was wrapped in a blanket of high temperature alumina insulation, which was inserted into the tube, and then the end plates were reattached.

### 3.14.3 System Evaluation

In order to allow testing of the microwave regeneration method with a carbon-loaded filter under engine conditions in a test cell at the Cummins Technical Center, the filter was put into a stainless steel 'can' following current exhaust system practices in the diesel engine industry.

The canned prototype filter was returned to FMT, and a microwave feed system was installed. The canned filter was heated with FMT's microwave system, which supplied 1 kW of electrical power to the magnetron. To validate laboratory results a proof of concept evaluation was planned for the microwave filter system, as shown in Figure 3.14.7.

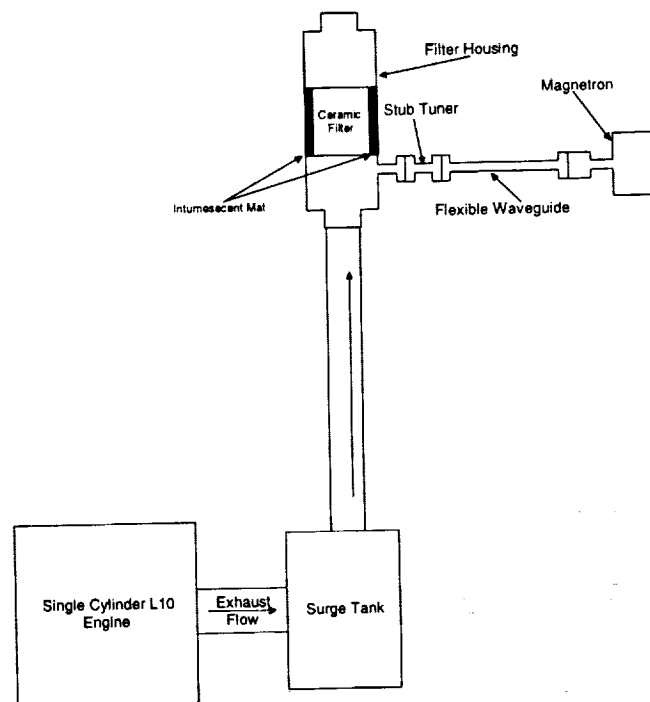


**Figure 3.14.7:** Test cell evaluation of microwave particulate filter.

The primary objective of the evaluation was to determine if a microwave filter could, in fact, oxidize particulate (regenerate) from a diesel engine. Two distinct evaluations were conducted to

assess the regeneration capability of the microwave system. The first evaluation assessed regeneration capabilities without exhaust flow. The engine was operated for ten hours at 1500 rpm producing 17.2 kW. During this period engine back pressure was monitored but not recorded. At the end of the loading period the engine was switched off and power to magnetron was engaged. The absence of exhaust flow required the injection of air to provide sufficient oxygen to oxidize carbon.

The second evaluation measured the systems ability to regenerate while the engine continued to operate. Once the back pressure doubled, engine operation was set to idle (800 rpm) and power to the magnetron was engaged.

Two methods used to detect regeneration include 1) temperature and 2) exhaust manifold back pressure. Thermocouples inserted into the bed of the filter recorded temperature spikes which could indicate regeneration. Although temperature measurements provide adequate detection capabilities, back pressure measurements provide more useful information. Back pressure readings can signal when to start the regeneration process and the effectiveness of the process. Traditionally Cummins has initiated regeneration once the back pressure doubles its starting value at the same operating condition. The 2x rule allows collection of sufficient particulate to produce a measurable event without melting the filter because of the extreme exotherms associated with carbon oxidation.

Testing without exhaust flow demonstrated that it was possible to heat a filter system to the temperatures necessary for regeneration by microwaves. Time and temperature history of the three thermocouples, Figure 3.14.8, show the center region achieved temperatures necessary to oxidize carbon.

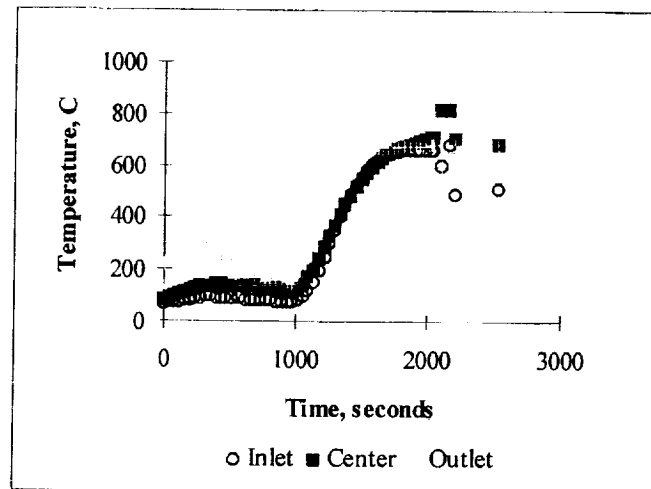


**Figure 3.14.8:** Magnetron power turned on at 1000 seconds.

The temperature fluctuations during the first one thousand seconds reflect system integrity evaluation and leak check using partial power. After applying full magnetron power, temperatures increase rapidly to 600°C and began leveling, an indication of insufficient oxygen. Terminating the exhaust flow also decreased air supply to the filter. An injection of ambient air into the system resulted in a temperature spike to 760°C; the sudden increase suggest carbon oxidation. A second injection resulted in cooler temperatures suggesting completion of the reaction. Results obtained attempting to regenerate in the presence of exhaust flow proved very positive.

Figure 3.14.9 details the time history of both temperature and engine back pressure readings. Prior to dropping the engine to low idle the back pressure measured 18 kPa and temperature readings exceeded 425°C. Cooler exhaust temperatures associated with idling slightly decreased filter temperatures. However, within seconds of switching on the microwave power, temperature of the center region increased very rapidly to 760°C, the inlet and outlet temperatures increased slightly. Twenty five seconds after peaking at 760°C the center temperature decreased and all temperatures converged to 425°C, the same as before the temperature spike. A review of exhaust back pressure results indicates a 50% decrease occurred after the temperature spike.

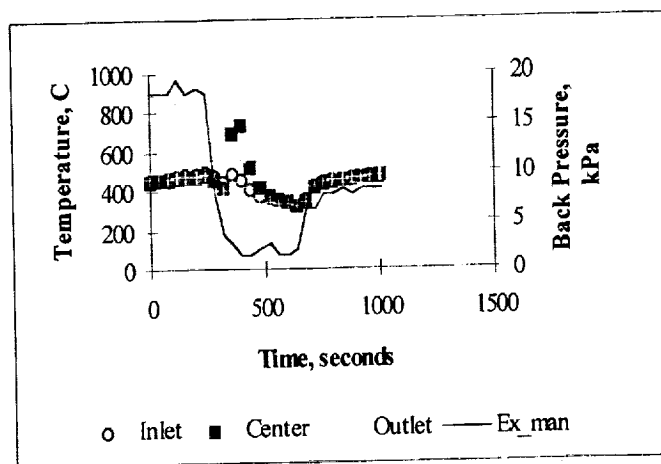


**Figure 3.14.9:** Temperature increase observed at engine idle speed with magnetron powered.

### 3.14.4 Economics

Estimates of filter costs were obtained for 50,000 and 100,000 units per year. These estimates range from \$1000.00 to \$1500.00 for complete filters. It is too early to realistically estimate manufacturing costs, but these initial estimates provide incentive to continue the investigation. As a comparison, a cordierite wall flow filter with diesel burner was estimated to be in the same dollar range. The diesel fired burner, however, has numerous drawbacks. Thermal stresses in the cordierite filter were too high for the cordierite concept to survive heavy duty diesel applications.



During the course of the program, the potential health risks in working with silicon carbide whiskers, and the high cost of whisker materials necessitated the investigation of other ceramic fibers that did not have the disadvantages associated with the silicon carbide whiskers. Through Cummins internal funding, other fiber systems were obtained which consisted of oxide fibers with a chemical vapor deposited silicon carbide coating. The coating was observed to couple readily with a 2.45 GHz microwave energy and permits a new avenue for particulate trap development.

#### **3.14.5 Conclusions - Silicon Carbide Particulate Trap**

- A composite particulate filter has been developed which is heated using microwave energy. Temperature measurements indicate that the temperatures achieved were sufficient to oxidize diesel particulate without exhaust flow.
- Back pressure and temperature data strongly suggest the occurrence of regeneration during low idle engine operation. A key concern is the detection of the regeneration event. Back pressure and to a lesser degree temperature readings are indicators of the regeneration event. However, localized heating in the filter may go undetected.
- Improved methods of detecting regeneration of the filter are required for development purposes.

### 3.15 *Lightweight Low Magnetic Signature Engine Development*

Traditionally diesel engines have been manufactured from predominantly ferrous materials due to performance and durability demands. The objectives of this research program were to develop the analytical methods, materials, manufacturing technology and engine components for lighter weight, reduced magnetic signature diesel engines without sacrificing performance or durability. It was not the objective of the program to develop a production engine. However, in order to validate and calibrate the analytical tools developed it was deemed necessary to build an engine which could be evaluated. The Cummins 6B engine was chosen for this study for a number of reasons including availability of tooling and cost effective manufacturing of prototypes.

During this first year of the program several deliverables were completed including the building and testing of an engine with an aluminum head and block. A similarly configured engine was delivered to the Navy along with a baseline cast iron engine for noise and magnetic signature measurements. Analytical models for the head and block were developed and calibrated against running engine data. These models were used to study the effect of including reinforcement in the combustion face of the head and in the main bearing saddles of the block. The model identified weak areas in the block in the main bearing saddle which were confirmed by engine testing and structural mechanics testing. Further modifications to the model were made to better define the loads in the block in the region of the failure location.

#### 3.15.1 Aluminum Cylinder Head Analysis

The objective of this analysis was to investigate the potential for casting the cylinder head of the Cummins 6B engine from an aluminum alloy by developing a baseline single cylinder sector model of the engine using current casting dimensions. The cast iron baseline model would incorporate assembly, thermal and peak cylinder pressure loads, and representative cast iron properties. The change in results of applying aluminum material properties to the same model would be the basis of any design recommendations for an aluminum head. This initial piece of work was carried out as part of a Cummins funded project and provided a basis for the more extensive analysis conducted under this contract.

In the initial stage of the work a solid model of the head was created using ProEngineer, ProMesh and COSMOS. The head was modeled using cast iron (baseline) and aluminum properties as given in Table 3.15.1.

**Table 3.15.1:** Material properties

Material	Elastic Modulus (GPa)	Conductivity (W/M.K)	Poisson's ratio ( $\mu$ )	Coeff. of thermal expansion ( $\alpha/^{\circ}\text{C}$ )
Cast iron	103.4	0.355	0.26	13
Aluminum	72.4	1.09	0.33	20.9

The baseline model was calibrated using experimental data from a Cummins 94 B-Series 186 kW engine. The predicted results were shown to be in good agreement with the measured values around the valve bridge. Figure 3.15.1 shows the calculated temperature distribution of the cast iron firedeck, where the maximum temperature in the valve bridge was on the order of 253°C.

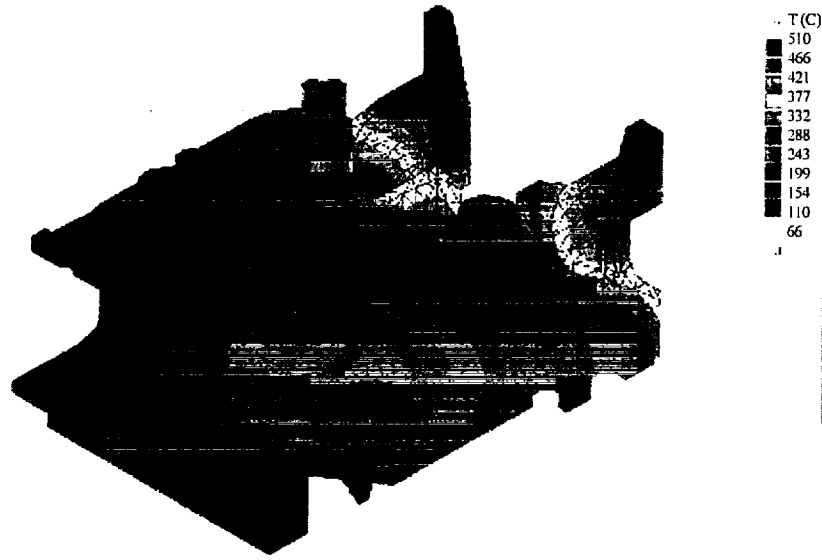


**Figure 3.15.1:** Temperature distribution for the cast iron firedeck.

The calculated stresses from cylinder pressure appeared to be relatively small compared to the stress from assembly and thermal gradients. However, for the aluminum the temperature distributions were more uniform. Therefore the thermal stresses were lower in the aluminum. Local yielding was expected at the capscrew locations in the aluminum cylinder head and redesign or modification is needed in this area.

When aluminum properties were used in the model, the results of this analysis showed that the valve bridge temperature was lower in the aluminum than in the cast iron and that the stresses were reduced by approximately 62%, as shown in Table 3.15.2.

**Table 3.15.2:** Temperature and stresses between valve ports

Material	Temperature (°C)	Von Mises Stress (MPa)	
		Assy & Temp.	Assy; Temp. & PCP
Aluminum 339	205	52	58.9
Cast iron	292	162	155

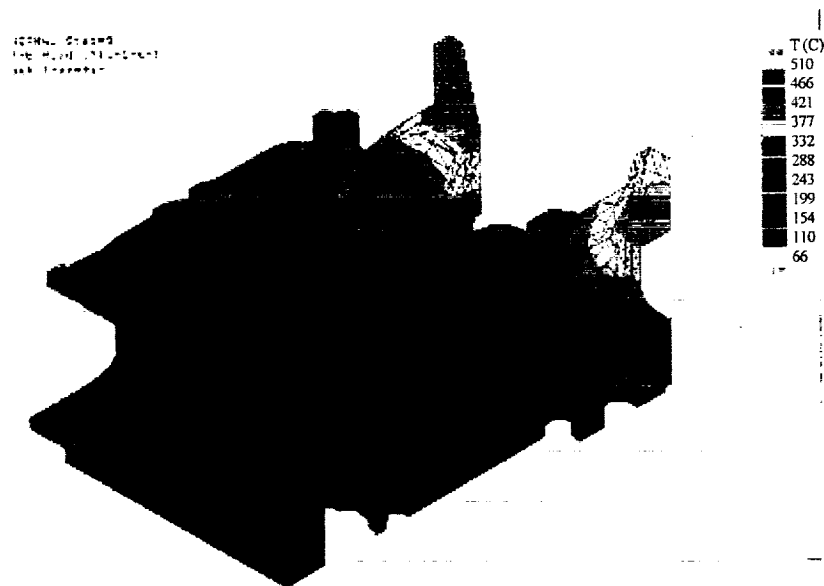


**Figure 3.15.2:** Temperature distribution for the aluminum firedeck.

The hottest region of the cylinder head was shown to be the exhaust flange which was approximately 498°C. Figure 3.15.2 shows the predicted temperature distributions for the aluminum cylinder head where the maximum temperature was 406°C in the flange. From this analysis it was concluded that the temperature in the exhaust port flange was excessive for the aluminum and will have to be redesigned to provide cooling to the entire port.

This initial Cummins funded model was a relatively coarse representation of the head which provided reasonable temperature estimates. However, to accurately predict stresses in the valve bridge region it was necessary to have a much finer mesh density. A local model of the deck face with a much finer mesh density was assessed against a range of boundary conditions in order to check for sensitivity to the boundary conditions. It was found that the local model was not very sensitive to the rest of the material and it was concluded that the local model could be used for the next steps in the analytical work. This work was undertaken as part of Task 9 of the DOE In-Cylinder Components contract.

The local model was essentially made up of four parts, the deckface, intake valve seat, exhaust valve seat and a bow tie insert in the valve bridge region. The shape of the valve bridge insert prompted the nickname “bow tie” and the resulting 3-D mesh geometry is shown in Figure 3.15.3.

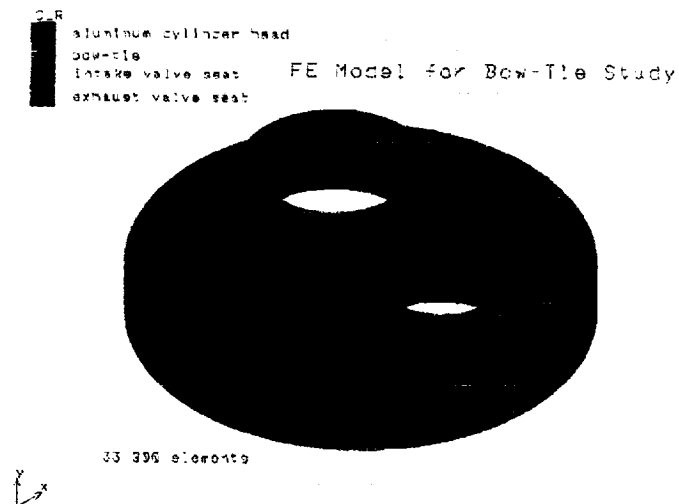


**Figure 3.15.3:** Local 3-D mesh geometry of 6 B-Series aluminum cylinder head with bow tie.

Based on the stress analysis of the full head model, thermal stress dominates the stress distribution in the valve bridge area under full power conditions. Therefore only the thermal stresses were considered in the subsequent analysis. The thermal stress results were considered on a linear basis, which clearly cannot be applied when the material yields or creeps. However, the ratio of the linear stress to yield strength can be used for comparison of different materials and geometry considerations.

A steady state thermal analysis was conducted for the baseline aluminum head and the results compared to measurements made on a running engine where thermocouples were located in various locations throughout the head. The data from the running engine were then used to calibrate the model.

The maximum valve bridge temperature calculated from this refined and calibrated local model was 26°C higher than the original coarse mesh model estimated. This indicated that the results of the original model were reasonable.

A thermal stress solution was calculated based on the steady state temperature distributions after calibration. Figure 3.15.4 shows the stresses on the firedeck where the maximum compressive stress was 188 MPa at 233°C, which indicates that yielding may occur in the valve bridge under the applied loads.

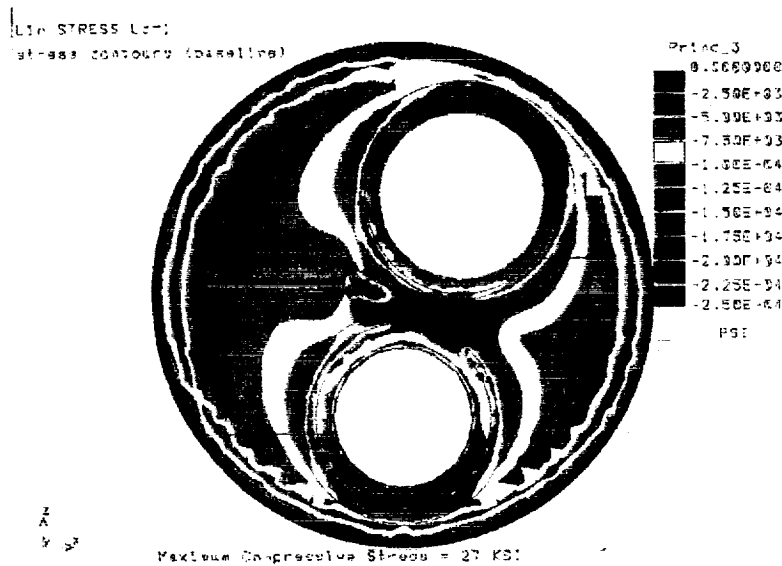


**Figure 3.15.4:** Thermal stress contours on the firedeck for the aluminum baseline.

This data is an indication that the stresses and/or temperatures in the valve bridge for the modeled engine conditions are too high for aluminum. Therefore, valve bridge reinforcement may be required in order to achieve the required durability for the cylinder head. Three candidate bow tie insert materials were chosen for study: gray cast iron, Niresist and 304 stainless steel. Various thickness of insert, insert diameter and location were chose for study which also included an entire deck face insert.

It was calculated from the analysis that the compressive stress in the valve bridge was lowest with gray iron. The maximum compressive stress was reduced by 13% with a gray iron bow tie even though temperature increased by 17% compared to the baseline aluminum. Based on the comparison with the yield strength at elevated temperature, it was concluded that the gray iron bow tie was the best choice for a reinforcement of an aluminum cylinder head. The moderate temperature increase relative to the other materials would also keep the interface stresses at a minimum.

Various bow tie thicknesses were investigated to determine the effect on thermal stresses. It was found that both compressive stress and temperature decrease as thickness decreases. A summary of the data is given in Figure 3.15.5, showing that 304 stainless steel and the baseline aluminum alloy were unacceptable, since at operating temperature for these materials the ratio of applied stress to yield strength is greater than unity.

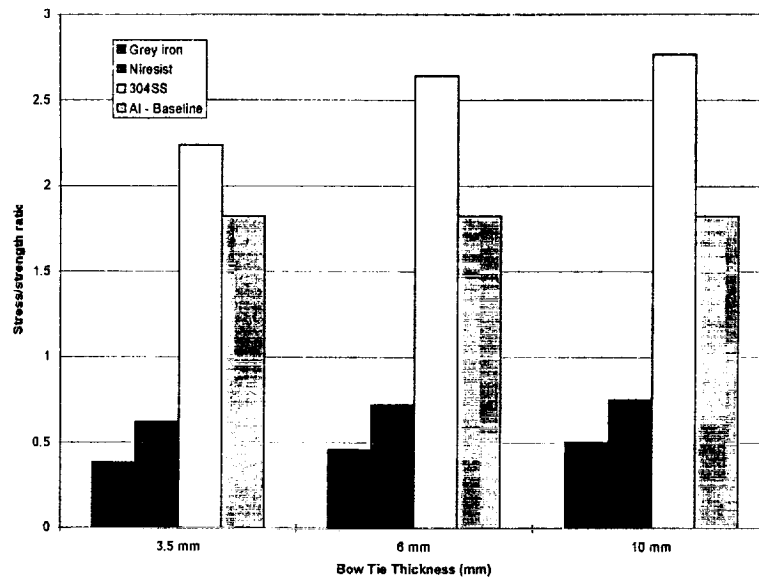


**Figure 3.15.5:** Effect of the bow-tie material and thickness on the stress/strength ratio on the valve bridge.

Next, bow tie location and size were evaluated and it was observed that bow tie location and size had little influence on the temperature and compressive stress in the valve bridge area, as long as the bow tie covered the minimum width region of the valve bridge.

Finally, a transient thermal stress analysis was conducted in order to determine if the steady state full power was the worst case during an engine thermal cycle. The transient acceleration thermal computation was simulated by stepping from room temperature conditions to the engine full power conditions; the deceleration thermal computation was simulated by stepping from the full power conditions back to room temperature. It was found that the compressive stress was dominant in both acceleration and deceleration, and that the steady state was the worst case, as shown in Table 3.15.3.

**Table 3.15.3:** Maximum compressive stress (P3) and temperature values (T) during an engine thermal cycle

Bow Tie Geometry and Configuration	Location: Center of combustion face Diameter = 55 mm and thickness = 6 mm					
	Thermal Conditions		Accel @ 5 sec		Steady state	
	P3 (MPa)	T (°C)	P3 (MPa)	T (°C)	P3 (MPa)	T (°C)
Gray iron bow tie	-138.6	222°C	-163.4	277	-78.6	155
Aluminum baseline	-140.6	187	-188.2	234	-56.5	144

The temperature and stress results with the three bow tie material candidates, various thicknesses, diameters and locations were obtained by applying the boundary conditions after calibration.

Table 3.15.4 is a summary of the temperature and stress results for the gray iron with an optimum geometry configuration compared to the aluminum baseline.

**Table 3.15.4:** Final results of the bow tie study

	Optimal Geometry Configuration	Results of Optimal Geometry	Results for the Aluminum Baseline
Bow Tie Material	gray cast iron	T = 263 - 277°C P <sub>3</sub> /YS = 0.38 - 0.46	T = 234°C P <sub>3</sub> /YS <sub>ET</sub> = 1.82
Bow Tie Thickness	3.5 - 6 mm		
Bow Tie Location and Geometry	45 - 60 mm center of the ring		

The principal conclusions of the analysis were :

- Gray cast iron was the best choice for the bow tie from the candidate materials considered.
- Both compressive stress and temperature decrease as the bow tie thickness decreases.
- The bow tie location and size have little influence on the compressive stress and temperature in the valve bridge area.
- Compressive stresses were dominant in the valve bridge area during the engine thermal cycle and the steady state was the worst case.

Based on the results and recommendations of this analysis a parametric study was completed to determine the optimum properties for a bow tie material using the model which was developed. The 3-D finite element model was used to study the sensitivity of thermal stress in the bow tie to materials properties. The objective was to find the least thermal/mechanical mismatch by the variation of the bow tie materials properties with the three candidate cylinder head aluminum alloys. The results of this study will be used to guide the selection of materials for the head and bow tie development activity.

Modifications to the existing model were made to allow representation of the stiffness of the head beyond the fire ring by creating a boundary region such that an equivalent Young's modulus could be assigned to the material in the boundary region.

The valve seat press fit causes an assembly stress in the valve bridge which depends on the interference between the seat and the head. Existing thermal boundary conditions were used for the analysis and the results were based on the same linear solution.

Assembly stresses were calculated and shown to affect the mean stress only. The maximum assembly stress values in the valve bridge area with the three aluminum alloys considered for both the aluminum baseline and bow tie case are shown in Table 3.15.5.



**Table 3.15.5:** Assembly stress results due to valve seat insert press fit

Case	Material	Stress (MPa) @ minimum interference	Stress (MPa) @ medium interference	Stress (MPa) @ maximum interference
Baseline	Al-354	40	60.7	81.4
	Al-319	40.7	62	83.4
	Al-390	46.2	69.6	93.8
Bow tie	Al-354	55.2	82.7	111
	Al-319	54.5	82.7	110.3
	Al-390	53.8	82	109.6

The sensitivity of thermal stress to the bow tie thermal properties was studied in order to determine optimum bow tie material properties which cause the least thermal mismatch in the valve bridge area. The thermal stresses were calculated with the optimum material properties for several candidate head alloys. It was found in the earlier analysis that the gray iron was a good material for the insert so the investigation was initiated at the properties of the cast iron. The Young's moduli of the aluminum head and bow tie materials do not influence the thermal mismatch, even though they affect the thermal stress, and therefore the modulus of gray iron was used in the analysis.

Analysis was carried out varying the thermal conductivity and expansion of the bow tie material and it was found that as long as the fatigue strength of the material was no lower than gray iron, a 30-50% higher thermal conductivity and 15-20% lower thermal expansion coefficient compared to gray iron should eliminate potential fatigue cracking problem in the valve bridge. Larger changes in thermal properties were not advantageous since they could result in a tensile mean stress and these materials are also more difficult to produce.

Thermal stresses were then calculated for the three different head alloys (354-T6, 319-T6 and 390-T6) for the baseline case, gray iron bow tie and two optimum materials defined as Case 1 ( $1.3K/0.85\alpha$ ) and Case 2 ( $1.5K/0.8\alpha$ ), where  $K$  is thermal conductivity and  $\alpha$  is thermal expansion coefficient for the insert material. For the purpose of comparing different aluminum alloys and bow tie materials stress/strength ratio and alternating stress fatigue limit ratios are shown in Figures 3.15.6 and 3.15.7 respectively.

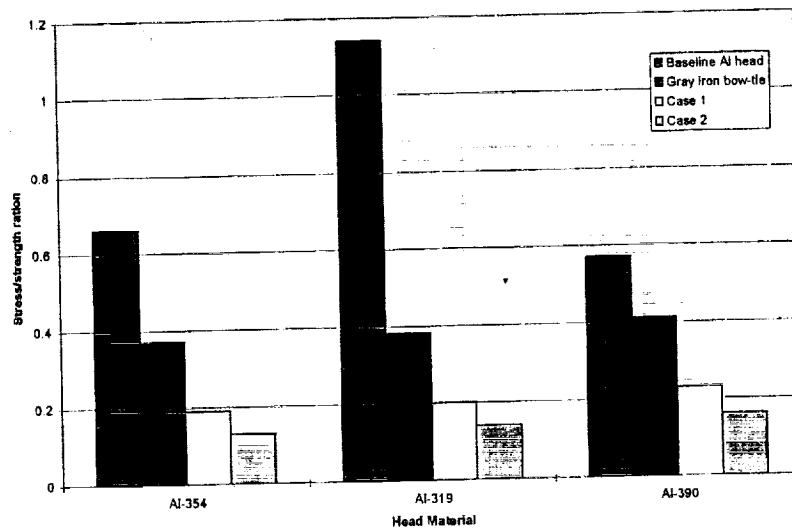


**Figure 3.15.6:** Effect of bow-tie insert material and aluminum head alloy on the stress/strength ratio in the valve bridge.

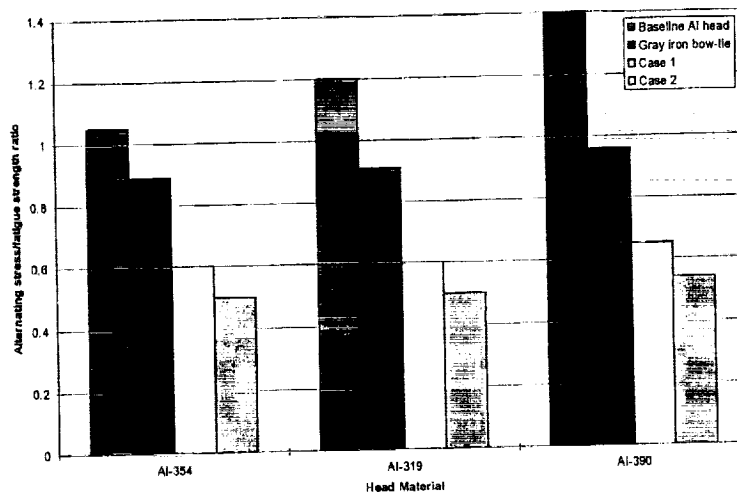


**Figure 3.15.7:** Effect of bow-tie insert material and aluminum head alloy on the ratio of alternating stress to fatigue strength in the valve bridge.

From this analysis the 354-T6 alloy is the best candidate material of the three, and with the optimum bow tie material properties both the stress/strength and the alternating stress/fatigue limit ratios are less than one.

It was concluded:

- The optimum bow tie thermal properties are 30-50% higher thermal conductivity and 15-20% lower thermal expansion coefficient compared to gray iron if Young's modulus and fatigue limit of the bow tie material are close to those of gray iron.

- The best aluminum alloy of the three investigated was found to be the 354-T6 alloy.

The assembly stresses do not influence the valve bridge fatigue problem to a large extent, even though the assembly stress values are quite high, because the mean stress is compressive.

### 3.15.2 Aluminum Cylinder Block Analysis

The objective of this analysis was to investigate the potential for casting the cylinder block of the Cummins 6 B-Series engine from an aluminum alloy by developing a baseline single cylinder sector model of the engine using current cast iron casting dimensions. The cast iron baseline model would incorporate assembly, thermal and peak cylinder pressure loads and gray iron material properties. The change in results of applying aluminum material properties to the same model would be the basis of any design recommendations for an aluminum block. This initial piece of work was carried out as part of a Cummins funded project and provided a basis for the more extensive analysis conducted under this contract.

A solid model for the block section was created using ProEngineer and the boundary conditions, and material properties were applied using ProMesh and COSMOS. For the analysis, which was completed early in the project, the aluminum alloy properties used were for a 339-T5 alloy. The main bearing cap material was ductile iron (standard production) and for comparison a steel main bearing cap was also used in the analysis. Figures 3.15.8 and 3.15.9 show the temperature distributions obtained for the cast iron and aluminum blocks respectively and in figures 3.15.10 and 3.15.11 show the stresses in the block under 13.8 MPa cylinder pressure loading in addition to the assembly and thermal loads.

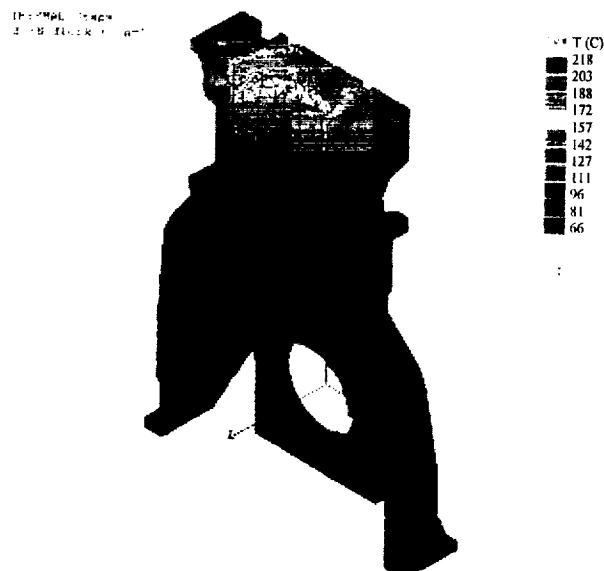


**Figure 3.15.8:** Temperature plot for the cast iron cylinder block - bore side.

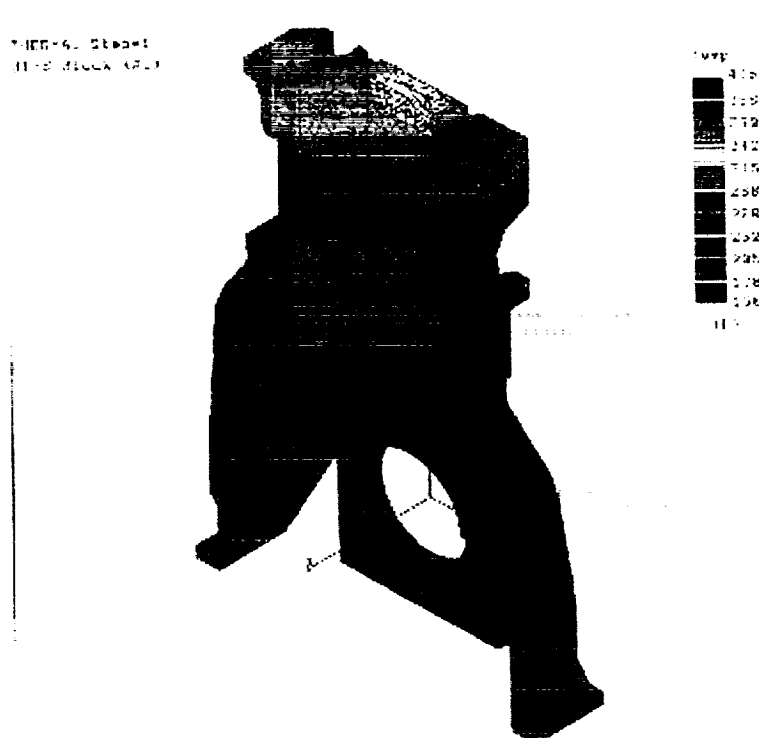


**Figure 3.15.9:** Temperature plot for the aluminum cylinder block - bore side.

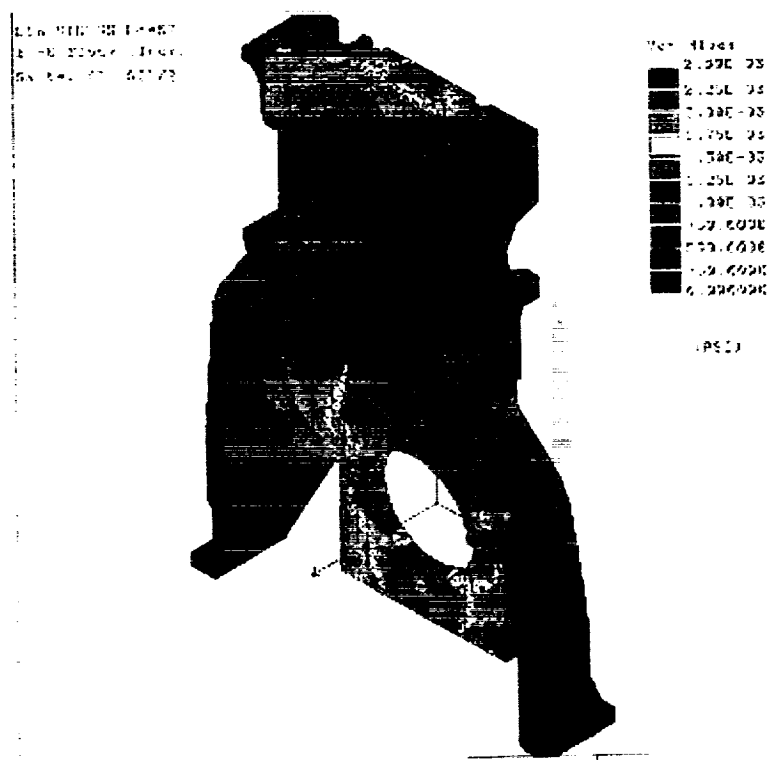


**Figure 3.15.10:** Alternating stresses in the cast iron cylinder block.

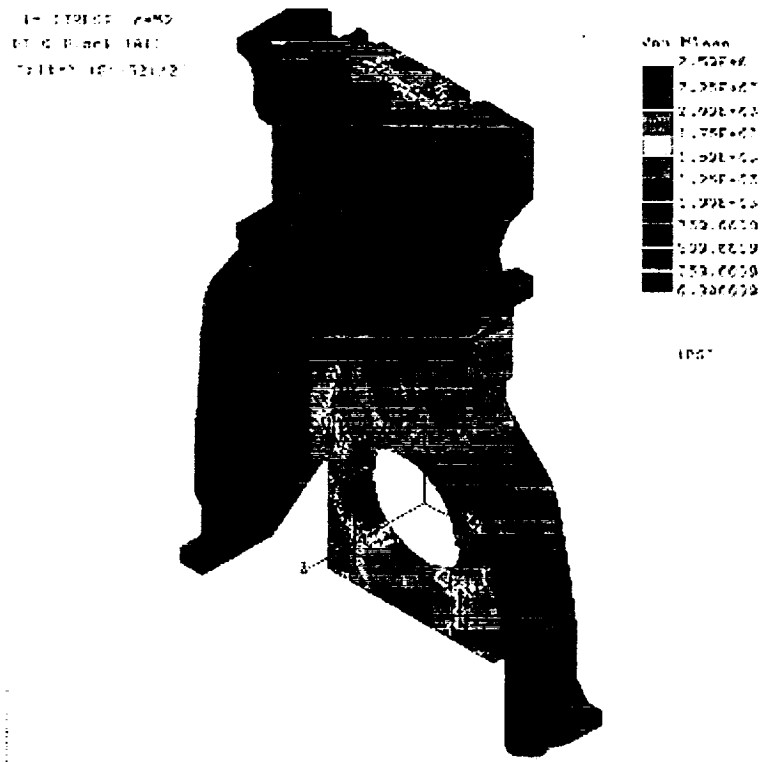


**Figure 3.15.11:** Alternating stresses in the aluminum cylinder block.

Due to a higher thermal conductivity it was observed that the temperature distributions in the aluminum alloy were more uniform than in the cast iron. Also, the calculated stresses in the aluminum block were of the same pattern, but marginally lower than the predicted stresses in the cast iron block. Both material models indicated adequate strength.

The stiffness of the aluminum block of the same dimensions of the cast iron block is lower, due to the lower modulus of elasticity. The lower stiffness results in increased vertical stretch of the block between the firedeck and the crankshaft bore for the cylinder under firing conditions relative to the adjacent cylinders. The increased stretch may also cause excessive bending loads on the crankshaft. Thickening the block in this region had little calculated effect on the result, but the use of a steel main bearing cap indicated that this could potentially reduce the displacement to that of the cast iron/nodular iron combination.

Lastly, the cylinder head and main bearing capscrew engagement regions were areas which have high calculated stresses. From this analysis, it was determined that the aluminum block would require reinforcement in the region of thread engagement. With that exception the aluminum alloy block appeared to be capable of replacing the cast iron block for engine weight reduction. Based on this analysis it was recommended that higher strength inserts be incorporated in the thread engagement regions of the aluminum block.

It was concluded from the analysis :

- Based on the thermal-static analysis the aluminum block was structurally applicable for the 119 kW (13.8 MPa peak cylinder pressure) load case investigated.
- Local effects of capscrew thread engagement were expected to be too high for aluminum without local reinforcement.
- Calculated temperature distributions in the aluminum block were more uniform than in the cast iron, which results in marginally lower stresses. The maximum temperature is 38°C lower in the aluminum block compared to the cast iron.
- The stiffness of the aluminum block was 20% lower than that of the cast iron and results in 20% more vertical block stretch between the head deck and main bearing saddles at 13.8 MPa cylinder pressure. The use of a steel main bearing cap with the aluminum block appeared to result in equivalent stretch to the cast iron block with a ductile iron bearing cap.

Modifications to the block model were made to facilitate investigation of:

- the influence of 50% contact on the interface between the liner and the cylinder block,
- influence of the bonded liner on the cylinder block stretch and
- aluminum cylinder block reinforcements to find reinforcements that will reduce the block stretch to an equivalent value to that observed in a cast iron block at an equivalent cylinder pressure and the same main bearing cap material.

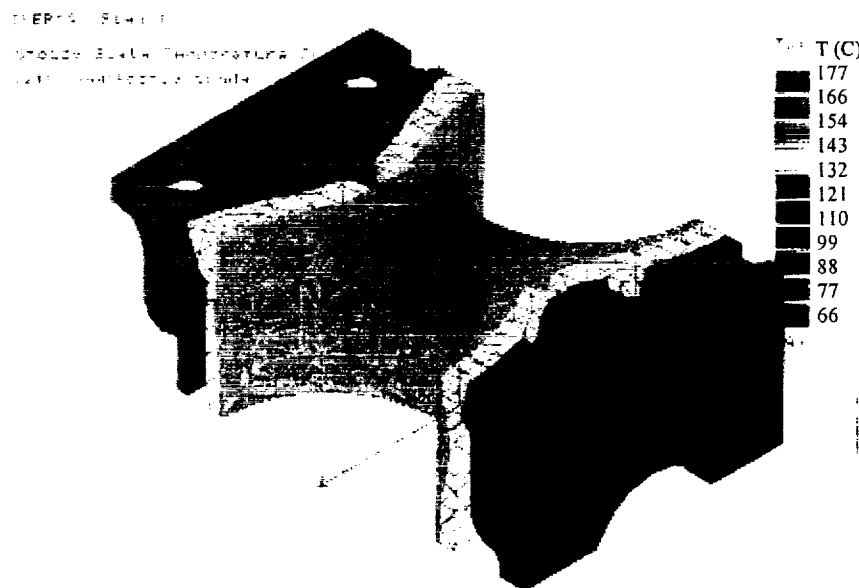


**Figure 3.15.12:** Steady state temperature distribution with perfectly bonded cylinder liners.

The 3-D model was used to calculate the temperature distribution for given thermal boundary conditions and it was found that there was less than 1% difference in temperature between a cylinder block with a perfectly bonded cylinder liner (Figure 3.15.12) and a block without a cylinder liner. It was concluded that the liner had very little influence on the steady state temperature distribution in the aluminum block.

A 2-D block-liner-interface model was developed and used to investigate the influence of 50% contact on the interface on temperature distributions in the aluminum block. The conductivity of the interface was assumed to be an average value of the conductivity's of the liner and the cylinder block. However, 50% contact on the interface is difficult to model using FE analysis and according to the conduction equation, this interface is equivalent to an interface with 100% contact, but using one half the thermal conductivity which can be readily represented. This approach was used and the results indicated that there was very little effect on the steady state temperature distribution for 50% contact compared to 100% contact. However with only 1% contact it was observed that there was a major difference between 1% and 100% contact.

In the original 3-D block model, the liner was not included in the analysis. In order to use this model, the cylinder liner stiffness was represented by an increase in the Young's modulus of the bore region. By assuming that the increase in Young's modulus is equal to the product of the ratio's of their thickness and Young's modulus of the cylinder liner the equivalent modulus of the bore region was determined and used to take account of the presence of a liner on the block stretch. It was found that the presence of the cylinder liner had very little influence on the block stretch (approximately 1.5% difference at peak cylinder pressure).

Figure 3.15.13 shows the vertical strain distribution of the aluminum cylinder block due to a peak cylinder pressure of 10.3 MPa.

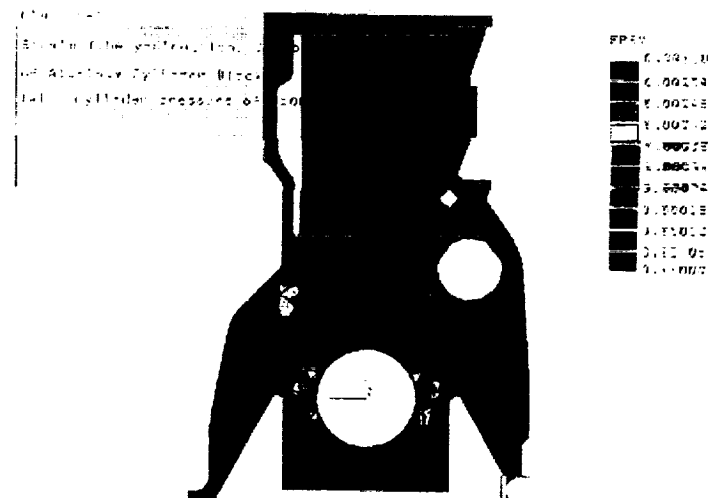


**Figure 3.15.13:** Strain (in the y-direction) contours of aluminum cylinder block.

The results show that the block stretch is sensitive to the main bearing cap and a simple way to reinforce the main bearing cap is to substitute steel for ductile iron. Table 3.15.6 lists the results of the cylinder block stretch due to peak cylinder pressure with different cylinder block and main bearing cap materials. The change of ductile iron to steel can reduce the stretch in the aluminum block from 30% to 12% compared to the cast iron block stretch.

**Table 3.15.6:** Results of the cylinder block stretch with different materials

Block Material	Main Bearing Cap Material	Stretch (mm)	Difference (%)
cast iron	ductile iron	0.094	-
Al (390)	ductile iron	0.122	30
Al (390)	steel	0.106	12

High strains in the regions between the bore and the block-cap interfaces and low strains in other regions suggests that an effective way to reinforce the block is to cast in steel inserts in the regions between the bore and the block-cap interface. These inserts may be located in the regions highlighted in the plot in Figure 3.15.14.

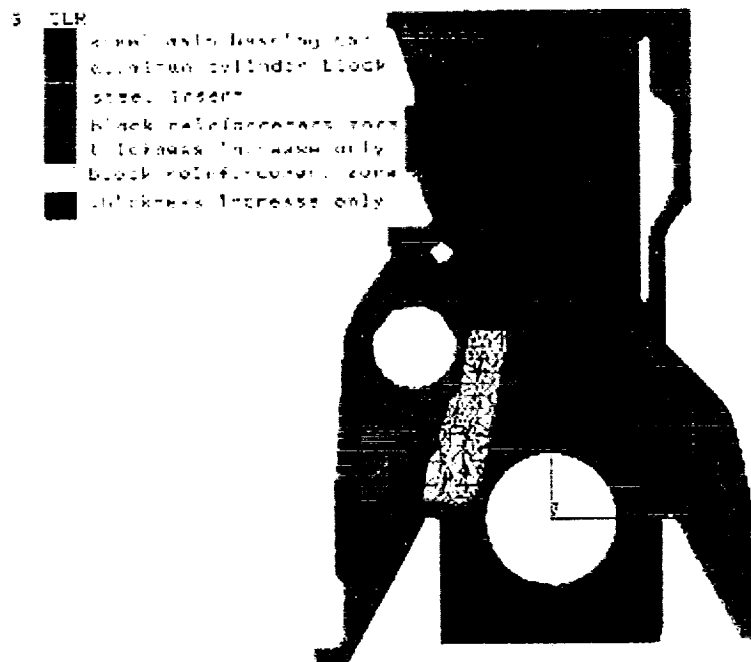


**Figure 3.15.14:** Cylinder block model showing the zones reinforced by steel inserts.

The block reinforcements were represented by an equivalent Young's modulus in a similar way to that used for the cylinder liners. Table 3.15.7 lists the results of the cylinder block stretch due to peak cylinder pressure with the block reinforcements. The results show that the aluminum



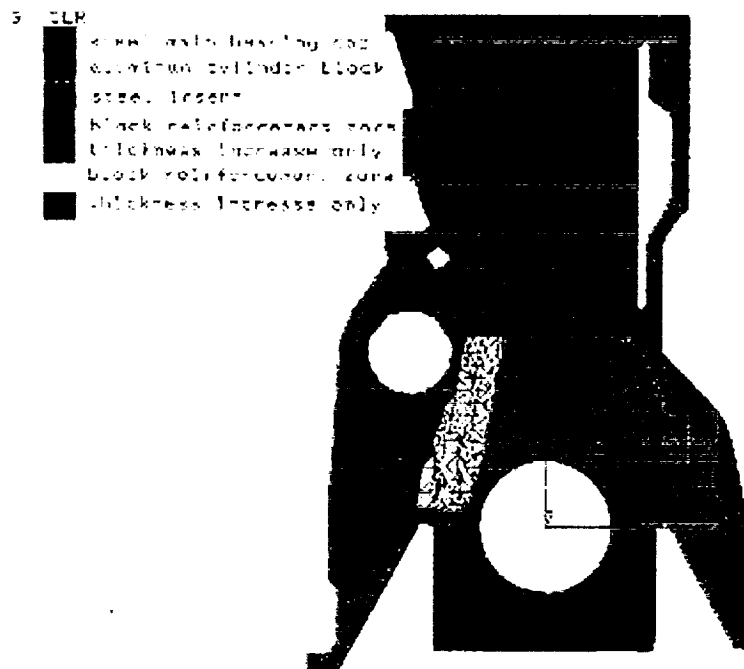


**Figure 3.15.14:** Cylinder block model showing the zones reinforced by steel inserts.

The block reinforcements were represented by an equivalent Young's modulus in a similar way to that used for the cylinder liners. Table 3.15.7 lists the results of the cylinder block stretch due to peak cylinder pressure with the block reinforcements. The results show that the aluminum cylinder block stretch with the steel main bearing cap and proposed inserts was equivalent to the cast iron cylinder block stretch.

**Table 3.15.7:** Results of block stretch with steel reinforcements

Block Material	Main Bearing cap material	E (zones 1 & 2) (GPa)	E (zones 3 & 4) (GPa)	Stretch (mm)	Difference (%)
cast iron	ductile iron	81.4	81.4	0.094	-
Al (390)	steel	144	206.8	0.094	0

The 3-D block-cap model was used to calculate the stress distribution due to the insert interface pressure. In order to correctly represent the interaction between the block/cap and the bearing insert, a two step analysis was proposed to calculate stress distribution due to bolt assembly loads, the thermal loads and peak cylinder pressure. In order to approximately represent the interaction between the insert and the crankshaft, the deformed shape of the insert was controlled in the determination of the stress distribution due to peak cylinder pressure. Finally, the analytical data were calibrated using strain gage data from a running engine

Based on the analysis it was concluded:

- The model can be used to calculate the stresses due to assembly loads, the thermal loads and the cylinder pressure.
- Fatigue analysis at several locations showed that fatigue cracks were not expected in the block and main bearing cap, except in the capscrew engagement region.
- The block stretch due to cylinder pressure is 30% higher in the aluminum block than in the cast iron block.
- Incorporating steel inserts in the main bearing saddles in combination with steel main bearing caps reduces block stretch in the aluminum block to a level equivalent to that in the baseline gray cast iron block.

Under Task 9 of the contract the block model developed at Cummins was modified to take into account the findings of the previous work and to analyze certain locations in the block including the capscrew engagement region. In the early analysis only one geometry of main bearing saddle was analyzed but in reality there are several differences in geometry depending on which main bearing saddle is considered. Therefore, further analytical work was performed.

A thread engagement model was developed to allow specific calculation of the stresses in this region so the fatigue durability of the block could be assessed in this high stress area. Previous analysis, along with the results of block fatigue tests, showed there was an issue with fatigue cracks initiating at the capscrew last thread engagement in the main bearing saddle. The main objective of the analysis was to first, investigate the local stress distribution resulting from the main bearing cap capscrew engagement with the baseline saddle geometry and second, evaluate the effect of steel reinforcement in the rear main bearing saddle which was the most sensitive of the saddles. The model could then be used to predict fatigue life based on the material fatigue properties developed for the alloy (Section 3.15.3).

The rear main bearing saddle (#7) was modeled using Pro/Engineer, along with the main bearing capscrew, main bearing cap and main bearing saddle insert. A detailed finite element mesh of the assembly was generated using Pro/Mesh in Pro/Engineer.

In order to model the interaction between the capscrew and the saddle a methodology was developed to simulate the actual thread force distribution. This thread force distribution can then be calibrated if a strain gage is located close to the last thread. The calculation of local stress distributions in threaded connections is difficult to analyze and a unique approach was developed. In order to simulate the interaction between the capscrew and saddle, a series of thin discs were used to represent the engaged threads. A series of assumed force distributions were applied to the discs to model the actual thread force distribution, which was calibrated from strain gage data, and the total force was equal to the bolt load.

For calculations it was not necessary to deal with individual threads and therefore the same mesh geometry as for the assembly load case was used. The dynamic stress was calculated by applying uniform pressure over an angle on the main bearing. This pressure zone angle was then calibrated from the test data.

An assembly stress was calculated for both saddle #5 and saddle #7 and the maximum stress at the ends of the capscrew was found to be approximately 145 MPa for both. It was found that the assembly stress was high at the capscrew ends on the inside of the saddle, but drops to zero quickly toward the outside of the saddle, as shown in Figure 3.15.15. Very little difference was observed in the assembly stresses between the exhaust and cam bore sides of the engine.

A dynamic stress analysis was then carried out at a 13.8 MPa cylinder pressure. The results of the analysis for the center plane of the capscrew holes of saddle #7 are shown in figure 3.15.16 and figure 3.15.17 shows dynamic stress contours at the capscrew ends.

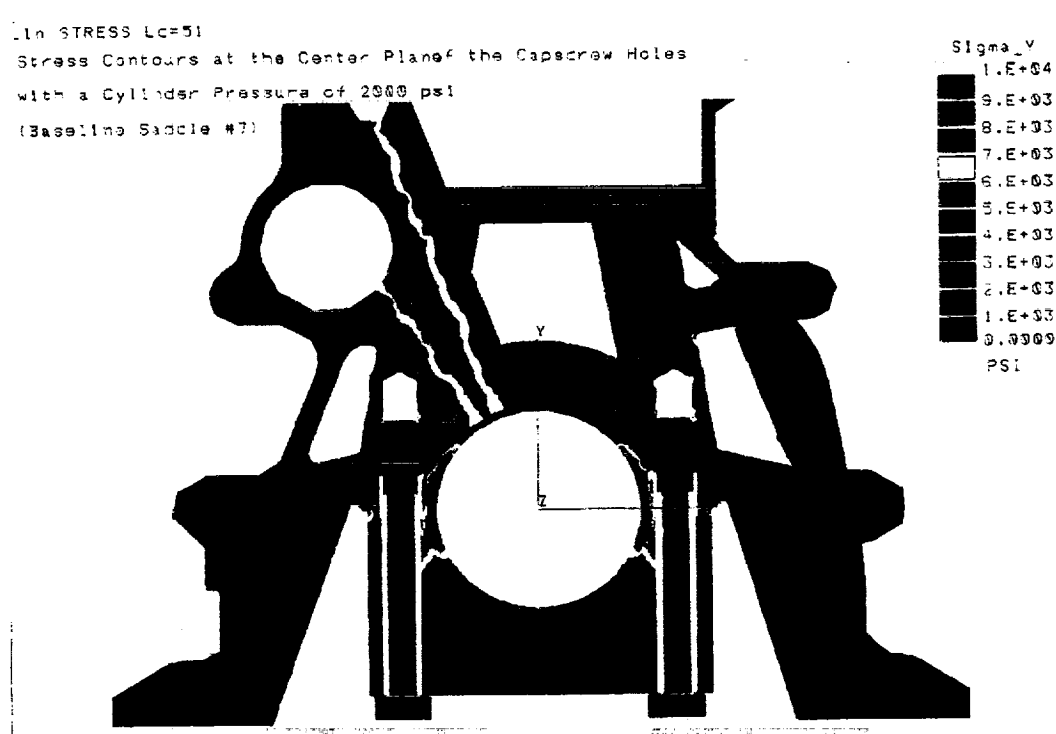


**Figure 3.15.16:** Dynamic stress contours in the center planes of the capscrew holes.

In this case the stress was high at the capscrew ends, but unlike the assembly stresses shown in Figure 3.15.15, remains high across the whole cross section, as can be seen in Figure 3.15.17. Results for the maximum stresses at the capscrew ends of saddles #5 and #7 after calibration are shown compared in figure 3.15.18, where it can be seen that the stresses are higher in saddle #7.

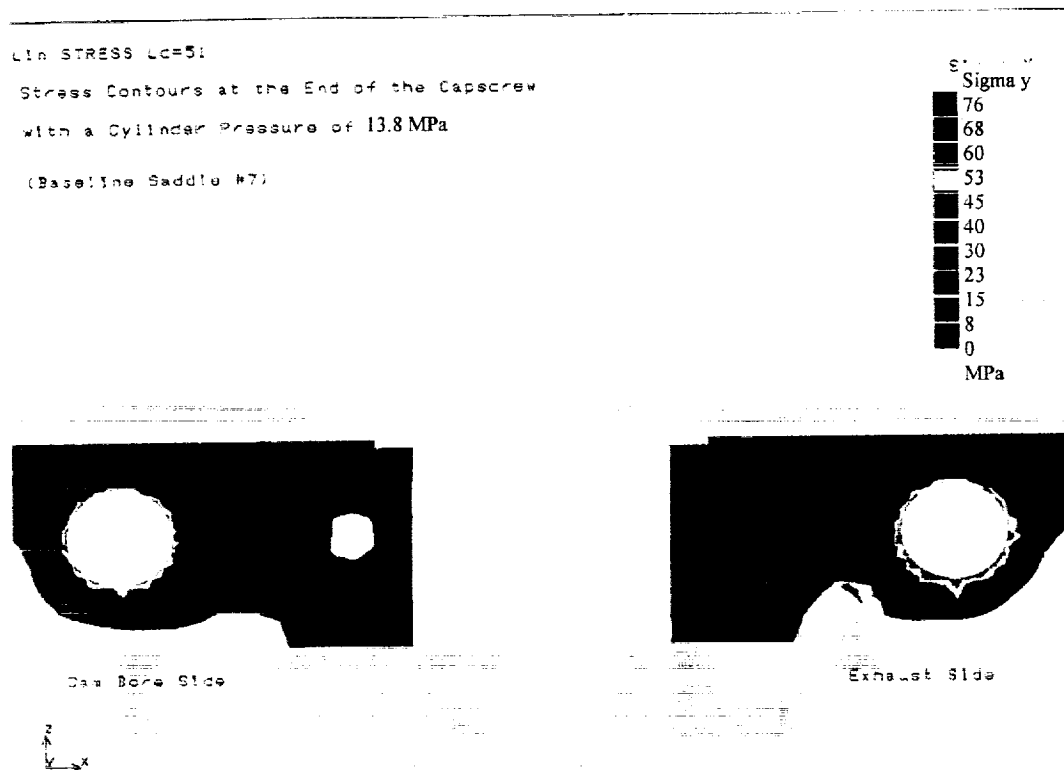


**Figure 3.15.17:** Dynamic stress contours at the ends of the capscrews in saddle #7.

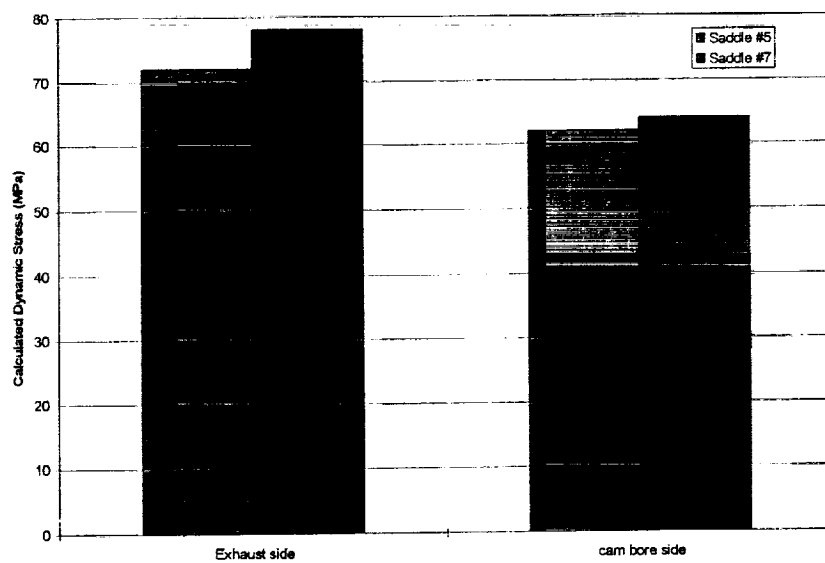


**Figure 3.15.18:** Maximum stresses comparison between the exhaust side and cam bore side at the capscrew ends of saddles #5 and #7.

It was predicted that the maximum dynamic stress at the capscrew end on the exhaust side (major thrust side) was 18% higher than on the cam bore side. The average dynamic stress across the cross section was 15-20% higher on the exhaust side, which is consistent with the block fatigue test results.

The effect of bearing clearance on the dynamic stress was also considered. If the gap between the bearing and the crankshaft after deformation with the dynamic loading is negligible, the relative displacement at both ends of the bearing is equal to the bearing clearance. It was found from the analysis that the stress at the capscrew ends is not very sensitive to the bearing clearances, but the stress at the bottom of the main bearing cap is very sensitive to the bearing clearances.

Based on the assembly and the dynamic stress obtained, mean stress ( $\sigma_m$ ) and alternating stress ( $\sigma_a$ ) can be determined. If these are compared to the fatigue properties of the material as determined from the measurements made as part of the project (Section 3.15.3). The results of the analysis of the main bearing saddles are shown compared in the Goodman diagram in Figure 3.15.19.

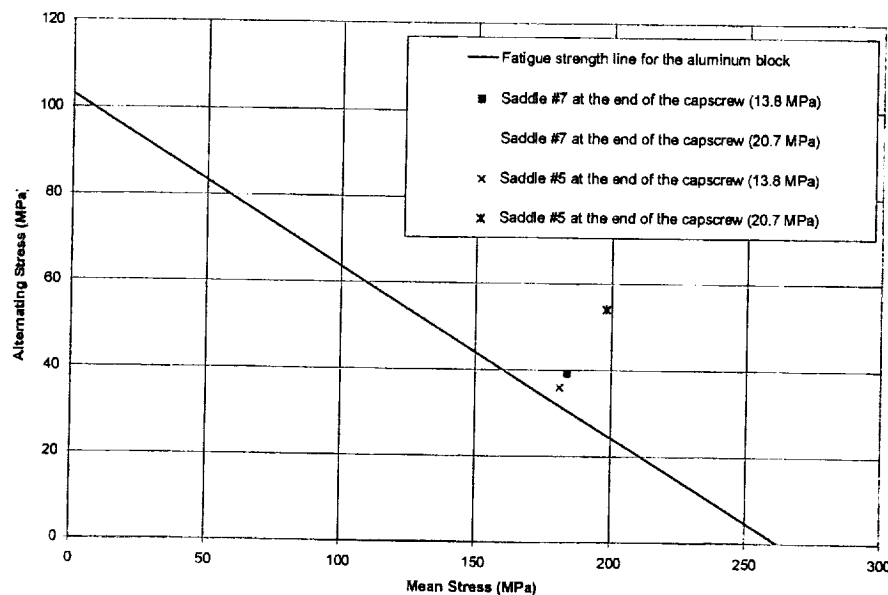


**Figure 3.15.19:** Modified Goodman diagram comparing saddles #5 and #7.

Based on a fatigue limit of 103 MPa at  $10^8$  cycles it is clear that failure of the main bearing saddle would be expected from the end of the capscrew. This prediction was consistent with the results of the block fatigue tests.

The effort was the modification of the model to determine the effect of the placement of steel inserts in the main bearing saddles on the durability of the main bearing saddles. In order to do this a 3D FE model was created to represent saddle #7 (with saddle inserts). The resulting

assembly stress contours are shown in Figure 3.15.20 where the maximum stress is 255 MPa at the capscrew ends and 52 MPa at the interface between the saddle inserts and the block.

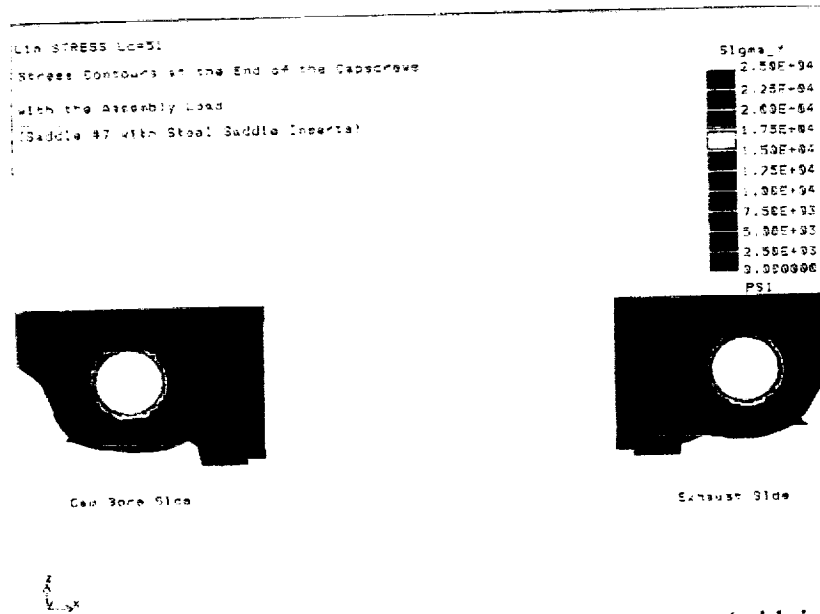


**Figure 3.15.20:** Assembly stress contours at the ends of the capscrews (with insert).

The dynamic stress contours at 13.8 MPa cylinder pressure are shown in Figure 3.15.21 for the centerplane of the capscrew holes and in Figure 3.15.22 at the capscrew ends.

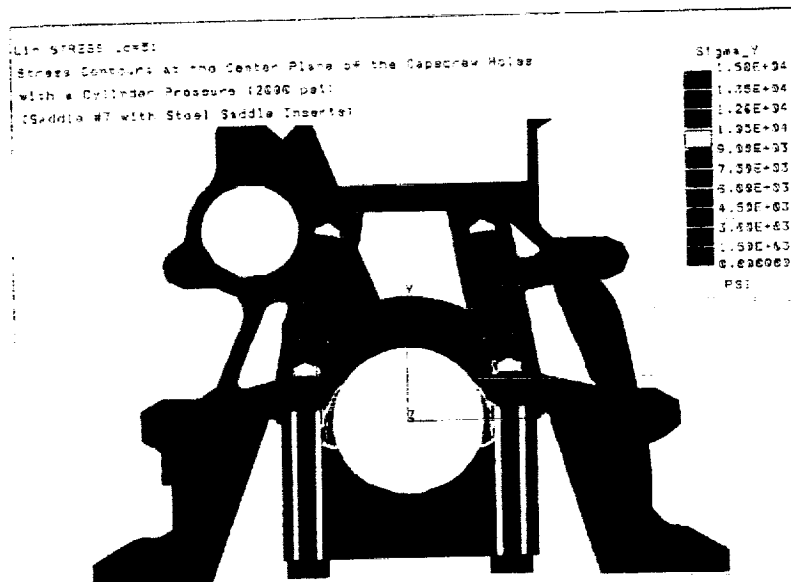


**Figure 3.15.21:** Dynamic stress contours in the center plane of the capscrew holes (with saddle inserts).

It was predicted that the stress at the capscrew ends was 95 MPa on the exhaust side (major thrust) and 87 MPa on the cam bore side. The maximum stress on the interface between the saddle inserts and the block is 52 MPa on the exhaust side and 48 MPa on the cam bore side.

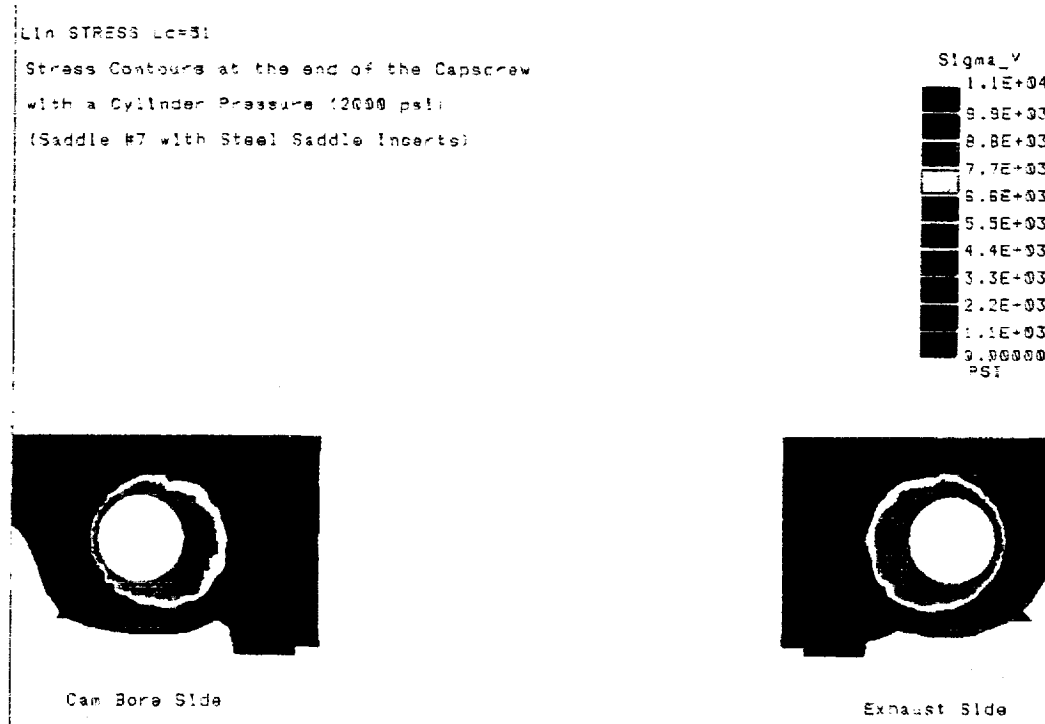


**Figure 3.15.22:** Dynamic stress contours at the ends of the capscrews (with saddle inserts).

Based on the assembly and dynamic stress calculated, mean stress and alternating stress at the capscrew end and at the interface between the saddle inserts and the block were calculated. The alternating stress for fully reversed loading (S) was estimated using the Goodman relationship and the results of the fatigue analysis results with cylinder pressures of 13.8 MPa and 20.7 MPa are shown compared in Figure 3.15.23. The results of the analysis indicate that the incorporation of steel inserts should eliminate the cracking problem if the bonding between the steel inserts and the block is sufficient.

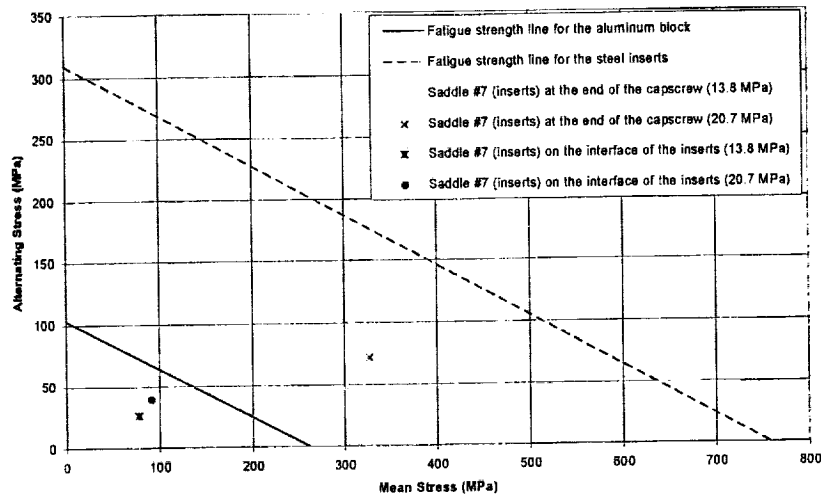


**Figure 3.15.23:** A modified Goodman diagram for saddle #7 with and without saddle inserts.

The principal conclusions from the analysis were:

- The model predicted high assembly stresses and high dynamic stresses at the ends of the main bearing capscrews.
- Local assembly stress was found to be similar for both the exhaust side (major thrust) and cam bore side of the engine. However, the maximum dynamic stresses at the capscrew end were found to be 18% higher on the exhaust side.
- The maximum dynamic stress at the capscrew ends is 7% higher in saddle #7 than in saddle #5 (the average dynamic stress in the cross section is 15-30% higher in saddle #7). These results are consistent with block fatigue test data.
- The stress at the bottom of the main bearing cap was more sensitive to the bearing clearances than the stress at the ends of the capscrews.
- With steel inserts in saddle #7, the assembly and dynamic stresses at the capscrew ends and on the interface between the saddle inserts and the block were significantly reduced relative to the corresponding fatigue strength.

The fatigue analysis predicted that a crack would be expected at the end of the main bearing cap capscrew on the exhaust side of saddle #7. The steel inserts would eliminate the cracking if the bonding between the saddle inserts and the block is sufficiently strong.

### 3.15.3 Mechanical Properties of Aluminum Alloys for Cylinder Blocks and Heads

The development of a mechanical and physical property database of aluminum casting alloys was necessary to provide accurate input to the analytical models required to define the critical areas and design issues for diesel engines. A survey of the literature revealed a lack of available data,



particularly elevated temperature modulus and fatigue strength. A data collection program was initiated to obtain the necessary data.

The three alloys chosen for investigation were 319-T6, 354-T6 and 390-T6, which are standard aluminum silicon casting alloys used for automotive applications. Alloy 390 was also tested in a T5 condition due to difficulties in T6 heat treating which caused quench cracks. The 390 alloy has been used for blocks and 319 alloy is a typical aluminum cylinder head material. Testing was conducted at room temperature and up to 260°C after long term thermal aging in order to analyze the effect of long term exposure to the engine operating temperature on the material properties. Measurements of tensile, compressive fatigue, and axial fatigue properties were obtained from room temperature to 260°C. Tests were also conducted to investigate the effect of exposure time at the engine operating temperatures by overaging the aluminum alloys for 100 and 500 hours.

The test specimens were obtained from head and block castings, which were not fully optimized in terms of the Dendrite Arm Spacing (DAS) and microporosity. The data summarized in this report represents the results of the tests completed on these original castings. Additional work is planned on optimized castings to allow for a comprehensive evaluation of the structural property relationships for these materials.

The results of the Young's modulus measurements are shown in Figure 3.15.24 as a function of temperature after 500 hours thermal aging.

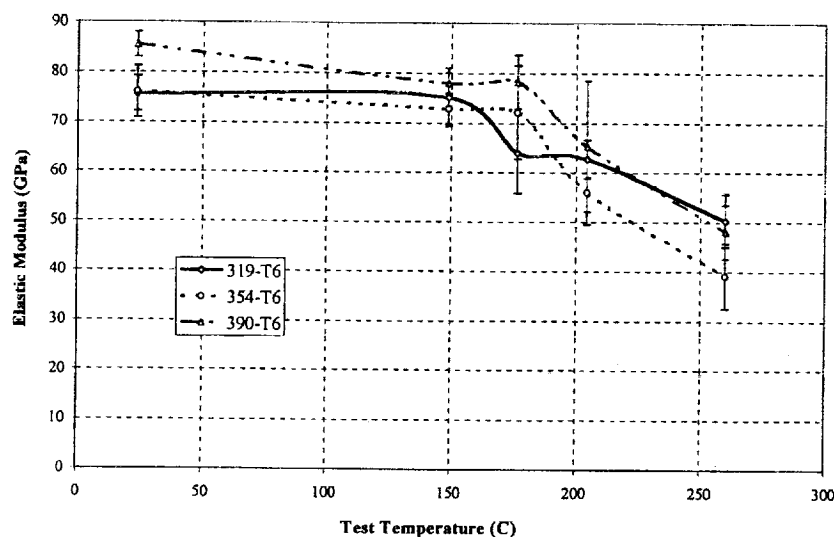


**Figure 3.15.24:** Elastic modulus as a function of temperature after 500 hours thermal aging.

For temperatures up to 177°C the 390-T6 alloy consistently exhibited approximately 10% higher elastic modulus than the other alloys. At 204°C and 260°C the 390-T6 and 319-T6 material

appeared similar and approximately 15% higher than the 354-T6 alloy. The higher modulus in the 390 alloy is a result of the high concentration of primary silicon particles.

The elastic modulus measurements were obtained by using an extensometer and strain gage measurements. This work was conducted since the measured moduli were found to be slightly higher than any of the literature values. The results of the study showed that the two measurement techniques correlated very well with an average difference in readings of 0.8% over all the test temperatures. The measured results were found to be slightly higher than those reported in the literature.

Significant differences in the strength of the 390 alloy were observed in the T5 and T6 condition, as shown in Figure 3.15.25.

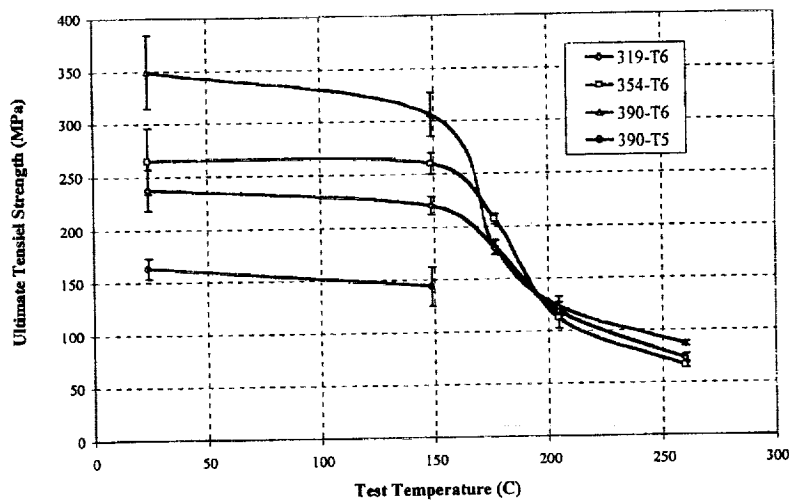


**Figure 3.15.25:** Ultimate tensile strength as a function of temperature after 500 hours thermal aging.

The 390-T6 alloy exhibited approximately 15% and 28% improvement in strength over the 354-T6 and 319-T6 alloys respectively at room temperature (RT) and 149°C. After thermally aging for 500 hours at 204°C and 260°C the 390-T6 alloy had a higher strength than the other two alloys that had comparable strengths.

An important parameter to the thermal fatigue resistance of the materials for the head is compressive yield strength, which is shown as a function of temperature in Figure 3.15.26.

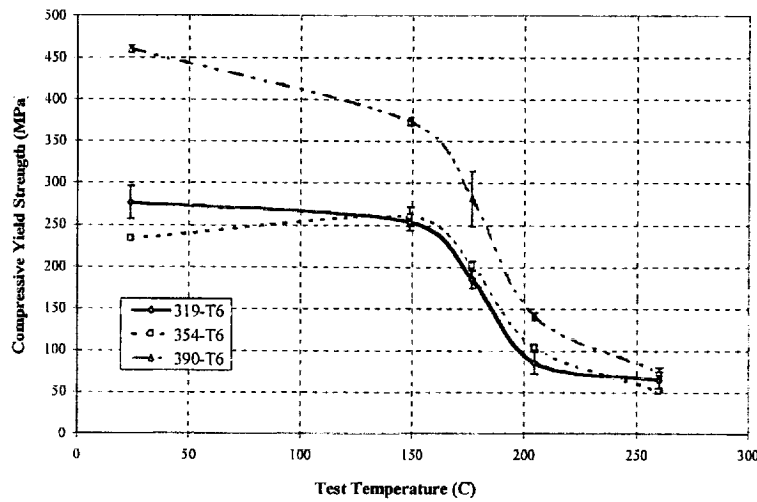


**Figure 3.15.26:** Compressive yield strength as a function of temperature after 500 hours thermal aging.

The 390-T6 alloy had a higher compressive yield strength, which is a result of the high concentration of primary silicon particles in the matrix, over the whole range of temperatures tested. The 319-T6 and 354-T6 alloys had similar strengths. It should be noted that the compressive yield strength was found to be significantly reduced after 500 hours of thermal aging at 204°C and 260°C (45% and 75% respectively). This clearly indicates that the data used for analytical work must take account of the thermal aging that occurs during engine operation otherwise the results will be optimistic.

At temperatures below 177°C all three alloys exhibited little or no elongation to failure, as shown in Figure 3.15.27. At 204°C, the ductility of 354-T6 was almost the same as that of the 319-T6 alloy. At 260°C the ductility of 354-T6 alloy was much better than that of the 319-T6 alloy with the 390-T6 material having the lowest ductility over the whole range of temperatures tested.

Axial fatigue tests were conducted on all three alloys at RT, 204°C and 260°C. The 319-T6 and 354-T6 alloys exhibited similar properties, which were approximately 30% better than those of the 390-T6 alloy at RT, as shown in Figure 3.15.28. The fatigue data for the 390-T5 and 390-T6 material also exhibited significantly more scatter, which is most likely a result of the significant porosity observed in the materials. Figure 3.15.29 shows the results of the tests at 260°C after 100 hours thermal aging. Similar results were observed for tests at 204°C after 500 hours of thermal aging (not shown). Both overaging results exhibited similar trends as those at RT.

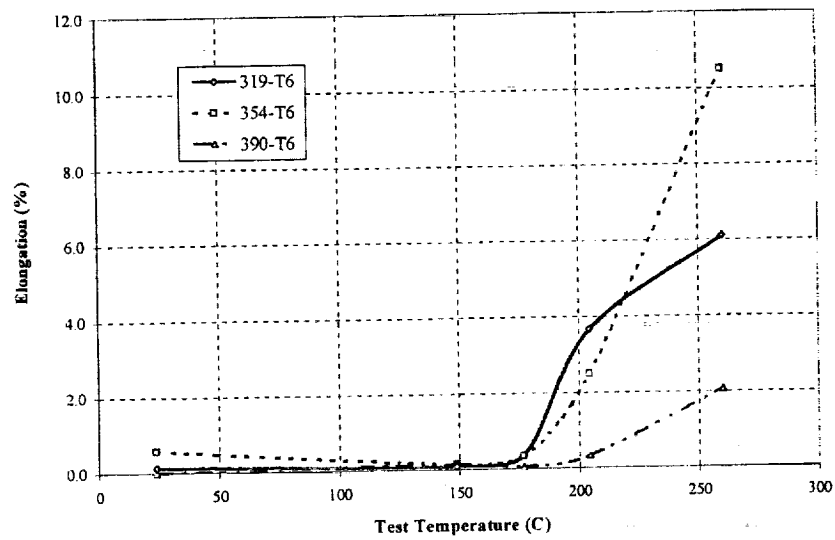


**Figure 3.15.27:** Elongation as a function of temperature after 500 hours thermal aging.

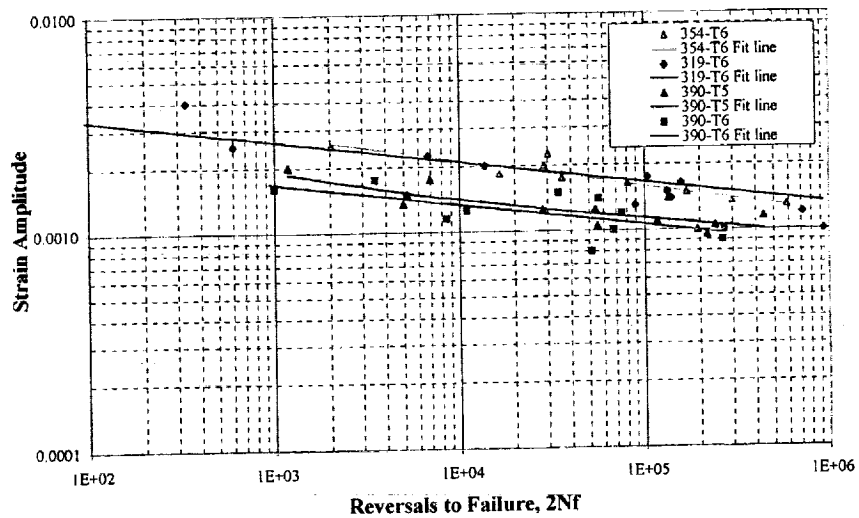


**Figure 3.15.28:** Strain-life fatigue data for the aluminum alloys at room temperature.

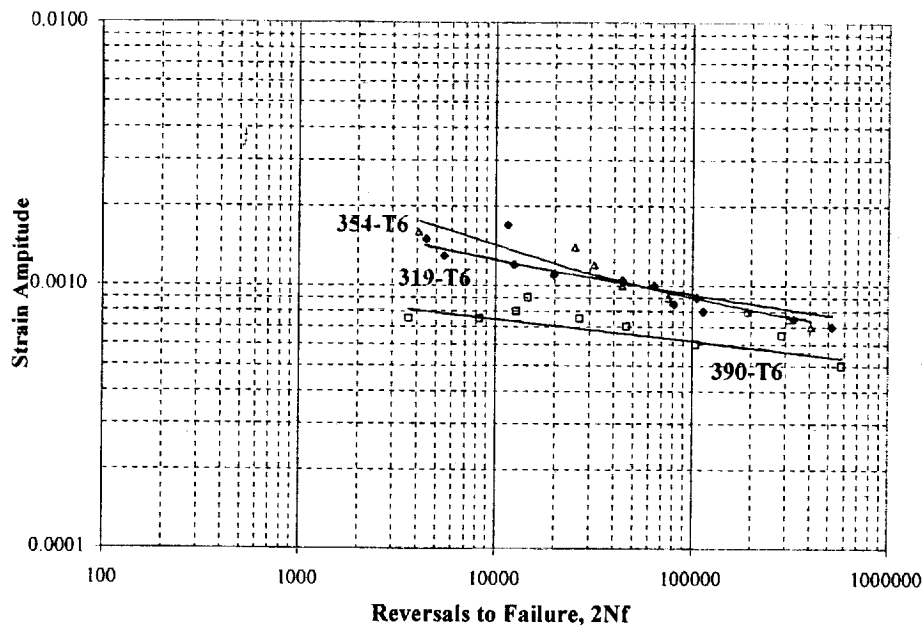


**Figure 3.15.29:** Strain-life fatigue data for the aluminum alloys tested at 260°C after 100 hours of thermal aging.

It should be noted that the casting process was not optimized at that time of manufacture such that the casting quality was not in its best condition. The presence of excessive amounts of porosity and large secondary dendrite arm spacing (DAS) in some of the samples precludes definitive conclusions. However, the evaluation of the mechanical properties of the candidate alloys in the same level of casting quality provides an indication of the trends as a function of temperature and thermally aging conditions.

In summary, 390-T6 alloy exhibited the highest modulus, UTS and compressive yield strength as compared to the 319-T6 and 354-T6 alloys. However, the 390-T6 alloy had very limited ductility. This low ductility coupled with excessive porosity was most likely responsible for the lower fatigue strength observed in the 390-T6 alloy, and the increased fatigue data scatter. Overall the mechanical properties of the 319-T6 and 354-T6 alloys were observed to be similar.

Constrained thermal fatigue testing of the three candidate alloys was also conducted. These tests were conducted at Climax Research Services (CRS) in Detroit. Alloys 319, 354 and 390 were tested in the T6 temper condition. Thermal stress hysteresis curves were measured for the three alloys at a maximum temperature of 260°C and for the 354 and 390 alloys at 204°C. Thermal fatigue testing of all three alloys was also conducted with a thermal cycle from 66°C to 288°C.

Thermally induced stresses are generated by mounting the specimens in a rigid test frame and heating the center portion of the sample with an induction heating coil while water cooling both ends of the specimen. Thermal expansion of the specimen center in combination with the rigid

test fixture result in the development of compressive stresses within the specimen on heating. A thorough discussion of the experimental apparatus has been presented elsewhere.

The intent of thermal stress hysteresis is to first determine the nature of stress relaxation at high temperature and second to provide a measurement of the plastic strain which occurs within the specimen for a range of thermal cycles (i.e. maximum and minimum temperatures). Measurements of thermal stress hysteresis suggest that the deformation is minimum for all of the cycles having a peak temperature of 204°C, whereas the specimens experienced significant deformation during the 260°C peak temperature testing. The material studied could be expected to perform well at service temperatures not exceeding 204°C; however, these three alloys would have finite lives for maximum service temperatures at or above 260°C.

Thermal fatigue testing at a maximum temperature of 288°C shows that among the three alloys the 319 material had the longest life (average life 832 cycles) followed by the 354 alloy (638 cycles), with the 390 alloy having the shortest life (366 cycles). The 354 specimens incurred the most strain (bulging) per cycle (approximately 25%) with 390 alloy showing the least strain per cycle (approximately 4%) which was expected based on its low ductility.

The difference in the strain per cycle was small at peak temperature of 260°C, the difference in the strain per cycle was much larger, and readily measurable, at peak temperature of 288°C. Considering these results, and the low axial fatigue strength and ductility of 390-T6 as compared to either 319-T6 or 354-T6, the 390-T6 material is not recommended for use as a cylinder head material.

In the next phase of mechanical property testing, the specimens will be taken from head and block castings with a refined structure. The head castings will be chilled in the deck face to achieve better casting quality (less porosity and fine DAS). Future block castings will be cast by Alcoa with their proprietary Level Pour process and with the thickened bulkhead in the bearing saddle areas. The test results will be reported separately.

It was concluded from the evaluations:

- Alloy 354-T6 is recommended for cylinder blocks due to its good mechanical properties and ease of castability.
- Alloy 354-T6 or 319-T6 are recommended for cylinder heads due to their ductility, axial fatigue strength, and thermal fatigue properties.

### **3.15.4 Structural Analysis and Testing**

#### **3.15.4.1 Cylinder Block**

Measurements of strain were required under cylinder pressure loading to validate the results of the FE analysis of the block. Photostress coatings were used to locate the high stress regions for the placement of strain gages, followed by subsequent strain gage analysis. The prediction of

fatigue factors or design limits was based on the mechanical property data discussed in section 3.15.3 - **Mechanical Properties of Aluminum Alloys for Cylinder Blocks and Heads.**

#### 3.15.4.1.1 Photostress Analysis

The photostress coating was applied to the block in areas identified as high stress areas from the limited engine testing and mechanical test work. The cylinders were statically pressurized with grease to determine the locations of the major stress concentrations and the directions of the principal stresses. The photostress coated main bulkhead regions were initially loaded with main capscrew torque application. An example of the results is given in Figure 3.15.30.

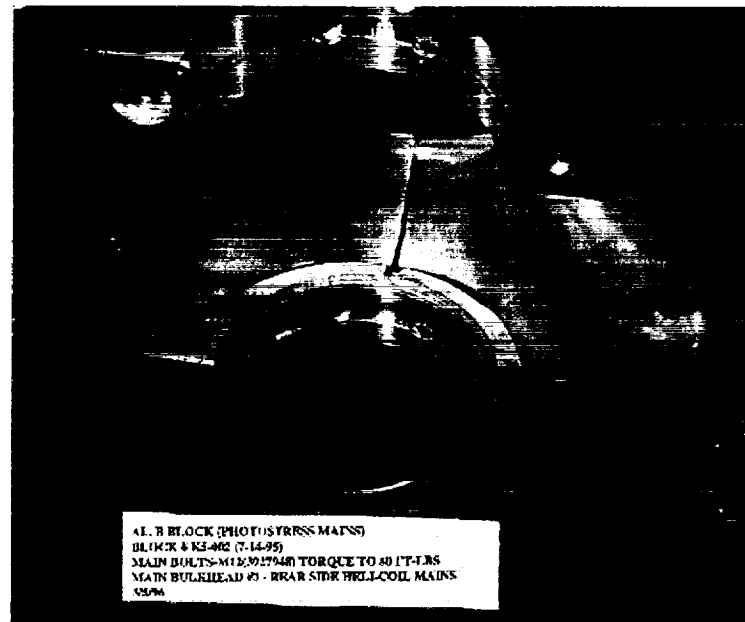


**Figure 3.15.30:** Photostress results on main bearing saddles with the application of bolt torque.

These data show that a high compressive load is developed in the boss region. Following this test, pistons were installed in the block, along with a dummy crank section which was designed to simulate the bending of the crank during cylinder pressure application. The head bolts were torqued and then cylinder pressure applied using static grease pressure to various cylinder pressures. An example of this is shown in Figure 3.15.31 for comparison to Figure 3.15.30, where only the effect of torque loading is shown.

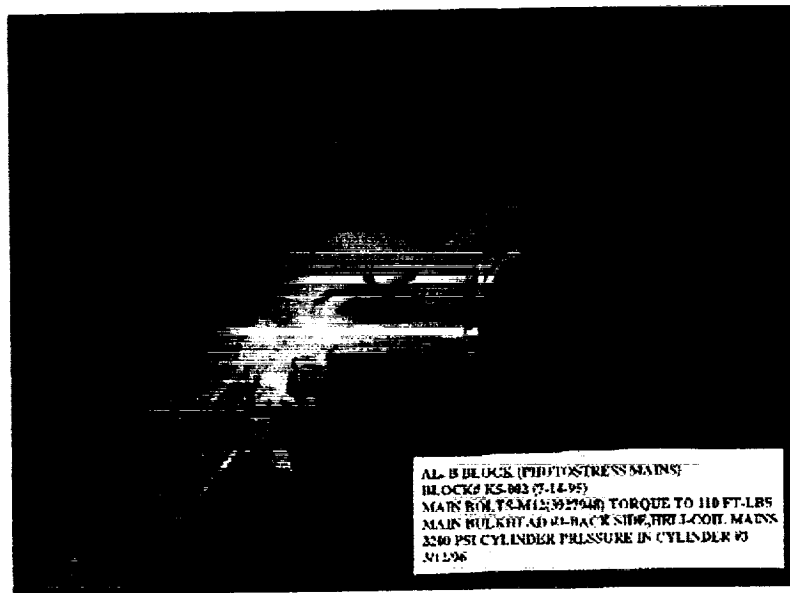


**Figure 3.15.31:** Photostress results on the main bearing saddle with the application of 15.2 MPa cylinder pressure.

Three interesting visual observations were made. First, the most active stress concentration region corresponds to the main bulkhead surface near the end of the main capscrew thread engagement, which correlated well with the location of the fatigue cracks observed on the engine and rig tested blocks, and with the stress analysis. Second, the exhaust side main bulkhead surface near the end of the capscrew thread indicated a higher order of stresses than on the intake side, which also correlates well with the fatigue failures which occurred and the stress analysis work. Finally, a significant reduction on the compressive stress generated from the bolt torque work. This reduction is of concern and analysis was recommended to determine if main cap separation occurs.

#### **3.15.4.1.2 Strain Gage Analysis**

Based on the results of the photostress evaluation several locations were identified for the application of strain gages. Another block was strain gaged as shown in the example in Figure 3.15.32, and an evaluation carried out similar to that described previously.



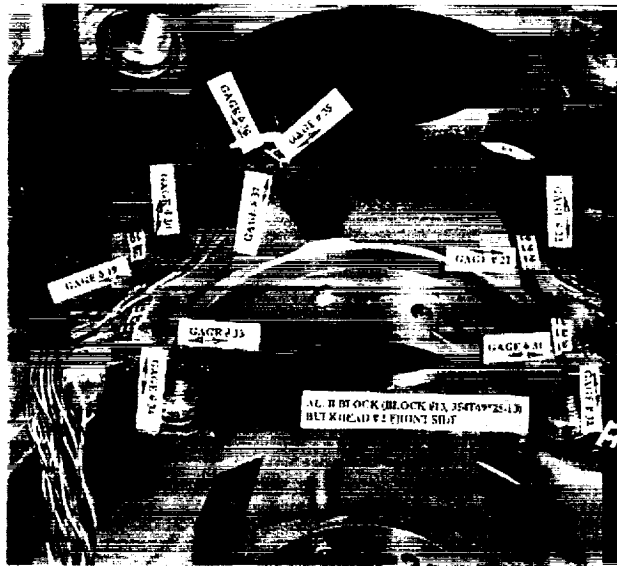


**Figure 3.15.32:** Location of strain gages in the main bulkhead region.

Measurement of the stresses resulting from the bolt torques and from cylinder pressure were made over a range of pressures. The strains at each gage location were plotted as a function of cylinder pressure and the mean and alternating strains calculated from the Young's modulus. The mean and alternating loads were then plotted on a Goodman diagram, from which the design margins (Fatigue factors) were calculated at each location. A design margin of less than two is typically unacceptable when the mean stress at the location is tensile. An example of this is shown in Figure 3.15.33 where the strain gage was located close to the end of the capscrew and at 20.7 MPa cylinder pressure had a design margin of less than two.

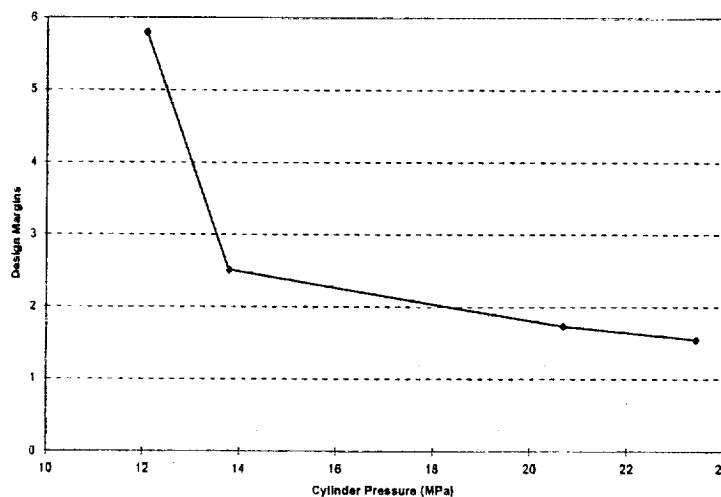


**Figure 3.15.33:** Design margin as a function of cylinder pressure for the location at the end of the capscrew in the main bearing saddles.

This location corresponds to the region the analytical model predicted high stresses and where fatigue failure was observed during engine and rig testing. Overall, the data were consistent with the results of the mechanical tests, and with the results from the FE analysis. However, these data will now be used to recalibrate and refine the finite element model developed for the block. This effort will improve the overall accuracy and allow further life prediction work to be undertaken for different alloys.

### 3.15.4.1.3 Block Fatigue Test

Testing of cylinder blocks was conducted in the Applied Mechanics Laboratory using a hydraulic rig to determine the fatigue resistance of the block. Initially the 390-T5 alloy block from test Engine #1 (See section 3.15.7.1 - Engine #1) was subjected to test, recognizing this had previously been run on engine test. Subsequently, the blocks evaluated were cast from 354-T6 alloy and the data are summarized in Figure 3.15.34. The 390-T6 alloy block tested initially had 14 mm capscrews and failed after 30,000 cycles at 15.8 MPa, which is significantly lower than the 354-T6 alloy blocks.

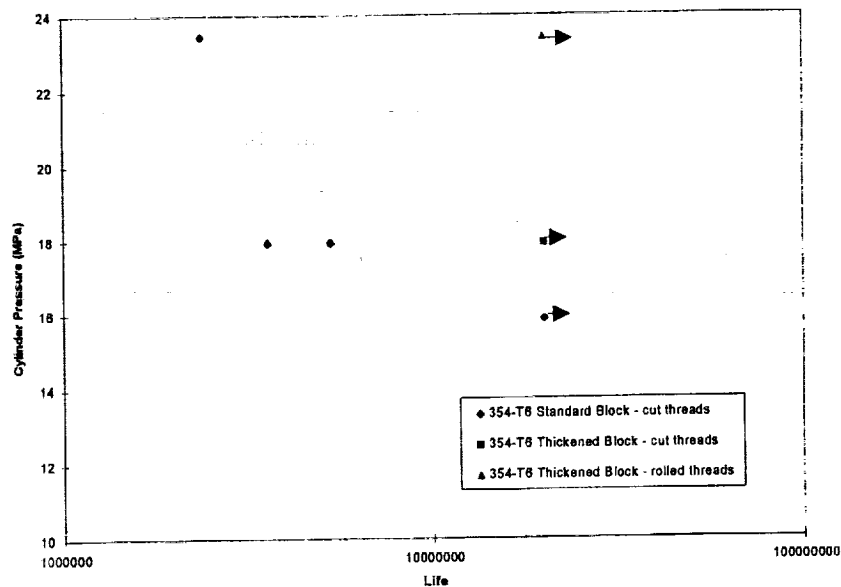


Figure 3.15.34: Cylinder block fatigue data.

These blocks had M12 (12mm) main capscrews with helicoil inserts in the threads. Cracks were found in a number of areas in the block including the main bearing saddles, the location consistent with the high stress areas predicted by the FE analysis. The 390-T5 block was shown to have significantly reduced durability, as compared to the 354-T6 blocks. This result was not considered surprising based on the fact that the block structure was not optimized and the block had been previously engine tested. Typical crack locations are shown in Figure 3.15.35.



**Figure 3.15.35:** Crack locations in the aluminum cylinder block.

A second crack location was observed in the region of the main bearing saddles at the radius between the machined bolt boss and the cast bulkhead (this area can be seen in the upper left corner of Figure 3.15.35). The data show that the blocks tested had lower durability than the cast iron equivalent. Cast iron survived up to 23.4 MPa.

Based on the results of the tests a modification was made to the block design, where the main bearing saddles were thickened to increase the load carrying capability in this region, as shown in Figure 3.15.36.

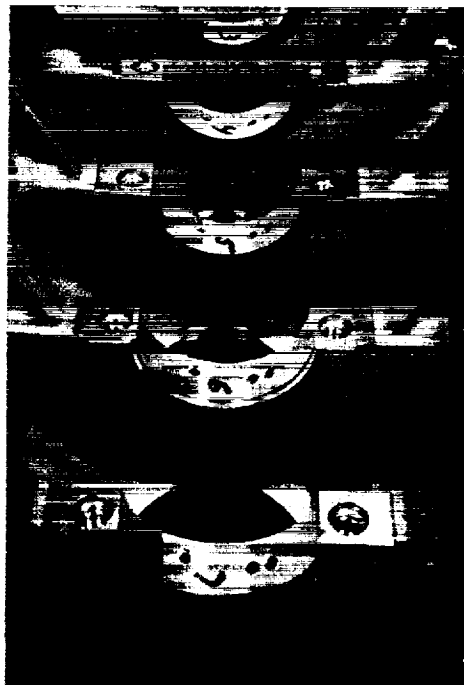


**Figure 3.15.36:** Cylinder block with thickened main bearing saddles.

The blocks cast using Alcoa's Level Pour process and were machined with M12 (12mm) main capscrew helicoil inserts installed. Test were conducted at 17.9 MPa and no cracking of the main bearing saddles was observed. Cracking of the rear face cup plug below the head deck did occur, but the test was considered successful because of the improved durability of the main bearing saddles. These results are compared with those on standard blocks in Figure 3.15.34.

Modification of the block to include rolled threads, rather than the helicoils was then considered as a potential improvement to obtain further durability. In order to evaluate the potential improvement of using rolled threads a test specimen was developed and tested in an MTS servohydraulic test frame. The specimens were machined from 356 aluminum barstock material and specimens with the M12 helicoil inserts were directly compared with specimens that had M12 roll form threads. The results of these tests are plotted in Figure 3.15.37, where a 33% improvement in fatigue strength was observed for the rolled threads as compared to the helicoils.

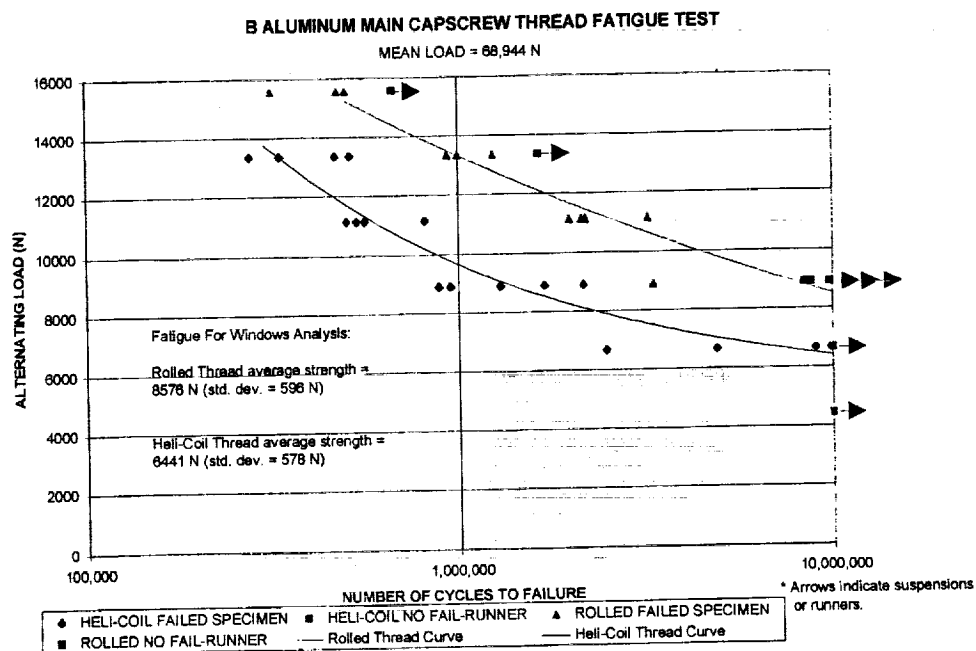


**Figure 3.15.37:** Comparison of the fatigue strength of threads with helicoil inserts and rolled threads.

Failure analysis was conducted on the test specimens to ensure that the failure mode was the same as that experienced in the actual cylinder blocks. This analysis confirmed that the fatigue cracks initiated at the root of the thread at the end of the capscrew engagement, which is the same location as determined in the cylinder blocks. These results indicate that the MTS load frame can be effectively used to evaluate the difference in fatigue strength of different thread types and that modifying the blocks to have rolled threads in the main bearing saddles provides some improvement in durability.

Cylinder blocks with thickened bulkheads were then machined with rolled threads for fatigue testing and the results indicate a significant increase in main bearing saddle durability. The results of the initial tests are shown in Figure 3.15.34 for comparison to the previous data. The results clearly show that a significant improvement in durability occurs with the application of rolled threads, where no failure of the main bearing saddles was experienced at 23.4 MPa after 10,000,000 cycles. Cracks were observed in the water jacket at the intersection between the cylinder wall and the top deck of the block after 6,500,000 cycles and additional testing of cylinders 5 and 6 resulted in cracking of the cup plug on the rear face of the block.

Further work will be required to correct these problems, but testing of the main bearing saddles is still in process. It should be noted that no failure of the main bearing saddles in a cast iron block is experienced at this pressure after 10,000,000 cycles. These results are therefore very encouraging for the development of a durable aluminum cylinder block.

#### **3.15.4.2 Cylinder Head**

Several areas of the head were identified as potential weaknesses. These included increased head lift due to the lower stiffness of the aluminum compared to the cast iron, mushrooming of the head bolt bosses, insufficient exhaust manifold bolt holding strength and reduced ability to withstand cylinder pressure and thermal loading. Testing to assess the head lift and cylinder pressure resistance were conducted in the Applied Mechanics Laboratory, the other factors were assessed using engine tests, as discussed in Section 3.15.7 - **Engine Testing and Validation**.

##### **3.15.4.2.1 Head Lift**

A head lift study was completed to evaluate the possibility of designing a new gasket for the aluminum head. The excessive deflection of the aluminum may require an improved sealing method at the combustion ring of the gasket. Three head materials were evaluated, 319-T6, 354-T6 and 390-T6.

In summary, it was found that the aluminum heads deflected more than the cast iron B-Series cylinder head. For a peak cylinder pressure of 12.4 MPa the maximum head lift values were of the order of 10  $\mu\text{m}$  and at 16.5 MPa were of the order of 18  $\mu\text{m}$  at some locations. It was concluded that the current gasket may be sufficient and should be evaluated at 12.4 MPa and 16.5 MPa to determine if it is sufficient and following this a specific gasket could be tailored for the aluminum with the ability to seal up to 16.5 MPa without issue with the current bolt loads. The lift data may also be used to determine the weak point in the head as far as vertical deflection is concerned and be used for design guidelines for enhancing the durability of the head.

##### **3.15.4.2.2 Cylinder Pressure Resistance**

Due to the lower strength of the aluminum as compared to cast iron, it was concluded that the heads may not be able to withstand the same cylinder pressures as the iron head. Previous data indicates that the cast iron head survives a hydraulic pressure test at 18.6 and 22.8 MPa, but fails at 24.8 MPa. The aluminum heads were therefore pressure tested at 18.6 and 24.8 MPa and the results are shown in Figure 3.15.38.

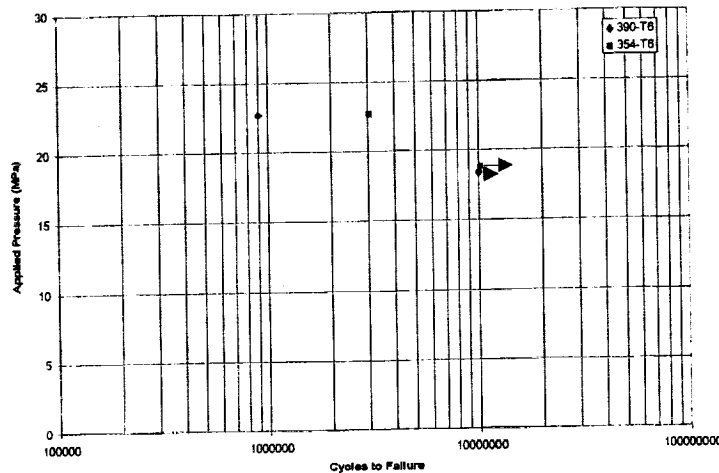


**Figure 3.15.38:** Hydraulic pressure test results on aluminum alloy heads.

Mechanical failure occurred during the test at 22.8 MPa, which is below the limit defined for the cast iron heads. Analysis of the failures showed that fatigue cracks initiated at the base of the exhaust valve spring seat on the water jacket side and then propagated throughout the head.

Shrinkage porosity was found to be associated with both failures and the presence of dispersed shrinkage porosity throughout the thin section in the region where the crack occurred may reduce the overall fatigue strength of the material. However, it should be noted that these were the initial head samples, where the microstructure was not optimized and further work is in process with the casting supplier to improve this.

### 3.15.5 Structural Reinforcement Strategy

Based on the results of the FE analysis and test work a strategy was developed for reinforcing both the head and block to provide improved mechanical and thermal resistance. The test results indicated the thermal loads on the head may be beyond the durability limits of the current aluminum alloy. Unreinforced aluminum may be insufficient to resist thermal cracking in regions such as the valve bridge area of the firedeck.

Analytical work conducted early in the program provided guidance on the design and location of the inserts in the valve bridge region. Two basic designs were chosen for study, a “bow tie” insert which reinforces only the region between the valves, and reinforcement of the whole combustion face.

In addition, inserts were also pressed into the valve seats and valve guides, since it was concluded that these would not have sufficient durability in the parent aluminum. The B-Series engine is manufactured with parent cast iron valve seats, by induction hardening these regions of the cylinder head. However, Cummins manufactures a rebuild kit of inserts for these two regions and for the initial test work it was determined these could be used.

For the block, the main bearing saddles were shown to have lower durability than the cast iron equivalent at a given engine load. From the analytical work it was shown that the aluminum block stiffness was much lower than the cast iron. The placement of steel reinforcing inserts in the main bearing saddle regions could reduce the stretch of the block to a similar value to that of cast iron. This reinforcement has a significant impact on the loads which the bearings and crankshaft experience. Inserts were designed based upon the results of the FE analysis and within the limits of the geometry of the block in the region of the main bearing saddles as shown in Figure 3.15.39.

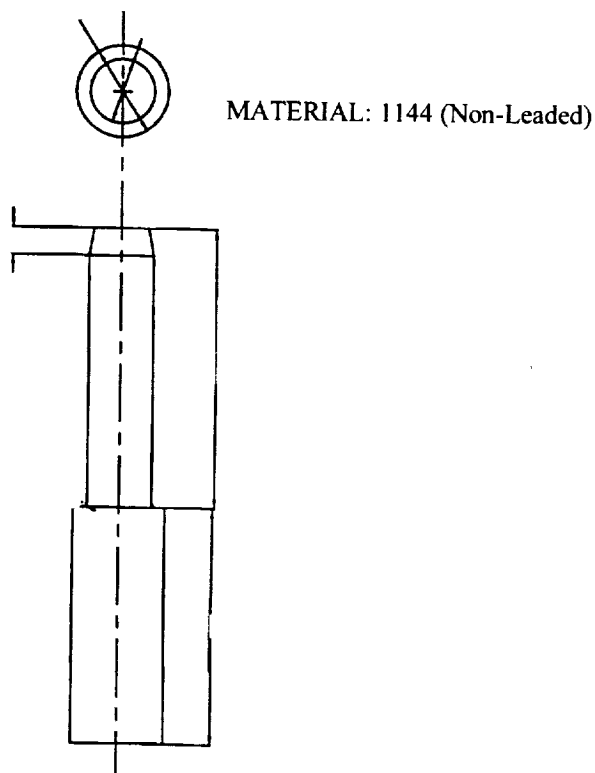


**Figure 3.15.39:** Main bearing saddle inserts.

It was also noted that the aluminum cylinder bores would be insufficient to resist the applied duty cycle and an alternate cylinder liner surface was required. The B-Series engine is manufactured with parent bore cylinder walls. However, to allow rebuild of the engine Cummins manufactures thin walled cast iron cylinder liners. These liners were installed into the aluminum block to allow testing.

### **3.15.6 Metallurgical Bonding Study**

Following the determination that the blocks and heads may require reinforcement, which should be metallurgically bonded into the structure a literature study was initiated on the metallurgical bonding of aluminum to dissimilar metals and the use of lightweight head and block castings in heavy duty diesel engines. This work was completed prior to the start of the contract, but for completeness the results are briefly reviewed.

The results of the initial analytical work and testing indicated there were several areas of both the head and block where the durability was insufficient for a heavy duty diesel engine. Inserts placed at critical locations (defined by high stresses, temperature or wear requirements) need to be strongly bonded in place in order to transfer the stress and heat to the surrounding casting. It is expected that the required strength and heat transfer characteristics can be achieved by forming a metallurgical bond between the insert and casting.

It was concluded that a variety of processes can be used to metallurgically bond aluminum to dissimilar metal inserts. The processes include friction welding, diffusion bonding, brazing, casting in place and some fusion welding processes. The location, geometry and composition of the insert and casting determine which processes are appropriate for a given insert. Special attention must be paid to the disruption or removal of the surface oxides from the surfaces to be joined, particularly in the case of aluminum oxide.

The control over the growth of intermetallic compounds during the bonding process is also very important. Control can be achieved by coating the insert with a third material, silver for example, that acts as a diffusion barrier preventing the formation of ordered intermetallics. Coatings may also be used to promote diffusion and hence the formation of a good metallurgical bond between the insert and casting. The most promising insert coatings were found to be silver, copper, zinc and tin. These can be used in elemental form, alloyed with each other or alloyed with aluminum. Many of these alloys are commercial brazing and soldering materials. It was determined that phosphate coatings of zinc or nickel may also prove effective.

These data were used to provide the direction for a research program initiated to optimize the bond strength between aluminum castings and reinforcing inserts. Initial results of this program show the application of smooth coatings of pure Zn, Zn-5 wt. %Al and Zn-10 wt.% Al could be obtained by hot dip coatings. The use of fluxes was found to be essential to the formation of an interface free of porosity. Pure Zn coatings and Zn-Al coatings with aluminum contents greater than 10 wt.% did not yield good metallurgical bonds. Coating times produced with an immersion time of one minute generally produced higher strengths than those dip coated for three minutes. Prior to T6 heat treatment, interface strength of the 10 wt.% Al were greater than the 5 wt.% Al, but after T6 heat treatment the interface strengths were comparable.

Metallographic work was conducted on the bonds using various optical and electron microscopy techniques. It was found that the bonds formed were composed of layered Al-Fe-Si phases, similar to those produced from the Alfin process and additionally little or no Zinc was found in the bonds. The hardness of the bonds was consistent with hardness results obtained for Alfin bonds. Severe degradation of the bond region was observed during T6 heat treatment, which included the formation of large pores and cracks in the bond region. The bond was approximately four times thicker after T6 heat treatment. Further analysis is in process and the results will be reported at a later date.



### 3.15.7 Engine Testing and Validation

Initial engine tests were conducted in order to measure the strains and temperatures in the aluminum based engine to allow calibration of the FE models and assessment of the integrity of the engine.

#### 3.15.7.1 Engine #1

The first test was designed to demonstrate the mechanical integrity of the cylinder block and cylinder head in a running engine and provide strain gage data for calibration of the FE model. The head was instrumented with four strain gages and the block with twenty strain gages. Dynamic strains were measured along with the operating conditions of the engine. The engine was built to a 119 kW configuration, with a 319-T6 alloy head and 390-T5 alloy block.

##### 3.15.7.1.1 Engine #1, Test 1

The engine was run at several test points as shown in Table 3.15.8.

**Table 3.15.8:** Engine test points - Engine #1, Test 1

Test Point	Speed (rpm)	Load (N-m)	Condition
1	800	none	Idle
2	1000	176	50% max. no air load
3	1600	271	50% torque peak
4	2500	230	50% rated
5	1000	352	Maximum no air load
6	1600	542	Torque peak
7	2500	461	Rated 119kW

All the engine test points were achieved except for the 119 kW point. The maximum horsepower achieved was 112 kW due to an issue with the air intake temperature control, leading to an excessively high intake air temperature. Dynamic strain gage output was recorded throughout the test and was used to calibrate the FE model discussed previously.

After the test was complete the engine was disassembled and the block showed no signs of distress. The cylinder liners remained in place with no apparent movement. The head was also inspected and exhibited no signs of distress. The valve seats and guides remained in place and measurements indicated that there was no sign of warping.

Following this test the block was machined to place thermocouples near the top of the cylinder liners. The head was also machined for thermocouples in the valve bridge area and for a pressure transducer.

#### **3.15.7.1.2 Engine #1, Test 2**

The second test was used to measure dynamic strains, valve bridge temperatures, cylinder wall temperatures, and cylinder pressure in a running engine with an aluminum block and head. The engine was the same as used in Test 1 except the fuel pump and injectors were changed to uprate the power to 172 kW. Additionally, the timing on the fuel pump was advanced to increase the cylinder pressure. The test was planned to explore the operating range from idle to 172 kW rated conditions. The plan also included the test points run in Test 1, to provide temperature and cylinder pressure data.

The maximum power achieved from the engine was 179 kW at 2500 rpm. Maximum torque was 965 N-m at 1400 rpm. Peak cylinder pressure attained was 16.4 MPa at the same peak torque condition. The peak valve bridge temperature was 207°C, which occurred during the same high torque point. The maximum cylinder liner temperature was 124°C, which occurred at 2347 rpm and 757 N-m of torque.

After test the engine was disassembled and inspected. The block was found to be cracked in the #7 main bearing saddle, the location consistent with the end of the capscrews (last thread engagement). This region was consistent with the high stress locations identified by the FE analysis and confirms a weakness in the block, which needs to be addressed in future designs. It should be noted that these were initial block castings, where the microstructure and heat treatment were not optimized.

#### **3.15.7.2 Engine #2**

The second engine was intended to map cylinder pressures, provide an engine for noise measurements and gain further understanding of the failure modes under cyclic loading conditions. The engine was built as a 142 kW engine with a 319-T6 alloy cylinder head and 390-T5 alloy cylinder block.

##### **3.15.7.2.1 Engine #2, Test 1**

The engine was run for ten hours on a break-in cycle. The test points given in Table 3.15.9 were taken to measure cylinder pressure at normal engine timing. The highest pressure recorded was 11.1 MPa at 2500 rpm and 570 N-m torque.

**Table 3.15.9:** Engine test points, Engine #2, Test 1

Test Point	Speed (rpm)	Load (N-m)	Condition
1	800	none	Idle
2	1000	176	50% max. no air load
3	1600	271	50% torque peak
4	2500	230	50% rated
5	1000	352	Maximum no air load
6	1600	542	Torque peak
7	2500	461	Rated 119kW
8	1600	643	Torque peak 141.7kW
9	2500	542	Rated 141.7kW

#### 3.15.7.2.2 Engine #2, Test 2

The engine was run in a noise test for ten hours at Cummins' noise facility. The results of the test indicated the noise levels in the aluminum engine were similar to the cast iron engine, when the two engines were operated under full load. However, when the engines were operated at half load and no load conditions, the aluminum engine noise levels were typically one to two dB louder after averaging the noise levels on all four sides.

#### 3.15.7.2.3 Engine #2, Test 3

The objective was to subject the engine to an endurance test with cyclic loading for 500 hours. The conditions for the cyclic endurance test are given in Table 3.15.10.

**Table 3.15.10:** Cyclic endurance test conditions

Condition	Speed (rpm)	Load (N-m)	Duration (s)
Low idle	840	-	144
Torque peak	1600	596	36
Rated	2600	588	360
High idle	3000	-	36
Rated	2600	588	144
Lug down	2600 - 1600	596	36
Torque peak	1600	596	108
Rated	2600	588	36

After 13 hours of test the engine was shut down due to high blowby, high vibration and an oil leak out of the rear of the engine. After disassembly the block was found to have four cracked main bearing saddles. It appears that the #7 main bearing saddle cracked first, followed by the #6, #5 and then in the front (#1).

### **3.15.7.3 Engine #3**

The engine was built as a 119 kW engine, with a power rating chosen to minimize the risk of bearing saddle failure, using a 319-T6 alloy head and 390-T5 alloy block. The engine was run at Cummins to develop the torque curves and check operation. The engine was shipped to the Naval Surface Warfare Center for noise and magnetic signature measurements.

### **3.15.8 Cylinder Head Testing**

Several key investigations for the aluminum cylinder head were identified as mushrooming of the head bolt bosses, insufficient exhaust manifold bolt holding strength and reduced thermal cycle tolerance. A 319-T6 alloy head was run on a cyclic endurance test (thermal cycle), the test conditions as summarized in Table 3.15.10.

This test was chosen to begin investigating the aluminum head mechanical performance under moderate thermal cycle conditions. Prior to this only limited test hours had been accumulated on the aluminum head, due to the failure of the aluminum blocks. Therefore the test was completed using a standard cast iron block to allow longer test hours. The issue of differential expansion between the aluminum and cast iron was considered analytically and it was concluded that this should not affect the current test. The test was run with a standard B-Series gasket and appeared to performed well during the test.

It was observed that the head bolt bosses experienced severe mushrooming and radial cracking during the test. Some of the head bolts experienced significant torque loss during the test, particularly on those adjacent to the exhaust manifold. Steel washers were used to distribute the load from the head bolt caps to the bosses, but significant brinelling of the washers into the aluminum was observed. Solutions to this problem, including steel reinforcement, are under investigation and will be incorporated in future test plans.

The head experience failure of the exhaust manifold bolt threads and separation of the manifold from the head. Keenserts, trade name, were installed after 92 hours to keep the test running and were tightened after 225 hours as they were pulling out of the parent aluminum. Modifications to the head are under development to solve this issue.

No cracks were observed in the valve bridges at the end of the 250 hour test and it was concluded a more rigorous test would be required to determine combustion face limits of the head, in conjunction with the FE analysis.

The engine was then reassembled for further test and ran 40 hours in a thermal abuse test. When the engine was disassembled fine cracks were observed in the valve bridges. Analysis of the data is in process and the results will be reported at a later date.

### **3.15.9 Lightweight Connecting Rods**

Following the goal of producing a lighter weight engine with decreased magnetic signature, a preliminary evaluation of light weight, non-magnetic materials for connecting rods was undertaken. Since the light weight engine is based on the B engine, B engine connecting rods

were used as the base design for this study. This study focused on the materials for light weight connecting rods, though both materials and design can be changed to lower the weight of the connecting rod. Materials and design are interdependent; the material properties determine the design limits, and the design requirements limit the usable materials.

A light weight rod that is otherwise equivalent to the current steel rod would lower the overall weight of the engine which would increase performance. Another benefit of a light weight rod is reduced inertia. The less the rods weigh; the less energy is lost in their motion. Table 3.15.11 illustrates the performance benefits of a lighter weight connecting rod. The reduction in inertia is more significant in gasoline engines because they run at higher rpm's. At 6000 rpm, a 33.5 % lighter connecting rod translates into a 16.4% lower maximum axial load at the crank end.<sup>2</sup> Diesel engines run at lower rpm's such that the inertial component of the forces on a connecting rod is only about one third of the total loading. The majority of the load on the connecting rod is from firing. Correspondingly, all the examples of light weight rods found in the literature were for gasoline powered cars, motorcycles, or race cars. No examples of diesel engines with light weight connecting rods were found.

**Table 3.15.11:** Example of benefits of a lighter weight connecting rod

Engine type:	In-line 4 cylinder, 2.3 liter, DOHC, 16 valve
Material:	From steel to titanium alloy
Weight reduction:	35 %
Maximum power:	increased 2.0%
Torque:	increased 1.3 to 3.0% at full range
Fuel Consumption:	decreased 2.0% at maximum power

A key issue when considering a change to the connecting rod is the connecting rod's compatibility with the piston pin. In an automobile engine, the piston pin is usually press fit into the rod. In a diesel engine, the pin rotates within the pin bore of the rod. Thus, the pin bore is a bearing surface. Brass bushings are used with the current steel rods and pins.

Different properties are critical to the connecting rod and pin. For the connecting rod, fatigue strength, compressive strength (to resist buckling) and stiffness are the important parameters. For the piston pin, wear, stiffness, dimension stability (for maintaining clearance), and fatigue strength are all important.

Table 3.15.12 lists a variety of materials that could be considered for light weight and/or non-magnetic connecting rods. Powder forged steel, titanium, metal matrix composite (MMC), and hybrid rods are all being used by automotive companies (see Comments, Table 3.15.12). Powder forged steel rods are lighter in weight than conventional forged rods, but they are not non-magnetic. Powder forged connecting rods will be discussed because of their light weight and widespread use in gasoline powered engines. The austenitic stainless steel, 304, is included because it is non-magnetic. The density of 304 is greater than that of the current steel and the

strength and modulus are not better so a rod made from 304 would have to be heavier than the current rod. Thus, 304 can be eliminated from further consideration.

**Table 3.15.12:** Alternate materials for connecting rods

Material	Modulus GPa (Msi)	UTS MPa (ksi)	CTE 10 <sup>-6</sup> /°F	Density g/cm <sup>3</sup>	Cost factor	Comments
Current steel	200 (29)	862 (125)	6.8	7.85	1	1538 modified
Powder forged steel (7 alloys)	205 (30)	758-1000 (110-145)		7.8	0.8	Ford, Porsche, Toyota, GM
304, austenitic	193 (28)	593 (86)	10.4	7.9		not magnetic, not light weight
Titanium (4 alloys)	115 (18)	1100 (160)	4.4-5.6	4.5	7 to 45	Honda
MMC (15 types)	95-265 (14-38)	245-552 (36-80)	6.5-10	2.75- 3.46	2	Toyota, Honda
Hybrid	titanium and carbon fiber reinforced polymide					Daimler-Benz

To maintain compatibility, the piston pin material may have to be changed if the connecting rod material is changed. A pin could be made from MMC with or without a coating or a steel shell. A titanium pin could also be developed. Burgess-Norton, a current pin supplier, and MMCC, a MMC company, have completed preliminary work on a composite pin.

Powder forged steel rods are widely used in automotive applications where high rpm's make the lighter weight of these rods desirable. Powder forged connecting rods are lighter than conventionally forged rods due to a combination of better weight balance and better material properties. Powder forged rods are also cheaper to produce than conventionally forged rods. However, these steel rods do not reduce magnetic signature.

For a light weight and non-magnetic connecting rod, two grades of titanium, a free machining grade (Ti-3Al-2V with sulfur and rare earths), an automotive grade (Ti64A) and MMC's (eg. 2124 with 60 Vf.% alumina and Lanxide alloys with alumina or SiC particulate) are worth further investigation. Titanium rods could be powder forged which would take advantage of some of the cost reduction benefits described for powder steel rods. Krebsöge has expertise in modeling connecting rods and could fabricate prototype rods from powdered titanium. Teledyne Portland Forge and Dynamet (a titanium powder company) are interested in powder forging titanium rods.

The production of an MMC rod requires more redesign work than producing a titanium rod. Two companies that work with MMC's, MMCC and Lanxide-DuPont, have the necessary material and development capabilities to produce prototype connecting rods with some help on the design requirements of a connecting rod.

There is no quantitative information on performance improvement with a light weight connecting rod or magnetic signature reduction by a non-magnetic rod. Before pursuing production of a light weight connecting rod, the reduction in the magnetic signature with a non-magnetic rod and the increase in performance from a light weight connecting rod must be quantified. It should be noted that when changing the connecting rod material, compatibility with the piston pin needs to be considered so an analysis of the piston pin should be included in the connecting rod study to insure compatibility.

#### **3.15.10 Lightweight Low Magnetic Signature Main Bearing Caps**

The development of a lightweight low magnetic signature main bearing cap was seen as a way of introducing an MMC into the project without adding significant risk. The replacement of the ductile iron cap (sand cast, 65-45-12; SAE J343, D4512 alloy) could save approximately two thirds of the weight of the main bearing caps (0.5 kg versus 1.9 kg) and provide a low magnetic signature. The initial challenge of this project was to identify potential materials that would have the fatigue strength (193 - 207 MPa) and stiffness (166 GPa) of the required materials.

The low cost and low density of aluminum make reinforced aluminum metal matrix composites a good choice for the application. The reinforced materials must have low density, high stiffness and high strength. Ceramic reinforcements, including oxides, carbides and nitrides, and carbon/graphite were considered. These reinforcements are available in different forms, which in order of decreasing cost are: continuous fiber, chopped fiber, whisker and particulates

A project was initiated with Cast Metal Composites (CMC) to identify materials that could be used, then manufacture samples for material tests to verify the required properties and finally, if a successful candidate was identified, manufacture a limited number of main bearing caps for further testing. A technical literature review was conducted to examine the commercially available aluminum and MMC materials, along with the developmental MMC materials produced by CMC. Theoretical and empirical models for predicting the mechanical and physical properties of MMC materials were also examined.

Based on this review of the commercially available composite materials, and the theoretical and empirical models for modulus and strength of metal matrix composite materials, CMC recommended the development of squeeze cast 50-55 Vf.%  $\text{Al}_2\text{O}_3$ /aluminum and 50-55 Vf.%  $\text{SiC}_p$ /aluminum MMC materials for the application. These two materials have the capability to meet the mechanical property requirements for the application, while providing a >50% reduction in material density compared to ductile iron. The materials also provide a low cost materials solution by virtue of the low materials cost for  $\text{Al}_2\text{O}_3$  and  $\text{SiC}$  particulate.

Preforms of  $\text{Al}_2\text{O}_3$  and  $\text{SiC}_p$  were then developed to produce samples for tensile and fatigue test. These preforms were then infiltrated with a Al332 type alloy using CMC's squeeze casting press and heat treated to a T7 condition. These samples were provided to Cummins for microstructural evaluation and for machining of samples for tensile and fatigue test.

Both the 50-55 v/o  $\text{SiC}_p$ /Al MMC and 50-55 v/o  $\text{Al}_2\text{O}_3$ /Al MMC materials exhibited about the same microstructural characteristics. The distribution of particulate reinforcement in both MMC

materials was found to be uniform. The tensile test results indicate that the elastic modulus, tensile strength and elongation of both MMC materials were about the same. Both MMC materials exhibited the modulus of about 170 GPa, which is comparable to that of the ductile iron main bearing cap material. The ultimate tensile strength (UTS) of both MMC's are slightly lower than that of ductile iron. Due to the high volume fraction of reinforcement in both MMC's, both materials failed in a brittle manner such that no yield strength could not be determined. Apparently, the current ductile iron material exhibits a much better yield strength than that of either MMC material. The elongation of both MMC's were all very low, about 0.1%. This is expected due to the highly loaded particulate reinforcement.

Both MMC materials exhibited about the same tensile properties and met the requirement for high modulus. However, the UTS, yield strength and ductility of either material were lower than that for the current ductile iron materials. However, the tensile strength and ductility are not considered the most significant properties since the design is limited by stiffness and fatigue strength.

Rotating beam fatigue tests were conducted on both materials. Results of the testing indicated that the median fatigue strengths for the 50-55 v/o SiCp/Al MMC and 50-55 v/o Al<sub>2</sub>O<sub>3</sub>p/Al MMC were 235 MPa and 186 MPa respectively at 10<sup>7</sup> cycles. Figure 3.15.40 shows a comparison between the S-N curves of both MMC materials. It is apparent that the 50-55 v/o SiCp/Al MMC exhibits better fatigue strength than the 50-55 v/o Al<sub>2</sub>O<sub>3</sub>p/Al MMC.

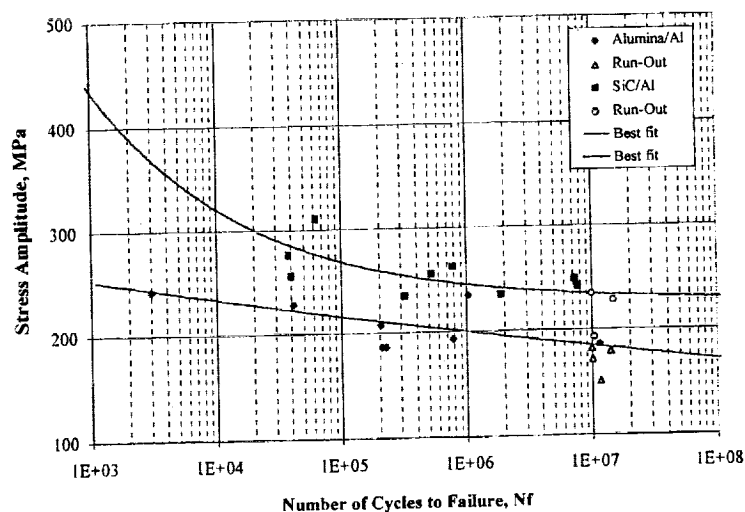


**Figure 3.15.40:** Comparison of fatigue curves for the 50-55 Vf.% SiCp/Al and Al<sub>2</sub>O<sub>3</sub>/Al MMC's at room temperature.

The current ductile iron main bearing cap material requires 193 MPa fatigue strength and therefore it is clear that only the 50-55 Vf.% SiCp/Al MMC can meet the requirement.



The tensile properties and fatigue strength of the selected MMC material was then used in a finite element analysis to evaluate the preform geometry and determine the performance of an MMC cap. The results of the analytical work will be reported at a later date.

### **3.15.11 Conclusions - Lightweight Low Magnetic Signature Engine Development**

- The engine ran successfully and achieved a maximum torque of 965 N-m at 1400 rpm and a maximum horsepower of 179 kW at 2500 rpm. These data were used as input to the FE models and as a validation of the predictive work. Noise testing indicated that the engine was similar to the cast iron when the engine was operated at full load, but was 1 to 2 db higher at half and no load conditions.
- An FE model of the cylinder head was developed which predicted that the best aluminum alloy of those investigated was the 354-T6 alloy. Mechanical property data confirmed this to be the case. The optimum bow tie thermal properties predicted were 30-50% higher thermal conductivity and 15-20% lower thermal expansion coefficient compared to gray iron if Young's modulus and fatigue limit of the bow tie material are close to those of gray iron.
- Both compressive stress and temperature decrease as the bow tie thickness decreases, but the bow tie location and size have little influence on the compressive stress and temperature in the valve bridge area. Compressive stress is dominant in the valve bridge area during the engine thermal cycle and the steady state is the worst case.
- Regions of the head identified as weaknesses included the deformation and cracking of the head bolt bosses, insufficient exhaust manifold bolt holding strength and reinforcement of the valve bridge region of the head may be required to prevent cracking.
- A FE model of the cylinder block was developed which predicted that the aluminum block was structurally applicable for the 119 kW (13.8 MPa) load case investigated. Fatigue analysis at several locations showed that fatigue cracks were not expected in the block and main bearing cap, except in the capscrew engagement region. A thread engagement model was developed which predicted that cracks would initiate at the last thread engagement of the capscrews. This was confirmed by results of the photostress analysis and strain gage data, and fatigue testing of cylinder blocks induced cracks which were consistent with the predicted locations. Finally, engine test data was found to be consistent with the FEA. Incorporation of a steel insert should eliminate the fatigue cracking observed provided that the bonding between the saddle inserts and the block is sufficiently strong.
- The stiffness of the aluminum block is 20% lower than that of the cast iron and results in 20%-30% more vertical block stretch between the head deck and main bearing saddles at 13.8 MPa cylinder pressure. The use of a steel main bearing cap appeared to give equivalent stretch to the cast iron block with a nodular iron bearing cap, particularly if used in conjunction with an insert in the main bearing saddle.
- Several potential processes were identified to metallurgically bond inserts into the block and head. These processes include friction welding, diffusion bonding, brazing, casting in place and some fusion welding processes. The appropriate method is dependent on location, geometry and composition of the insert and casting. Control over the growth of intermetallics

can be achieved by using a third material on the insert to act as a diffusion barrier or promote diffusion. These have significant influence on the strength of the bond formed.

For a light weight and non-magnetic connecting rod, two grades of titanium, a free machining grade (Ti-3Al-2V with sulfur and rare earths) and an automotive grade (Ti64A), and MMC's (eg. 2124 with 60 Vf.% alumina and Lanxide alloys with alumina or SiC particulate) are worth further investigation. Titanium rods could be powder forged which would take advantage of some of the cost reduction benefits described for powder steel rods. Krebsöge in Germany has expertise in modeling connecting rods and could make prototype rods from titanium powder. Teledyne Portland Forge and Dynamet (a titanium powder company) are interested in manufacturing powder forging titanium rods. Producing an MMC rod requires more redesign work than producing a titanium rod. Two companies that work with MMC's, MMCC and Lanxide-DuPont, have the necessary material and development capabilities to produce prototype connecting rods.

An MMC material was developed for the main bearing caps. The material had equivalent stiffness and fatigue strength to the ductile iron currently in use. FE analysis is in process to determine the preform geometry and assess the use of an MMC in this application.

#### 4. Acknowledgments

Many people contributed to this project on the development of in-cylinder components. Some of these contributors will remain nameless due to the short memory of the authors. First and foremost the financial assistance of the Department of Energy and Cummins Engine Company, Inc. are gratefully acknowledged. The foresight and guidance of John Fairbanks of the Heavy Duty Transport Technology Program were instrumental in this development effort. The efforts of the program monitors, Joe Notardonato, and then Jim Wood of NASA, and finally Mark Valco of the Army Research Laboratory greatly contributed to the overall effort.

This program had many subcontractors and contributors throughout the United States and Europe. In order to test components many suppliers were team members on this project. Special thanks to Dr. Mielke at Kolbenschmidt AG for the design and development of the spherical joint piston. C&A Tool developed special machining processes and assisted in material selection for the spherical joint piston. Without the assistance of Dick Conrow at C&A Tool, demonstration of the spherical joint piston would not have been possible. Cylinder heads were cast by Motor Casting Corporation, guided by Roger Nicaloy. Special research and guidance was provided by Dr. Jack Wallace at Case Western Reserve University on metal castings. Ceramic ports were developed by Coors Ceramics using the expertise of Rick Kleiner, Jerry Giles and Doug Coors, and LoTec by Santoosh Limaye for the cylinder heads. Precision Castings Corporation provided special castings of nickel aluminide and titanium aluminide for evaluation. Special piston thermal barrier coatings were applied under the direction of Dick Novak, Al Scharman, Janet Linsey and other team members at United Technologies Research Center.

In the area of exhaust aftertreatment, a number of efforts should be acknowledged, including the efforts of Dick Nixdorf of ReMaxCo, David Stinton at Oak Ridge National Laboratory on CVI coatings and basic research and development, Thermal Ceramics on ceramic paper development, Composite Innovations on CVI coating, ART on ceramic fiber development, and FMT on microwave heating units.

Cummins subsidiaries had key roles and responsibilities during this program. Holset supplied turbocharger wheels and variable geometry hardware. Cummins Piston Ring Division provided piston rings. Modeling efforts by Dan Richardson and coating application by Freidoon Rastegar were instrumental in engine testing. Fleetguard developed ceramic particulate filter technology. Special thanks go to Bill Haberkamp at Fleetguard for developing ceramic filter paper requirements and filter manufacturing techniques.

Within Cummins Technical Center, many investigators assisted this effort. The efforts of Jim Patten who provided guidance throughout the program and program managers, Dean Reichenbach and Ed Owens, were greatly appreciated. Special thanks to engineers who worked and provided much of the talent described in these reports. Initial design efforts by Dave Wildeman, Craig Barnes, Steve Barnes and Kurt Schoenegge and others were appreciated. Additional design efforts were conducted by Anthony Cooper, Ken Harder, Tom McKinley, and Jason Beckfort on the spherical joint piston socket. Closely coupled with design was heat transfer; understanding of this area and key contributions were made by Dale Tree, Dan Oren, Henry Ng, Gary Hunter, Kevin Hoag, Sharon Cressman, Angie May and others who assisted in

this critical area. Efforts of John Mulloy and Harold Weber on advanced turbocharger concepts, Carl McDonald on particulate filters and Randy Stafford on ceramics were greatly appreciated. Detailed engineering of Doug Anderson and Reg Berry in conducting many of the single cylinder tests is gratefully acknowledged. They were assisted by very talented technicians. Special thanks to Lonnie Davis, Henry Stott, Terry Miller, and Brent Richardson for all their efforts, recommendations, efficiency and assistance on this program. Steve Archuleta, Mike Galarno, and Richard Varo provided engineering on an advanced piston telemetry system required to understand the spherical joint piston.

Recent efforts on lightweight engine materials were supported by Paul Becker, Yong Ching Chen, Cheryl Klepser, Kevin Beutler, Dave Ruch, Steve Majors and Mike Warwick at Cummins. Castings at CMI demonstrated the potential of aluminum cylinder blocks and heads. Structural analysis of engine concepts by Dick Belish, Jeff Sullivan, and Mike Gron of Coltec, Inc. were instrumental in the rapid prototyping of aluminum componentry. Materials from Ralph Maier at Cast Metal Composites, Inc. demonstrated the feasibility of metal matrix composite bearing caps. Jim Zwick at Felpro conducted analytic analysis to develop the gasket designs.

Many others within Cummins, as well as government agencies and national labs and subcontractors have a major impact on this effort. In summary, we thank them for their contributions.

Finally, the assistance of Bev Adams and Brenda Beard of Cummins for their secretarial support and the efforts of Susan Adams of Answers for the final manuscript preparation are gratefully acknowledged.

## 5. References

1. Brown, D. T. and Eckert, B. O., "The Rotating Piston 50 Years On," Sulzer Brothers Limited, June 1988.
2. Burrahm, R. W., Davis, J. K., Perry, W. D. and De Los Santos, A., "Development of a Piston Temperature Telemetry System," SAE Paper 920232.
3. Assanis, D. N. and Friedmann, F., "A Telemetry Linkage System for Piston Temperature Measurements in a Diesel Engine," SAE Paper 910299.
4. Barna, G. L., Brumm, D. B. and Anderson, C. L., "An Infrared Telemetry Technique for Making Piston Temperature Measurements," SAE Paper 910051.
5. Lawrason, G. C. and Rollwitz, W. L., "Temperature Telemetry Technique for Reciprocating Engines Is Applied to Measuring Piston-Pin Bearing Temperature in Diesel Engine," SAE Paper 670026.
6. Hoag, K. L., Brands, M. C. and Bryzik, W., "Cummins TACOM Adiabatic Engine Program," SAE Paper 850356.
7. Yonushonis, T. M., "Thick Thermal Barrier Coatings for Diesel Components," NASA CR-187111.
8. U.S. Army Tank Automotive Command (TACOM) under Contracts DAAE 07-84-C-R082 and DAAE 07-91-C-R005.
9. Novak, R. C., Matarese, A. P., Huston, R. P., Scharman, A. J., and Yonushonis, T. M., "Development of Thick Thermal Barrier Coatings for Diesel Applications," Materials and Manufacturing Processes, 7(1), 15- 30, (1992).
10. Yonushonis, T. M., Stafford, R. J., Ahmed, T., Favro, L. D., Kuo, P. K., and Thomas, R. L., "Infrared Thermal Wave Imaging of Thermal Barrier Coatings for Diesel Applications," Bulletin of the American Ceramic Society, 71(8), (1992).
11. Takeuchi, Y., Kokini, K., and Yonushonis, T. M., "Thermal Barrier Coating Development for Pistons," Proceedings of the 1992 Coatings for Advanced Heat Engines Workshop, August 3 - 6, (1992).
12. Takeuchi, Y., "Thermal Fracture of Ceramic Thermal Barrier Coatings," M. S. Thesis, Purdue University, (1991).
13. Case, M. M., "Mechanisms of Interface Crack Initiation in Multilayer Thermal Barrier Coatings Under Thermal Loads," M. S. Thesis, Purdue University, (1993).
14. Kokini, K., Takeuchi, T. R., and Choules, B. D., "Surface Thermal Cracking of Thermal Barrier Coatings Owing to Stress Realization: Zirconia vs. Mullite," Surface and Coatings Technology, 82, 77-82, (1996).
15. Tree, D. R., Oren, D. C., Yonushonis, T. M., and Wiczynski, P.D., "Experimental Measurements on the Effects of Insulated Pistons on Engine Performance and Heat Transfer," SAE Paper 960317.

16. Yonushonis, T. M. and Scharman, A. J., "Ceramic Thermal Barrier Coating for Rapid Thermal Cycling Applications," Patent No. 5,320,909, (June 14, 1994).
17. Morel, T., Fort, E. F., and Blumberg, P., "Effect of Insulation Strategy on Diesel Engine Heat Rejection and Performance," SAE Paper 850506.
18. Bryzik, W. and Kamo, R., "TACOM / Cummins Adiabatic Engine Program," SAE Paper 830314.
19. Woschni, G., Spindler, W. and Kolesa, K., "Heat Insulation of Combustion Chamber Walls - A Measure to Decrease the Fuel Consumption of I.C. Engines?," SAE Paper 870339.
20. Furuhashi, S. and Enomoto, Y., "Heat Transfer Into Ceramic Combustion Wall of Internal Combustion Engines," SAE Paper 870153.
21. Morel, T., Wahiduzzaman, S., Tree, D. R. and DeWitt, D. P., "Effect of Speed, Load, and Location on Heat Transfer in a Diesel Engine - Measurements and Predictions," SAE Paper 870154.
22. Morel, T., Wahiduzzaman, S. and Fort, E. F., "Heat Transfer Experiments in an Insulated Diesel Engine," SAE Paper No. 880186.
23. Morel, T., Wahiduzzaman, S. Fort, E., Tree, D. R., DeWitt, D. P. and Kreider, K. G., "Heat Transfer in a Cooled and an Insulated Diesel Engine," SAE Paper 890572.
24. Assanis, D. N., Friedmann, F. A., Wiese, K. L., Zuluzec, M. J. and Rigsbee, J. M., "A Prototype Thin Film Thermocouple for Transient Heat Transfer Measurements in Ceramic-Coated Combustion Chambers," SAE Paper 900691.
25. Beardsley, M.B. and Larson, H.J., "Thick Thermal Barrier Coatings For Diesel Components," DOE/NASA Final Report, Contract #DEN3-332.
26. Mueller, M., "In-Cylinder Flame Temperature, Soot Concentration and Heat Transfer Measurements in a Low-Heat-Rejection Diesel Engine," M.S. Thesis, University of Wisconsin-Madison.
27. Hay, N., Barr, W.G. and French, B.A., "Effect of Ceramic Insulation on the Performance of Heat Release Pattern and Heat Transfer in a Turbocharged Diesel Engine," ImechE c382/095, pp 283-291.
28. Huang, J. C. and Borman, G. L., "Measurements of Instantaneous Heat Flux to Metal and Ceramic Surfaces in a Diesel Engine," SAE Paper 870155.
29. Tsutsumi, Y., Nomura, K. and Nakamura, N., "Effect of Mirror-Finished Combustion Chamber on Heat Loss," JSAE Review, Vol.11, No.2.
30. Cartellieri, W. P. and Wachter, W. F., "Status Report on a Preliminary Survey of Strategies to Meet US-1991 HD Diesel Emission Standards without Exhaust Gas Aftertreatment," SAE Paper 870342.
31. Cartellieri, W. P. and Heroz, P. L., "Swirl Supported or Quiescent Combustion for 1990's Heavy-Duty DI Diesel Engines - An Analysis," SAE Paper 880342.

32. Reichenbach, D. H., Hoag, K. L., Frish Cressman, S. R. and Manon, A. R., "Development of Advanced In-Cylinder Components and Tribological Systems for Low Heat Rejection Diesel Engines," NASA CR-187159.
33. Gundlach, R. B., B. Ross, A. Hetke, S. Valtierra and J. F. Mojica, "Thermal Fatigue Resistance of Hypereutectic Aluminum-Silicon Casting Alloys," AFS Transactions, Vol. 102, 1994.
34. Folgar, F., J. E., Widrig, and J. W. Hunt, "Design, Fabrication and Performance of Fiber FP/Metal Matrix Composite Connecting Rods," SAE Paper 870406.
35. Tanaka, I., T. Shimamoto, T. Yamaguchi, and J. Noguchi, "Engine Weight Reduction Using Alternative Light Materials," SAE Paper 922090.

## 6. Appendices

### 6.1 Appendix I - LE-55 Performance Development

The Cummins In-Cylinder Components program involved the research and development of in-cylinder components to facilitate achieving the DOE and Cummins objectives of a low emissions, 55% thermally efficient (LE-55) diesel engine. The LE-55 engine recipe required high peak cylinder pressures on the order of 19.3 MPa at 1500 rpm with a reciprocator Brake Mean Effective Pressure (BMEP) of 2.54 MPa and a reciprocator Brake Specific Fuel Consumption (BSFC) of 175 g/kW-hr for a turbocompounded system BSFC of 152 g/kW-hr. In order to evaluate the performance of the LE-55 in-cylinder components developed on this program it was necessary to test the components under LE-55 in-cylinder operating conditions. This appendix describes the work done to achieve the LE-55 in-cylinder operating conditions in the single cylinder research engine.

#### 6.1.1 Performance Basis Development

The LE-55 engine recipe, derived through the use of Cummins TRANSENG computer simulation code, included a two-stage turbocharged, turbocompounded, multi-cylinder diesel engine based on the Cummins 10 liter (L10) engine platform. The evaluation of the in-cylinder components developed on this program was to be performed on a single cylinder version of the L10 (Single Cylinder Engine or SCE L10). The SCE L10 was not equipped with a turbocharger nor turbocompound hardware (reciprocator only). Also, the SCE L10 did not incorporate on-board auxiliary hardware such as oil, water, and fuel pumps. All of the differences between a multi-cylinder LE-55 and the SCE L10 would make a comparison of operating conditions on a brake specific basis impractical. The challenge was to achieve comparable in-cylinder operating conditions with the SCE L10 as one would expect in a multi-cylinder LE-55 diesel engine.

A point of comparison between the multi-cylinder LE-55 and the SCE L10 was determined after reviewing the four-stroke, diesel cycle. Assuming that the same mass of charge air and fuel is provided to each engine, the in-cylinder conditions should be the same between intake valve closing and exhaust valve opening for each engine. This is the compression-combustion-expansion portion of the engine cycle. Work derived during compression-combustion-expansion portion of the cycle is given by the Gross Indicated Mean Effective Pressure (GIMEP) as defined as follows.

$$\text{GIMEP} = \int_{\text{BDC}_{\text{int}}}^{\text{BDC}_{\text{exh}}} \left[ \frac{P}{D} \right] dV \quad (4\text{-stroke only}) \quad \text{I.1}$$

where,

P = Cylinder pressure

V = Cylinder volume

D = Engine displacement rate

Therefore, in order to define operating parameters to set up SCE L10 engine operation the LE-55 performance targets were converted to reciprocator (no turbocharger or turbocompound) gross



indicated values. The Gross Indicated Specific Fuel Consumption equivalent to the LE-55 target of 152 g/bkW-hr was calculated to be 167.9 g/gikW-hr. The value of 167.9 g/gikW-hr was used as the SCE L10 performance target for the program.

### 6.1.2 Engine Test Verification

Gross indicated engine performance parameters are based on in-cylinder pressure measurements. Initial SCE L10 performance development was performed on a cylinder pressure instrumented engine equipped with a Cummins PT mechanical (fixed timing) fuel system. Early testing showed that the PT fuel system could not deliver fuel to the SCE L10 in a manner to achieve the LE-55 operating conditions. The fuel system was then switched over to a Cummins 1991 CELECT electronic fuel system. The fuel system switch involved a change in camshaft and injector as well as the addition of electronic controls. The electronic controls provided the ability to control fueling rate and injection timing in real time. This was a vast improvement over the time consuming requirement of physically replacing a cam timing key in order to change injection timing with the PT fuel system.

SCE L10 testing with the Cummins 1991 CELECT electronic fuel system provided fuel consumption results within +7.5% of the target of 167.9 g/gikW-hr. At this time in the program the Cummins 1994 CELECT fuel system became available for preproduction use. The 1994 CELECT fuel system hardware included a "fast cam" and a high lift injector. The "fast cam" incorporated a steep ramp injector cam lobe for shortened injection duration. The high lift injector provided additional capacity to inject a large mass of fuel. The combination of the "fast cam" and the high lift injector provided the ability to inject large amounts of fuel very quickly. The 1994 CELECT fuel system hardware was installed in the SCE L10 and placed on test.

Table I.1 shows the SCE L10 operating condition achieved using the 1994 Cummins CELECT fuel system hardware.

**Table I.1:** SCE L10 operating condition achieved using the 1994 Cummins fuel system hardware

Parameter	Operating Value
Engine speed	1497 rpm
Fuel rate	8.90 kg/hr
GIMEP	2.51 MPa
Air/Fuel	31.5
Peak cylinder pressure	22.1 MPa

The operating condition shown above equates to a GISFC of 170.4 g/gikW-hr. This GISFC is within +1.5% of the target of 167.9 g/gikW-hr. A LogP-LogV graph of cylinder pressure (English units) measured at the operating point is shown in Figure I.1.

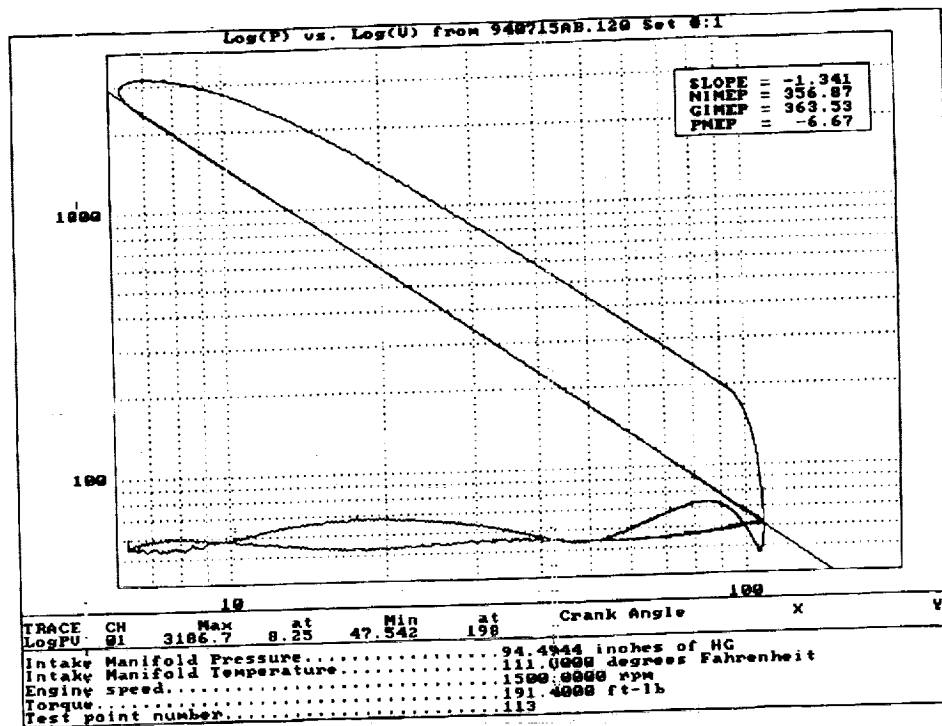


Figure I.1: LogP-LogV plot of cylinder pressure at LE-55 operating point.

The SCE L10 operating condition shown above was considered suitable for evaluating the in-cylinder components at LE-55 in-cylinder operating conditions. All SCE L10 operating parameters were recorded for future reference in setting up the SCE L10 at the LE-55 operating point.

## 6.2 Appendix II - LE-55 Emissions Prediction

The LE-55 program was an effort to understand what a diesel engine would need to achieve a goal of 55% thermal efficiency. In Phase 1 of the program, Cummins' engine simulation computer code, TRANSENG, was used to extrapolate a diesel engine design to achieve the thermal efficiency goal. The engine modeled was based on the 1989 Cummins L10. In Phase 4 of the program, an attempt was made to extrapolate the emissions performance of the simulated LE-55 engine using a predictive emissions module within TRANSENG. The results of the emissions prediction are presented here.

### 6.2.1 Methodology

The objective of this exercise was to extrapolate LE-55 engine emissions over the EPA FTP transient cycle for heavy duty diesel engines. However, the TRANSENG computer program simulates single point, steady state diesel engine operation. In order to utilize the TRANSENG code for LE-55 engine emissions prediction it was proposed to simulate the EPA FTP with a multi-mode, steady state simulation.

The AVL 8-Mode Cycle [Ref 31][Ref 32] was used for the simulation. The cycle, consisting of eight engine modes (speed and load combinations), was used to predict transient emissions by applying weighting factors proportional to each mode's contribution to the total emission levels. The 8-Mode average was weighted using both percent time and power. The percent time weighting factors used along with the overall calculation are shown in Table II.1.

**Table II.1:** Heavy duty diesel transient test simulation by 8-Mode cycle

Mode Number (i)	Speed <sup>1</sup> (%)	Load <sup>2</sup> (%)	Weighting Factor (% Time)
1	0	0	35.01
2	11	25	6.34
3	21	63	2.91
4	32	84	3.34
5	100	18	8.40
6	95	40	10.45
7	95	69	10.21
8	89	95	7.34

<sup>1</sup> 0% = Low Idle Speed  
100% = Rated Speed

$$\text{Speed (rpm)} = \text{Low Idle (rpm)} + \text{Speed (\%)} \times \frac{(\text{Rated Speed (rpm)} - \text{Low Idle Speed (rpm)})}{100 \%}$$

<sup>2</sup> Load percent at each speed

$$^3 \text{ BS Emission (g / bhp - hr) } = \frac{\sum_{i=1}^8 (\text{Emission Rate (g / hr)}_i \times \text{Weighting Factor}_i)}{\sum_{i=1}^8 (\text{Power (bhp)}_i \times \text{Weighting Factor}_i)}$$

The approach taken was to calibrate the TRANSENG simulation with measured emission data from a 1994 L10 engine. The 1994 L10 had the same displacement as the LE-55 concept engine and was of such advanced diesel engine design as to represent state-of-the art. The 1994 L10 was tested over both the EPA FTP Cycle and the 8-Mode Cycle. Comparison between the measured and simulated emissions data (NO<sub>x</sub> and Particulate) is presented in the next section.

### 6.2.2 Measured and Simulated Data Comparison

Measured engine emissions data were obtained from a 1994 L10 design validation engine. Comparison between the 8-Mode measured engine data and 8-Mode TRANSENG simulated data is shown in Table II.1. For bsNO<sub>x</sub>, the simulation at individual modes shows some significant errors. The weighted average comparison, however, works out to be fairly good. The bsParticulate simulation shows a similar trend with the notable exception that the mode 1 bsParticulate was predicted to be 0.000. This is counter to the experimental trend.

**Table II.2:** Comparison of measured and simulated 8-Mode data - 1994 L10 design validation engine

Mode	bsNO <sub>x</sub> (g/bhp-hr)		bsParticulate (g/bhp-hr)	
	Measured	Simulated	Measured	Simulated
1	16.47	16.91	0.174	0.000
2	8.56	16.64	0.018	0.001
3	6.88	14.91	0.017	0.004
4	5.55	10.10	0.014	0.008
5	5.88	10.21	0.064	0.012
6	4.07	4.46	0.039	0.026
7	4.22	3.97	0.022	0.033
8	5.60	5.67	0.014	0.028
8-Mode Weighted Avg.	5.36	6.53	0.0287	0.0241

A problem in the 8-Mode TRANSENG simulation is capturing the particulate contributions at low engine load and speed. For example, Mode 1 is essentially zero engine load at low idle speed. Under these conditions there is an increase in particulate that the TRANSENG predictive emissions module did not capture. The most significant reason for 0.000 predicted particulate is that at lower engine loads the premixed burn fraction (heat release rate) increases. At Mode 1, the heat release rate is almost 100% premixed burn. The TRANSENG predictive emissions module assumes that the premixed burn's contribution to particulate is zero. Therefore, the more premixed burn, the lower the particulate predicted. Other factors such as increased oil

consumption tend to increase the measured particulate at low engine loads causing the TRANSENG predictive emissions module results to diverge from the measured data.

Since the TRANSENG predictive emissions module is essentially a fit to measured data, it was suggested that it would be possible to fit this particular data set in order to improve the predicted emissions. The improvement could be made by adjusting coefficients within the module in order to match the measured data. However, the new coefficients would not be portable to other engines or engine models. The fit would have to be rematched to each data set and would not be useful for predicting emissions for concept engines such as the LE-55. A tailored data fit was not used in this exercise. A summary comparison among the simulated 8-Mode weighted average, measured EPA FTP and measured 8-Mode data is shown in Table II.3.

**Table II.3:** Summary comparison of simulated 8-Mode weighted average, measured EPA FTP and measured 8-Mode data

	bsNO <sub>x</sub> (g/bhp-hr)	EPA FTP (Δ%)	8-Mode (Δ%)	bsParticulate (g/bhp-hr)	EPA FTP (Δ%)	8-Mode (Δ%)
Simulation	6.53	+31	+22	0.024	-64	-16

### 6.2.3 LE-55 Emissions Prediction

As the final step in this exercise the calibrated TRANSENG computer simulation was run at the LE-55 conditions (rated - 354 kW and 1500 rpm) to predict emission levels for the concept engine. The simulation results were compared to the Mode 8 data from the previous runs since Mode 8 is closest to the rated power of the 1994 L10. The LE-55 TRANSENG computer simulation incorporated the heat release rate correlation from the 1994 L10 TRANSENG simulation.

The TRANSENG simulation predicted 2.62 g/bhp-hr bsNO<sub>x</sub> and 0.0179 g/bhp-hr bsParticulate for the LE-55 concept engine. These emissions values compare to 6.62 g/bhp-hr bsNO<sub>x</sub> and 0.0132 g/bhp-hr bsParticulate for the 1994 L10 engine at Mode 8. These results suggest a large improvement in NO<sub>x</sub> with only a small increase in particulate.

Several possible reasons for the improvement in bsNO<sub>x</sub> were identified. The higher power of the LE-55 concept engine immediately leads to a decrease in the brake specific value as long as the overall production does not increase as rapidly. A lower intake manifold temperature was achieved due to a high aftercooler effectiveness (considered to be ideal). A higher turbocharger efficiency was assumed (75% versus 55%) which contributes to a higher intake manifold pressure and an increase in trapped in-cylinder mass. The increased trapped mass causes the peak cylinder temperature to be lower which decreases NO<sub>x</sub> production. The overall effect of these changes is to decrease the bsNO<sub>x</sub> emission value. These results are specific to the LE-55 operating point and would be difficult to reproduce over a wide operating range. However, the

LE-55 concept engine was meant to demonstrate the capability to meet certain emissions objectives even if a single operating condition. In reality, single mode operation is not uncommon in certain applications (i.e., stationary power generation).

The higher particulate value is likely due to the same factors. A higher trapped mass leads to a lower end-of-combustion (EOC) flame temperature. The TRANSENG emission prediction module correlates more particulate with lower EOC flame temperatures. The rationale behind this is that higher temperatures tend to burn up the remaining particulate with the last temperature a particulate mass would see being the EOC flame temperature. Therefore, the classic NO<sub>x</sub>/Particulate tradeoff is reflected in these results.

#### **6.2.4 Conclusions - LE-55 Emissions Prediction**

- The results from the TRANSENG emission prediction module were within 29% of bsNO<sub>x</sub> and 76% of bsParticulate as compared with measured EPA FTP data.
- The TRANSENG emission prediction module after being calibrated with measured data is estimated to have an accuracy of approximately  $\pm 20\%$ .
- The predicted emission for the LE-55 concept engine showed that the engine had significantly lower bsNO<sub>x</sub> and higher bsParticulate than the 1994 L10 engine at rated speed and load. These predicted values were attributed to higher efficiency turbomachinery and a high effectiveness aftercooler leading to a higher trapped in-cylinder mass and lower end-of-combustion flame temperatures.

### **6.3 Appendix III - CD-50 Performance Analysis**

The initial proposal for the follow-on phase to Phase 4 of the program was structured around a Clean Diesel - 50% thermally efficient (CD-50) engine concept. The CD-50 proposal was to incorporate defined emissions limits ( $\frac{1}{2}$  of year 1998 standards) constrained within 50% thermal efficiency.

A computer analysis was conducted to revisit the LE-55 concept simulation conducted in Phase I of the program [Ref 33] under the revised emissions and thermal efficiency objectives. An M11 turbocompound engine was chosen as the engine platform for this analysis. The simulation was performed using Cummins engine simulation computer program - TRANSENG. In an attempt to achieve the performance defined by the CD-50 proposal, several subsystem improvements were implemented into the baseline engine configuration files developed with TRANSENG. These improvements included:

- Insulated intake and exhaust ports
- Reduced FMEP
- Shortened heat release duration
- Improved turbomachinery efficiencies

After addition of these improvements, the program OPTDES was applied to optimize the files for minimum BSFC (maximum thermal efficiency) under a set of established constraints. In this appendix, the magnitude of each improvement along with assumptions made during implementation are quantified. Variable geometry turbomachinery and two-stage turbocharging were also considered as additions to the optimized engine and their effects are discussed in detail.

#### **6.3.1 Baseline Engine Optimization**

##### **6.3.1.1 TRANSENG Calibration**

Measured performance data were obtained for the M11 turbocompound engine. Baseline TRANSENG input files were generated to match this data over a range of engine speeds (1200, 1400, 1600, and 1800 rpm) at full load. Results of the data match displayed little deviation from accepted tolerances.

After establishing credible baseline files, the horsepower rating was set at each speed according to the torque curve for the M11. The goal of this study was to maximize thermal efficiency with primary concentration aimed at speed-load combinations along the torque curve(full load) shown in Table III.1.

**Table III.1: M11 torque curve speeds and loads**

Engine Speed (rpm)	Brake Torque (N-m)
1200	1966 (247 kW)
1400	1898 (277 kW)
1600	1830 (306 kW)
1800	1780 (336 kW)
2100	1424 (313 kW)

Investigation of these speed-load combinations allowed comparison of engine performance parameters at peak torque, peak power, and cruise speeds.

### 6.3.1.2 Baseline Optimization

The optimization program package, OPTDES, was utilized with TRANSENG to optimize the baseline files at each torque curve speed-load combination. The objective of the optimization was to maximize thermal efficiency (minimize BSFC) under constraints established at the beginning of this exercise. These constraints included,

Peak cylinder pressure: Limits of 15.5, 19.3, 20.7, and 23.4 MPa

Minimum steady-state air-fuel ratio at standard conditions (152 m):

RPM	A/F
1200	19
1400	20
1600	23
1800+	25

Turbo turbine inlet temperature: 677°C or lower at standard conditions

Rotor Speed: 115 krpm or lower

Ambient Conditions:

Pressure: 100 kPa

Temperature: 25°C

Inlet restriction: 2.5 kPa at 336 kW operating point

Stack restriction: 6.8 kPa at 336 kW operating point

Charge Air Cooler restriction: 10.2 kPa at 336 kW operating point

The OPTDES package contains a matrix program which uses an input file of analysis variables to execute a matrix of runs by TRANSENG. The analysis variables chosen for this study were start



of injection, turbo turbine casing size, and power turbine casing size. Multiple combinations of the analysis variables created the matrix. Table III.2 summarizes the optimization results for a peak cylinder pressure (PCP) limit of 19.3 MPa. This constraint provided the optimum BSFC at all speed-load combinations because the limit was never achieved. Higher PCP limits produced the same optimal solution. It should be noted that since the engine was re-optimized at each speed, the turbine casing sizes (mass flow factors) vary along the torque curve. This allowed comparison of an ideal casing size to the current hardware.

**Table III.2:** Optimization results for baseline TRANSENG input files at each speed-load combination along the torque curve (PCP < 19.3 MPa)

Engine Speed (rpm)	1802	1602	1402	1202
Brake Power (kW)	336	306	277	247
Brake Torque (N-m)	1779	1826	1890	1961
Start of Combustion (°bTDC)	12.0	10.0	8.0	3.7
Turbo Turbine Mass Flow Factor	1.097	1.017	1.000	.9007
Power Turbine Mass Flow Factor	1.013	.9897	1.000	1.088
PCP (MPa)	18.9	19.1	18.1	19.0
A/F	25.0	24.7	24.8	25.5
Turbo Inlet Temp (°C)	595	568	571	552
Rotor Speed (rpm)	95209	92250	90496	90620
BSFC (g/bkW hr)	188	185	185	184
Thermal Efficiency (%)	44.3	45.0	45.1	45.2

The only constraint which appeared limiting during optimization was air-fuel ratio at 1800 rpm. However, the air-fuel ratio at all speed-load combinations was within 2% of 25.0. This led to the conclusion that air-fuel ratio is not limited significantly at 1800 rpm, but that tradeoffs in heat transfer, power turbine work, and air handling losses in the engine created an optimal air-fuel ratio value at all engine speeds.

Another observation was that flow factors at cruise speeds (1400 and 1600 rpm) were nearly one, which means the current baseline engine can achieve near minimum BSFC at full load without hardware modification.

### 6.3.2 Application of Subsystem Improvements

Several subsystem improvements were applied to the baseline engine configuration in an attempt to increase thermal efficiency. These improvements were port insulation, shortened heat release duration, reduced FMEP, and improved turbomachinery efficiencies. The following sections describe the procedures for implementation of these improvements into the baseline TRANSENG files.

### 6.3.2.1 Port Insulation

The elements of port heat transfer were modeled with the resistance network shown in Figure III.1. For simplicity, the port was modeled as a hollow cylinder and Figure III.1 displays the cross-section. It should be noted that the wall material was gray cast iron.

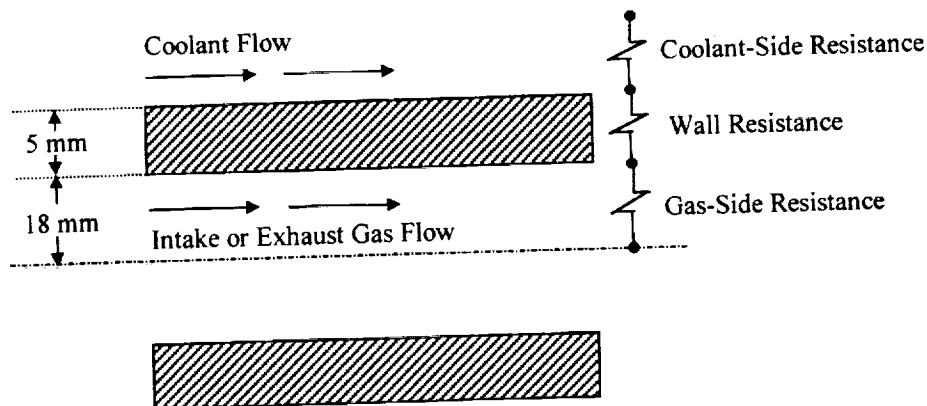


**Figure III.1:** Cross-section of port with corresponding heat transfer elements.

Several heat transfer and geometrical variables were needed to compute each resistance.

- Gas-side resistance → surface area, convection coefficient, and temperature
- Coolant-side resistance → surface area, convection coefficient, and temperature
- Wall resistance → thermal conductivity, inner diameter, outer diameter, and characteristic length

All geometrical variables were obtained from production 1994 M11 intake and exhaust port drawings. Intake and exhaust port wall resistances were then calculated with the following equation:

$$R_{\text{wall}} = \ln(r_2 / r_1) / (2 \times \pi \times L \times k) \quad \text{III.1}$$

$r_2$  - outer port radius

$r_1$  - inner port radius

$L$  - characteristic length (cylinder assumption)

$k$  - wall thermal conductivity

Gas-side resistance was calculated by TRANSENG upon input of the gas-side wall temperature. Coolant-side resistance was calculated by TRANSENG upon input of the coolant type, temperature, and convection coefficient. The convection coefficient was calculated from the following three equations:

$$Re = [\rho \times V \times D] / \mu$$

III.2

where,

$Re_D$  - Reynold's number

$\rho$  - coolant density

$V$  - coolant velocity

$D$  - characteristic diameter

$\mu$  - coolant dynamic viscosity

$$Nu = 0.023 \times Re_D^{0.8} \times Pr^{0.3}$$

III.3

where,

$Nu$  - Nusselt number

$Pr$  - Prandtl number

$$h = [Nu \times k] / D$$

III.4

where,

$h$  - convection coefficient

$k$  - thermal conductivity of coolant

The major change in the resistance network displayed in Figure III.1 after insulation was wall resistance. The modeled wall resistance used was based on a combination of three materials in series rather than just gray cast iron. Figure III.2 illustrates the insulated wall model. The model was based on port insulation development work done on the LE-55 program. This development work, however, involved a unique cylinder head cooling scheme (oil based) which differed from conventional water jacket designs. The oil cooled design is capable of cooling the cylinder head due to lower head heat transfer rates as a result of the insulation. Engine performance, however, differs only slightly between each design, so the water jacket model was implemented in TRANSENG for simplicity.

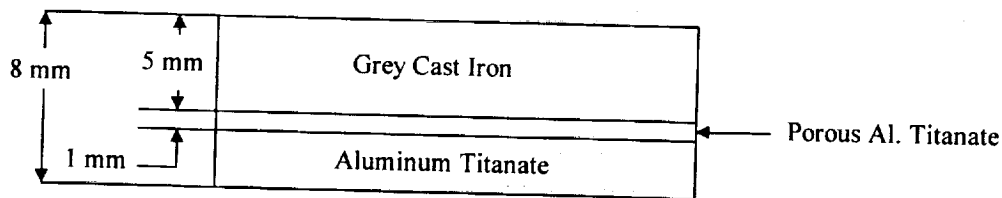


Figure III.2: Port wall with insulation.

The aluminum titanate insert was cast into the cylinder head. Porous aluminum titanate was used as a compliant layer creating a gap between the insert and cast iron and creating a large resistance to heat transfer due its low thermal conductivity. The only numerical changes required in

TRANSENG to implement this model were wall resistance and coolant-side surface area because the port inside dimensions were unchanged.

#### **6.3.2.2 Shortened Heat Release Duration**

Enhancing combustion chamber mixing with swirl or increasing injection pressure are effective means for shortening the heat release duration and improving fuel economy. For this study, a 20% decrease in heat release duration was assumed reasonable based on previous development work in this area.

In TRANSENG, the heat release model at each engine speed was created with files generated using test cell measurements that related heat release rate to crank angle. To simulate a shorter duration, these files were compressed so that the total crank rotation of heat release decreased by 20%.

#### **6.3.2.3 Reduced FMEP**

FMEP was calculated in TRANSENG with the following equation:

$$\text{FMEP} = A + B \times (\text{MeanPistonSpeed}) + C \times (\text{PeakCylinder Pressure}) \quad \text{III.5}$$

where,

A, B, & C are constants

A 21 kPa reduction in FMEP was deemed reasonable at 1500 rpm for this exercise. FMEP variance with rpm is approximately linear. Therefore, the decrease in FMEP at all other engine speeds was determined by extrapolation.

After decreasing the baseline FMEP at each engine speed according to above assumption, equation III.5 can be re-solved for a new value of the constant B. This value for B should be the same at all engine speeds because of the linear relationship between FMEP decrease and changes in mean piston speed (or engine speed, as mentioned above).

#### **6.3.2.4 Improved Turbomachinery Efficiencies**

Turbomachinery efficiencies of 90% for the compressor, 85% for the turbocharger turbine, and 87% for the power turbine were assumed to be achievable upon further research and development. Application of these improvements in TRANSENG required scaling the maximum efficiency in each performance map to the improved efficiency value.

#### **6.3.3 Optimization at "Design Point"**

The greatest amount of fuel is burned near 1600 rpm. This is the engine speed at which the vehicle is geared to handle common road speeds (97 kph). Because turbocompound engine fuel consumption improvements are most evident at full load, the "design point" was chosen to be 1600 rpm (307 kW).

All improvements discussed in the previous section were implemented at the design point. OPTDES was then applied to optimize thermal efficiency under the same constraints and analysis variables as the baseline. Table III.3 displays the comparison between the baseline and improved engine configurations.

**Table III.3:** Comparison of engine performance parameters (baseline versus improved) at the "Design Point"

Parameter	Baseline	Improved
Turbo Turbine Mass Flow Factor	1.017	1.099
Power Turbine Mass Flow Factor	0.9897	0.9020
Start of Combustion ( $^{\circ}$ bTDC)	10.0	5.8
PCP (MPa)	19.1	18.9
A/F	24.7	27.8
Rotor Speed (rpm)	92250	94493
Turbine Inlet Temperature ( $^{\circ}$ C)	568	513
BSFC (g/bkW-hr)	185	174
Thermal Efficiency ( % )	45.0	47.9

The minimum BSFC was 174 g/bkW-hr, which was worse than the desired objective. The improved engine configuration was similar to the baseline in that the maximum PCP was reached before the 19.3 MPa limit. Table III.4 presents the BSFC and thermal efficiency values during sequential addition of each improvement. This allowed comparison of each improvement magnitude relative to fuel economy.

**Table III.4:** Magnitude of each improvement relative to fuel economy

Improvement	BSFC (g/bkW-hr)	Thermal Efficiency ( % )	$\Delta$ BSFC
Baseline	185.0	45.0	-
Port Insulation	184.7	45.1	0.3
Lower FMEP	182.9	45.5	2.1
Shorter Heat Release Duration	180.9	46.0	4.1
Higher Turbomachinery Efficiencies	173.8	47.9	11.2

As expected, improvement in turbomachinery efficiencies had the strongest impact on fuel economy( $\approx$  63%). The improved efficiencies decreased air handling losses (lower PMEP), and directly improved open cycle efficiency and, thus, thermal efficiency. This was evident from the relation:

$$\eta_{\text{thermal}} = \eta_{\text{open}} \times \eta_{\text{closed}} \times \eta_{\text{mechanical}}$$

It should be noted that the engine was more sensitive to increases in turbo efficiencies rather than power turbine efficiencies because the power turbine was providing less work (lower  $\Delta T$ ). Also relevant to the turbomachinery improvement addition was the observed change in mass flow factors (casing sizes). The optimal turbo turbine flow factor increased with higher turbomachinery efficiencies. This occurred because a swallowing capacity increase was needed to compensate for a larger efficiency.

Due to a smaller pressure ratio across the turbo turbine, the power turbine pressure ratio was allowed to increase without increasing exhaust manifold pressure (PMEP). The result was a decrease in the optimal mass flow factor for the power turbine.

Another important observation from Table BI was that port insulation had little effect ( $\approx 3\%$ ) on engine performance. This occurred because heat rates flowing into the intake air and out of the exhaust gas were a small fraction of the input fuel energy rate. Dramatic changes in these heat rates had little effect on fuel economy. Also, gas-side resistance accounted for over half of the total resistance. Thus, changing only wall resistance had limited impact.

Lower FMEP and a shorter heat release duration provided approximately 34% of the total improvement. The decrease in FMEP improves mechanical efficiency which directly improves thermal efficiency according to equation III.6. The magnitude of improvement due to changes in heat release duration is dependent on engine speed. Improvement will be more pronounced at higher speeds.

### 6.3.4 Fixed Versus "Ideal" Variable Geometry Turbomachinery

To investigate the effects of "ideal" variable geometry (VG) turbomachinery, OPTDES was used to optimize each torque curve operating point for the improved engine without constraining the mass flow factors. This was compared to a fixed geometry (FG) engine in which all mass flow factors were equal to the values obtained for the "Design Point" as shown in Table III.3. Table III.5 presents the comparison in terms of BSFC.

**Table III.5:** Comparison of "Ideal" VG and FG turbomachinery

Operating Point	BSFC - "Ideal VG" (g/bkW-hr)	BSFC - FG (g/bkW-hr)	$\Delta$ BSFC
1800 rpm (336 bkW)	176	176	0
1600 rpm (306 bkW)	174	174	0
1400 rpm (277 bkW)	174	174	0
1200 rpm (247 bkW)	174	175	1

It was evident from the results generated in Table III.5 that ideal VG turbomachinery would provide a slight benefit over FG in fuel economy at one operating point. The improvement

occurred at 1200 rpm because the optimal turbo turbine flow factor (VG) was significantly smaller than the design point flow factor (FG) because of a lower engine airflow. The opposite was true for the power turbine. The optimal power turbine flow factor (VG) was significantly larger in order to compensate for the higher pressure ratio across the turbo turbine in comparison to the design point.

The “ideal” estimate, however, is an upper bound of improvement. Application of VG in a “real” engine could not achieve this improvement due to inefficiencies during turndown. It has been shown that VG may even hinder performance in comparison to fixed geometry situations.

### 6.3.5 Two Stage Turbocharging

Two-stage turbocharging was another alternative investigated in an attempt to increase thermal efficiency. Figure III.3 is a diagram of the two-stage compression model. This was the basis for thermodynamic calculations.

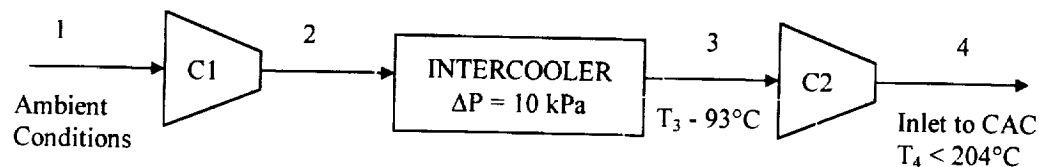


**Figure III.3:** Diagram of two-stage compression model.

The temperature constraint at the outlet in Figure III.3 was needed to assure the yield strength of the charge air cooler aluminum was not compromised. The pressure drop across the intercooler and the inlet temperature into the second compressor were assumed. Inlet pressure ratios ( $P_2/P_1$ ) were used as the independent variable from which the outlet pressure ratio ( $P_4/P_3$ ) could be determined. ( $P_4$  was held constant so boost pressure did not change.) The important result from this manipulation was the total power required for compression of the charge air. The power for each compressor was calculated with the following equation:

$$\text{Power} = \left[ (\dot{m} \times c_p \times T_{\text{inlet}}) / \eta \right] \times \left[ \text{PR}^{(k-1)/k} - 1 \right] \quad \text{III.7}$$

where,

$\dot{m}$  - air mass flow

$c_p$  - specific heat

$T_{\text{inlet}}$  - inlet temperature to compressor of interest

$\eta$  - compressor efficiency

PR - pressure ratio

$k$  - ratio of specific heat to specific volume

The goal of two-stage turbocharging was to decrease the power required to compress the charge air, which ultimately improves fuel economy. Results were generated over a large range of

pressure ratios. The compressor efficiency was assumed to be the same for each compressor and equivalent to the value observed in the TRANSENG output file at the design point.

It was found that required power actually increased at all pressure ratios. The pressure drop across the intercooler was significant due to the low overall pressure ratio across the entire system. Two-stage turbocharging with intercooling is most effective when large pressure ratios are a necessity (high horsepower engines). Thus, an increase was not a surprise.

The next step was to remove the intercooler and apply the ideal pressure ratio across each compressor. The ideal intermediate pressure between each compressor was found according to the equation:

$$P_{\text{IdealIntermediate}} = [P_{\text{Inlet}(C1)} \times P_{\text{Outlet}(C2)}]^{1/2} \quad \text{III.8}$$

The efficiency for each compressor was then corrected according to the map at the new pressure ratio. The resulting improvement was 0.25 bkW, which would provide a near negligible benefit in fuel economy (~ 0.1% BSFC). Once again, as with VG, the initial hardware cost outweighed expected benefits.

### 6.3.6 Conclusions - CD-50 Performance Analysis

Several important conclusions drawn from the CD-50 analysis follow.

- Addition of all subsystem improvements at the "Design Point" (1600 rpm and 306 kW) increased thermal efficiency from 45.0% to 47.9% (BSFC changed from 185 g/bkW-hr to 174 g/bkW-hr). Therefore, the goal of the study was not achieved under the given constraints.
- The magnitude of each improvement as a percent of the total was as follows:
  1. Port insulation - 2.7%
  2. Lower FMEP - 16.2%
  3. Shorter heat release - 17.3%
  4. Improved turbomachinery efficiencies - 63.2%
- Higher turbomachinery efficiencies had the most pronounced effect due to dramatic improvements in engine air handling losses. Future endeavors to lower fuel economy should emphasize this area of improvement.
- Reducing the heat rates into the intake air and out of the exhaust gas with port insulation had little effect on fuel economy because the rates were a small fraction of the total fuel input energy rate.
- "Ideal" VG turbomachinery provides a small benefit in fuel economy. However, inefficiencies in the "real" application may actually hinder engine performance.
- Two-stage turbocharging worsens fuel economy because pressure drops across the intercooler are significant in comparison to the overall pressure ratio.



#### 6.4 Appendix IV - Piston Surface Porosity Volume Calculation

Mercury porosimetry is a standard technique for characterization of porous materials. The technique relies on the fact that pressure required to force a non-wetting liquid into a pore depends on the pore size.<sup>‡</sup> Mercury is used in porosimetry since it does not wet most solids.

Four metal coated pistons (rough bond coated, low porosity coated, medium porosity coated and high porosity coated) were submitted for porosimetry analysis. Of the porosimetry data reported, the Total Intrusion Volume or total pore volume was of the greatest interest in this investigation. Because the thickness of each coating was not the same, a means for comparing the total pore volume among the different coatings was required. A decision was made to express the total pore volume as a percent of the total coating volume. However, a method for determining the coating volume was required.

Figure IV.1 is a representation of a piston crown sample used in the porosimetry analysis. The sample is shown as a steel (non-porous) substrate sprayed with a NiCr coating. An expression for total pore volume is shown below.

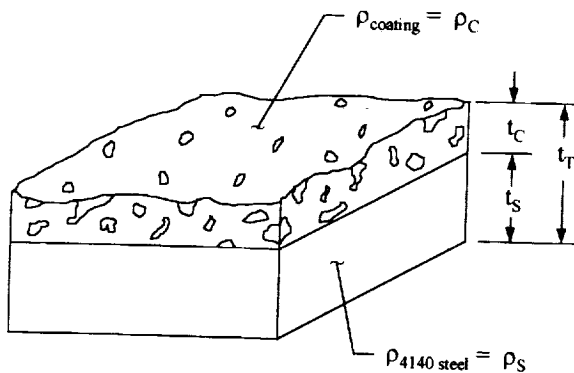
$$V_P = \frac{V_I}{(V_C + V_I)} \times 100\% \quad \text{IV.1}$$

$V_P \equiv$  Pore volume (%)

$V_I \equiv$  Intrusion volume

$V_C \equiv$  Coating volume

The intrusion volume is available from the porosimetry analysis. The coating volume can be calculated from additional measurements made during the porosimetry analysis. Derivation of the expression for the coating volume follows.



where,

$t_T$  = Sample thickness

$t_C$  = Coating thickness

$t_S$  = Steel substrate thickness

$\rho_C$  = Density of coating

$\rho_S$  = Density of 4140 steel substrate

Figure IV.1: Porosimetry sample.

The volume of the coating as defined by the coating thickness multiplied by the coating's projected planar area is the sum of the volume of the NiCr and the pore volume. The volume of the steel substrate ( $V_s$ ) is defined as the substrate thickness multiplied by the same planar area. These definitions are shown in equations IV.2 and IV.3.

$$(V_c + V_i) = t_c \times A_p \quad \text{IV.2}$$

$$V_s = t_s \times A_p \quad \text{IV.3}$$

Substitution of equation IV.3 into equation IV.2 yields equation IV.4.

$$\frac{t_c}{t_s} = \frac{(V_c + V_i)}{V_s} \quad \text{IV.4}$$

The mass of the porosimetry sample ( $M_s$ ) can be expressed as in equation IV.5.

$$M_s = \rho_s V_s + \rho_c V_c \quad \text{IV.5}$$

Equations IV.4 and IV.5 represent a system of two equations with two unknowns ( $V_s$  and  $V_c$ ). By solving Equation IV.5 for  $V_s$  and substituting  $V_s$  into Equation IV.4 an expression for the coating volume is obtained as shown in Equation IV.6.

$$V_c = \frac{\frac{t_c}{t_s} M_s - \rho_s V_i}{\rho_s + \frac{t_c}{t_s} \rho_c} \quad \text{IV.6}$$

The sample mass ( $M_s$ ), sample thickness ( $t_c$ ), and intrusion volume ( $V_i$ ) were obtained from the porosimetry analysis. The coating thickness ( $t_c$ ) was obtained from the spray coating vendor. The steel substrate thickness ( $t_s$ ) can be calculated knowing the sample thickness and the coating thickness. The density of the NiCr coating and the 4140 steel substrate were taken as 8.3 g/cm<sup>3</sup> and 7.8 g/cm<sup>3</sup>, respectively. The data used to calculate the pore volume as a percentage of the NiCr coating volume in Table 3.12.7 (see Section 3.12.1.2 **Experimental Measurements on the Effects of Piston Surface Roughness and Porosity - Experimental Method**) are shown in Table IV.1.

**Table IV.1:** Data used to calculate total pore volume

Piston Coating	Sample Mass (g)	Sample Thickness (mm)	Coating Thickness (mm)	Intrusion Volume (mm <sup>3</sup> )
Low Porosity	35.0	2.06	0.60	410
Medium Porosity	33.5	2.11	0.70	771
High Porosity	19.7	2.13	0.60	390

“PMI Automated Porosimeter - Enhanced Version Instruction Manual.” Porous Materials, Inc.



REPORT DOCUMENTATION PAGE			Form Approved OMB No. 0704-0188	
Public reporting burden for this collection of information is estimated to average 1 hour per response, including the time for reviewing instructions, searching existing data sources, gathering and maintaining the data needed, and completing and reviewing the collection of information. Send comments regarding this burden estimate or any other aspect of this collection of information, including suggestions for reducing this burden, to Washington Headquarters Services, Directorate for Information Operations and Reports, 1215 Jefferson Davis Highway, Suite 1204, Arlington, VA 22202-4302, and to the Office of Management and Budget, Paperwork Reduction Project (0704-0188), Washington, DC 20503				
1. AGENCY USE ONLY (Leave blank)	2. REPORT DATE June 1999	3. REPORT TYPE AND DATES COVERED Final Contractor Report		
4. TITLE AND SUBTITLE Development of Advanced In-Cylinder Components and Tribological Systems for Low Heat Rejection Diesel Engines Phases 2, 3, and 4 Final Report		5. FUNDING NUMBERS  DEN3-375		
6. AUTHOR(S) T.M. Yonushonis, P.D. Wiczynski, M.R. Myers, D.D. Anderson, A.C. McDonald, H.G. Weber, D.E. Richardson, R.J. Stafford, and M.G. Naylor				
7. PERFORMING ORGANIZATION NAME(S) AND ADDRESS(ES) Cummins Engine Company MC50183 1900 McKinley Avenue Columbus, Indiana 47201		8. PERFORMING ORGANIZATION REPORT NUMBER  E-11749		
9. SPONSORING/MONITORING AGENCY NAME(S) AND ADDRESS(ES) U.S. Army Research Laboratory Cleveland, Ohio 44135-3191  NASA Glenn Research Center Cleveland, Ohio 44135-3191		10. SPONSORING/MONITORING AGENCY REPORT NUMBER U.S. Department of Energy Office of Vehicle and Engine R&D Washington, D.C. 20545  NASA CR-1999-209163 DOE/NASA/0375-2 ARL-CR-442		
11. SUPPLEMENTARY NOTES  Prepared under Interagency Agreement DE-AI05-960R22547. Project Manager, Mark J. Valco, U.S. Army Research Laboratory, NASA Glenn Research Center, organization code 5950, (216) 433-3717.				
12a. DISTRIBUTION/AVAILABILITY STATEMENT  Unclassified - Unlimited Subject Category: 37  This publication is available from the NASA Center for AeroSpace Information, (301) 621-0390.		12b. DISTRIBUTION CODE		
13. ABSTRACT (Maximum 200 words)  In-cylinder components and tribological system concepts were designed, fabricated and tested at conditions anticipated for a 55% thermal efficiency heavy duty diesel engine for the year 2000 and beyond. A Cummins L10 single cylinder research engine was used to evaluate a spherical joint piston and connecting rod with 19.3 MPa (2800 psi) peak cylinder pressure capability, a thermal fatigue resistant insulated cylinder head, radial combustion seal cylinder liners, a highly compliant steel top compression ring, a variable geometry turbocharger, and a microwave heated particulate trap. Components successfully demonstrated in the final test included spherical joint connecting rod with a fiber reinforced piston, high conformability steel top rings with wear resistant coatings, ceramic exhaust ports with strategic oil cooling and radial combustion seal cylinder liner with cooling jacket transfer fins. A Cummins 6B diesel was used to develop the analytical methods, materials, manufacturing technology and engine components for lighter weight diesel engines without sacrificing performance or durability. A 6B diesel engine was built and tested to calibrate analytical models for the aluminum cylinder head and aluminum block.				
14. SUBJECT TERMS  Diesel engine; Engine Components; Turbocharger; Piston Rings; Lightweight diesel		15. NUMBER OF PAGES 289		
		16. PRICE CODE A13		
17. SECURITY CLASSIFICATION OF REPORT Unclassified	18. SECURITY CLASSIFICATION OF THIS PAGE Unclassified	19. SECURITY CLASSIFICATION OF ABSTRACT Unclassified	20. LIMITATION OF ABSTRACT	

